3D Bioprinting of Hyaline Cartilage using Nasal Chondrocytes

by

Xiaoyi Lan

A thesis submitted in partial fulfillment of the requirements for the degree of

Doctor of Philosophy

in

Civil (Cross-disciplinary)

Department of Civil and Environmental Engineering

University of Alberta

Abstract

Hyaline cartilage is a strong and flexible connective tissue found throughout the human body. It provides important structural and functional support for the nose, ribs, larynx, and trachea. Due to the avascular nature of the hyaline cartilage, its defects or lesions are non-regeneratable and non-healing, which can progress into diseases such as osteoarthritis (OA) or nasal airway obstruction and result in severe clinical complications. Cell-based cartilage tissue engineering using 3D bioprinting techniques can generate functionalized cartilage replacement *in vitro* using autologous cells, which can become a promising prospective treatment for these defects and lesions. The 3D bioprinting techniques allow on-demand fabrication of engineered and patient-specific cartilage tissue to replace damaged tissue and restore normal cartilage functions. However, existing 3D bioprinting research primarily focuses on the formulation and engineering of biomaterials, yet lacks thorough biochemical evaluations and substantial evidence to indicate the clinical potential of the bioprinted cartilage. To address this challenge, this thesis focuses on 3D bioprinting and regeneration of hyaline cartilage using naturally derived polymer, with in-depth evaluations of appropriate cell sources, *in vitro,* and *in vivo* biochemical and biomechanical performance of the engineered tissue.

Chapter 1 introduces the research topic with a review of hyaline cartilage structure, biochemical and biomechanical properties, potential cell source for engineered cartilage tissue, and suitable bioink materials used for 3D bioprinting. This review suggests that nasal chondrocytes are among the most suitable cell sources for hyaline cartilage regeneration. Chapter 2 provides

insights into the rheological and viscoelastic properties of collagen and their roles in micro-extrusion bioprinting.

The first project (Chapter 3) describes the 3D bioprinting of cartilage tissue using nasal chondrocytes laden type I collagen as bioink. A biomimicry shape with non-cytotoxicity was generated using a state-of-the-art freeform reversible embedding of suspended hydrogels (FRESH) 3D bioprinting technique. The engineered cartilage showed comparable biochemical properties to native nasal cartilage. The mechanical characterization and in vivo stability of the engineered nasal cartilage substitutes were needed to further support its potential for clinical application and formation of patient-specific surgical-ready shapes. Therefore, the second project (Chapter 4) extends this study and investigates chondrogenic culture's effects on the biochemical and mechanical properties of bioprinted constructs of nasal chondrocytes *in vitro* and *in vivo* in nude mice. Engineered nasal cartilage from nasal chondrocytes seeded on clinically approved type I/III collagen membrane scaffolds (Chondro-Gide) served as a control. The results showed excellent *in vitro* and *in vivo* performances comparable to those of clinically approved scaffolds. To further improve the printability and the shape integrity of collagen bioink, the third project (Chapter 5) used pre-crosslinked methacrylate collagen with thiolate hyaluronic acid and Poly(ethylene glycol) diacrylate (PEGDA) crosslinker as a bioink to investigate the printability and *in vitro* chondrogenesis. This novel bioink showed significantly improved printability, shape and size retention, and biochemical indicators compared to a collagen-only bioink.

This thesis extensively studied 3D bioprinting and regeneration of hyaline cartilage using type I collagen-based hydrogels with nasal chondrocytes. The study results pave the way for the clinical application of 3D bioprinting to treat cartilage defects.

Preface

This thesis is an original work by Xiaoyi Lan. Studies with human tissue were conducted in accordance with the research ethics approval from the clinical ethics board of the University of Alberta (ID: Pro00018778). The animal research work was conducted and approved in accordance with the protocol approved by the University of Alberta Animal Care User Committee (Study ID: AUP00001363).

As of October 2022, Chapter 1 is under review by Annals of Biomedical Engineering. Chapter 2-4 and Appendix A have been accepted or published in peer-reviewed journals. The detailed references and author contributions are listed below.

Chapter 1 has been submitted for publication in parts as Xiaoyi Lan, Yaman Boluk and Adetola B. Adesida, "3D bioprinting of hyaline cartilage using nasal chondrocytes". XL was responsible for the literature review, manuscript writing. YB and ABA were supervisory authors and contributed to the study design and manuscript editing.

Chapter 2 has been accepted for publication in part as: Xiaoyi Lan, Adetola B. Adesida, and Yaman Boluk, "Rheological and Viscoelastic Properties of Collagens and Their Role on Bioprinting by Micro-extrusion" Biomedical Material. XL was responsible for the literature review and manuscript writing. YB and ABA were supervisory authors and contributed to the study design and manuscript writing.

Chapter 3 has been published in parts as: Xiaoyi Lan, Yan Liang, Esra JN Erkut, Melanie Kunze, Aillette Mulet-Sierra, Tianxing Gong, Martin Osswald, Khalid Ansari, Hadi Seikaly,

Yaman Boluk, and Adetola B Adesida, “Bioprinting of human nasoseptal chondrocytes-laden collagen hydrogel for cartilage tissue engineering” The FASEB Journal, Journal vol.35, no. 3, p. e21191, 2021. XL conducted the experiments and was responsible for experimental design, data acquisition, analysis, and manuscript writing. YL, EJNE, MK and AMS were involved in immunofluorescence, gene expression, and cell culture experiments. MO, KA, and HS were involved in nasal cartilage procurement and review. TG contributed to the final manuscript review. YB conceived the rheological studies, supervised the study, and was responsible for the final manuscript review. ABA conceived the biological part of the study and supervised the study, and was responsible for the final review of the manuscript.

Chapter 4 has been published in parts as: Xiaoyi Lan, Yan Liang, Margaret Vyhlidal, Esra JN Erkut, Melanie Kunze, Aillette Mulet-Sierra, Martin Osswald, Khalid Ansari, Hadi Seikaly, Yaman Boluk, and Adetola B Adesida, “*In vitro* maturation and *in vivo* stability of bioprinted human nasal cartilage” Journal of Tissue Engineering, vol.13, p.20417314221086368, 2022. XL conducted the experiments and was responsible for experimental design, data acquisition, analysis, and manuscript writing. YL and MK contributed to the animal surgery. MV contributed to the manuscript writing. EJNE, MV, MK, and AMS were involved in immunofluorescence, gene expression, and cell culture. MO, KA, and HS were involved in nasal cartilage procurement and review. YB was involved in supervision and final manuscript review. ABA conceived and supervised the study, and was responsible for writing and final review of the manuscript.

Appendix A has been published in parts as: Xiaoyi Lan, Zhiyao Ma, Alexander R. A. Szojka, Melanie Kunze, Aillette Mulet-Sierra, Margaret Vyhlidal, Yaman Boluk and Adetola B

Adesida, “TEMPO-Oxidized Cellulose Nanofiber-Alginate Hydrogel as a Bioink for Human Meniscus Tissue Engineering” Frontiers in bioengineering and biotechnology, p.1033, 2021. XL designed and conducted the experiments and was responsible for data acquisition, analysis, and initial manuscript writing. ZM assisted with the data analysis, immunofluorescence staining, and manuscript writing. AS helped with mechanical testing and manuscript editing. MK performed qRT-PCR. AMS assisted with cell isolation and culture. MV helped with histology and cDNA preparation. YB and AA conceived the study, supervised the study, and were responsible for writing and the final review of the manuscript.

Acknowledgements

I still remember that my first meeting with my supervisors was a sunny afternoon in June 2017. During that meeting, I was introduced to a new world of biomaterial and tissue engineering, a completely different field from my undergraduate study. Little that I know that it became a fun, challenging, and rewarding five-year journey. First and foremost, I would like to express my sincere gratitude to my two supervisors, Dr. Adetola Adesida and Dr. Yaman Boluk, for introducing me to this fascinating research area and teaching me how to become an independent researcher. They were incredibly supportive throughout my research training and provided valuable guidance to help me tackle any obstacles along this journey. Their enthusiasm, vision and rigorous work ethic has inspired me to continue the research and achieve this Ph.D. degree.

I also want to express my appreciation to my advisory committee member Dr. Larry Unsworth, for reviewing my candidacy report and the thesis and providing his valuable comments. I would like to thank the examiners throughout the training. I thank Dr. Hasan Uludag and Dr. Samar Adeeb for their thoughtful input and constructive questions at my candidacy exam.

I would also like to thank my dear colleagues (and friends) who have supported and encouraged me through the last five years. I would particularly thank two of the senior PhDs, Dr. Yan Liang and Dr. Alexander Szojka, and two of the technicians, Aillette Mulet-Sierra and Melanie Kunze, at Dr. Adesida's lab. They were extremely generous in teaching me all the experimental techniques and biology knowledge. I also want to thank Zhiyao (Hilda) Ma for helping with the MATLAB and Python scripts for data analysis and my experiments. I would be remiss in not mentioning the other incredible colleagues and collaborators I have worked with over the past

five years, including Austyn Roelofs, Andrea Dimitrov, Clayton Molter, David (Xinzheyang) Li, Erica Chang, Esra Erkut, Hoda Elkhenany, Dr. Guoju Hong, Jonathan Stolz, Dr. Kezhou Wu, Dr. Lindsey Westover, Malou Sopcak, Margaret Vyhlidal, Dr. Michael Turner, Dr. Maria Alexiou, Dr. Rita de C´assia Marqueti, Dr. Ryan Chee, Samia Rahman, Safiyyah Oni, and Dr. Yussef Esparza.

I would like to extend my thanks to my friends Anky, Cindy, Erin, Hilda, Kelvin, Jingyi, Joanna, Lydia, Mathilda, Song, Tiffany and Yiyi. Their friendship and support during my Ph.D. journey mean the world to me. I also want to thank my dear and lovely fluffy friend, Maya, for bringing joy and companionship.

I want to say a heartful thank you to my parents for their unconditional love, encouragement, and financial support. Their belief in me has kept my motivation high during this process. Lastly, I wish to thank my fiancé, Sheng Nian Zhang, who has stood by me through all my travails, my fits of pique and impatience over the past five years. He gave me unconditional support and love and inspired me to grow, improve, and become a better me.

Table of Contents

CHAPTER 1. 3D BIOPRINTING OF HYALINE CARTILAGE USING NASAL CHONDROCYTES 1

1.1 INTRODUCTION 2

1.2 STRUCTURE, COMPOSITION, AND MECHANICAL PROPERTY OF NASAL AND ARTICULAR CARTILAGES 5

1.2.1 Structure 5

1.2.2 Biochemical composition 8

1.2.3 Mechanical properties 11

1.3 PREFERRED CELL SOURCES FOR CARTILAGE TISSUE ENGINEERING 13

1.3.1 Mesenchymal stem cells (MSCs) 14

1.3.2 Neural crest-derived stem cell (NCSC) 15

1.3.3 Articular chondrocytes (AC) and nasal chondrocytes (NC) 16

1.4 3D BIOPRINTING FOR CARTILAGE TISSUE ENGINEERING 19

1.5 BIOINK MATERIALS FOR CARTILAGE TISSUE ENGINEERING 23

1.5.1 Rheology 24

1.5.2 Crosslinking 25

1.5.3 Cell-biomaterial interactions 27

1.6 SUMMARY AND RESEARCH OBJECTIVES 27

CHAPTER 2. RHEOLOGICAL AND VISCOELASTIC PROPERTIES OF COLLAGENS AND THEIR ROLE IN BIOPRINTING BY MICRO-EXTRUSION 32

2.1 BACKGROUND ON BIOPRINTING OF HYDROGELS 33

2.2 COLLAGEN AS A BIOPRINTING MATERIAL 37

2.2.1 Structure 37

2.2.2 Extraction, Fibrillogenesis, and Crosslinking 39

2.2.3 Rheological Properties 46

2.2.3.1 Steady-state Shear Flow 48

2.2.3.2 Oscillatory Shear 57

2.2.3.3 Creep and Recovery 70

2.3 BIOPRINTING BY MICRO-EXTRUSION 71

2.3.1 Filament Extrusion 72

2.3.1.1 Needle (capillary die) flow 74

2.3.1.2 Filament Swell 80
2.3.1.3 Filament Distortion 82
2.3.2 Layer-stacking, Bonding, and Shape integrity 83
2.4 Cell Viability 85
2.5 Concluding Remarks and Future Directions 88
CHAPTER 3. BIOPRINTING OF HUMAN NASOSEPTAL CHONDROCYTES-LADEN COLLAGEN HYDROGEL FOR CARTILAGE TISSUE ENGINEERING..... 102
3.1 Introduction 103
3.2 Material and Methods 106
3.2.1 Human-derived Chondrocyte Isolation 106
3.2.2 Chondrocyte-laden Bioink Preparation 106
3.2.3 Rheological Characterization of Bioink and Printability Assessment 107
3.2.4 3D Bioprinting of type I collagen Hydrogel 107
3.2.5 Cell Viability Assay of Bioprinted Construct 108
3.2.6 Structural Integrity and Microstructural Details Evaluation of Bioprinted Construct. 109
3.2.7 Evaluations of the Effectiveness of Cartilage Tissue Formation 109
3.2.7.1 Sulfated glycosaminoglycan and DNA quantification 109
3.2.7.2 Histological and Immunolabeling 110
3.2.7.3 Real-time PCR 111
3.2.8 Statistics 112
3.3 Results 113
3.3.1 Bioink Characterization and FRESH 3D Bioprinting 113
3.3.2 Assessment of Tissue Engineered Nasal Cartilage 117
3.4 Discussion 122
3.5 Conclusions 126
3.6 Supplementary material 127
3.6.1 Fluid Dynamic Modelling of Bioprinter 127
3.6.2 LIVE/DEAD results 130
3.6.3 Donor Information 130
3.6.4 Bern score – a semi-quantitative scale to evaluate neocartilage 131

CHAPTER 4. *IN VITRO* MATURATION AND *IN VIVO* STABILITY OF BIOPRINTED HUMAN NASAL CARTILAGE 133

4.1 INTRODUCTION 134

4.2 MATERIALS AND METHODS 137

4.2.1 Ethics 137

4.2.2 Human nasal chondrocyte isolation 137

4.2.3 Nasal chondrocyte-laden bioink preparation 138

4.2.4 3D bioprinting of type I collagen hydrogels and cell seeding of Chondro-Gide scaffolds 139

4.2.5 Culture condition 140

4.2.5.1 *In vitro* culture condition 140

4.2.5.2 *In vivo* culture condition 141

4.2.6 Live/Dead Assay 142

4.2.7 Evaluation of cartilage formation 142

4.2.7.1 Sulfated glycosaminoglycans per DNA quantification 142

4.2.7.2 Histology and Immunofluorescence 143

4.2.7.3 Real-time RT-qPCR 146

4.2.8 Mechanical properties of cell seeded Chondro-Gide scaffolds and bioprinted constructs 147

4.2.9 Microstructure of cell seeded Chondro-Gide scaffolds and bioprinted constructs 148

4.2.10 Semi-quantitative Analysis 148

4.2.11 Data Analysis and Statistical Methods 149

4.3 RESULTS 149

4.3.1 3D bioprinting of engineered cartilage with autologous shapes 149

4.3.2 Live/Dead analysis of bioprinted constructs 150

4.3.3 Histological analysis of *in vitro* engineered cartilages 151

4.3.4 GAG/DNA quantification of *in vitro* engineered cartilages 155

4.3.5 Mechanical properties of *in vitro* engineered cartilages 156

4.3.6 SEM of *in vitro* engineered cartilages 157

4.3.7 Gene expression of *in vitro* engineered cartilages 158

4.3.8 Gross morphology of engineered cartilages after *in vivo* implantation in nude mice 161

4.3.9 Histology and immunofluorescence after *in vivo* implantation 163

4.3.10 Mechanical property after *in vivo* implantation 165
4.4 Discussion 166
4.5 Conclusion 173
4.6 Supplementary Material 174
CHAPTER 5. PRE-CROSSLINKED HYALURONIC ACID AND COLLAGEN BIOINK FOR CARTILAGE TISSUE ENGINEERING 181
5.1 Introduction 182
5.2 Materials and Methods 185
5.2.1 Human nasal chondrocyte isolation and expansion 185
5.2.2 Nasal chondrocyte-laden bioink preparation 187
5.2.3 Rheology characterization and 3D bioprinting process 187
5.2.4 Live/Dead Assay 188
5.2.5 Evaluation of cartilage formation 189
5.2.5.1 Gross morphology pictures and the contraction/swelling ratio 189
5.2.5.2 Sulfated glycosaminoglycans per DNA quantification 190
5.2.5.3 Histology and Immunofluorescence 190
5.2.5.4 Real-time qRT-PCR 191
5.2.6 Mechanical properties of engineered cartilage tissue 192
5.2.7 Data analysis and statistical method 193
5.3 Results 194
5.3.1 Rheology characterization and 3D bioprinting of engineered cartilage with autologous shapes 194
5.3.2 Gross morphology and contractility of *in vitro* engineered cartilage 197
5.3.3 Histological analysis of *in vitro* engineered cartilages 198
5.3.4 GAG/DNA quantification of *in vitro* engineered cartilages 199
5.3.5 Mechanical properties of *in vitro* engineered cartilages 200
5.3.6 Gene expression of *in vitro* engineered cartilage 200
5.4 Discussion 203
5.5 Conclusion 210
CHAPTER 6. CONCLUSION AND FUTURE WORK 211
6.1 Major Conclusions and Contributions 211
6.2 Future Work 212

REFERENCES..... 215

APPENDIX A. TEMPO-OXIDIZED CELLULOSE NANOFIBER-ALGINATE HYDROGEL AS A BIOINK FOR HUMAN MENISCUS TISSUE ENGINEERING..... 245

A.1 INTRODUCTION 246

A.2 MATERIALS AND METHODS 249

A.2.1 TCNF Synthesis and Preparation of TCNF/ALG Precursors 249

A.2.2 Rheological Characterization of TCNF/ALG Precursors as Potential Bioink Materials 250

A.2.3 Assessment of Printing Fidelity Before and After Crosslinking 251

A.2.4 Isolation of Human Meniscus Fibrochondrocytes 252

A.2.5 3D Bioprinting of TCNF/ALG and Collagen Bioinks..... 252

A.2.6 Viability in Bioprinted Constructs 253

A.2.7 Structural Integrity and Microstructural Evaluation of Bioprinted Constructs .. 253

A.2.8 Histological and Immunofluorescent Evaluation of Matrix Formation..... 254

A.2.9 Gene Expression Analysis 255

A.2.10 Biomechanical Characterization by Stress Relaxation Tests..... 256

A.2.11 Statistical Analysis..... 256

A.3 RESULTS 257

A.3.1 Rheology, and Printing Fidelity of TCNF/ALG Precursors 257

A.3.2 Histological and Biochemical Assessments..... 263

A.4 DISCUSSION 268

A.5 SUPPLEMENTARY MATERIAL..... 273

List of Tables

Table 1.1 Brief review of the printing method[106] 22

Table 1.2 3D bioprinted cartilage using nasal chondrocytes 30

Table 2.1 Crosslinking methods of collagens and their rheological/mechanical characterizations 43

Table 2.2 The power-law and Carreau model flow descriptions of collagen gels and solutions. 52

Table 2.3 Summary of recent research (2017-2022) on collagen and its 3D-printing applications 92

Table 3.1 Primer sequences for real-time PCR 112

Table 3.2 The Power Law fit of viscosity vs. shear rate curve 114

Table 4.1. Donors Information 138

Table 4.2. Primer Sequences for Real-Time RT-qPCR 146

Table 4.3. Bending modulus before and after implantation 166

Table 5.1.Donors Information 185

Table 5.2 Formulation of each group of bioink 187

Table 5.3 Primer Sequences for Real-Time qRT-PCR 192

List of Figures

Figure 1.1. Schematic diagram of (A) human nasal cartilage anatomy and (B) articular cartilage anatomy 7

Figure 1.2. A structural comparison between (A) articular cartilage and (B) nasal cartilage. 8

Figure 1.3. Schematic diamgram of commonly used bioprinting method, (A) Micro-extrusion Bioprinter, (B) Inkjet Bioprinter (C) Laser-assisted Bioprinter..... 21

Figure 2.1 Schematic display of factors playing roles in bioprinting. 37

Figure 2.2 The schematization of collagen structures: (a) Left-handed single polypeptide chain, (b) Right-handed triple helix (tertiary structure) structure of procollagen assembly, (c) Enzymes cleaved ends of procollagens form tropocollagen assembly, (d) Fibrils formed by rope-like coils of coils structure (tropocollagen units both within and between microfibers are cross-linked covalently), and (d) Fibers are bundles of twisted fibrils (Copyright (2021) National Academy of Science [176]). 38

Figure 2.3 Fibrils' diameter as a function of fibrillogenesis collagen concentration (adopted from [190]). 41

Figure 2.4 (a) Steady viscosity (η) against the shear rate of acidic solutions of collagen $\gamma(d\gamma/dt)$ for various collagen concentrations 0.6 $mg.ml^{-1} \leq c \leq 16$ $mg.ml^{-1}$ (Collagen concentrations in units of mg/mL are marked next to each curve), (b) Reduced viscosity (η_{sp}/c) against the collagen concentration. (adopted from [190]). 49

Figure 2.5 The viscosity and first normal stress coefficient as a function of shear rate for 35 mg/mL in a neutral solution (viscosity vs. share rate are replotted from [215]). 51

Figure 2.6 Storage G′ (O) and Loss G″ (△) moduli vs. frequency (a) at 16 mg mL^{-1}; (b) at 27 mg mL^{-1}, 48 mg mL^{-1}, 112 mg mL^{-1}, and 300 mg mL^{-1} (from [190]). 59

Figure 2.7 Shear viscosity and complex viscosity against shear rate and oscillation frequency (Cox-Merz plots) of 1.0% collagen in acetic acid solutions of (a) 2 M, (b) 0.1 M (adopted from [210]). 62

Figure 2.8 Temperature dependence of storage modulus (G') and tangent delta (tan δ) of 4% collagen (a) in acetic acid solution, (b) in the culture medium DMEM. (from [162]). 63

Figure 2.9 Maximum storage modulus and gelation temperature of collagen at different concentrations (from [162]). 64

Figure 2.10 Elastic modulus vs. frequency sweep of glutaraldehyde crosslinked collagen scaffolds (from [243]). 66

Figure 2.11 The storage modulus of collagen bioink (8 mg/mL in 0.5 mm riboflavin solution) as a function of pH (a) G'_0 of collagen bioink at 4 °C before gelation. (b) G'_∞ collagen bioink after complete gelation at 37 °C (from [212]). 67

Figure 2.12 Changes in viscoelastic properties of genipin crosslinked collagen (from [162]). 68

Figure 2.13 Amplitude sweep carried out up to 250% strain with the OHA2500/GC/ADH hydrogel (Adopted from [250]). 70

Figure 2.14 **a)**Creep compliance , **b**)recovery compliance rate curves of collagen solutions crosslinked with various GTA/collagen (w/w) ratios a: 0:1, b: 0.01:1, c: 0.03:1, d: 0.05:1, e: 0.1:1) (Adopted from [197]). 71

Figure 2.15 Types of gel drive systems in micro-extrusion 3D-printing..... 73

Figure 2.16 Schematics of needle rearrangements used in calculations: (a) straight circular needle; (b) converging conical needle. 75

Figure 2.17 Applied experimental and calculated needle pressures vs. measured flow rate in (a) cylindrical geometry with needle length: 19.0 mm, needle diameter: 0.60 mm; (b) conical geometry with needle length: 19.0 mm, entrance diameter: 4.2 mm, exit diameter: 0.41 mm (unpublished results)..... 77

Figure 2.18 Computational fluid dynamic analysis of the printing setup. The red/orange colour indicates regions of high shear stress in the simulation with apparent differences between the straight and the conical needle geometries (adopted from *[225]*). 78

Figure 2.19 The likely streamline rearrangement of fluid after exiting from a capillary. 80

Figure 2.20 Extrusion of a 0.4% borax solution (A) smooth surface at the lowest speed (W_e=2.8, (B) development of a small roughness at intermediate speed (W_e=4.9), (C) well-developed melt fracture at the highest speed (W_e=8.4) (from [255]). 82

Figure 2.21 (a) Layer-stacking stage of bioprinting, (b) stacking of filament layers, (c) bonding of two filaments. 84

Figure 2.22 a) Evaluation of printability under three different states *[233]*, b) Printed construct at different concentrations. The printability parameter, Pr, is defined as $L^2/4A$ where the L and A is the filament perimeter and area, respectively (from *[233]*). 85

Figure 3.1 Printability characteristics of cell-free and cell-laden collagen hydrogel. (A) Steady state flow sweep from shear rate of 0.001 s -1 to 1000 s -1. The dash line represents the linear fit based on Power Law model; (B) The theoretical extrusion velocity as well as the measured extrusion velocity vs. input pressures; (C) The theoretical wall shear stress vs. the extrusion velocity. 114

Figure 3.2 Rheological characterization of cell-free and cell-laden collagen hydrogel. (A) Oscillatory temperature sweep results of bioinks and gelatin bath at 1 Hz and 1% strain, from 4°C to 45 °C. G' represents the storage modulus and G'' stands for the loss modulus; (B) The frequency sweep results of NCs-laden and NCs-free bioinks from 1 rad/s to 100 rad/s at 1% strain and 20 °C. 115

Figure 3.3 Gross appearance and cell-viability assessment of FRESH structures of (A) 3D model of the square block, human nose, and cylindrical disc parts are imported to Slic3r and the previews of the sliced parts are displayed. Image of 3D bioprinted structures in gelatin support bath (GSB) captured before incubation. After 30 minutes of incubation, image of the 3D bioprinted structures. The support bath was carefully aspirated, and PBS was added. (B) LIVE/DEAD assay of 20G and 22G needles, after 3 days of chondrogenic culture. The green color represents the viable cells, red color represents the dead cells. (C) Gross morphology of FRESH bioprinted construct before and after 6 weeks of culture. 116

Figure 3.4 Safranin O histological assessment of native and bio-printed cartilage quality. The Safranin-O staining of NCs-free and NCs-laden constructs and the native cartilage tissue after 6-week *in vitro* culture (A – L); (M) The semi-quantitative analysis of cartilaginous tissue formation based upon the Bern Score. (n = 6 blinded individual observers). Scale bar = 100 µm. 118

Figure 3.5 Wet weight and biochemical quantification of cartilage matrix production. The normalized values of GAG quantities between bioprinted scaffolds and the native cartilage tissue with respect to the total quantity of DNA (µg/µg) and the total wet weight of specimen (µg/mg). The asterisk symbol (*) indicates that values are significantly different at $p < 0.05$. (n = 4 donors for bioprinted scaffolds and 6 for native cartilage tissues) 119

Figure 3.6 Type I and II collagen immunofluorescence of native and bio-printed cartilage. The immunofluorescence results of NCs-free, NCs-laden constructs and the native cartilage tissue after 6-week *in vitro* culture. The blue color from DAPI staining indicates cell nuclei, the red and green colors represent the presence of type I and type II collagens, respectively. Scale bar = 100 µm. 120

Figure 3.7 Ultrastructural characterization of bio-printed of cell-free and cell-laden collagen hydrogel. The microstructures of NCs-free (A-D) and NCs-laden (E-H) constructs after 6-week *in vitro* culture taken by SEM; (A, B, E & F) show the microstructure on the construct surface and (C, D, G & H) show the cross-section of the construct. Scale bar = 5 µm. 121

Figure 3.8 Molecular gene expression characteristics of native and bio-printed cartilage. (A) The fold changes of genes expressed in the bioengineered cartilage scaffold of 6-week *in vitro* culture as compared to the monolayer of NCs; (B) The fold changes of genes expressed in the bioengineered cartilage scaffold of 6-week *in vitro* culture as compared to the native cartilage tissue. Genes with fold changes increased by 2-fold or reduced by

one-half are defined as significant upregulated or downregulated, respectively. ($p < 0.05$) 122

Figure 4.1. Schematic diagram of experimental design..... 140

Figure 4.2. Gross morphology of the FRESH printed structure. (A) 3D model of a right lower lateral nasal cartilage from CT imaging and (B) the preview of the sliced nasal cartilage using Slic3r software. (C) 3D bioprinted lower lateral nasal cartilage in gelatin support bath before and (D) after 30 minutes incubation in 37 °C. Following the 30-minute incubation, the support bath was aspirated, and PBS was added..... 150

Figure 4.3. (a) Live/dead assay (b) cell viability over culture time. Paired t-tests were done to compare cell viability between Day 1 vs. 3 weeks, 3 weeks vs. 6 weeks, and 6 weeks vs. 9 weeks. * Represents $0.01<p<0.05$. Scale bar: 100µm 151

Figure 4.4. Histological and biochemical analysis of *in vitro* constructs across culture time. (a) Safranin-O/Fast green Staining, (b) Masson's Trichrome staining, and (c) GAG/DNA of *in vitro* constructs. Black arrows indicate tissue areas that have (a) positive Safranin-O staining for aggrecan or (b) positive aniline blue for collagen (b). Data were analyzed by two-way ANOVA and corrected with the Bonferroni *post hoc* test. GAG; glycosaminoglycan, NS; non-significant, WW; wet weight. Scale bar: 100µm. Star (*) represent the significant difference with regarding of culture time after Bonferroni *post hoc* correction: * represents $0.01<p<0.05$, ** represents $0.001<p<0.01$, *** represents $0.0001<p<0.001$, **** represents $p<0.00001$. Pound (#) represent the significant difference with regarding of scaffold type after Bonferroni *post hoc* correction: # represents $0.01<p<0.05$, ## represents $0.001<p<0.01$, ### represents $0.0001<p<0.001$, #### represents $p<0.00001$. 154

Figure 4.5. Immunofluorescence of in vitro constructs across culture time. (a) Type I (red) and II (green) collagen, and (b) Type X collagen (red). The blue color is from DAPI staining, which indicate cell nuclei. Scale bar: 100µm..... 155

Figure 4.6. (a) Suturability of Chondro-Gide scaffolds and bioprinted constructs across culture time. Images are taken at 0.65x and 1.60x magnification. (b) Bending modulus of in vitro constructs across culture time. Data was analyzed by two-way ANOVA and corrected with the Bonferroni post-hoc test. NS; non-significant. Scale bars: 6 mm and 3 mm for 0.65x and 1.60x, respectively. Star (*) represent the significant difference with regarding of culture time after Bonferroni post hoc correction: * represents $0.01<p<0.05$, ** represents $0.001<p<0.01$, *** represents $0.0001<p<0.001$, **** represents $p<0.00001$. Pound (#) represent the significant difference with regarding of scaffold type after Bonferroni post hoc correction: # represents $0.01<p<0.05$, ## represents $0.001<p<0.01$, ### represents $0.0001<p<0.001$, #### represents $p<0.00001$..... 157

Figure 4.7. SEM imaging of in vitro constructs across culture time. Magnification of images is 35x, 100x, 1000x, and 2000x. Scale bars are 100µm, 10µm, and 2µm for 35x/100x, 1000x, and 2000x, respectively. 158

Figure 4.8. Gene expression of in vitro constructs. Values shown are 2-ΔCt values from RT-qPCR. Statistics were done using ΔCt values. Data was analyzed by two-way ANOVA and corrected with the Bonferroni post-hoc test. Housekeeping genes used were ACTB, B2M, and YWHAZ. n=6 donors (in duplicate). NS; non-significant. Star (*) represent the significant difference with regarding of culture time after Bonferroni post hoc correction: * represents 0.01<p <0.05, ** represents 0.001<p<0.01, *** represents 0.0001<p<0.001, **** represents p<0.00001. Pound (#) represent the significant difference with regarding of scaffold type after Bonferroni post hoc correction: # represents 0.01<p <0.05, ## represents 0.001<p<0.01, ### represents 0.0001<p<0.001, #### represents p<0.00001. 160

Figure 4.9. (a) Gross morphology of constructs and scaffolds before and after implantation (b) Histology and immunofluorescence of in vivo bone formation proteins, including type X collagen (red represents positive type X collagen, which is a marker of chondrocyte hypertrophy), CD31 (green represents positive CD31, CD31 is a marker of angiogenesis), BSP (red represents positive bone sialoprotein formation), and Alizarin Red (Orange color represents positive calcification). COL10; type X collagen, CD31; cluster of differentiation 31, BSP; bone sialoprotein. Scale bar: 100µm. 162

Figure 4.10. Histology and immunofluorescence of chondrogenic related proteins, including Safranin-O/Fast Green straining, Masson's Trichrome staining, and type I and II collagens immunofluorescence. Scale bar: 100µm..... 165

Figure 5.1 Reaction mechanism of the COLMA, COLMA+THA, COLMA+PEGDA bioinks 184

Figure 5.2 Schematic Diagram of the experimental setup 186

Figure 5.3 3D-bioprinting related rheological and cell viability characterization. (A) The steady state flow sweeps of three bioinks, strain rate from 0.001 to 1000 s^{-1}, at 16°C (without UV crosslinking) (B) The temperature ramp sweep of three bioinks from 16°C to 40°C at 10 rad/s (without UV crosslinking) (C) The frequency sweep of three bioinks, angular frequency from 1-100 rad/s (without UV crosslinking) at 16°C (D) The frequency sweep of three bioinks, angular frequency from 1-100 rad/s (after UV crosslinking) at 16°C (E) 3D bioprinted mesh structure using three bioinks. Scale bar: 1 cm (F) Quantified cell viability of bioprinted constructs before and after UV crosslinking (n=4), Star (*) represent the significant difference with regarding of types of bioink after Tukey's post hoc correction: * represents 0.01<p <0.05, ** represents 0.001<p<0.01, *** represents 0.0001<p<0.001, **** represents p<0.0001. Pound (#) represent the significant difference with regarding of the effect of UV curing after Tukey's post hoc correction: # represents 0.01<p <0.05, ## represents 0.001<p<0.01, ### represents 0.0001<p<0.001, #### represents p<0.0001. (G) Live/dead images after bioprinting, with and without UV crosslinking, live cell appears green and dead cell appears red, Scale bar: 100µm 196

Figure 5.4 (A) Gross morphology of engineered cartilage using COLMA, COLMA+THA, COLMA+THA+PEGDA bioink materials with nasal chondrocytes after 6 weeks of *in vitro* chondrogenic culture. Scale bar: 2mm (B) The contractility (negative -) and the swelling (positive +) of the construct compared to the initial casting area (29mm2). (C) the absolute area changes of the constructs before and after *in vitro* culture. 197

Figure 5.5 Qualitative histology and immunofluorescence investigation of cartilaginous ECM for engineered cartilages (A) Safranin-O staining (red or pink represents proteoglycan, green represents collagen-based protein), type I collagen and II staining (red represents type I collagen, green represents type II collagen, blue represents DAPI), Collagen X staining (red represents collagen X, blue represents DAPI). Quantitative physical and biochemical analysis of engineered cartilages (B) DNA content in the constructs (C) GAG/DNA (D) Weight wet (WW) (E) GAG/WW. p values are from one-way ANOVA with Tukey's post hoc test. Star (*) represent the significant difference with regarding of types of bioink after Tukey's post hoc correction: * represents $0.01<p<0.05$, ** represents $0.001<p<0.01$, *** represents $0.0001<p<0.001$, **** represents $p<0.0001$. 198

Figure 5.6 Mechanical property of the bioinks, (A) Example of strain steps and data acquisition of the unconfined compression test (B) Equilibrium modulus as a function of the cumulative strain (n=5) (c) Peak modulus as a function of the cumulative strain (n=5). Star (*) represent the significant difference with regarding of types of bioink after Tukey's post hoc correction: * represents $0.01<p<0.05$, ** represents $0.001<p<0.01$, *** represents $0.0001<p<0.001$, **** represents $p<0.0001$. 200

Figure 5.7 **(**a) Hyaline cartilage related gene expression of the engineered cartilage after 6 weeks of *in vitro* chondrogenic culture (n=5). (b) Pearson correlation heatmap of analyzed factors. Star (*) represent the significant difference with regarding of types of bioink after Tukey's post hoc correction: * represents $0.01<p<0.05$, ** represents $0.001<p<0.01$, *** represents $0.0001<p<0.001$, **** represents $p<0.0001$..... 202

Figure A.1 Schematic diagram of the experimental design. (A) Biomaterial formation and characterization, (B) engineered tissue formation, and (C) evaluation of engineered tissues. 249

Figure A.2 Fourier transform infrared spectroscopy of the pure cotton cellulose and TCNF. 258

Figure A.3 The rheology behaviors of the TCNF/ALG precursors. (A) the steady state flow sweeps, strain rate from 0.001 to 1000 s-1 (B) three-step recovery and thixotropic behavior, low shear rate at 1 s-1 for 100 s for initial and final step, high shear rate at 1000 s-1 for 100s for middle step, (C) loss tangent of the TCNF/ALG precursors from 1 to 100 rad/s. The formulations are described in Table A.1..... 261

Figure A.4 (A) Printed mesh structures using different formulations of TCNF/ALG precursors (B) Live/dead images of the (B1) 7030, (B2) 8020, and (B3) COL bioinks.

Live cells appear green and dead cells red. (C) Quantitative cell viability of the Live/Dead assay images 263

Figure A.5 Safranin-O staining (red, stained negatively charged proteoglycans and the TCNF) with Fast Green counterstain (green, stained proteins) and cells stained with hematoxylin of (A & B) 7030, (C & D) 8020, and (E & F) COL I bioinks. Scale bar is 100 μm. . 264

Figure A.6 Immunofluorescent staining of (A, B, & C) of aggrecan (red), (D, E & F) collagens I and II (red and green, respectively), and (G, H & I) collagen X. The staining of nuclei is blue. Scale bar is 100 μm 265

Figure A.7 SEM images of the bioprinted constructs after 6 weeks of *in vitro* culture, (A & B) the cross-section of the 7030 bioink (C & D) surface of the 7030 bioink, (E & F) cross-section of the 8020 bioink, (G & H) surface of the 8020 bioink 265

Figure A.8 Fibrocartilage related gene expression of bioprinted constructs after 6 weeks of *in vitro* chondrogenic culture (n=3). * represents $p<0.05$ 267

Figure A.9 Mechanical properties of the bioprinted constructs: (A) an example of data acquisition of the strain-controlled unconfined compression test (B) the peak modulus as a function of the cumulative strain (n=3). * represents $p<0.05$ 268

Figure A.S 1 Safranin-O staining of the empty TCNF/ALG scaffold (A) 7030 (B) 8020. Scale bar is 100 μm 273

List of Abbreviation

3D	three-dimensional
AC	articular chondrocyte
AD-MSC	adipose-derived stem cell
AM	additive manufacturing
BM-MSC	bone marrow-derived MSC
BSP	bone Sialoprotein
CAD	computer-aided design
CNF	cellulose nanofiber
COLMA	methacrylate collagen
CPD	cumulative population doubling
CZ	calcified zone
DAPI	4’,6-diamidino-2’- phenylindole
dECM	decellularized extracellular matrix
DMEM	Dulbecco’s Modified Eagle Medium
DZ	deep zone
ECM	extracellular matrix
EDAC	1-ethyl-3-(3-dimethyl aminopropyl) carbodiimide
E_Y	young’s modulus
FGF	fibroblast growth factor
FRESH	freeform reversible embedding of suspended hydrogel
G'	Storage modulus

G"	loss modulus
GAG	glycosaminoglycans
GC	glycol chitosan
GMP	good manufacturing practice
GTA	glutaraldehyde
H_A	aggregate moduli
HA	hyaluronic acid
HDMI	1,6 hexamethylene diisocyanate
HEPES	4-(2-hydroxyethyl)-1-piperazineethanesulfonic acid
HGSC	human gingival stem cells
HPLSC	human periodontal ligament stem cells
iPSC	induce pluripotent stem cells
ITS	insulin-transferrin-selenium
LAB	laser-assisted bioprinting
LAP	lithium phenyl-2,4,6-trimethylbenzoylphosphinate
LLC	lower lateral cartilage
LOX	lysyl oxidase
MDC	mesoderm-derived cells
MSC	mesenchymal stem cells
MZ	middle zone
NC	nasal chondrocytes/nasoseptal chondrocytes
NCDC	neural crest-derived cells

OA	osteoarthritis
OHA	partially oxidized hyaluronate
P2	passage 2
PCL	polycaprolactone
PD	population doubling
PEGDA	poly (ethylene glycol) diacrylate
PGA	polyglycolide
PLA	polylactic acid
PLGA	poly(lactic-co-glycolic acid)
rBM	reconstituted basement membrane matrix
RGD	arginine-glycine-aspartic
SM-MSC	synovial membrane MSC
SZ	superficial zone
TGF-β	transforming growth factor beta
THA	thiolate hyaluronic acid
ULC	upper lateral cartilage
UTS	ultimate tensile strength

CHAPTER 1. 3D bioprinting of hyaline cartilage using nasal chondrocytes

Contribution author: Xiaoyi Lan, Yaman Boluk, Adetola B. Adesida

Chapter 1 has been submitted for publication in parts as:

Xiaoyi Lan, Yaman Boluk and Adetola B. Adesida, “3D bioprinting of hyaline cartilage using nasal chondrocytes”.

1.1 Introduction

Cartilage is the main type of connective tissue throughout the human body, serving various structural and functional purposes and exists in different types in our joints, spine, lungs, ears and nose. Three types of cartilage are found in the human body, including hyaline, elastic, and fibrous, characterized based on histological criteria and mechanical properties[1]. Among them, hyaline cartilage is the most common type of cartilage found in the ribs, nose, articular, larynx and trachea. The hyaline cartilages cover the bone ends to create a low friction environment and cushion the joint surface; they can also act as structural supports and contribute to the elasticity of the nose, ribs, larynx, and trachea[1]. The orthopedical and maxillofacial regions are two of the most common regions for hyaline cartilage defects. It is estimated that 37% of adults over 65 years in USA suffers osteoarthritis which is characterized by progressive loss of hyaline cartilage[2]. Deviated nasal septum has been observed in 80% of the general population and it is a major cause of airway obstruction[3]. Defective hyaline cartilage, depending on its location, can also lead to different diseases and affect donor-site functions[4]. These defects are usually caused by injury, wear and tear, congenital malformation, skin cancer removal, to mention a few. Due to the lack of vascularity, damaged hyaline cartilage has limited spontaneous self-repair and regenerative capabilities. Therefore, special therapies are needed to repair the damaged hyaline cartilage[4].

In the orthopedics, articular cartilage injury is a significant risk factor for the development of osteoarthritis (OA) – a condition causing significant patient morbidity and substantial cost to the health care systems. The current treatment modalities include marrow stimulation, osteochondral

tissue transplantation using autograft or allograft, cell-free biomaterial matrix implantation and autologous chondrocyte transplantation[5].

In the maxillofacial region, damage or malformation of the nose cartilage structures may compromise nasal airway function or facial aesthetics. Nasal cartilage repair usually involves the transplantation of cartilage grafts from other anatomical sites in lieu of the damaged tissue to modify or rebuild the framework of the nose. These grafts are then covered by a skin flap, acting as structural support to resist the force of contraction and fill the loss of nasal cartilages or fibromuscular fatty tissues in the alar lobule area. Currently, the commonly used nasal cartilage graft materials include autologous cartilage grafts, allogeneic grafts, and synthetic materials [6].

Despite positive outcomes reported using these treatments [7-16], several inherent shortcomings still exist with these established treatment modalities. The marrow stimulation in the orthopedic region is not appropriate for large defects, resulting in resurfacing with fibrocartilage[17], which presumably does not adequately restore joint congruity and loses distribution in joints with larger critical-sized defects[18]. Autografts used in osteochondral and maxillofacial regions can produce donor site morbidity[6]. The autografts from rib cartilage are also associated with warping and calcification for maxillofacial reconstruction[6]. The synthetic material used for the maxillofacial region has the issue of infection, foreign body reaction, dislocation and extrusion[6]. Allograft transplantation is logistically challenging given the need for testing the infectious diseases, sterilization, high resorption rate, and donor-recipient size and shape matching[6]. Thus, alternative techniques that consider both the biocompatibility and the complexity related to the anatomical 3D geometry are essential for treating cartilage defects.

In recent years, cell-based tissue-engineered cartilage grafts using 3D bioprinting technology have demonstrated the potential to overcome the shortcomings of conventional cartilage grafts[3, 6]. The traditional cell-based engineered cartilage grafts are designed to utilize the patient's cell embedded within a biomaterial scaffold to regenerate a "live" cartilage tissue *in vitro*, then implanted into the patient. However, this method is limited by the size/shape of biomaterial scaffold, lack of spatial control over the placement of functional constituents (including biomaterials and cells) in the fabricated structure. On the other hand, the 3D bioprinting strategy allows the fabrication of patient-specific geometry and provides specific functional requirements for each cartilage defect. For example, 3D bioprinting can provide personalized cartilage grafts for patients with nasal defects; it can also spatially pattern cells and biomaterials for articular cartilage defects, which are usually anisotropic and have zone variations. To successfully yield an optimal 3D bioprinted cartilage graft for clinical translation, three key elements need to be satisfied: 1) successful *in vitro* differentiation of the 3D bioprinted construct under chondrogenic culture, 2) mechanical properties similar to native tissue, and 3) further stability and maturation *in vivo,* in terms of maintaining the cartilage phenotype of the graft and new tissue formation. The current 3D bioprinting research mainly focuses on biomaterial and *in vitro* performance of the 3D bioprinted constructs, but it still lacks in-depth discussion regarding the cell selections and the *in vivo* stability after printing. In recent years, nasal chondrocytes (NC), as a neural crest derived cell source has demonstrated the ability to retain chondrocytic phenotype across serial cloning, as well as respond to physical forces that resemble joint loading and adapt to heterotopic transplantation site[19-21]. Based on these findings, NCs laden-tissue engineered cartilage grafts were clinically used in nasal reconstructive surgery and to repair articular cartilage defects[6, 22, 23].

In this review, we first review the intrinsic properties of native nasal cartilage and articular cartilage to establish the requirement for 3D bioprinting of cartilage tissue. We then aim to review the current literature and provide opinions on the cell selection, bioprinter, and bioink materials. We also identified the current challenges and the directions for future developments in hyaline cartilage regeneration.

1.2 Structure, composition, and mechanical property of nasal and articular cartilages

1.2.1 Structure

Articular cartilage is a thin connective tissue layer covering the surfaces of diarthrodial joints. It rests on a firmly fixed subchondral osseous plate, and the other end of the articular cartilage blends gradually with the synovial membrane and periosteum, as shown in Figure 1.1A. The thickness of human adult articular cartilage is about 2-4mm[24, 25]. The unique properties of articular cartilage permit the distribution of high loads, maintenance of low contact stresses, and creation of a low friction environment during movement and shock absorption[24].

Articular cartilage exhibits a zone difference, where each zone provide different functional properties for the cartilage tissue. Each of the zone, including the superficial zone (SZ), middle zone (MZ), deep zone (DZ), and calcified zone (CZ), are differentiated by their matrix composition, cell morphology, and mechanical properties[26, 27]. Figure 1.2A illustrates the non-homogenous distribution of cells and ECMs in zones of matured articular cartilage. SZ accounts for 10-20% of the total articular cartilage thickness, surrounded by thin but densely packed collagen fibrils oriented parallel to the articular surface. The chondrocytes in the superficial zone of the matrix, are usually flatter, smaller, and more densely packed compared to the cells found deeper in the

matrix. SZ also contains the highest collagen density within the tissue but has the lowest percentage of aggrecan compared to other zones. The MZ constitutes 40-60% of the total volume of articular cartilage and comprises of proteoglycans and thicker collagen fibrils. This layer harbors cells that are more spherical in shape and exhibit a lower cell density, in addition to the highest proteoglycan content within the tissue. The orientation of collagen fibrils in the MZ undergoes a transition, characterized by a shift from a parallel alignment in the SZ to a random orientation within the MZ. DZ is located between MZ and CZ layers, which represents approximately 30% of AC volume. Deep zone contains the lowest level of cell density but the largest collagen fibril in diameter. The collagen fibrils transit from random orientation in MZ to perpendicular (radial) orientation in the DZ to strengthen the bond between cartilage and bone. In DZ, the chondrocytes are parallel to the organized collagen fibres. The size of the collagen fibre gradually increases from SZ to DZ, but with decreased collagen and water content. CZ is the transitional zone from articular cartilage to subchondral bone. The chondrocytes in the calcified zone usually express the hypertrophic phenotype. CZ contains small cells within a matrix that has chondroid properties and is speckled with apatitic salts [27-29].

The nose is the prominent structure that provides air passage for respiration and provides the sense to smell. Due to its central location, it also plays a vital role in facial aesthetics. The skeleton of the nose is formed by three types of tissue: bone, cartilage, and fibro-fatty tissue. Although bones contribute to the skeletal framework of a human nose, the external shape is mainly attributed to the soft tissue structures (cartilage, fibro-fatty tissue) rather than the underlying bones[30]. Nasal cartilages are hyaline cartilages categorized into three structures or functional subunits: nasal septum cartilage, paired upper lateral cartilage (ULC), and paired lower lateral cartilage (LLC), as shown in Figure 1.1B. The nasal septal cartilage, also known as the central

septum, divides the nose into two cavities. It provides midline structural support for the soft lateral side wall and helps resist deformation [3]. The ULC extends off the septum and interfaces with the upper nasal bones and lateral maxilla [3]. The ULC and septum cartilage form the soft lateral sidewall and medial wall of the nasal vault, which maintains normal airflow through the nose and plays a significant role in the overall anatomic shape of the nose[3, 31]. The LLCs, also known as alar cartilages, form the nasal tip and constitute the external valve [3].

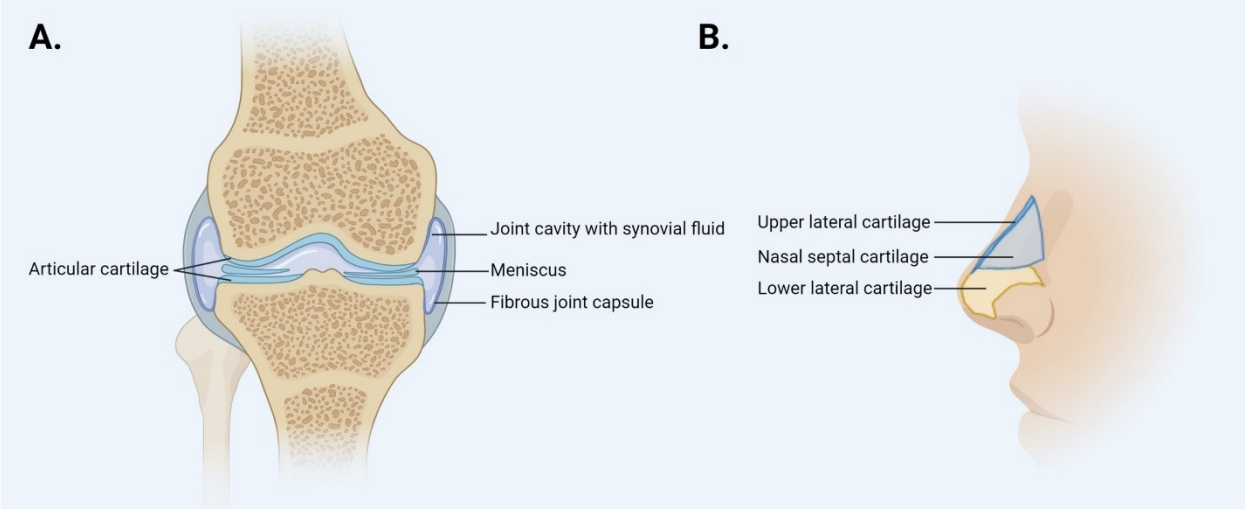

Figure 1.1. Schematic diagram of (A) human nasal cartilage anatomy and (B) articular cartilage anatomy

Similar to articular cartilage, nasal cartilage also exhibit zone differences, including superficial (peripheral), intermediate and central zone, as shown in Figure 1.2B. Popko et al. found a distinct transition of cell numbers, morphology, and orientation from the surface to the central zone in both septum cartilage and LLC: chondrocytes gradually become larger and more rounded with decreasing cell numbers. The nasal cartilage surface usually contains numerous small and flat chondrocytes orienting parallel to the surface. The central zone has less numerous, clustered, lager, oval-shaped chondrocytes oriented perpendicular to the surface [32]. These differences represent the change in form and position between younger and mature cells [32]. The reason for

the transition in position is still underdetermined. Nasal cartilage also shows distinct collagen deposition in different zones. The peripheral zone shows more intense collagen staining than the central zone, and this observation is more evident in septal cartilage than LLC [32]. Also, using Herovici and Lawson staining, the matrix of the peripheral zones for both septal and LLC stains light blue, a characteristic of young collagen. In contrast, the matrix of the central zone has a more reddish colour, specific to mature collagen [32].

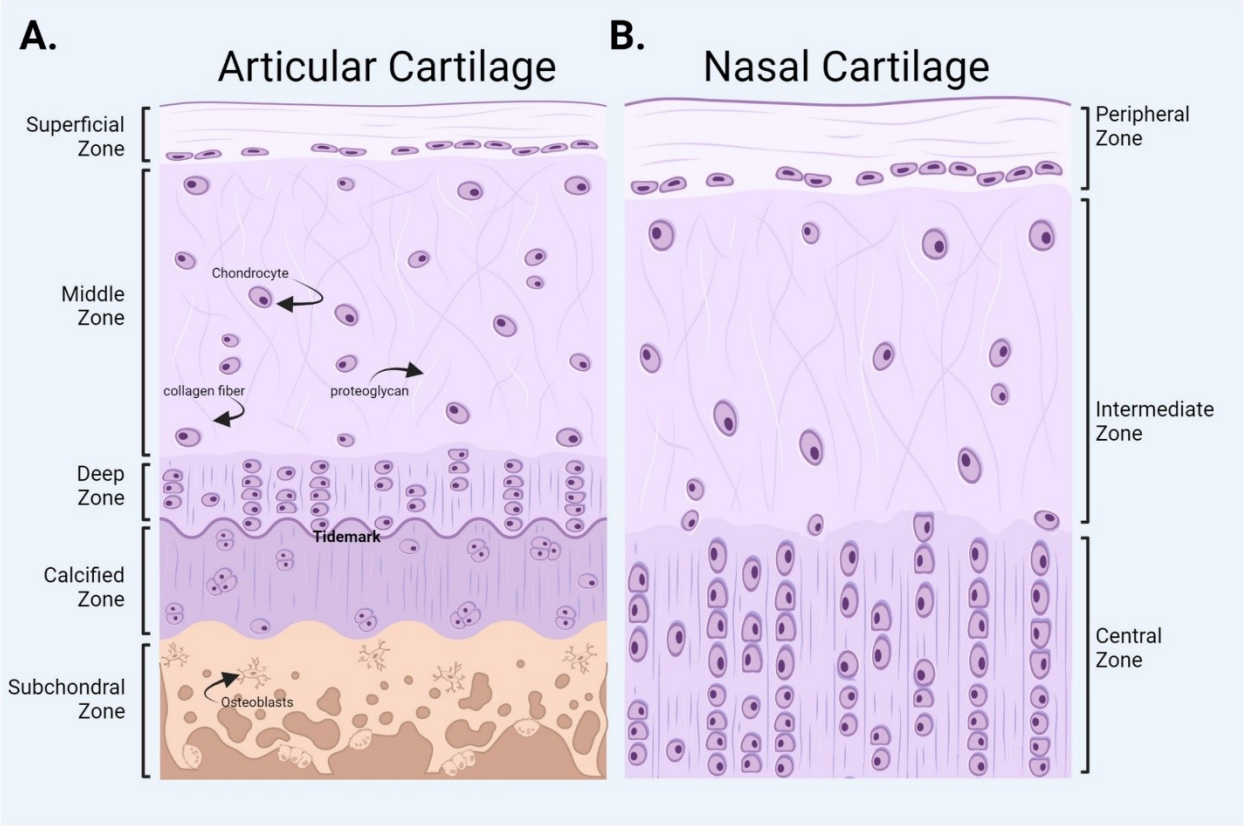

Figure 1.2. A structural comparison between (A) articular cartilage and (B) nasal cartilage.

1.2.2 Biochemical composition

Cartilage has a relatively simple composition, with only 3-5 % of cells (chondrocytes) and 95% of extracellular matrix (ECM) by mass, where the ECM is primarily type II collagen and

proteoglycan[27, 33]. This ECM is essential in regulating chondrocyte functions and provide the cartilage structure and specific mechanical properties[34].

In hyaline cartilage, the ECM occupies a significant volume fraction of the tissue and is responsible for its primary functions. For example, proteoglycan provides swelling pressure, and collagen provides structural support [1]. Cartilage functions are engendered by the supramolecular system, including the collagen-containing fibrils and large cartilage-specific proteoglycans [1].

The articular cartilage ECM consists of 60-85% of water and a macromolecular framework of collagens (10-30%), proteoglycans (3-10%), and some minor non-collagenous protein[35]. The predominant collagen type in articular cartilage is type II collagen, which accounts for approximately 90-95% of the total collagen dry weight[35]. Type II collagen is a fibrillar collagen composed of three α1(II) chains encoded by a single gene, *COL2A1*. Except for type II, other types of collagens are presented, including type III, VI, IX, X, XI, XI and XIV. Type II, IX and XI collagen can form a reinforcing heteropolymer in the ECM[36]. Type X collagen (Collagen X) contributes to regulating the ossification of cartilage[37]. Ideally, a tissue-engineered hyaline cartilage construct should yield high type II collagen content and minimal type X collagen content. Proteoglycans are protein monomers that are heavily modified with glycosylation. They consist of a protein core attached by one or several glycosaminoglycans (GAG). The GAG is a linear carbohydrate polymer that is composed of repeating disaccharides, which are mainly chondroitin sulfate and keratin sulfate[29]. Aggrecan is the largest in size and the most abundant by weight among cartilage proteoglycans, which possesses more than 100 chondroitin sulfate and keratin sulfate GAG chains. It's an aggregate proteoglycan and its structure is characterized by its multimolecular complex composed of hyaluronan, various GAG (such as keratin sulfate and

chondroitin sulfate) and link protein[29]. This complex serves to stabilize the cartilage matrix and confer upon it its characteristic mechanical properties, which GAGs provide swelling pressure and contribute to distributing and resisting the compressive load by binding to the water molecules. Versican is another type of aggregate protein found in articular cartilage, but at significantly lower levels. Nonaggregating proteoglycans, such as decorin, biglycan, and fibromodulin, is characterized by their unique ability to interact with collagen. Despite being smaller in size than aggrecan, these molecules may be present in similar molar quantities. These proteoglycans are structurally related, but differ in the composition and function of their glycosaminoglycans. Decorin and biglycan are characterized by the presence of one and two dermatan sulfate chains, respectively, whereas fibromodulin has several keratin sulfate chains. Decorin and fibromodulin play a role in fibrillogenesis and inter-fibril interactions by interacting with type II collagen fibrils in the matrix, while biglycan is primarily found in the vicinity of chondrocytes and may interact with collagen VI[27].

In the nasal cartilage, both LLC and nasal septum show abundant staining for type II collagen and slight staining in type I collagen [32, 38]. Several papers characterized the biochemical contents of nasal septal cartilage[39-42]. However, these studies have shown inconsistent results regarding collagen content, glycosaminoglycan content, and cellularity among research groups. Homicz et al. showed that human nasal septal cartilage contains 77.7% water, 7.7% collagen, and 2.9% GAG in wet weight, with 24.9 million cells per gram[39]. Neuman et al. showed that nasal septal cartilage contains 1.7% of GAG and 73.9% collagen in wet weight with 24.9 million cells per gram[40]. Another research group shows that nasal septal cartilage contains 4.3% GAG and 14.1% of the collagen in wet weight[41]. Our research group has measured human septal cartilage containing 4.6% of GAG in wet weight and 22.47 million cells per gram[42].

Biochemical properties are critical engineering design criteria for the evaluation of cartilage tissue engineering. Additional study may be needed to unequivocally determine the biochemical content of articular cartilage and nasal cartilage regarding age, gender, race, etc. For articular cartilage, it is important to characterize the biochemical contents of different zones. And for nasal cartilage, it is also interesting to characterize the biochemical content of LLC, and ULC, since most reported values are for nasal septal cartilage.

1.2.3 Mechanical properties

The engineered cartilage must also possess satisfying mechanical strength to ensure its ability to be sutured during surgery and withstand stress after implant. Therefore, the mechanical properties of human hyaline cartilages must be understood to establish the design basis for the engineered tissue.

To date, most literature characterized the articular cartilage by compressive moduli as the articular cartilage tissue frequently experiences compressive load during physiological activities[43-49]. Major weight-bearing joints for articular cartilage experience compressive loading stress between 0.5-7.7 MPa, and the average compression amplitude typically leads to about 13% strain[48]. Native human articular cartilage has aggregate moduli (H_A) of 0.08-2 MPa[49]. The dynamic moduli (E_D) of the tissue also increase non-linearly with the increasing strain [49]. In addition, native articular cartilage sustains a constant state of static pretension caused by negatively charged proteoglycan retaining fluid throughout the ECM. Consequently, the collagen in the cartilage matrix imposes tension that allows the tissue to swell without rupture. Therefore, some of the study also measures the tension properties of articular cartilage, which are usually

quantified by Young's modulus (E_Y) and the ultimate tensile strength (UTS). The E_Y of native articular cartilage is around 5-25 MPa, and UTS is 2-8 MPa[49].

Like articular cartilage, the mechanical properties of nasal cartilage have been characterized mostly by compression. The nasal septal cartilage's lower stiffness and upper stiffness are 0.41 ± 0.21 and 19.30 ± 6.80 MPa at 50% strain/min, respectively[50]. The compressive Young's modulus of the nasal septal cartilage is varied topographically. The posterior nasal septum (3.47 ± 0.26 MPa) was significantly greater than the anterior nasal septum (2.50 ± 0.32 MPa), but no differences were observed between the nasal septum's superior and inferior regions[51]. The test orientation also affects the nasal septal cartilage's confined compression (aggregation) moduli. Richmon et al tested the septal cartilage of 21 patients ranging from 18-74 years of age, with approximately 6mm* 1mm*1mm slices. The vertical and cephalic-caudal orientations resulted in aggregate moduli of 0.7 ± 0.12 and 0.66 ± 0.01 MPa, respectively, which were significantly stiffer than the medial orientation (0.44 ± 0.04 MPa)[52]. Overall, the septum cartilage (2.72 ± 0.63MPa) has a significant higher compressive Young' s modulus than LLC (2.09 ± 0.81 MPa) and ULC (0.98 ± 0.29 MPa)[51]. The LLC's compressive elastic modulus was also significantly higher than that of the ULC[51].

Other studies have characterized the tension or bending properties of the nasal cartilage. The human nasal septum's tensile equilibrium modulus, dynamic modulus, and strength (maximum stress) were measured to be 3.01 ± 0.39, 4.99 ± 0.49, and 1.90 ± 0.24 MPa, respectively [53]. The tensile failure strain of nasal septal cartilage was reported to be 35%[53]. Another study demonstrated considerable variability in measured tensile modulus for the septum (4.82–32.76 MPa), LLC (1.82–15.28 MPa), and ULC (5.43–28.63 MPa), which could be attributed to its

small sample size (n = 3) [54]. The flexural modulus based on three-point bending tests of nasal septal cartilage was measured to be 1.97 ± 1.25 MPa[55].

Several mechanical testing protocols have been reported in the literature, and the lack of consistency in the testing method and the format of presentation makes the comparison between studies difficult at times and may lead to misinterpretations of the native cartilage. This suggests the need to establish standardized testing methods for both native and engineered hyaline cartilage.

1.3 Preferred cell sources for cartilage tissue engineering

Besides biomaterial, the other important component of a bioink – cell, is not well discussed in most of the current research in 3D bioprinting of cartilage tissues. In fact, cell source plays a vital role in bioprinting and will impact the performance of the printed structure both *in vitro* and *in vivo*. In this section, we will provide insights into suitable cell sources that have the potential for the clinical translation of tissue-engineered bioprinted cartilage.

Hyaline cartilages originate from either mesoderm or ectoderm. The formation of cartilages in the limbs is contributed by mesoderm-derived cells (MDC) from somite and lateral plates. In contrast, the formation of cartilages in the head and neck region is accounted from the neural crest-derived cells (NCDCs)[19, 56-58]. Because MDC and NCCs shared the capacity to generate hyaline cartilage, their progenies are considered appropriate cell sources for hyaline cartilage regeneration. The progenies of MDCs commonly used for cartilage tissue engineering are mesenchymal stem cells (MSC) and articular chondrocyte (AC), and the progenies of NCDCs including nasal chondrocytes (NCs) and neural crest-derived stem cells (NCSCs)[28]. The

following sections discuss the effectiveness of these cell sources for cartilage tissue engineering in terms of their *in vitro* post-expansion chondrogenic re-differentiation potential, and *in vivo* stability.

1.3.1 Mesenchymal stem cells (MSCs)

Mesenchymal stem cells (MSCs) have been attractive cell sources for cartilage tissue engineering in the past decade, as they can be isolated from a wide variety of tissue, exhibit a capacity for rapid expansion, and readily differentiate into chondrocytes after numerous expansions. MSCs derived from various regions, including bone marrow, adipose tissue, periosteum, and synovium, have all been found to possess the greatest ability for chondrogenesis. Our group has previously summarized the current progress of MSCs-based treatment and underlying barriers to cartilage tissue engineering.[59]

While many clinical trials and research focus on cartilage repair, increasing evidence shows that MSCs may not be the most appropriate cell source for cartilage therapy[17, 18, 60]. The challenge associated with the MSCs is how to differentiate the isolated MSCs toward a desired chondrogenic phenotype. A clinical study shows fibrous cartilage formation in joint defects after MSC implantation[17]. Chondrogenic differentiation of MSC with TGF-β1 or TGF-β3 *in vitro* results in unstable cartilage after implantation *in vivo*. For example, adipose-derived stem cell (AD-MSC), synovial membrane MSC (SM-MSC) and bone marrow-derived MSC (BM-MSC) derived cartilage underwent calcification when implanted *in vivo*[60-62]. When human BM-MSC was co-cultured with human nasal chondrocytes, BM-MSC showed increased GAG and type II collagen, and decreased collagen X in pellet culture models [63]. However, in a more detail and comprehensive study from our group, the co-cultured nasal chondrocytes and BM-MSC

did not maintain the chondrogenic phenotype and underwent premature hypertrophy and calcification *in vivo [64]*. On the other hand, nasal chondrocytes alone maintain the chondrogenic phenotype[64]. Considering the *in vivo* stability in terms of hypertrophic, calcification, and fibrocartilage formation, MSC has become a less suitable cell source for cartilage regeneration.

1.3.2 Neural crest-derived stem cell (NCSC)

NCSC can be identified not only from the early embryonic stage but also from adult tissue[65, 66]. NCSC were discovered in the bone marrow and dorsal root ganglia, heart, skin, gut, and carotid body, as well as several cranial tissues such as the cornea, iris, dental pulp, herd plate, and oral mucosa[28, 65].

Dental stem cell populations are the most investigated NCSCs, which showed similar properties to those of mesenchymal stem cells in terms of their ability to self-renew and the multilineage differentiation potential[65-67]. Ferre et al demonstrated that human gingival stem cells (HGSCs) can differentiate into osteogenic, chondrogenic, and synoviocyte lineages. Positive type II collagen and glycosaminoglycan staining and mostly negative type X collagen staining are shown in the chondrogenic differentiated HGSC pellet[68]. Moshaverinia et al. investigated the *in vitro* chondrogenic capacity of HGSC and human periodontal ligament stem cells (HPLSC) in 3D arginine-glycine-aspartic (RGD)-coupled alginate hydrogel with TGF-β1 ligand, then compared them with BM-MSC. The results showed that HGSC and HPLSC expressed specific MSC surface markers such as CD73, CD105, CD146, and CD166 but did not express hematopoietic lineage markers such as CD34 and CD45. After four weeks of *in vitro* chondrogenic culture, HPLSCs showed higher expression of SOX9 and COL2A1 genes than BM-MSCs and HGSC, while no significant difference was observed between HGSC and BM-MSC. After eight

weeks of subcutaneous *in vivo* implantation in nude mice, HPLSCs revealed more type II collagen production than GMSC and BM-MSC[69]. A recent review has summarized the chondrogenic potential of the NCSC and induce pluripotent stem cells (iPSC)-derived neural crest cells[28]. Although the above literature has shown that NCSC and iPSC-derived neural crest cells show positive chondrogenicity results, there is still a lack of research studies to investigate the chondrogenic capacities between various populations of NCSC or compare the *in vivo* stability between NCSC and BM-MSC.

1.3.3 Articular chondrocytes (AC) and nasal chondrocytes (NC)

Chondrocytes, such as articular chondrocytes (AC) and nasal chondrocytes (NC), are potential cell sources for hyaline cartilage tissue engineering, which are obtained from articular and nasal septum cartilages, respectively. Although articular cartilage and nasal septum cartilage share the same hyaline cartilage nature and produce the same pattern of ECM, NC and AC originated from different germ layers. As previously mentioned, NC originated from the neural crest, while AC developed from the mesoderm layer[19].

In orthopedic application, isolation of chondrocytes from the joint surface is complex. Therefore, researchers have considered using non-articular "heterotopic" chondrocytes such as NC as an alternative cell source since they are easier to harvest, have a lower risk of donor site morbidity, and possess a higher proliferation capacity from a broad age range of humans [70]. In the past 20 years, much research around cartilage tissue engineering has proven that NC can generate better quality of engineering hyaline cartilage in terms of higher type II collagen content and proteoglycan content both *in vitro* and *in vivo*[21, 23, 71-73]. NC are also found to have a significantly higher proliferation rate than articular cartilage (four times of population doubling rate, 4.22

doubling per week for NC, and 1.12 for AC). Within a short period, a large number of NC can be achieved in a monolayer cell culture[74].

Engineered hyaline cartilage using NC is able to maintain a similar or even better cartilaginous tissue forming capacity than AC under the conditions imitating the injured articular environment[75]. They can also respond to the physical forces that resemble the joint loading, suggesting that the engineered cartilage by NC implanted in articular cartilage defect could further mature and improve the biochemical and mechanical properties under the mechanical stimulation of the joint movement[21]. A large animal study using goat was carried out by Mumme et al. in 2016 to compare the outcome of tissue-engineered cartilage using NC and AC for articular defect repair *in vivo*[76]. Engineered cartilage using NC can form the characteristic structures of articular cartilage and integrate efficiently with the adjacent tissue. The AC group had a significantly increased subchondral bone area that was a signal for osteoarthritis, which was not detected in nasal chondrocyte grafts. These findings paved the way for NC-based cartilage tissue engineering for articular cartilage implant[76]. Eventually, in 2016, the first human trial to repair focal articular cartilage injuries using nasal chondrocytes showed compelling results[23]. Ten patients with symptomatic traumatic cartilage defect were repaired using autologous NC tissue engineered grafts. After a 24-month follow-up (n=9, one patient excluded due to the independent sport injuries), a self-assessed outcome score and MRI-based estimation indicate a satisfactory clinical outcome without any adverse reaction after implantation. No adverse reaction at the site of septum cartilage biopsy. Clinical scores for pain relief, knee function in daily living, functions in sport and recreation, and knee-related quality of life were markedly improved. The water and collagen content of the repair tissue showed similar composition to healthy native articular cartilage. The significant increase of GAG content from 6 to 24 months indicates the maturation of

the repair tissue. This study demonstrated that tissue engineered cartilage generated by autologous NC can be clinically used for articular cartilage lesion repair in load-bearing knee joint[23].

NC can also be used for orthotopic application, mainly focusing on the maxillofacial region. Farhadi et al investigated whether the pre-cultivation of engineered nasal cartilage graft using human NC would increase the suture retention strength and bending property both *in vitro* and *in vivo*. Results showed that 2 weeks of chondrogenic preculture enhanced the bending and tensile strength *in vitro* and *in vivo* [77]. Our group has shown that tissue-engineered cartilage with pure NC can maintain the chondrogenic phenotype after 5 weeks of subcutaneous *in vivo* implantation in nude mice, while a co-culture of the NC and BM-MSC, or BM-MSC alone, failed to maintain the chondrogenic phenotype and have been shown to undergo hypertrophy and calcification *in vivo*.[64] In 2014, the first human trial using human NC seeded engineered cartilage for the repair of nasal alar lobe defect after the skin cancer tumor resection were reported and showed compelling results. The functional assessments, including cutaneous sensibility, structural stability, and airflow resistance, all show similar or better than the opposite nostrils. No local or systemic adverse events were recorded after 12 months of implantation[78]. This result has proved that NC is a safe and robust cell source for tissue-engineered cartilage.

In summary, NC show positive results in terms of better proliferation and chondrogenic capacity than AC *in vitro* and *in vivo*, more stable chondrogenic phenotype *in vivo* than MSC. Furthermore, NC also can be used for temporomandibular joint regeneration and auricular cartilage regeneration and provide an autologous cell source for intervertebral disc repair[22].

1.4 3D bioprinting for cartilage tissue engineering

For the conventional cartilage tissue-engineered nasal cartilage, porous scaffolds are fabricated from biomaterials and subsequently seeded with cells. Three-dimensional (3D) bioprinting approaches allow a rapid additive fabrication of patient-specific, anatomically-, or surgical ready-shaped engineered functional tissue by incorporating tissue engineering techniques [79, 80]. Similar to existing 3D printing techniques, once a 3D model of the tissue is developed through computer-aided design (CAD) tools, a "bioink", a biomaterial precursor pre-mixed with cells, are loaded into the 3D bioprinter then precisely dispensed from a movable printing head into the designed shape. Next, the printed structure needs to be physically or chemically crosslinked to retain its 3D structure after printing.

The conventional tissue engineering approaches can be described as top-down, whereas scaffolds are prepared first, and cells are seeded within[81]. Limited by the inherent disadvantages of the conventional techniques, scaffold-based tissues often fail to reflect both the micro and macro architecture of the native tissues. To address problems associated with top-down methods and improve the controllability of the fabrication process[82], a micro-scale bottom-up technique, three-dimensional (3D) bioprinting, has been applied to tissue engineering[83]. 3D bioprinting is a form of additive manufacturing (AM), in which the distribution of cells in biomaterial is pre-defined, and particular geometry of tissues is built up layer-by-layer at micrometre resolution. Unlike conventional approaches, 3D bioprinting introduces additional options, such as the choice of materials, cell types, and growth factors[79], allowing rapid and high-throughput tissue fabrication.

Although 3D printing has evolved significantly since its invention decades ago and a wide range of techniques are accessible today, the process of 3D bioprinting can be classified into four general steps: (1) image data acquisition, (2) material selection, (3) bioprinting, and (4) functionalization[84]. The 3D models of tissue to be fabricated are usually obtained and reconstructed by tomography (CT) or magnetic resonance imaging (MRI). These data would be further modified to a bioprinter-compatible format in which printing path and parameters, such as cartridge temperature, printing pressure, and printing speed, are defined [85]. The selection of materials includes not only base scaffold materials but also cell types and growth factors. Based on the intended application and structural complexity of the construct, the most suitable printing technique should be chosen accordingly. The final step to generate functional tissues or organs from 3D bioprinting is to culture the printed constructs under appropriate mechanical and/or biochemical stimulation.

As mentioned above, the choice of 3D printing techniques is crucial for the structural and functional integrity of fabricated constructs. With the rapid evolution of 3D printing fields, various printing machines have been developed. Among them, extrusion bioprinting[86-88], inkjet [89-91] and laser-assisted bioprinting [92, 93] are the three primary printing techniques in tissue engineering (Figure 1.3).

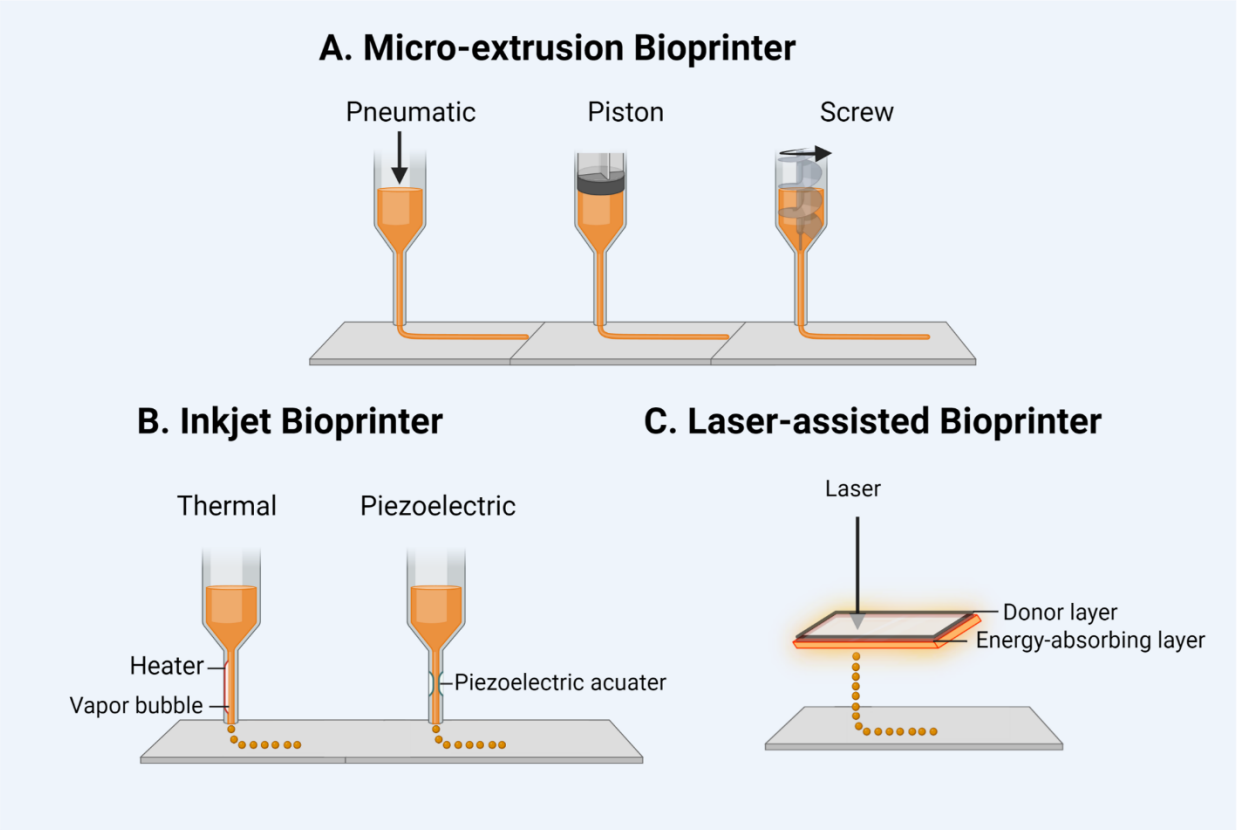

Figure 1.3. Schematic diamgram of commonly used bioprinting method, (A) Micro-extrusion Bioprinter, (B) Inkjet Bioprinter (C) Laser-assisted Bioprinter

Extrusion bioprinters (direct ink writing) can produce uninterrupted cylindrical lines under a continuous force generated by either air pressure or mechanical pressure. The most attractive feature of extrusion bioprinters is their high compatibility with a wide range of viscosities of materials and various concentrations of cells [94]. However, the large mechanical stress induced by the extrusion process can harm the encapsulated cells and potentially reduce cell viability and construct functionality. In addition to the most common skin regeneration application[86], extrusion bioprinting is also widely used in tissue engineering of bone[95, 96], cartilage[97], skin [98], and muscle[99], organoid production[100], and drug screening[101, 102].

Unlike continuous filament-based extrusion bioprinting, inkjet (drop-on-demand, DoD) bioprinting works on a droplet basis. During the printing process, discrete droplets with controllable size are generated by a jetting element (thermal or piezoelectric actuator) and dispensed on a printing bed by following a particular spatial pattern. Due to the mechanical limitation of the jetting element, only materials with low viscosity and cell density can be printed via inkjet printers[103]. While inkjet bioprinting is restricted to a relatively smaller range of materials, cell viability (around 80-95%) has been demonstrated to be higher in different types of materials [104-106].

Laser-assisted bioprinting (LAB) is a non-contact, nozzle-free printing method in which a droplet is propelled from a layer of suspended bioink by a focused laser pulse and collected on the receiving platform. Compared to extrusion and inkjet printing, LAB can print biomaterials with higher viscosity and cell density at a finer resolution. More importantly, no mechanical stress is induced during the printing process, which is beneficial for encapsulated cells to maintain a viable state (95%)[107]. Although LAB is more advanced than the other two printing techniques, its adoption is limited by the high cost and complexity of the system. Also, the potential side effect of laser exposure on cells and materials has not been fully explored. The current application of LAB mainly focuses on bone tissue engineering [92, 108], with a few studies on blood vessels [109] and skin[110]. A brief review of advantage and disadvantage of the printing method are summarized in the table below.

Table 1.1 Brief review of the printing method[106]

	Extrusion	**Inkjet**	**Laser-assisted**
Advantage	Simple and widely used and well-established. Can print in large volume. Can print with wide range of hydrogel	Ability to print low viscosity biomaterials. Fast	Can create constructs with high resolution and mechanical strength. Can deposit

	precursors as bioink material. Ability to print high cell densities	fabrication speed. Low cost	biomaterial in both solid and liquid form
Disadvantage	Limited precision. Only work on certain viscosity range. Can damage delicate cell during printing	Limited by the size of the inkjet nozzle. Inability to provide continuous flow. Hard to build up printed layers. Low cell densities	High cost. Thermal damage of cells due the laser irritation
Speed	Slow	Fast	Medium
Cost	Moderate	Low	High
Cell viability	Good	Good	Medium

With cartilage tissue engineering, a broad scope of cells, materials, and growth factors combinations have been attempted to fabricate cartilaginous tissues [111-114]. To adapt to the wide range of bioink viscosities and cell seeding densities, the most commonly used bioprinting techniques are extrusion bioprinting and inkjet. Both have been demonstrated to be safe and have shown promising outcomes.

1.5 Bioink materials for cartilage tissue engineering

Most bioink materials, in the form of hydrogel precursors, are natural and synthetic polymers or a blend of both. The natural polymer suitable for 3D bioprinting can be categorized into polysaccharide-based (such as alginate, cellulose, hyaluronic acid, chitosan, etc.) and protein-based (such as collagen, gelatin, fibrin, decellularized extracellular matrix (dECM) etc.). Natural polymers have the advantage of low cytotoxicity, excellent biocompatibility, and resemblance to the ECM. However, they generally exhibit batch-to-batch variations and inferior mechanical

properties. Synthetic materials such as poly(ethylene glycol) (PEG), Pluronic acid (poloxamer) usually have a tailorable mechanical property, but their cytotoxicity and biocompatibility are generally concerning. To design a biomaterial for bioink formulation, the rheology, biocompatibility, crosslinking behaviour, and cell-material interactions are critical parameters to consider.

1.5.1 Rheology

The rheological behaviour of the bioink is critical for the 3D bioprinting process. A rheometer is usually used to characterize the precursor solution characteristics. The three most relevant rheological parameters for the bioink include (1) shear responses, (2) recovery time, and (3) yield stress. The bioink needs to have a shear thinning property, rapid recovery time, and the presence of yield stress. Shear-thinning allows for the decreasing proportional shear force required for flow, allowing ease of extrusion through small orifice sizes. Therefore, it can protect the printed cells while achieving high resolution [115]. The recovery time of the material, which is the time required for the bioink to return to the original state after flow, is also vital for high-resolution bioprinting [115]. Bioinks with relatively fast recovery time are ideal for bioprinting applications as the immediate return to equilibrium after dispensing may aid with the printing fidelity and the homogeneous incorporation of encapsulated cells[115]. Yield stress is required for a material to begin to deform under applied shear stress. Together with the shear-thinning property and a fast recovery time, bioinks that exhibit yield stress would naturally resist deformation and maintain the printed structure[115].

1.5.2 Crosslinking

After bioprinting, bioink requires chemical or physical crosslinking to form a hydrogel. Chemically crosslinked hydrogels are distinguished by forming covalent bonds between the polymers to create an interconnected network. The chemical crosslinking can be photo-crosslinked and enzymic/reaction-based [115]. The most popular photo-crosslinked functional group used in 3D bioprinting is the methacrylate group, which can quickly form polymer because of the reactive double bonds. Methacrylate functional groups can be grafted with natural polymers, such as gelatin, collagen, hyaluronic acid, alginate, etc., and mixed with cells and photo-initiators to form bioinks. This bioink can be crosslinked in UV light to provide mechanical property and structural integrity to the bioprinted constructs. The limitation of the photoinitiated hydrogels is their requirement for light penetration. Therefore, opaque materials may encounter crosslinking issues with limited light penetration. In addition, UV light may also cause cell damage[115].

The enzymic/reaction-based crosslinked hydrogels are generally initiated by mixing two solutions or incubating the bioprinting structure into a crosslinking solution[115]. Enzymatic crosslinking is an attractive method to crosslink protein-based polymers in 3D bioprinting due to the mildness of enzymatic reactions, which can minimize cell damage. Only a few enzymatic crosslinking methods have been used in 3D bioprinting cartilage tissue, most of which are combined with other crosslinking methods[116, 117]. Chemical reaction-based crosslinking can occur by covalent bonding between polymetric chains through various chemical reactions. Several synthetic chemical crosslinkers have been used in cartilage tissue engineering scaffolds, such as glutaraldehyde, formaldehyde, and ethylene oxide[118, 119]. However, they are rarely used in 3D bioprinting due to high cytotoxicity to the pre-mixed cells. Natural crosslinkers, such as genipin

and riboflavin (Vitamin B) are the more suitable options for 3D bioprinting[120, 121]. Chemical crosslinking methods such as Schiff's base reaction have also improved the printability of the 3D bioprinting construct.

Physical crosslinking can occur through ionic interaction or thermo-crosslinking, where the materials are held together by polymer entanglement and/or secondary forces without forming covalent bonds. Alginate is the most used ionic crosslinked material in 3D bioprinting. It can form a crosslinked network in the presence of divalent cations such as Ca^{2+} ions and Ba^{2+} ions. The divalent calcium ions form a bridge due to the attraction of negatively charged carboxylic acid groups between two neighboring alginate chains[115]. Collagen, which can be self-assembled to create a physical gel at specific temperatures and pH, is a commonly used thermo-crosslinking material [110, 115, 122-127]. Agarose is another polysaccharide-based bioink biomaterial that can thermally crosslink. Combinational hydrogels utilizing physical and chemical crosslinking principles are also commonly used in 3D bioprinting[128, 129]. The combinational hydrogel has potentially significant benefits, as they usually form more robust constructs after crosslinking.

Besides crosslinking, hydrogels can be coupled with other synthetic biomaterials, such as Polycaprolactone (PCL), poly(lactic-co-glycolic acid) (PLGA), Polyglycolide (PGA), Polylactic acid (PLA), and others, to improve the mechanical properties and maintain the uniform 3D structure. The mechanical properties have been dramatically enhanced by incorporating synthetic material[130-141].

1.5.3 Cell-biomaterial interactions

To create a tissue-engineered construct, the bioink needs to have cell adhesive motifs for cells to attach, proliferate and interact with the biomaterial to further produce functional ECM. The protein-based bioink materials such as collagen hydrogel are suitable biomaterial source to promote the generation functional tissue. Polysaccharide materials, such as alginate, agarose, chitosan, and cellulose, are biologically inert and non-adhesive for cells. Therefore, it is essential for these materials to either blend with another protein-based natural polymer (i.e. collagen, fibrin) or be modified with some cell adhesive motifs such as the RGD peptide sequence.

The development of bioink materials allows scientists to manipulate biological, biochemical, and biomechanical environments, alone with living cells, to create complex biological constructs. The cellular activity and cartilage formation depend on the biomaterial type and its mechanical properties [141]. The biological indicators of a suitable biomaterial for a particular tissue are measured by sustained cell viability, cell activities during culture (both short and long-term), cell-cell and cell- ECM interactions, functionality of the bioprinted constructs, and degradation time. As biomaterials are the basis of bioinks, it does not only dominate the mechanical properties of the bioinks and the bioprinted cartilage but also regulate cell activities. Selecting biomaterials that mimic the *in vivo* microenvironment of cartilage tissue is a critical design aspect for the clinical translation of bioprinted cartilage.

1.6 Summary and research objectives

Although research in cartilage bioprinting is growing exponentially, no studies have demonstrated the use of 3D bioprinted cartilage clinically. So far, the two clinical trials using NC

seeded on type I/III collagen scaffold in both maxillofacial and articular cartilage regions show clinically feasibility and safety[6, 23]. These clinical trials indicate enormous opportunities for 3D bioprinted cartilage in hyaline cartilage repair. To accelerate the clinical translation of 3D bioprinting in cartilage tissue engineering, NC are undoubtedly the superior cell source option to move forward.

To move 3D bioprinted cartilage towards clinical use, it is important to not only choose the appropriate cell source, but also match it with a suitable bioink material that can give the cells the necessary cues to produce enough matrix. The studies of 3D bioprinted neocartilage using NC are listed in Table 1.2. The biomaterials used are collagen, cellulose-alginate, alginate-gelatin, PCL-alginate, and PCL-collagen. Among the currently available bioink materials, we are particularly interested in collagen bioink, which is a major ECM for connectives tissue. Collagen can provide biochemical signals, which induce cellular differentiation and migration, further promote tissue regeneration. Type I collagen solution also have shear thinning property. In addition, it can be self-assembled at physiological pH and temperature to form hydrogel. Type I collagen are also well studied to have low immunogenic reaction. Current limitations to use type I collagen as bioink material is the low zero shear viscosity and low elastic modulus, which may not be able to provide enough mechanical properties that support the printed structure. The existing chemical crosslinking agent for collagen are also inadequate because they are usually toxic to the cells.

In this thesis, we aim to explore strategies to allow bioprinting of cartilage tissue using type I collagen based bioink, and investigating the *in vitro* maturation and *in vivo* stability of the bioprinted cartilage. The objectives of the thesis are to

1) Review the rheological and viscoelastic properties of collagens and their role in Micro-extrusion-based bioprinting
2) Utilize novel printing strategies to precisely print type I collagen bioink with human NC to generate tissue engineered cartilage in vitro
3) Investigate in vitro maturation and in vivo stability of bioprinted human NC
4) Pre-crosslink type I collagen to enhance the printability the bioprinted engineered cartilage

Table 1.2 3D bioprinted cartilage using nasal chondrocytes

Aim	**Cell source**	**Material & 3D printing Method**	**Mechanical evaluation**	**Biochemical and histological evaluation**	***In vitro*/ *In vivo* study**	**Ref.**
Compare the bioprinted nasal cartilage with clinically approved scaffold both *in vivo* and *in vitro*	Human nasal chondrocyte	Type I collagen bioink (Extrusion)	Yes (Bending Modulus)	Live/dead, Gross morphology, Histology (Safranin-O/Fast Green, Masson's Trichrome, Alizarin Red S), Immunofluorescence (Type I/II/X collagen, BSP, CD31), GAG/DNA, Gene expression	Yes/Yes (5 weeks in nude mice)	[142]
Evaluate the vascularization of tissue engineered cartilage after long-term *in vivo* implantation	Human nasal chondrocyte	Cellulose nanofiber (CNF)-Alginate bioink (Extrusion)	No	MRI imaging, Gross morphology, Histology (Alcian Blue van-Gieson and Safranin-O/Fast green), Immunohistochemical (CD31, Type II collagen)	No/Yes (30 days and 90 days)	[143]
Evaluate long-term chondrogenesis of 3D-bioprintied cartilage constructs	20% human nasal chondrocytes + 80% bone-marrow-derived MSCs, Or, 20% human nasal chondrocytes + 80% stromal vascular fraction stem cell	CNF-Alginate bioink (Extrusion)	Yes	Histology (Alcian Blue van-Gieson and Safranin-O/Fast green)	No/ Yes (8 and10 months in nude mice)	[144]
Compare the bioprinted nasal cartilage cultured *in vitro* with native cartilage tissue	Human nasal chondrocyte	Type I collagen bioink (Extrusion)	No	Live/dead, Gross morphology, Histology (Safranin-O/Fast Green), Immunofluorescence (Type I/II), GAG/DNA, GAG/WW, Gene expression	Yes/No	[42]
To evaluate the modification of material and the quality of 3D-printed cartilage constructs	human nasal chondrocytes	Bacterial Nanocellulose (Inkjet and Extrusion)	Yes	Gross morphology, Histology (Alcian Blue van-Gieson), Immunohistochemical (Type II collagen), FISH analysis,	No/ Yes (30 and 60 days in nude mice)	[145]
Evaluate the chondrogenic potential of 3D	20% human primary nasal chondrocytes	CNF-Alginate bioink (Extrusion)	No	Histology (Alcian Blue van-Gieson and Safranin-O/Fast green),	No/Yes (30 days	[146]

Aim	**Cell source**	**Material & 3D printing Method**	**Mechanical evaluation**	**Biochemical and histological evaluation**	***In vitro*/ *In vivo* study**	**Ref.**
bioprinted cartilage construct *in vivo*	+ 80% bone-marrow-derived MSCs			Immunofluorescence (Type II), FISH analysis,	and 60 days)	
Evaluate the redifferentiation capacity of human chondrocyte *in vitro*	Human nasal chondrocyte	PCL reinforced CNF-A bioink (Extrusion)	Yes	Live/dead, Gross morphology, Histology (Alcian Blue van-Gieson), Immunofluorescence (F-Actin), Immunohistochemical (COMP, Aggrecan, Type II collagen, Matrilin 3), GAG/DNA, Gene expression	Yes/No	[147]
To evaluate therapeutic potential of 3D-printed cartilage constructs	human nasal chondrocytes	PCL In-house 3D printing, seeded with collagen hydrogel	No	Cell proliferation assay, cell viability assay, Immunofluorescence (Aggrecan, Collagen type II, Sox9), SEM, Gene expression (COL2A1, SOX9), Western blot	Yes /No	[148]
To demonstrate to use of nanocellulose for 3D bioprinting of cartilage	human nasal chondrocytes	Nanocellulose-Alginate Inkjet 3D printing	Yes	Gross morphology, Cell Viability	Yes/No	[149]
To demonstrate the potential use of 3D printed constructs for cartilage tissue engineering	human nasal chondrocytes	Alginate-gelatin hydrogel, cross-linked by $CaCl_2$ and Transglutaminase Extrusion 3D printing	Yes	Gross morphology, Cell Viability, metabolic activity, Immunofluorescence (Collagen type I and II, Sox9, Proteoglycan)	Yes/No	[150]
To simplify the steps involved in the mixing of a cell suspension into a highly viscous bioink	human nasal chondrocytes	Nanocellulose-Alginate Extrusion 3D printing	No	Cell Viability, Histology (Alcian Blue, Masson's Trichrome)	Yes/No	[151]
To fabricate 3D printed construct for cartilage regeneration	human nasal chondrocytes	PCL-Alginate Multihead deposition system (MHDS)	No	Gross morphology, Cell Viability, SEM GAG/dry weight, DNA/dry weight Collagen/dry weight, Histology (Alcian Blue, H&E) Immunofluorescence (Collagen type II)	Yes/ Yes (4weeks in nude mice)	[130]

CHAPTER 2. Rheological and Viscoelastic Properties of Collagens and Their Role in Bioprinting by Micro-extrusion

Contribution author: Xiaoyi Lan, Adetola Adesida, Yaman Boluk

Chapter 2 has been accepted for publication in part as:

Xiaoyi Lan, Adetola B. Adesida, and Yaman Boluk, "Rheological and Viscoelastic Properties of Collagens and Their Role on Bioprinting by Micro-extrusion" Biomedical Material.

2.1 Background on bioprinting of hydrogels

Bioprinting is a promising tissue engineering process to restore, replace, and regenerate tissues and organs. The purpose of bioprinting is to build three-dimensional (3D) functional tissue-like constructs with hydrogels. Major bioprinting techniques are inkjet printing, laser-induced forward transfer, and micro-extrusion while employing either hydrogels or cell-laden hydrogels [152, 153]. These processes are designed to provide a platform to form extracellular matrix (ECM) with desired mechanical support characteristics while delivering living cells and growth factors for full restoration of targeted tissues[79].

Micro-extrusion-based bioprinting has been developed based on additive manufacturing (AM) principles by 3D printing [154]. It is one of the most versatile techniques which produces physically precise dimensions and outputs. Originally, additive manufacturing by 3D printing was developed to process molten thermoplastics and fabricate solid free-forms of three-dimensional physical parts directly from computer-aid design (CAD) files [83, 155]. However, unlike 3D printing of molten thermoplastics, bioprinting uses micro-extrusion of water-based hydrogels under ambient temperatures and applied tresses. Despite the excellent reviews on extrusion-based bioprinting[153, 156-158], there is a need to discuss filament (fiber) extrusion and layer stacking stages of the micro-extrusion process separately and link them to the rheology of the processed hydrogels. Here, we focus on the capillary flow in the capillary die (needle) and elastic phenomena at the capillary "exit," such as swell, sag, and surface roughness. Separately, we discuss molecular diffusion and bonding among layers and the formation of the constructs.

Hydrogels such as collagens are water-holding materials that are covalently or physically linkable into three-dimensional networks, and their structures are somewhat similar to natural

tissues[152]. The word “gel” is derived from “gelatin” and is used as a synonym for hydrogels. Gels can be generally described as two-component systems with dispersed or dissolved solid substances in a solvent (in the case of hydrogels, the solvent is water); they exhibit solid-like behavior, and their dispersed components and solvent form bi-continuous systems [159]. Using various formulation strategies, flow and crosslinking characteristics of hydrogels can be designed to offer the required bioprinting processing conditions and final product properties. Moreover, in highly hydrated structures, hydrogels can support the living to create an efficient and homogenous cell seeding environment. Hydrogels in bioprinting are processed at ambient temperatures in micro-extrusion-based 3D-printing devices by feeding into a cartridge and extruding from a specially designed needle (capillary die) into the form of filaments. Their rheological properties are crucial to form a uniform and precisely controlled filament dimensions while flowing through the needle. After extrusion, once filaments are stacked layer by layer, they must be fused to construct the desired porous, mesh-structured objects. This stage requires specific viscoelastic properties obtained by the gelling and crosslinking hydrogels. Augmentation of mechanical properties by crosslinking of hydrogels is necessary for building scaffolds with precise inner structures, pores, and girder sizes. Crosslinked networks must also hold swollen dimensions stable. In the final printed product form, the construct has to be biocompatible and to be able to mimic the ECM environment to support the living cells' adhesion, proliferation, and differentiation.

Hydrogels are combined with biologically active compounds and living cells and serve as a cell-delivery matrix before the bioprinting process or seeded after manufacturing scaffolds [160, 161]. The keys to the successful bioprinting of hydrogels are printability, biocompatibility, good mechanical properties, and high cell viability[162]. The most commonly used tissue engineering hydrogels are derived from biopolymers such as collagen, gelatin, fibrin, alginate, hyaluronic

acid, and chitosan[80, 163]. Relevant physical and chemical properties, such as viscosity, yield stress, shear-thinning, oscillatory linear shear flow, and crosslinking mechanisms of those natural polymers, have been discussed in the literature[152, 153].

In this study, we address the rheological properties of collagen networks and link their roles to the filament extrusion and layer stacking stages of extrusion-based bioprinting in depth. Collagen is a well-suited biomaterial for bioprinting because of its natural cell-binding sites, temperature-dependent gelation, and its degradability by enzymes[80, 162, 164, 165]. Therefore, it is one of the most commonly used biomaterials in biomedical and tissue engineering. Collagen has also been used as representative material in various review articles emphasizing bioprinting technologies[156, 166-168]. However, a detailed discussion of the micro-extrusion-based bioprinting process with the roles of comprehensive rheological properties of collagen hydrogels have been missing. Underneath the bioprinting process with collagen networks, the flow-related issues can be numerous, such as the orientation of collagen molecules under extensional flow in the “capillary exit” effects, swell, sag, surface fracture after capillary flow, molecular diffusion, interlayer bonding, and crosslinking among stacked filaments. Those concerns are expected to significantly impact bioprinting and affect the printed objects' integrity, precision, and cell viability. Unfortunately, there is little research done on them. Hence, the main objective of this paper is to discuss the rheology and flow behavior of collagen-based inks and cell-laden bioinks while focusing on the extrusion and layer stacking stages of micro-extrusion-based bioprinting. We discussed flow-related issues using polymer processing engineering principles[169, 170], as those discussions are equally valid for the bioprinting of other hydrogels and can be used as a guide for other bioprinting researchers.

Collagen is one of the most popular materials for bioprinting due to its hydrophilic structure, resulting in high viability and proliferation rates. However, the low viscosity of collagen solutions requires pre- or post-printing crosslinking to attain structural integrity in final constructs. In addition, as a natural product, variations in lot-to-lot extractions always exist and may affect the quality of bioprinted materials. Therefore, a better understanding of the collagens' structure and rheological properties and their impacts on various crosslinking, gelling, and flow strategies are needed. The outline of this review can also be used as a road map to investigate the bioprinting of other biopolymers, as presented in Figure 2.1. In Section 2.2, we first reviewed the chemical structure, fibrillogenesis, and crosslinking of collagens, followed by an extensive evaluation of their broad range of rheological properties. Some of the rheological properties which have never been considered previously in the evaluations of bioprinting of collagen networks and other hydrogels, such as first normal stress coefficient, extensional viscosity, comparison of steady shear vs. oscillatory linear complex viscosity (Cox-Merz Rule), and large amplitude oscillatory shear (LAOS), etc. are discussed. The stages of a bioprinting process, including filament extrusion and layer-stacking, and bonding are discussed in Section 2.3. Due to the lack of data on collagen hydrogels, this section's core part was prepared using established knowledge from polymer melt processing[169, 171, 172] and our specially-designed experiments. Straight capillary and converging cone-shaped needles were selected to investigate the flow behavior, such as such as normal stresses generation, and extensional deformation under steady shear flow during bioprinting process. The role of molecular structures of collagen and their crosslinking mechanisms on the interlayer molecular diffusion and bonding during the layer-stacking and fusion stage of bioprinting is also discussed. Finally, we briefly reviewed the role of extrusion and layer-stacking on the shape integrity and the cell viability of the constructed biomaterial in Section 2.4.

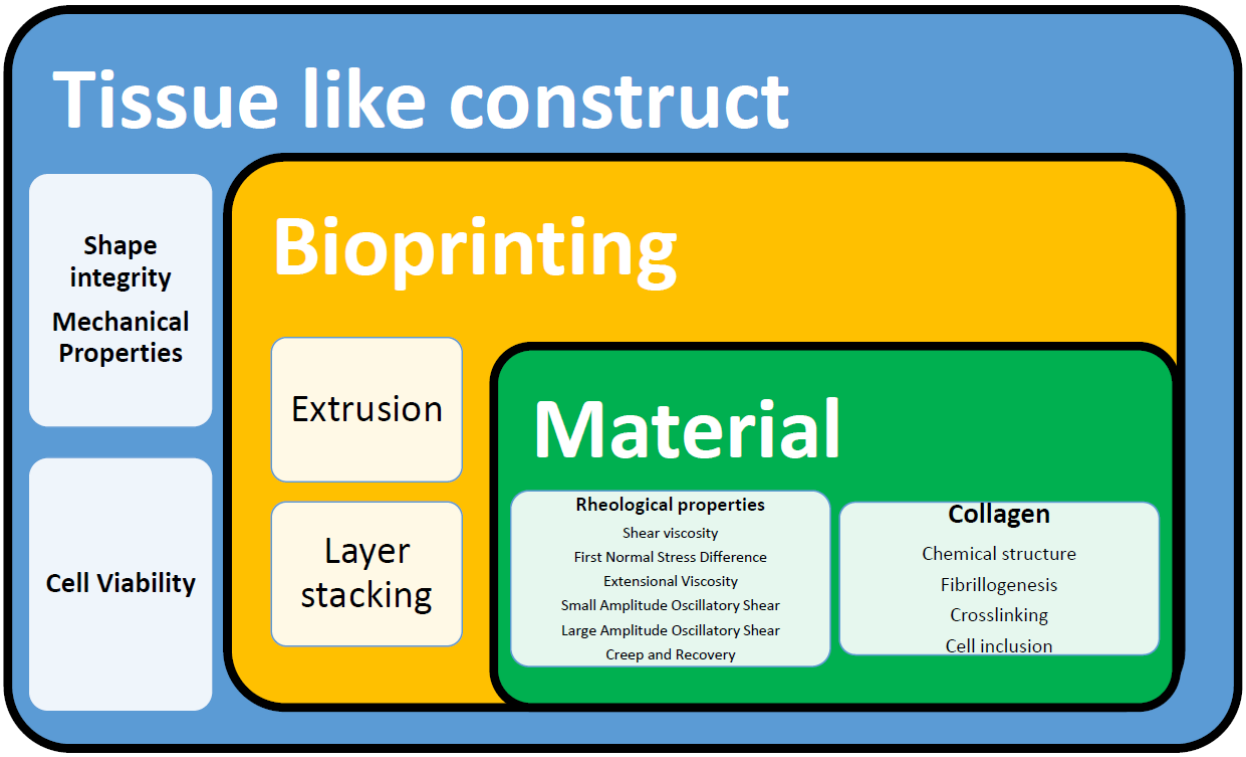

Figure 2.1 Schematic display of factors playing roles in bioprinting.

2.2 Collagen as a bioprinting material

2.2.1 Structure

Collagen, as a protein, is the most common structural polymer that exists in the extracellular matrix vertebrates and invertebrates. It is primarily found in the skin, bone, tendon, and connective tissue organs of human and animal bodies. There are 29 collagen types identified based on structure and presence in specific tissues[173], and they have been broadly classified as fibrillar and non-fibrillar types. Fibrillar collagens are commonly found in human bodies and can be subdivided into Type I (found in skin, tendons, vasculature, organs, bones); Type II (found in cartilage); Type III (found in reticulate); Type IV (found in basal lamina); and Type V (found in cell surfaces, hair, and placenta)[174]. Type I collagens have been actively and successfully used as

biomaterials due to their biocompatibility and low immunogenicity[175]. Collagen is formed in self-assembled structures at different length scales, usually in the form of elongated fibrils with a length greater than 500 µm, diameter greater than 500 nm, and consists of more than 10^7 molecules. [175-178]. The structural hierarchy of collagen fiber formation is illustrated in Figure 2.2. The primary structure of a collagen molecule is a polypeptide chain, which is formed from approximately 1000 residues (repeating units) and contains about 20 different types of amino acids. Each polypeptide molecule also called procollagen, forms a minor helix with a left-handed (secondary) structure. The left-handed single helix structure has ten residues per three turns and a pitch length of 0.9 nm. Polypeptide chains have regions containing the repeating amino acid motif Gly-X-Y-, where Gly is glycine and X and Y are other amino acids. The most frequent arrangements are Gly-Pro-Hyp where Pro is the proline and Hyp is the hydroxyproline.

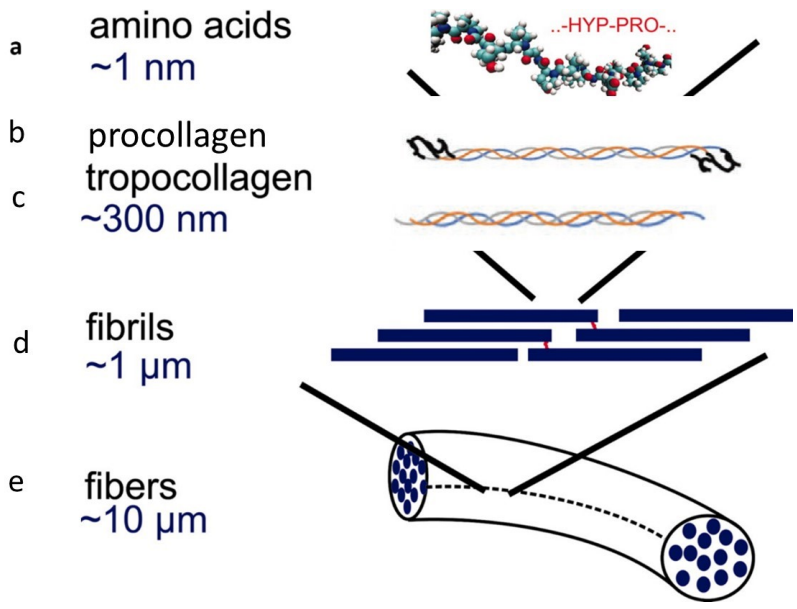

Figure 2.2 The schematization of collagen structures: (a) Left-handed single polypeptide chain, (b) Right-handed triple helix (tertiary structure) structure of procollagen assembly, (c) Enzymes cleaved ends of procollagens form tropocollagen assembly, (d) Fibrils formed by rope-like coils of coils structure (tropocollagen units both within and between microfibers are cross-linked covalently), and (d) Fibers are bundles of twisted fibrils (Copyright (2021) National Academy of Science [176]).

The primary helix structure of three procollagen strands is right-handed and assembled with loose ends which have large N- and C-terminal pro-peptides. This is the precursor of the tropocollagen ripple helix of procollagen. Tropocollagens are organized into a right-handed triple helix (tertiary structure) stabilized by removing C- and N- ends [179]. Glycine is at the core of tropocollagen, and X and Y are facing the surface. The Pro and Hyp of X groups bring rigidity to the tropocollagen and bring mechanical and thermal stability to collagen fibrils. Tropocollagen molecules have a molecular weight of approximately 345,000 g mol^{-1}, having 110,000 g mol^{-1} for each strand. The right-handed helix of tropocollagen has a pitch of about 9 nm, ten times larger than the left-handed single-strand helix pitch.

The packing and assembly of tropocollagen units and their intra- and inter-molecular crosslinking catalyzed by lysyl oxidase (LOX) into fibrils provide mechanical strength and enzymatic resistance to collagen fibers. With its tri-strand helix structure, tropocollagen is a rod-like shaped particle having a length of 300 nm and a diameter of ~1.7 nm. Fibrils are made of rods in an arrangement of parallel arrays, staggered with periodic spaces of 67 nm and multiples (quaternary structures) [180]. Finally, fibers with lengths in the order of 10 μm are formed by bundles of twisted fibrils. Overall, collagen molecules form a coiled-coil, rope-like conformation. Covalent cross-links between collagen molecules and proteoglycan matric between fibrils strengthen fibers and make them insoluble.

2.2.2 Extraction, Fibrillogenesis, and Crosslinking

Collagen molecules in aqueous solutions undergo a sharp thermal transition (melting) by heating and forming gelatins. Heating collagen fibers results in irreversible denaturation of tropocollagen units; it may cause partial or total separation of polypeptide strands, depending on the imino acid

content of collagen and the severity of breaking covalent bonds. Therefore, gelatins have low shape stability, poor mechanical strength, and low elasticity at room temperature[181]. Gelatin formulations are not preferable to collagens in bioprinting without covalent crosslinking, as gelatin may result in rapid chemical and physical degradation.

Compared to gelatin, collagens can be extracted from mammalian tissues either by acid, enzyme, or salt solubilization, depending on the source and type of the tissue[182, 183]. In a common route, extraction of Type I collagen from bovine tissues into dilute acetic acidic solutions releases single tropocollagen units. If it is challenging to extract collagens by acid solubilization, pepsin can be used as an enzyme in the extraction process. In addition, newly formed collagens in young tissues with less crosslinks can be extracted in cold neutral salt solutions.

When collagen solution is neutralized (pH is between 6.5-8.5) and kept at temperatures between 20-34 °C, collagen solutions undergo sol-gel transition due to the production of fibrils [184]. This process is also called fibrillogenesis, driven by the increase in entropy associated with the loss of water from the bound tropocollagens [185]. The critical *in vitro* fibrillogenesis concentration is of the order of 0.5 μg/ml. The fibril diameter is highly dependent on the fibrillogenesis process temperature. Lower fibrillogenesis temperatures generally result in broader fibrils, with up to 200 nm diameters at 20 °C, while higher temperature usually result thinner fibril, with diameter of 20±70 nm at 34 °C [186, 187]. Concentrations of collagen, pH and ionic strength are also known to affect the fibrillogenesis process[188]. The kinetics of the fibrillogenesis process is monitored by turbidity measurements[189]. Collagen concentration affects fibrillogenesis in a non-monotonous trend. Gobeaux et al. investigated the evolutions of fibril diameter vs. collagen concentration data by plotting their experimental data at semi-dilute and concentrated regimes

and included literature on dilute solutions (Figure 2.3) [190]. Fibril diameters vary from 10 nm to >100 nm after neutralization according to four concentration regimes: Region I (dilute regime); Region II (semi-dilute regime); Region III (concentrated regime with dominant repulsive interactions between triple helices); Region IV (concentrated regime with dominant attractive interactions). According to Gobeaux et al. [190], this behavior is explained as follows: overlapping and nucleation points result in a steady increase in fibril diameters with a concentration in Region I. Fibril diameter decreases with collagen concentration in Region II due to steric overlaps, and in Region IV due to attractive interactions. Overlapping segments between collagen molecules in domains II and IV become nucleation points at the early stages of fibrillogenesis. Higher numbers of nucleation points result in many but smaller diameter fibrils. In Region III, repulsive interactions compete with overlaps and again cause fiber diameter increased with concentration. Again, fewer nucleation points in Region III would lead to larger fibrils.

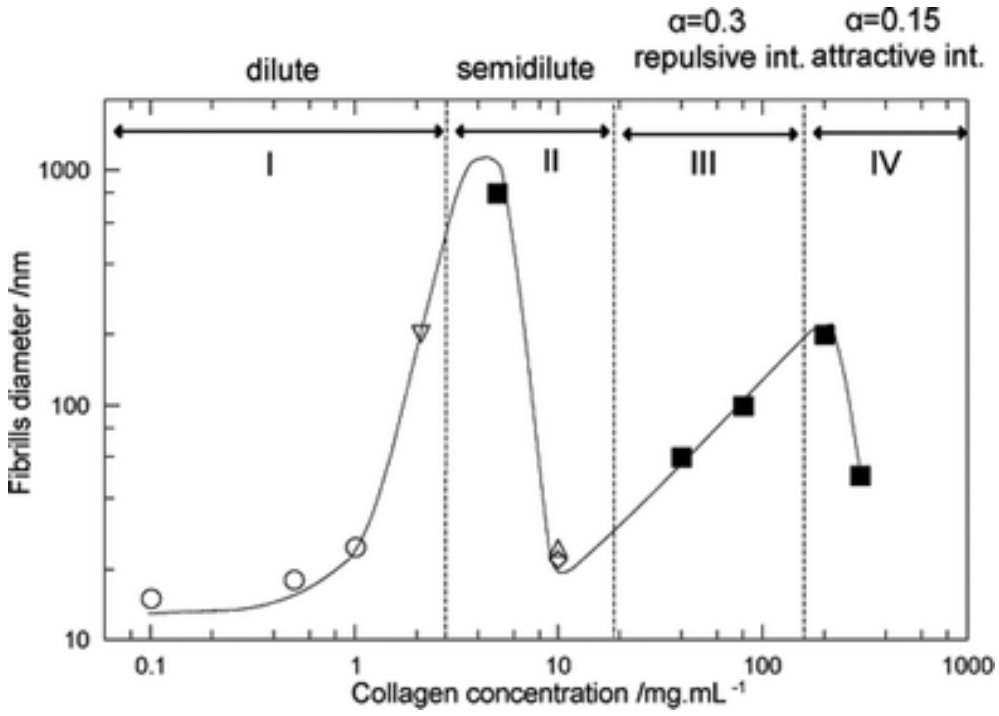

Figure 2.3 Fibrils' diameter as a function of fibrillogenesis collagen concentration (adopted from [190]).

Fibrillogenesis of Type I collagen generates larger fibril diameters compared to the fibrillogenic of Type V collagen. Mixing Type I collagen with Type V significantly decreases mean fibril diameter and variance[191]. On the other hand, the incorporation of macromolecules induces faster collagen fibril formation with increased porosity and thicker collagen fibrils [192]. Macromolecular crowding produces thick fibril networks with decreased susceptibility to proteinase-mediated degradation without significantly altering matrix stiffness[193]. Fibrillogenesis of solubilized collagens *in vitro* does not achieve the inherent fibril self-assembly *in vivo*. Hence, collagen biomaterials usually show poor mechanical properties, cell induced contraction, and rapid degradation. The collagen hydrogels must be subjected to exogenous crosslinking procedures to improve mechanical properties and stability. Those procedures can be classified as chemical, physical, and enzymatic methods, summarized in Table 2.1.

Major chemical crosslinking agents for collagen scaffolds are water-soluble aldehydes[194-197], carbodiimides[198-200], isocyanates[201, 202]. However, due to the cytotoxicity, crosslinking by these chemicals cannot be performed with the presence of cells. Other chemical crosslinking agents for collagens are carbohydrates such as ribose [203-205] and glucose[204, 206] and fruit or flowers extracted chemicals such as genipin[162, 207, 208] and proanthocyanidin[209], where these crosslinkers showed relatively low cytotoxicity, therefore they can be used in cells embedded systems. Crosslinking with carbohydrate mediation such as ribose and glucose results in slower collagen fibril formation but thicker fibril diameter with improved compressive modulus.

Table 2.1 Crosslinking methods of collagens and their rheological/mechanical characterizations

Crosslinking	**Solution**	**Rheological/mechanical characterizations**	**Targeted applications**
None[188, 190]	0.6-300 mg/mL Type I collagen in 500 mM acetic acid solution	Steady shear, creep-recovery	Biomimetic materials for medical applications
None[210]	10 mg/mL Type I collagen in 0.1-10 M acetic acid solution.	Steady shear, dynamic frequency sweep, creep-recovery	Provide theoretical guidance for future practical applications
Glutaraldehyde (GTA)[194]	Type I bovine tendon collagen in 0.05 m acetic acid	Compressive testing	Tissue engineering of articular cartilage and the association of chondrocyte contraction and the processes of mitosis and biosynthesis
Glutaraldehyde (GTA) [195]	Polyanionic soluble collagen	N/A	Production of new bone with prolonged presence of a mechanical barrier
Glutaraldehyde (GTA)[196, 197]	5mg/mL bovine skin collagen solution	Frequency sweep Steady-state shear, hysteresis loops, temperature sweep, creep recovery compliance.	Establishing mechanical models
1-ethyl-3-(3-dimethyl aminopropyl) carbodiimide (EDAC)[199]	Collagen in 3wt% hyaluronic acid (HA) solution with collagen/ HA=8:2	N/A	Porous scaffolds
1-ethyl-3-(3-dimethyl aminopropyl) carbodiimide(EDAC)[200]	100 mg/mL Type II collagen+(2.5-15%) cellulose nanocrystals in 0.05 M acetic acid	Creep-recovery, dynamic viscoelastic properties with a frequency sweep, strain sweep	Designed bio-inspired CNC/collagen hydrogels with anisotropic structure, which mimics the superficial structure of the native cartilage
1-ethyl-3(3-dimethyl aminopropyl) carbodiimide (EDAC)[198]	Type I collagen 0.5 wt% collagen in acetic acid	Ultimate tensile strength and percentage of elongation	N/A
1,6 hexamethylene diisocyanate (HDMI)[202]	Type I collagen from porcine dermal hides were decellularized with SDS	N/A	To compare leukocyte activation by commercially available biologic surgical materials
1,6 hexamethylene diisocyanate (HDMI)[201]	Pepsin solubilized Type I collagen solutions (5% w/v concentration in 0.5M acetic acid)	Uniaxial tensile testing	Scaffold fabrication
Ribose[203]	1% Type I collagen gel (pH=3.5)	Creep, static compression tests	3D collagen scaffolds

Crosslinking	Solution	Rheological/mechanical characterizations	Targeted applications
Ribose[205]	1% Type I collagen solution from equine tendon with MgHA	Frequency sweep with dynamic mechanical analysis	Bone tissue regeneration
Ribose[204]	Type I collagen in 0.1% acetic acid	Viscoelastic properties with frequency sweep	Subsequent interaction with MDA-MB-231 breast cancer cells
Glucose[204]	Type I collagen in 0.1% acetic acid	Viscoelastic properties with frequency sweep	Subsequent interaction with MDA-MB-231 breast cancer cells
Glucose[206]	Type I collagen from rat tail tendons and extracted in 0.1% sterile acetic acid	Compressive modulus	Independently modulating endothelial cell behavior.
Genipin[207]	Type I collagen from rat-tail, 9.58 mg/mL in 0.02 M acetic acid	N/A	N/A
Genipin[208]	Type I collagen from rat tail 2mg/mL	Dynamic viscoelastic properties with time sweep at a constant frequency	Injectable collagen gel scaffold.
Genipin[162]	Type-I collagen derived from porcine tendon	Oscillatory linear shear, complex viscosity, temperature sweep, frequency sweep	3D bioprinting of osteoblast-like cells
Proanthocyanidin[209]	Collagen/KGM (konjac glucomannan	Dynamic mechanical analysis with frequency sweep	Tissue-engineered graft for vascular application
Tannic acid[211]	2.54% collagen hydrogel. in 1% acetic solution	Steady-state shear flow, oscillatory measurements under squeezing flow, frequency sweep,	Dressings for wound healing and/or for obtaining porous matrices or films
Photocrosslinking[212]	Type I collagen at 4,8,12 mg/mL and riboflavin (0.5mM)	Dynamic viscoelastic properties with time and frequency sweep	3D bioprinting
Thermo-crosslinking[213]	Type I bovine collagen concentration 0.5-1.5% in 0.5M acetic acid	Dynamic viscoelastic properties with frequency sweep and temperature sweep	N/A
Thermo-crosslinking[214]	Type I Collagen with Pluronic F-127, collagen (1.5 -3 mg/ml), Pluronic (20-30% w/v)	Dynamic viscoelastic properties with frequency sweep and temperature sweep	3D bioprinting
Thermo-crosslinking[215]	Type I 3.5w/v Bovine collagen	Steady-state shear flow dynamic viscoelastic measurement with	3D bioprinting of nasal cartilage

Crosslinking	Solution	Rheological/mechanical characterizations	Targeted applications
		frequency sweep and temperature sweep	
Dehydrothermal treatment[216]	Freeze-dried collagen-glycosaminoglycan slurry	Compressive and tensile modulus	Porous scaffolds

Physical crosslinking methods for collagen-based scaffold are short-wavelength UV irradiation[217] and dehydrothermal treatment[213]. For unmodified collagen scaffold, the UV irradiation with short wavelength usually initiated free radical formation on tyrosyl and phenylalanyl residues, and these radicals are then bond together and induces intermolecular crosslinking, therefore result in better mechanical stability[217]. Dehydrothermal treatment with high vacuum and temperature removed the bounded water from collagen molecules exhaustively. The removal of water results in condensation reactions between the carboxyl and amino group in the amino acid [216, 217]. However, due to the harsh crosslinking procedure, both dehydrothermal and short-wavelength UV irradiation can cause the denaturation of collagen molecules and cannot used with the presence of cells. To crosslink the cell embedded system, a mild long-wavelength UV crosslinking can be used. For example, riboflavin as a photochemical agent can be mixed with collagen solution to strengthen the mechanical properties of collagen molecules using 365nm UV with 10s[212]. Collagen molecule can also be modified to form methacrylate collagen (COLMA), which can be crosslinked using 365nm UV with short curing time[218].

2.2.3 Rheological Properties

The state of fibrillogenesis and crosslinking dictates the rheological and viscoelastic properties of collagens, which govern the extruding, stacking, and structural integrity of bioprinted materials. Therefore, collagens' relevant rheological and viscoelastic properties will be reviewed first. Depending on the collagen solution concentrations, the collagen hydrogel formed by either fibrillogenesis or crosslinking showed both elastic and viscous properties to certain degrees, under varying time scales, temperatures, applied stresses, and strains. Their characterizations by rheological measurements are of interest in bioprinting for two reasons discussed below.

First, by measuring at least one of the stress components (shear stress, τ_{xy}) under extremely simple and well-defined small deformations or steady-state flow, we can obtain the viscoelastic properties or shear viscosity as functions of time, (shear) strain rate, and temperature. These properties, which we also call "material functions," shed light on the structure and organization of collagens by the denaturation and renaturation processes, the formation of fibrils, crosslinking, and cell inclusion. In addition, the source of feedstock tissues, extractions, and preparations of collagens result in sample to sample variations[156]. Meaningful but quick rheological characterization methods can also detect those deviations as quality control tools before the laborious preparation of cell-laden bioinks and bioprinting.

Secondly, characterization of material functions by rheological measurements allows us to predict how collagen gels behave under different stages of bioprinting processes. In addition, material functions are also needed to evaluate the development of mechanical strength of printed collagen filaments, which depends on adhesion among stacked filaments, molecular diffusion across their boundaries, and crosslinking. Therefore, understanding the interactions between the rheological properties of collagens and the bioprinting process conditions makes the development of bioinks formulations less time-consuming. Careful rheological characterization of collagen hydrogels serves as a screening strategy to save time and prevent unsuccessful prints.

Rheological measurements which are essential in the printing of collagen hydrogels are discussed here under two groups: 1) steady-state shear flow, and 2) time-dependent dynamic shear deformations. Time-dependent shear measurements are performed by applying different procedures such as small and large amplitude oscillatory shear, creep, and stress relaxation methods[172].

2.2.3.1 Steady-state Shear Flow

2.2.3.1.1 Shear Viscosity

Under a simple steady-state flow, the shear stress τ_{xy} is the function of only the shear rate $\dot{\gamma}_{xy}$. The shear rate dependent viscosities $\eta(\dot{\gamma})$ of collagen solutions and gels can be measured under a steady-state Couette flow using a "cone and plate" geometry. Figure 2.4A shows the viscosity vs. shear rate curves of Type I collagen in 500 mM acetic solution (pH=2.5) at concentrations up to 16 mg./mL(~1.6%) [190]. As discussed in the preceding section, collagen in acetic acid solutions exists in the tropocollagen form. Those collagen solutions exhibited a shear-dependent viscosity above the critical shear rates, depending on collagen concentration. At low shear rates (below a critical shear rate), the shear stress is proportional to the shear rate, and a Newtonian (*zero-shear-rate*) viscosity is observed. At higher shear rates, the viscosity decreases with the increasing shear rate. Increasing the collagen concentration steadily would shorten the Newtonian plateau and broaden the shear-thinning segment. Steady-state shear-thinning viscosity is the most important property of bioinks during the bioprinting processes. Nevertheless, most studies on bioprinting of collagen measure and use the complex viscosity vs. oscillation frequency (obtained under oscillatory measurement within linear deformation range) in the place of steady shear viscosity[214, 219]. We suggest exercising caution about this practice, which will be discussed later in this review.

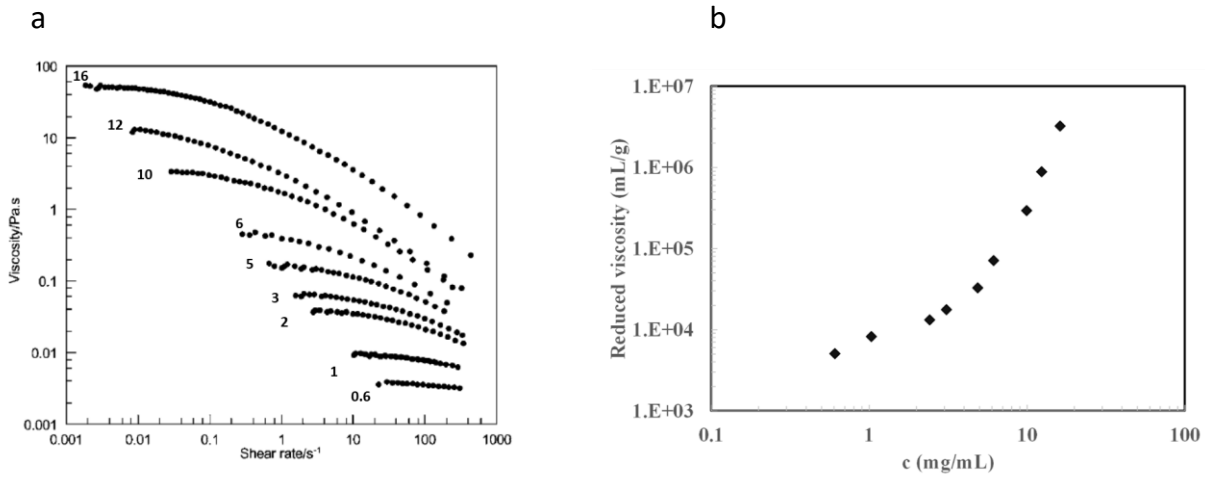

Figure 2.4 (a) Steady viscosity *(η)* against the shear rate of acidic solutions of collagen $\dot{\gamma}$ *(dγ/dt)* for various collagen concentrations 0.6 mg.ml^{-1} ≤ c ≤ 16 mg.ml^{-1} (Collagen concentrations in units of mg/mL are marked next to each curve), (b) Reduced viscosity (η_{sp}/c) against the collagen concentration. (adopted from [190]).

The effect of collagen concentration on the Newtonian (plateau) viscosity is best described by replotting the reduced viscosity as $\eta_{red} = \left(\frac{\eta-\eta_0}{\eta_0}\right)\frac{1}{c}$ vs. collagen concentration *c* (Figure 2.4B), where η is the zero-shear viscosity of collagen solution, and η_0 is the viscosity of the solvent. This plot is used to calculate the intrinsic viscosity [η] of collagen (765 ± 110 mL. g^{-1}), which is the y intercept of the reduced viscosity vs. collagen mass concentration plot (Figure 2.4B). A similar result of [η] (865 mL.g^{-1}) is also obtained for collagen (with M_w=300 kDa) solutions at a pH = 3.7 in another study[220]. The critical overlap concentration, c*, is the boundary separating the dilute and semi-dilute polymer solution. It can be determined by plotting a linear line (slope=1) from the inflection point of the Figure 2.4B, which is between 3-5 mg/mL in this case. One can also note that the morphological change from dilute to semi-dilute concentration regimes can also occur at the concentration where volume fractions (ϕ*) = (d/L)^2 [221]. This transition value also corresponds to approximately a concentration of 3 mg.ml^{-1}. A comprehensive

flow analysis of collagen solutions is carried out by Gudapati et al. while calculating intrinsic viscosities and overlapping concentrations of collagen and fibrinogen[222].

The rheological behavior of 35 mg/mL (~3.5%) collagen in a neutral buffer solution is presented in Figure 2.5[215]. As expected, the neutralization of the collagen solution at a relatively high collagen concentration resulted in thermos-induced sol-gel transition. The neutralization increased in concentration resulted the increases in both zero-shear-viscosity and the shear rate dependent behavior. A well-equipped rheometer with "cone-plate" geometry can only reach down to shear rates of 10^{-3} s^{-1} accurately. Therefore, a full zero-shear-rate plateau could not be fully obtained. Nevertheless, the zero-shear-rate viscosity of 35 mg/mL in the neutral solution was higher than 10,000 Pa.s, a drastic upsurge from the 200 Pa.s viscosity of 5.0 mg/mL collagen in the acetic acidic solution. On the other hand, the viscosity of collagen in the neutral solution declined in the order of four hundred times, while the shear rate increased from 10^{-2} s^{-1} to 1000 s^{-1} and exhibited a straight line with a negative slope on the log-log plot. The viscosity vs. shear rate slope is one of the most critical properties of collagen bioinks, which plays a crucial role in the bioprinting processes. The slope of the linear section was -0.794, which is consider as a relatively steep values among non-Newtonian fluids. This value is usually between -0.4 and -0.9 for specific polymer solutions and melts. The Ostwald-de Waele model of power-law viscosity vs. shear rate equation is usually used to describe the log-log straight line segment:

$$\eta = K(\dot{\gamma})^{n-1} \quad (1)$$

where two parameters: K (with units $Pa.s^n$) and n (dimensionless) are the power-law fit parameters. A smaller value of the flow index (n) indicates a more robust shear-thinning behavior of the fluid. Hence, extrusion materials with lower n could be more easily printed as the fluid viscosity

is lowered under the shear stress [223]. The consistency index K can also be considered as the viscosity at the shear rate of 1.0 s^{-1}. The collagen gel in Figure 2.5 has a K value of 83.3 $Pa.s^n$ and an n value of 0.214.

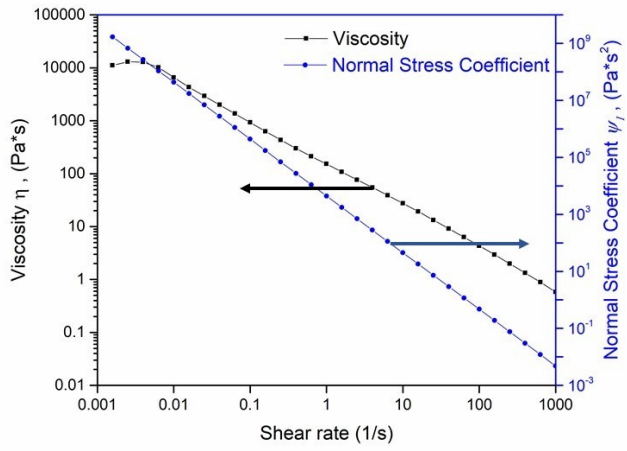

Figure 2.5 The viscosity and first normal stress coefficient as a function of shear rate for 35 mg/mL in a neutral solution (viscosity vs. share rate are replotted from [215]).

The two-parameter Ostwald-de Waele equation expresses the descending range of viscosity. However, it cannot describe the Newtonian zero-shear-rate viscosity plateau. Hence, the three-parameter (η_0, λ, m) Carreau model has sufficient flexibility to fit the experimental η vs. $\dot{\gamma}$ Curves of collagen solutions and gels. The Carreau model is:

$$\frac{\eta}{\eta_0} = [1 + (\lambda\dot{\gamma})^2]^{(m-1)/2} \qquad (2)$$

where η_0 is the zero-shear rate viscosity, λ is a time constant, and m is a dimensionless constant and corresponds to the "power-law" index. The collagen gel in Figure 2.5 has η_0, λ, m values of 14,891 Pa.s, 306.2 s, 0.211, respectively. The Carreau model describes not only the zero-shear rate viscosity η_0 and power-law exponent m, but also the time constant λ, which represents the transitional region between the zero-shear rate region and the power law region.

The steady-state flow behavior of various collagen solutions and gels fitted to the power law and the Carreau model are compiled from the literature and listed in Table 2.2. All collagen solutions behaved non-Newtonian shear-thinning fluids. As expected, increasing the collagen concentration increased its zero-shear-viscosity. Neutralizing collagen solutions resulted in gelation, increased both zero-shear-rate viscosity η_0 and increased the shear-thinning (lower n) characteristics [210]. As expected, the power-law and Carreau model give similar n and m values respectively for each collagen solution because the power-law equation is the limited expression of the Carreau model at high shear rates.

Table 2.2 The power-law and Carreau model flow descriptions of collagen gels and solutions.

	Samples		**Power-law model**			**Carreau Model**			
Source	**Collagen (mg/mL)**	**Acetic acid (M)**	**K (Pa.s^n)**	**n**	**R^2**	**η_0 (Pa.s)**	**λ(s)**	**m**	**R^2**
X. Lan et al. [215]	35	0.0	158.775	0.206	0.999	14,891	306.197	0.211	0.999
Yang et al.[210]	10	0.1	39.445	0.180	0.999	534.13	22.8	0.175	0.999
Yang et al.[210]	10	8.0	10.150	0.386	0.999	64.70	17.52	0.349	0.999

Another three-parameter (η_0, $\tau_{1/2}$, α) equation is the Ellis model, which gives viscosity η in terms of shear stress τ_{xy} rather than shear rate $\dot{\gamma}_{xy}$. After the plateau region, the model again exhibits the power-law region.

$$\frac{\eta}{\eta_0} = 1 + (\frac{\tau}{\tau_{1/2}})\alpha\text{-}1 \quad (3)$$

Data from Lan et al.[215] in Figure 2.5 can be fitted into the Ellis model with η_0, $\tau_{1/2}$, α values of 13,009.5 Pa.s, 50.72 Pa, 3.72 (dimensionless), respectively. The Ellis model's parameter α and power-law parameter are related by $n=1/\alpha$. The benefits of using the Ellis model in bioprinting

processes will be discussed in Section 2.3. Shear viscosities of collagen solutions are also fitted to Casson and Bingham models to show the yield stress values in addition to the Carreau model by Gudapati et al.[222]

Crosslinking of dilute collagen solutions increases the low shear rate viscosity and shear-thinning behavior. The increase in these properties also depends on the degree of crosslinking, governed by the type of crosslinking agent and/or method. For example, by crosslinking with GTA (varying between 0-10% GTA/collagen), the shear viscosity of collagen increased from 6.15 to 168.54 Pa·s at 0.1 s^{-1} shear rate, and the flow index decreased from 0.549 to 0.117[197].

Bioprinting of collagens is carried out either by incorporating living cells after the post printing of collagens or by extrusion with cell-loaded collagen, called bioinks [160]. The resolution of printed materials is highly dependent on the rheological properties of extruded hydrogels. Although numerous researchers have incorporated cells with collagens in bioprinting, few have reported the rheological properties of cell-laden bioinks.[212, 215, 219]. Diamantides et al. reported the effect of various cell concentrations on collagen's rheological properties[219]. In the range of 0-25 million cells per mL, as the cell concentration increases, the power-law index, *n* slightly decreases, which indicates an enhanced shear thinning behavior. These results agree with Lan et al., in which the presence of 10 million/mL nasal chondrocyte enriches the shear-thinning effect[215]. In general, incorporating cells in collagen hydrogels slightly reduces the power-law index of shear rate-dependent viscosity, depending on the cell type and concentration. Cell presence may cause the loss of the assembled interconnected collagen fibril network due to the disentanglement of collagens and makes the flow easier at the high shear rates. Nevertheless, as the cell concentration increases to 100 million/mL, the power-law index *n* starts to increase, as

shown in the Table 2 in [219]. One possible reason is that the high concentration of cells hinders the disassembly of the interconnected collagen fibril at high shear rates. In addition, Diamantides et al. [219] reported that the presence of cells results in higher zero-shear viscosity. However, Lan et al. observed a drop in low shear rate viscosity after adding the cells[215]. One possible reason is incorporating a culture medium during cell mixing and diluting the collagen system. Those results suggest that cell-laden collagens can be considered as suspensions of deformable particles (cells) in a viscoelastic media (collagen network)[224].

Overall, steady-state shear viscosity measurements provide invaluable information regarding the processability of collagen structures, and they are better suited to model the capillary extrusion stage of bioprinting. Nevertheless, it is less commonly used compared to oscillatory linear shear measurements.

2.2.3.1.2 First Normal Stress Coefficient

Hydrogel biomaterials as non-Newtonian fluids are expected to exhibit not only shear stress τ_{yx} but also other non-zero stress components under the shear flow. Normal stresses, τ_{xx} and τ_{yy} in the directions of x and y, are generated by non-Newtonian fluids with a simple shear flow of ($v_x = \dot{\gamma}_{yx}.y$, $v_y=0$, $v_z=0$). Those stresses cannot be measured independently; however their difference, τ_{xx}- τ_{yy} , walled the "first normal stress difference," can be measured while performing steady-state Couette flow in a cone-plate rotational rheometer[172]. As another material function, the first normal stress coefficient $\Psi_1(\dot{\gamma})$ is defined as:

$$\Psi_1(\dot{\gamma}) = \frac{\tau_{xx} - \tau_{yy}}{\dot{\gamma}_{yx}^2} \quad (4)$$

where τ_{xx}, τ_{yy} are normal stresses generated in x and y directions, while the shear flow is to the x-direction. The shear rate-dependent viscosity and the first normal stress coefficient are called "viscometric functions." One advantage of steady-state shear flow measurements using advanced rheometer is that the first normal stress coefficient data and the shear viscosity can be collected at the same time. Our group collected Ψ_1 vs. $\dot{\gamma}$ data while measuring η vs. $\dot{\gamma}$ of 3.5% collagen solution in a neutral buffer solution (Figure 2.5)[215]. According to continuum and molecular constitutive equations, the first normal stress coefficient (Ψ_1) should decrease with an increase in the shear rate. The decrease of Ψ_1 is twice as big as the rate of decrease of η with an increasing shear rate predicted for high molecular weight polymer melts[170]. Our results showed that the collagen hydrogel's first normal stress coefficient confirmed this prediction with the first normal stress and viscosity vs. shear rate slopes of -1.99 vs. -0.794, respectively. As discussed briefly here, the first normal stress difference of collagens and other hydrogels can easily be acquired while measuring the viscosity as a function of shear rate by using modern rotational rheometers. However, to our knowledge, this property has never been reported and used to indicate shear rate-dependent viscoelasticity by researchers investigating bioinks, including collagen hydrogels. We will discuss how hydrogels' first normal stress coefficient affects the micro-extrusion-based bioprinting in Section 2.3.1.

2.2.3.1.3 Extensional Viscosity

Unlike previous assessments in the literature [157, 225], micro-extrusion based on bioprinting of hydrogels biomaterials and bioinks cannot be described solely with a shear rate-dependent viscous flow. Uniaxial extensional deformation, and therefore extensional viscosity of hydrogels, can also play a role in an extrusion process [169, 171]. By measuring the first normal stress

coefficient, we have already shown that collagen hydrogels exhibit normal stresses in addition to the shear stress under the shear flow (Figure 2.5). Under simple elongational stress (τ_{xx}- τ_{yy}) with an extension towards *x*-direction, polymer melts and solutions exhibit elongational flow, which is described by elongational viscosity ($\eta_E = \frac{\tau_{xx}-\tau_{yy}}{\dot{\epsilon}}$) , where $\dot{\epsilon}$ is the principal extension rate. If any extensional flow exists, shear measurements are not enough to characterize the full flow behavior in micro-extrusion bioprinting. Moreover, the extensional viscosity of collagen gels will be valuable in describing the flow behavior in bioprinting and understand the structure of collagen gels. Cathey and Fuller measured the effective uniaxial extensional viscosities of collagen solutions up to the concentration of 0.23% in a 90% glycerin and 10% water solution [226]. At a semi-dilute concentration range (0.12%-0.23%), the extensional viscosity of collagen solutions exhibits strain-thinning behavior. According to this study, rod-shaped collagen molecules interact with each other more in the isotropic state than during the strong extension. Hence, the extensional viscosity is higher at low strain rates and declines as collagen molecules are aligned in the flow direction at higher strain rates. The results also showed that as the strain rates go to zero, the extensional viscosity of collagen solutions is very close to three times their respective shear viscosities ($\eta_E = 3\eta_0$), as expected by Trouton's law of viscosity[172]. However, the ratio of the enhancement of the extensional viscosity (η_E-$3\eta_0$) over the Trouton's law of extensional viscosity ($3\eta_0$) increases, as collagen concentration increases under shear thinning condition. At the highest concentration reported, (0.23%), this ratio is around 10 [226]. This extension viscosity data taken on the semi-dilute, shear-thinning collagen/glycerol solutions at high stain rate agree with the predictions of Batchelor's theory [226, 227]. Paten et al. investigated the crystallization of collagen by extensional flow as a critical mechanism in early tissue formation[228]. The role of

extensional flow has never been considered in the bioprinting of collagens. We will discuss the effect of extensional flow of collagens in micro-extrusion-based 3D printing in Section 2.3.1.

2.2.3.2 Oscillatory Shear

2.2.3.2.1 Small Amplitude Oscillatory Shear (SAOS)

The dynamic oscillatory shear test is the most commonly used rheological tool to investigate collagen hydrogels and crosslinked systems. The linear viscoelastic properties of the complex collagen fluids can be analyzed using small amplitude oscillatory shear tests within a linear range based on a well-established theoretical basis[172]. In this test with a parallel plate geometry, the upper plate undergoes small-amplitude sinusoidal oscillations with frequency (ω), while the stress-strain relationship is kept linear within the proportionality limit (Hookean). The response of shear stress to oscillating strain ($G^* = {}^{\tau}/_{\gamma}$) is separated into two components to obtain the storage (elastic) shear modulus (G') and loss (viscous) shear modulus (G"). The variations of G' and G'', as functions of the strain oscillation frequency (ω), are of interest because they describe the viscoelastic nature of hydrogels. The mechanical stress spectrum as a function of ω is also used to calculate complex viscosity ($|\eta^*|=|G^*|/\omega$) and phase angle ($\tan\delta=G"/G'$). Those properties are also called "linear dynamic-mechanical properties."

The dynamic mechanical experiments by sweeping the oscillation frequency at a constant small strain amplitude are used to investigate the frequency-dependent stress-strain behavior of collagen gels. This type of test is used to investigate the effects of collagen concentration [190, 213, 229], acetic acid concentration [210], temperature [213], and crosslinking chemicals [162, 212, 230, 231] on the viscoelasticity of collagen hydrogels and the shape integrity of the printed

material. Complex viscosity measurements as a function of frequency from those small-amplitude linear shear measurements are also used as surrogates to viscosity vs. shear rate measurements under steady-state [232, 233].

The effects of concentration on the dynamic mechanical properties of collagen solutions and gels in 0.1 M acetic acid are investigated within the linear deformation range (under 5% strain) by Lai et al. [213]. Complex viscosities (η^*) of 0.5, 0.75, 1.0, 1.25 and 1.5% collagen solutions in acetic acid are measured as functions of oscillation frequency (ω). Critical overlap concentration (c*) was predicted to be around 0.75%, based on an exponential increase in η^* above 0.75% [213]. This estimate in 0.1 M acetic acid solution is higher than the prediction of overlapping concentration ($c^* \approx 0.3$-0.5%) in 0.5 M acetic acid solution by Gobeaux et al. [190]. At low frequencies (ω), collagen solutions less than 1.25% in 0.5 M acetic acid solution exhibit higher loss modulus (G") than storage modulus (G'), while at higher frequencies, G' becomes higher than G". The reason for these is that the procollagen molecules do not have enough time to relax, and cause G'>G" at high frequencies, which means these solutions have no network structure, and there are no links between the collagen molecules. The characteristic relaxation time (λ) associated with a large-scale motion (or changes) in the structure of rod-shaped procollagen molecules can be obtained by the inverse of the frequency ($1/\omega$) when G' becomes equal to G" (crossover point). Increasing the collagen concentration from 0.75% to 1.25% results in an increase in λ value from around 0.5 s. (at 1.49 Hz) to longer than 100 s (above 0.01Hz). Above the collagen concentration of 1.5%, the collagen gel shows rubbery behavior, and G'>G" at all frequency sweep ranges [213]. This result agrees with the onset to elasticity concentration of 1.6% reported by Gobeaux et al. [190] for collagen in 0.5M acetic acid solutions.

According to Rouse's theory based on a series of beads-spring models, a dilute polymer solution at low values of frequency has to show G' ≈ $G\lambda^2\omega^2$ and G" ≈ $\eta_0\omega$, which means that the slopes of log G' and log G" versus log ω have to be 2 and 1, respectively. According to the same theory, at high frequencies, log G' has to be proportional with 0.5 log ω. Figure 2.6A shows the results of the 1.6% collagen solutions of Gobeaux et al. in 0.5 M acetic acid, which are consistent with the expectations established based on polymer solutions [190]. Nevertheless, the slope of log G'-log ω and log G"-log ω is not more than 0.7 and 0.5, respectively, in the case of Lai et al. [213].

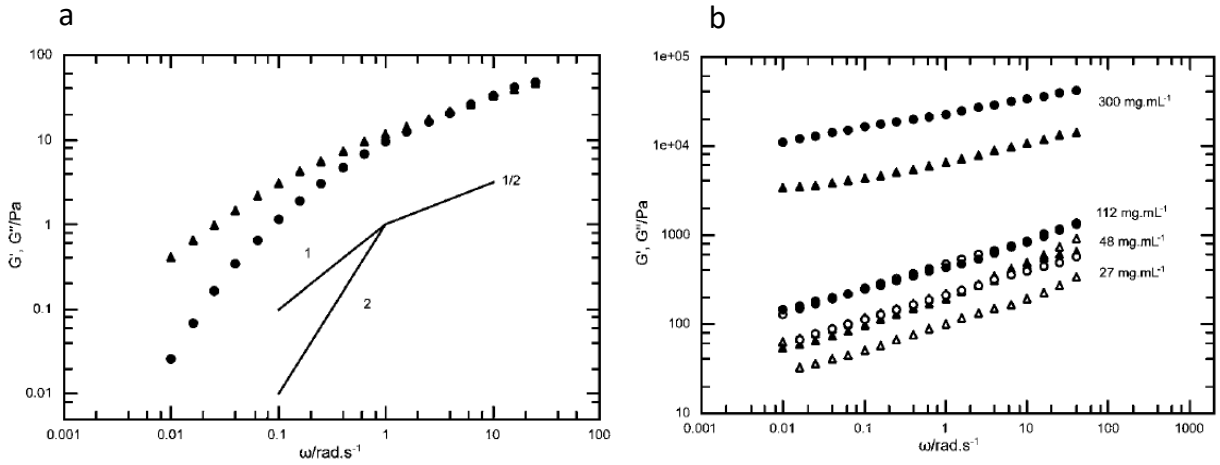

Figure 2.6 Storage G′ (O) and Loss G″ (△) moduli vs. frequency (a) at 16 mg mL^{-1}; (b) at 27 mg mL^{-1}, 48 mg mL^{-1}, 112 mg mL^{-1}, and 300 mg mL^{-1} (from [190]).

While Lai et al.'s [213] investigation is more focused on viscous semi-dilute concentrations (up to 1.5%), Gobeaux et al.'s [190] research on concentrated solutions is extended from 2.7% up to 30% (Figure 2.6B) in 0.5M acetic acid solutions. For concentrations above 2.7%, both G′ and G″ (while G′ > G″) showed a power-law frequency dependency ($G'(\omega) \propto G''(\omega) \propto \omega^{\beta}$) with the β value of 0.3 $\pm$0.02. This behavior is different from the viscoelastic properties of concentrated polymer solutions, where G' has the plateau and G" has non-monotonous frequency dependence due to the physical entanglements of macromolecules. The β value of 0.3 was lower than the

predicted value from the percolation theory (n ~ 2/3)[234]. However, in a neutral solution, Forgacs et al. [229] reported that the gel point both G′ and G″ of 0.17% collagen obey a scaling law with the critical exponent β = 0.7, and a critical loss angle being independent of frequency as predicted by percolation theory.

Yang et al. investigated the effect of acetic concentration in 1.0% collagen solutions by linear oscillatory shear flow [210]. As expected, acetic acid presence significantly affects the structure and gelation of collagen solutions. Collagen/acetic acid ratios of 100 (10 mg/mL collagen: 0.1 M Acetic acid) and 5 (10 mg/mL collagen: 2 M Acetic acid) resulted in G′ > G″ during the whole frequency sweep (from 0.01 to 10 Hz), and suggested gel structures. The 10 mg/mL collagen solution behaved like a dilute polymer solution at higher acetic solutions.

The effects of temperature and crosslinking on viscoelastic properties of collagens are discussed in Sections 2.2.3.2.3 and 2.2.3.2.4, respectively.

2.2.3.2.2 Cox-Merz Rule

In some cases, complex viscosities of collagens and other hydrogels are used in the place of steady shear viscosity [230, 233]. The shear viscosity (η) and dynamic complex viscosity (η^*) can be linked by the linear viscoelasticity at comparably low shear rates ($\dot{\gamma}$) and oscillation frequencies (ω). Often, these properties show similar shear rates and frequency dependent behaviors and have been described with an empirical law, called the “Cox-Merz rule” [172]. This rule is proposed for polymer solutions and melts and represents a simple relationship between linear and nonlinear viscoelastic properties by overlapping the steady-state shear viscosity, $\eta(\dot{\gamma})$ with the magnitude of complex viscosity, $|\eta^*|(\omega)$ while $\dot{\gamma} = \omega$. However, the Cox-Merz rule does not

hold universally. Therefore, we have investigated the validity of the Cox-Merz rule for some collagen solutions by replotting the relevant data.

Figure 2.7 shows how to verify the validity of the Cox-Merz rule. We superimposed the steady-shear viscosities $\eta(\dot{\gamma})$ and the small-strain oscillatory shear complex viscosities $|\eta^*|(\omega)$ for 1.0% collagen in 2 M and 0.1 M acetic acid solutions data obtained from the literature [210]. In the case of 2 M acetic acid solution, there was no overlapping and the Cox-Merz rule did not hold (Figure 2.7A). On the other hand, in 0.1 M acetic solution, the shear viscosity overlaps with the complex viscosity, and the Cox-Merz rule applies (Figure 2.7B). It is well known that the rule is valid for entangled molecules and percolated systems but not for suspensions. On the other hand, log G′ and log G″ vs. log ω are obtained for samples in 0.1 M and 2 M acetic acid and stated that they indicate the similar structure of collagen aggregates at relatively low acetic acid concentrations [210]. However, testing the Cox-Merz rule showed two different structures.

There are two implications of testing the Cox-Merz rule on collagen hydrogels. First of all, the validity or invalidity of the Cox-Merz rule is a suitable methodology for characterizing structures of collagen solutions. Secondly, before verifying the validity of the Cox-Merz rule, using $|\eta^*|(\omega)$ vs. ω data in the place of $\eta(\dot{\gamma})$ vs. $\dot{\gamma}$, for modeling, the 3D printing process can be erroneous.

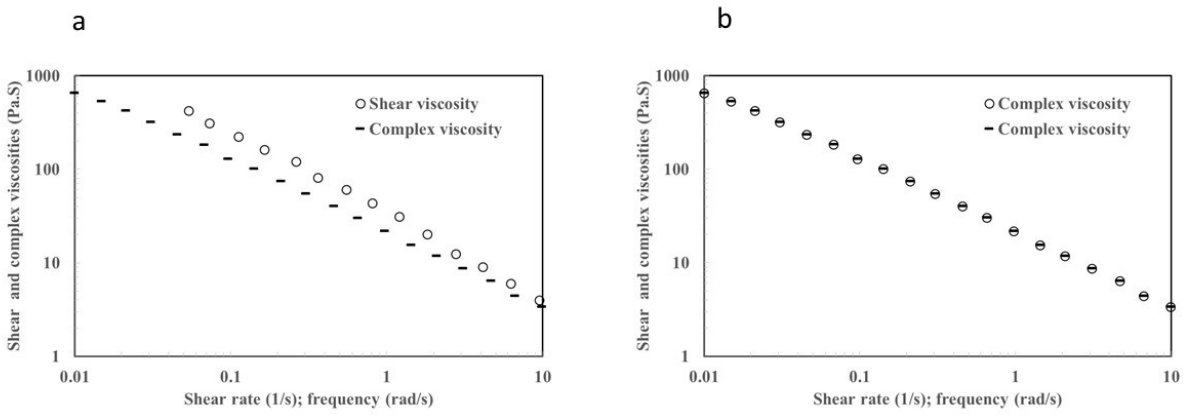

Figure 2.7 Shear viscosity and complex viscosity against shear rate and oscillation frequency (Cox-Merz plots) of 1.0% collagen in acetic acid solutions of (a) 2 M, (b) 0.1 M (adopted from [210]).

2.2.3.2.3 Temperature Dependence

Along with the collagen concentration and pH of the medium (neutral or acetic acid solutions), the temperature is an important variable affecting collagen gels' morphology and viscoelastic behavior through the fibrillogenesis process. Fabrication strategies are designed to control the temperatures of various components of bioprinting devices [162, 235].

Figure 2.8 shows the storage modulus (G′) and tan δ values of 4.0% collagen in acetic acid and neutral cultured medium for the temperature range between 10-50˚C as reported by Kim et al. [162]. In the case of the acetic acid solution, collagen is considered in its procollagen state, and its storage modulus decreases drastically above 30˚C due to the collapse of the collagen triple helix to a random coil structure (Figure 2.8A). The corresponding peak in tan δ is the "denaturation temperature." Below 30˚C, the storage modulus of the collagen in acetic acid solution gradually decreases, because of the free volume change with temperature. An opposite behavior is observed in the case of 4.0% collagen in the neutral culture medium (Figure 2.8B), the storage modulus has a maximum peak between 30-32˚C and drops drastically above 32˚C because of the

breakdown of the collagen structure. Lee et al report that the temperature that able to reach maximum storage modulus for 5% collagen in neutral solution is 36.2°C [231]. Reaching the maximum storage modulus and minimum loss modulus at gelation temperature is able to stabilize the bioprinted constructs. The gelation of the collagen is mainly because of the fibrillogenesis process, which we have discussed previously in Section 2.2.2. The fibrillogenesis process can be summarized into three steps: (1) fibril formation from several tropocollagens; (2) fibril growth in a linear direction; and (3) networking and structure formation[236, 237].

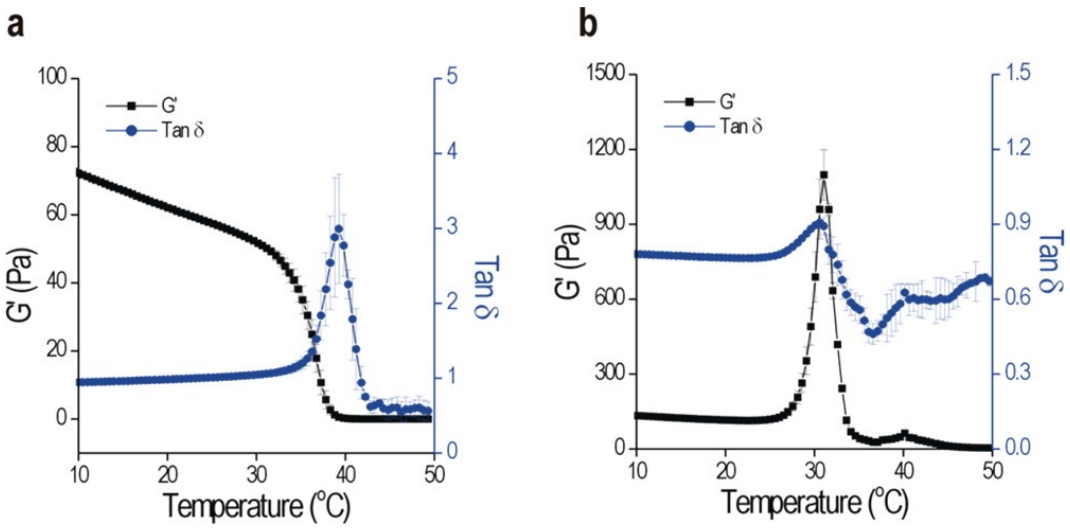

Figure 2.8 Temperature dependence of storage modulus (G') and tangent delta (tan δ) of 4% collagen (a) in acetic acid solution, (b) in the culture medium DMEM. (from [162]).

Kim et al. continued to investigate the gelation process in cell-laden (MG 63 with density=$1x10^6$ cells.ml^{-1}) 3, 5, and 7wt % collagen by measuring the storage modulus and tan δ [162]. According to this study, cell-laden collagens exhibited maximum G' between 30-40°C. The gelation temperature and the storage modulus of compositions increased as the weight fraction of collagen increased (Figure 2.9).

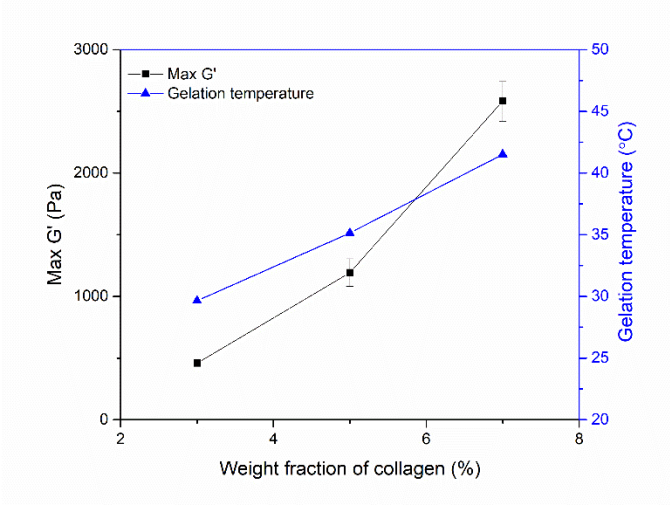

Figure 2.9 Maximum storage modulus and gelation temperature of collagen at different concentrations (from [162]).

During the micro-extrusion, even if the needle wall temperature is kept at the same temperature as the hydrogel at the reservoir, the temperature of the hydrogel may still rise due to viscous dissipation[238]. In this case, the viscosity can be calculated by the product of temperature term and shear rate-dependent viscosity terms, if the temperature is below the structural change region (<28 ^{O}C):

$$\eta = H(T)\eta_{T_0}(\dot{\gamma}) \tag{5}$$

An Arrhenius model is usually used for the temperature-dependent term [239].

$$H(T) = \exp\left[\alpha\left(\frac{1}{T} - \frac{1}{T_0}\right)\right] \tag{6}$$

where α is the activation energy. Note that H(T) is 1 at the reference temperature T_0. Equation 5 is useful if the hydrogel has high viscosity. However, in our micro-extrusion analysis, the flow was assumed to be isothermal.

2.2.3.2.4 Crosslinking and Gelation

In a bioprinting process, once hydrogel filaments are extruded, stacked, and bonded together, fabricated structures must establish higher mechanical properties than the extruded hydrogels and maintain the integrity of their shapes. Collagen hydrogels inherently have low mechanical properties that result in sagging and collapsing constructed layers and reducing the pore sizes of printed meshes. To overcome this problem, collagen hydrogels can be chemically crosslinked by immersing printed scaffolds into a crosslinking agent solution. Measurements of viscoelastic properties with oscillatory small deformation experiments can be used to evaluate the effects of crosslinking on the post-extrusion integrity of printed scaffolds.

Han et al. used a naturally-occurring proanthocyanidin (PA) obtained from grape seeds as a collagen crosslinking agent [240]. Melting temperature (T_m) was used to indicate the degree of crosslinking in those tests. According to that study, an optimal PA concentration of 0.5% increased T_m from 55 to 80^0C while showing no cytotoxicity. The crosslinking is postulated to arise from hydrogen bonds formed between the polyphenolic functional groups of PA and tropocollagen collagen.

Formaldehyde, glutaraldehyde, epoxy compounds, and carbodiimide have also been used as crosslinking agents for collagen, but all have certain toxicity levels, and controlling crosslinking rates is difficult [241, 242]. The addition of glutaraldehyde results in a reinforced structural framework and a substantially larger pore size. Melting temperature of the tendon increases from 55 to 84 ^{0}C with GTA crosslinking. Perez-Puayana et al. reported scaffold pore size and viscoelastic properties of glutaraldehyde crosslinked collagen scaffolds[243]. Figure 2.10 shows that

the presence of GTA increases the normal elastic modulus (E') of 1.0% collagen hydrogel. However, the increase in E' is higher at 0.1% than 0.3% GTA presence.

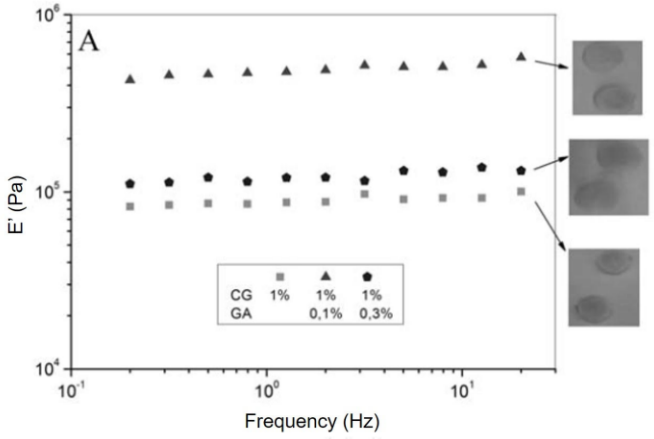

Figure 2.10 Elastic modulus vs. frequency sweep of glutaraldehyde crosslinked collagen scaffolds (from [243]).

Diamantides et al. investigated the linear viscoelastic properties of UV-activated riboflavin (at a concentration of 0.5 mM) in collagen (with concentrations 4,8,12 mg/mL) bioinks before, during, and after crosslinking to predict the kinetics of crosslinking, printability and cell viability [212]. Viscoelastic properties are measured at 1Hz and 0.5% strain. The data before and after crosslinking storage modulus results (G'_0 and G'_∞) as a function of pH are presented in Figure 2.11. According to this study, riboflavin crosslinking dramatically increases the storage moduli of collagen bioinks. The results from the pH study show that the storage modulus after gelation of collagen bioinks is highly dependent on pH, while its storage modulus before gelation changed very little with pH. On the other hand, the storage modulus of the bioink before gelation was the best predictor of bioink printability. As suggested by these findings, this study concludes that the best way to improve the printability of collagen bioinks is to increase the storage modulus of the ink before extrusion.

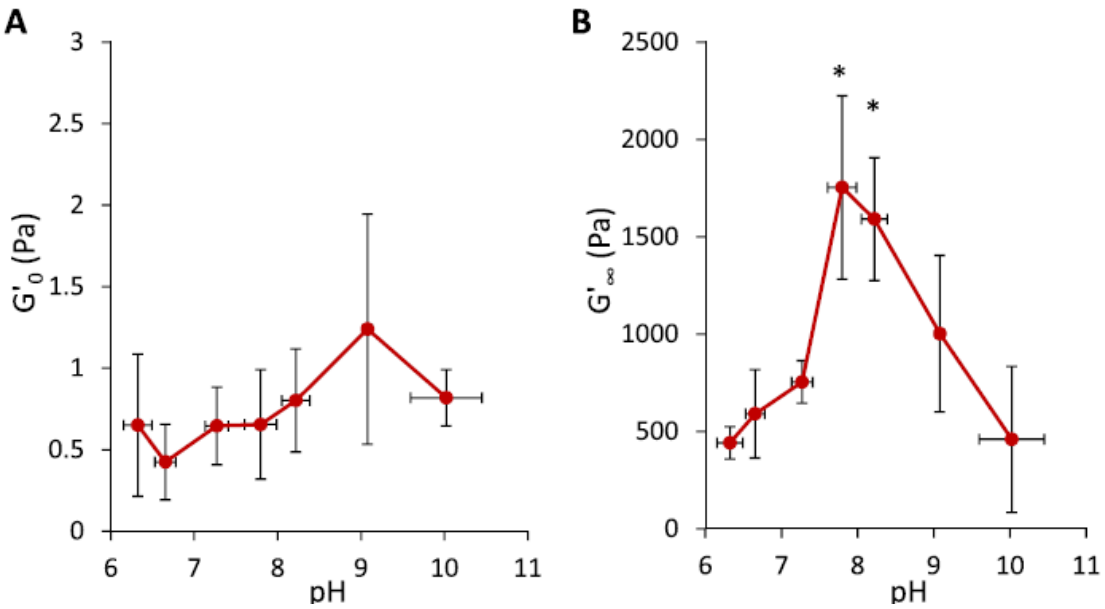

Figure 2.11 The storage modulus of collagen bioink (8 mg/mL in 0.5 mm riboflavin solution) as a function of pH (a) G'_0 of collagen bioink at 4 °C before gelation. (b) G'_∞ collagen bioink after complete gelation at 37 °C (from [212]).

In another study, tannic acid (TA) was used as a crosslinking agent, and its effect of up to 3% concentration was shown on the compressive modulus and cell activities of 3D printed collagen structures [231]. The maximum compressive strength of 50 kPa at 30% strain was obtained with 3% TA crosslinking compared to almost zero compressive strength without any TA crosslinking. The TA concentration of 0.5% increased the compressive strength to less than 10 kPa (at 30% strain) while offering reasonable biocompatibility.

Genipin was used as a crosslinking agent in 3D printing of cell-laden collagen hydrogels by Kim at al., and cell viability of over 95% was observed [162]. Figure 2.12 shows the storage modulus (G') of 5% collagen solution after post-curing of 5 min, 1 h, 3 h and 6 h in 1 mM and 5 mM genipin solutions. Both genipin solution concentrations in the curing bath and curing time increased the modulus significantly.

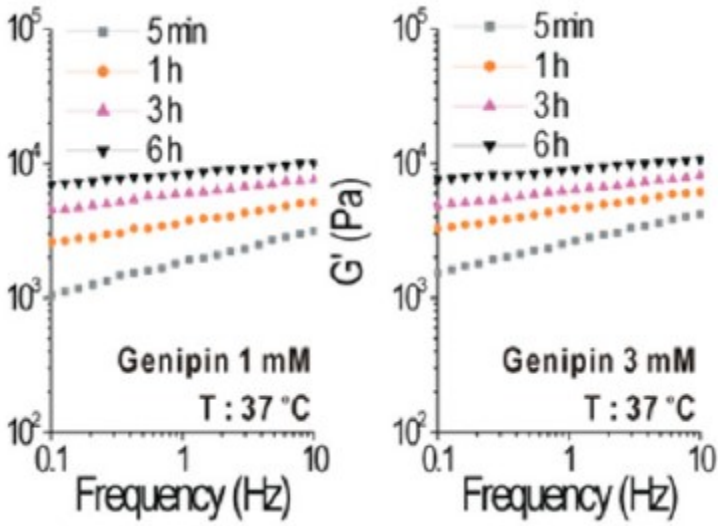

Figure 2.12 Changes in viscoelastic properties of genipin crosslinked collagen (from [162]).

The cell-laden collagen bioinks exhibit decreased storage moduli after gelation. They also show a slower gelation rate with higher cell density since the cells physically block the bindings necessary for collagen fiber's self-assembly[219]. This observation agrees with Lan et al.'s results[215].

2.2.3.2.5 Large Amplitude Oscillatory Shear (LAOS)

In the preceding four subsections, we discussed the characterization of collagen hydrogels with frequency sweeps tests at small (within the linear region) amplitude oscillatory shear strains. They have been widely used by employing well-established test protocols to investigate the linear viscoelastic properties of collagen networks[172]. Nevertheless, under various stages of bioprinting processes, particularly in micro-extrusion deformations are large and rapid and cannot be solely described by linear viscoelastic deformations constrained by small strain amplitudes. Collagen hydrogel networks exhibit complex nonlinear rheological responses outside the linear deformation range in those processes. To characterize the rheological behavior of the transition

from linear viscoelastic region to nonlinear viscoelastic region, a large amplitude oscillatory shear (LAOS) can be used. LAOS analyses are carried out by a sweeping strain amplitude at a predetermined angular frequency while recording the stress and strain data as a function of time. Then stress, strain, and time data are analyzed to determine the nonlinear viscoelastic coefficients of the material. Well-defined nonlinear test protocols for LAOS are given by Hyun et al.[244] and Ewoldt et al. [245] and applied to test hydrogels and other complex fluids [246-248]. The stress response output measured in the nonlinear region is usually not a perfect sinusoid stress with respect to the sinusoidal strain input.

Unfortunately, there are no collagen hydrogels measurements by using full test protocols of LAOS. Oscillatory strains with amplitude sweeps are applied to collagen in addition to fibrin, reconstituted basement membrane matrix (rBM), polyacrylamide and agarose gels and their shear storage moduli are measured without complete LAOS analysis[249]. Collagen, fibrin, and rBM show strain stiffening, but polyacrylamide and agarose were almost linearly elastic without significant change in modulus. Another amplitude sweep test with full LAOS protocol is performed to determine the strain (192%) that breaks the hydrogel network in bioprinted constructs of partially oxidized hyaluronate (OHA) and glycol chitosan (GC) in the presence of adipic acid dihydrazide (ADH) ([OHA2500] = 2 wt %, [GC] = 1, wt %, [ADH] = 0.3 wt %) (Figure 2.13) [250]. The authors suggested that full LAOS testing of collagen networks can explain the role of crosslinking on the network stiffness, network recovery rates and trade-off between stiffness and recovery rate.

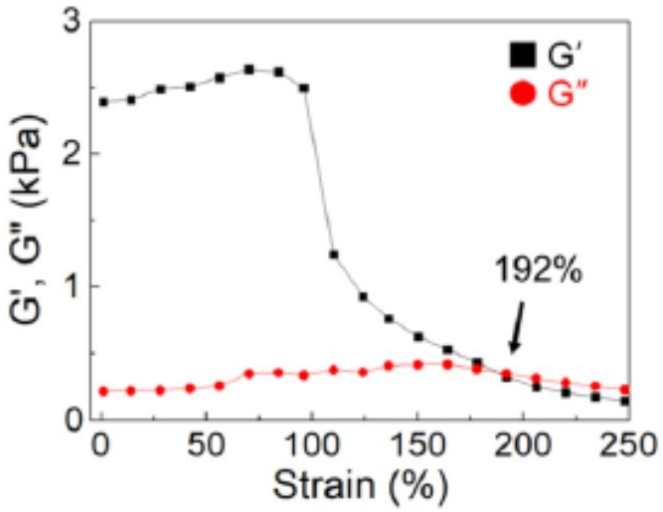

Figure 2.13 Amplitude sweep carried out up to 250% strain with the OHA2500/GC/ADH hydrogel (Adopted from [250]).

2.2.3.3 Creep and Recovery

The creep and recovery test method is used to characterize fibrillogenesis and crosslinking of collagens by differentiating viscous and elastic responses[188, 190, 196, 197, 200, 203, 210]. As discussed previously, the normal stress difference measurement under steady-state shear flow measures the shear rate dependency of the elasticity (Section2.2.3.1.2. It is useful while evaluating the capillary entrance and exit effects in micro extrusion and filament swell (Section 2.3). In comparison to normal stress difference, the creep and recovery measure the stress-dependency of viscous and elastic components while introducing the response time as an additional parameter that is more suitable to evaluate network formation by fibrillogenesis and crosslinking.

Time-dependent strain is measured while constant stress is applied in creep and released in recovery as step changes within the linear viscoelastic region of shear deformation. The strain and stress are interrelated with time-dependent compliance by $J(t)=\gamma(t)/\tau$ with a unit of 1/Pa. Usually, J(t) of creep data is fitted series of Maxwell and Kevin Voigt model, and J(t) of recovery is fitted

to a semi-empirical model. Figure 2.14 with outsourced data from Tian et al. shows the creep and recovery compliance data with the applied and released stress of 2 Pa. Collagen solutions are crosslinked with various amounts of GTA in 5% collagen solution[197]. An increased GTA concentration decreases creep compliance due to increased crosslinking density. Figure 2.14B shows the recovery rate once the applied stress is removed. Crosslinking bonds because of GTA addition hinders the intermolecular slippage, decreases the deformation, and speeds up the recovery rate.

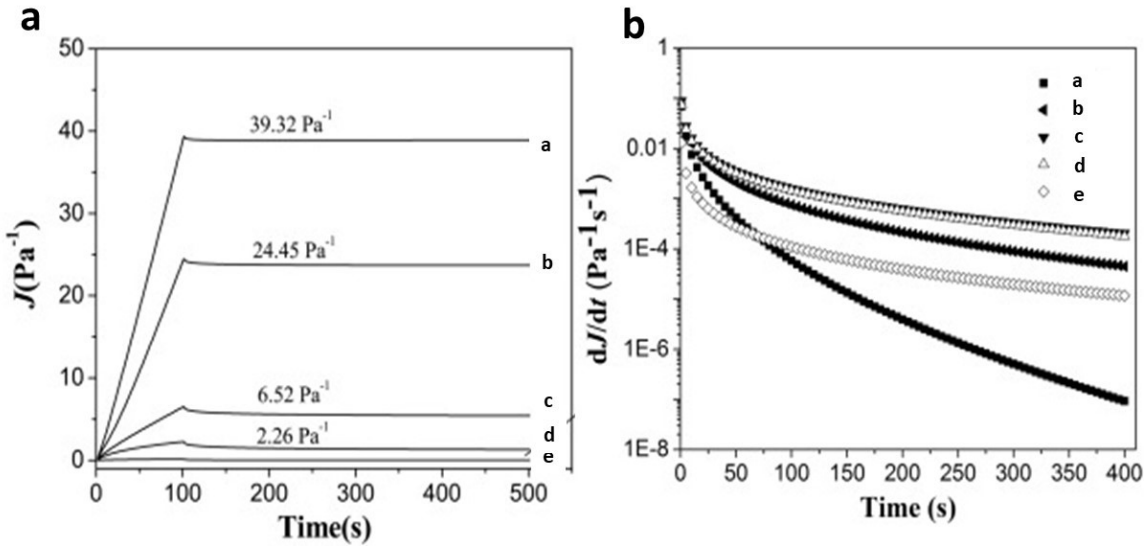

Figure 2.14 **a)**Creep compliance , **b**)recovery compliance rate curves of collagen solutions crosslinked with various GTA/collagen (w/w) ratios a: 0:1, b: 0.01:1, c: 0.03:1, d: 0.05:1, e: 0.1:1) (Adopted from [197]).

2.3 Bioprinting by micro-extrusion

Micro-extrusion is one of the common deposition-based bioprinting technique. Paxton et al. proposed a two-step initial screening to assess the bioprintability: fiber formation and layer stacking[157]. Here, by extending this approach, we are analyzing the flow and rheology related issues in two separate stages: 1) the extrusion of hydrogel filaments; and 2) stacking the extruded

filaments layer by applying polymer engineering science[169, 170]. Our discussion in this section is about the bioprinting of hydrogels in general, while bearing in mind the rheological properties of collagen gels.

2.3.1 Filament Extrusion

Filament extrusion is made by filling up the cartridge (also referred to as the "reservoir" or "barrel") with hydrogel and pushing the gel through the needle (also referred as the "capillary die"). By analogy to plastic extrusion, perhaps bioprinting can best be described as gel extrusion. The purpose of the gel extrusion is to produce a stable extrudate flow with a uniform filament diameter and smooth surface by precisely controlling the flow rate, pressure, and temperature. The flow of hydrogel through the needle can be driven and controlled by a piston movement, a pneumatic drive, or a rotating screw (Figure 2.15). The control of hydrogel flow from the cartridge to the needle is different in those three cases. In the case of piston movement, the controlled variable is the flow rate, which means the shear rate on the capillary needle wall. Therefore, to interpret the flow in a piston-driven gel extrusion, a "strain-controlled" measurement mode by a rheometer is more appropriate to generate viscosity vs. shear rate data. On the other hand, if the hydrogel flow is achieved by a pneumatic drive, the controlled variable is the head pressure which drives the gel through the needle. In other words, the operation is a "stress vs. flow" mode and obtaining viscosity vs. shear stress data from a "stress-controlled" mode of the rheometer is more suitable in this case. The flow by the screw motion in the cartridge is more complex than the previous two. The speed of the screw rotation controls both the pressure and flow rate [171]. The stress and shear rate in the needle depends on the coupling of the screw and needle's characteristics. Screw rotation not only directs flow in an axial direction but also generates transverse flow

in the screw channel [171]. A screw operation produces a better-homogenized hydrogel, but its impact on cell viability must be considered. Piston- and pneumatic-driven extruders are quasi-steady-state operations, and they are usually one-time loading which require the placement of sufficient gels in the cartridges to finish the bioprinting. On the contrary, a screw-driven operation is a steady-state operation with continuous gel-feeding. They can handle the fabrication of bigger or multiple parts.

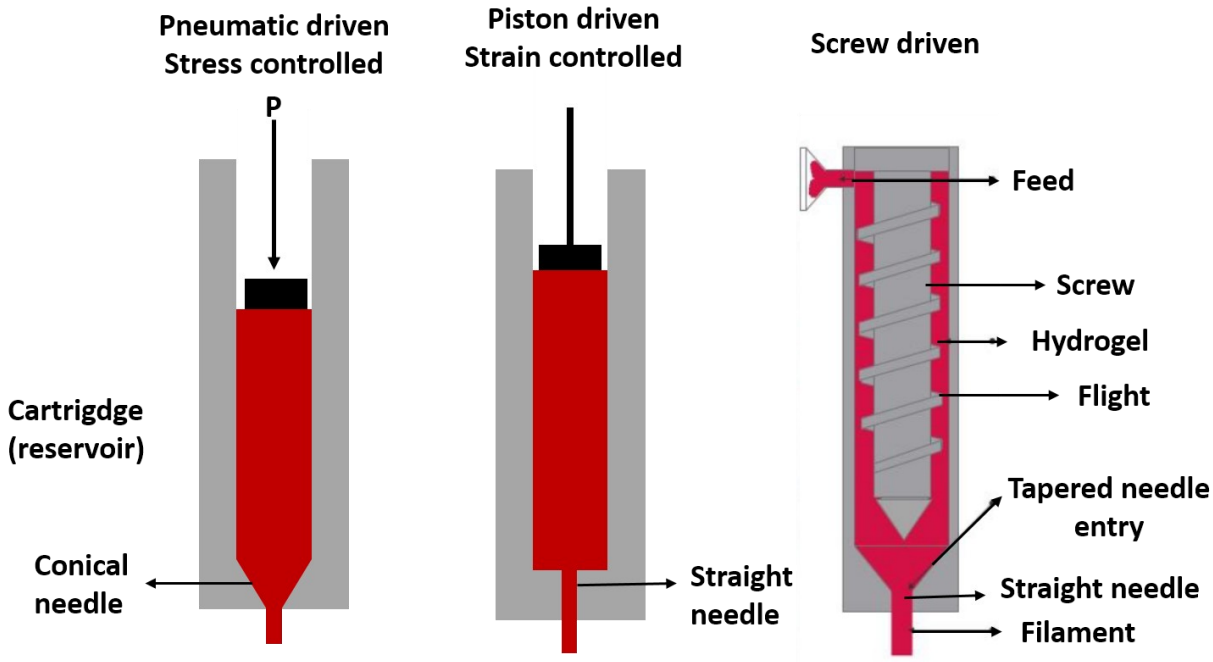

Figure 2.15 Types of gel drive systems in micro-extrusion 3D-printing

Cylindrical- or conical-shaped needles are most commonly used as capillary dies in the micro-extrusion of hydrogels (Figure 2.15). A pressure drop is generated while the hydrogel is pushed at a constant flow rate from the large-diameter cartridge through the small-diameter needle and then to the atmosphere:

$$P_0 - P_a = \Delta P_{cart} + \Delta P_{ent} + \Delta P_{needle} + \Delta P_{exit} \quad (7)$$

where P_0 is the pressure on top of the gel in the cartridge, $P_a\ is$ the atmospheric pressure at the exit of the needle, ΔP_{car} and ΔP_{needle} are the pressure drops in the cartridge and needle, respectively, and ΔP_{ent} and ΔP_{exit} are exit losses at the entrance and end of the needle, respectively. It is worth noting that the flow during the extrusion process is laminar, and the kinetic energy effect is neglected. The cartridge diameter of the micro-extruder is much larger than the needle diameter. Therefore, the pressure drop ΔP_{cart}in the cartridge can be neglected. ΔP_{exit} is expected to be small compared to the others and can also be neglected[251].

2.3.1.1 Needle (capillary die) flow

Our discussion focuses on the pressure-driven flow, the simplest and most common micro-extrusion method. The flow in the needle is discussed by considering the pressure drop along the needle's length and the entrance to the needle effect. The temperature rise due the viscous dissipation is not significant for relatively low viscosity collagen hydrogels. Hence, the micro-extrusion of collagen-based bioinks is considered isothermal without any frictional heating (H(T)=1 in Equation 5). The process variables that affect the filament extrusion by the pneumatic drive are reduced to only two: 1) applied pressure; and 2) needle geometry.

The pressure drop, $\Delta P_{circular}$ for a straight, circular needle with a length *l* and diameter *d* (Figure 2.16A) can be predicted through the Hagen-Poiseuille Equation for a power-law fluid [171].

$$\Delta P_{circular} = K\left[\frac{1+3n}{4n}\frac{32Q}{\pi d^3}\right]^n \frac{4l}{d} \tag{8}$$

where *K* and *n* are power-law constants described by Equation 1, and Q is the volumetric flow rate. The term $\frac{32Q}{\pi d^3}$ is called an apparent (nominal) shear rate, $\dot{\gamma}_a$.

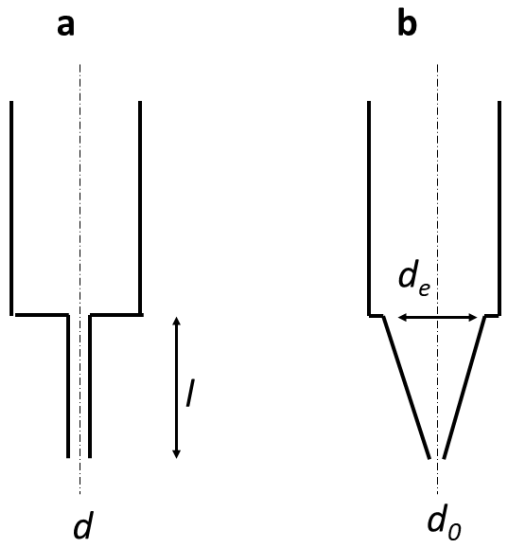

Figure 2.16 Schematics of needle rearrangements used in calculations: (a) straight circular needle; (b) converging conical needle.

The flow in the conical-shaped needle (Figure 2.16B) is best described by Cogswell's converging flow model [252]. The flow of non-Newtonian polymeric fluids through non-cylindrical dies has been extensively investigated in the literature [169, 171, 172]. The flow model developed for power-law viscoelastic polymeric melt has two parts: 1) shear deformation model for power-law fluid ($\eta = K(\dot{\gamma})^{n-1}$); and 2) elongational deformation mode.

$$\Delta P_{conical} = \left\{\frac{2}{3ntan\alpha} K \left[\frac{1+3n}{4n}\frac{32Q}{\pi d_0^3}\right]^n \left[1-\left(\frac{d_0}{d_e}\right)^{3n}\right]\right\} + \frac{(\eta_E)tan\alpha}{3}\left[\frac{32Q}{\pi d_0^3}\right]\left[1-\left(\frac{d_0}{d_e}\right)^{3n}\right] \quad (9)$$

where the first term comes from the shear stress effect, and the second term represents the elongational stress contribution. Diameters at the entrance and exit of the conical needle are denoted as d_e and d_o respectively, the half-angle of the conical needle is α, and the elongational viscosity is η_E. In most polymer flow cases, η_E is taken as equal to 3η (Trouton's law). However, as discussed in the preceding section, Trouton's law cannot hold, and the elongational viscosity η_E of

collagen hydrogels cannot be assumed as 3η at concentrations and shear rates used in micro-extrusion. Hence, caution has to be taken while modelling and predicting the flow of collagen gels in bioprinting.

Our group investigated the pressure losses due to the entrance effects in a non-tapered cylindrical needle and a conical needle by conducting two sets of collagen bioprinting experiments with the needle geometries schematically represented in Figure 2.16. For these experiments, 35 mg/mL collagens in a neutral solution was used. Its rheological properties were presented in Figure 2.5. Head pressure vs. flow rate data was collected for those two micro-extrusion cases and plotted in Figure 2.17A and B (designated as "Experiment"). The required head pressure values for measured flow rates were calculated using Equation 8 in the case of a non-tapered cylindrical needle, and Equation 9 in the case of a conical needle, and plotted in Figure 2.16A and B. The differences between the applied head pressures and the calculations based only on needle flow indicate the pressure ΔP_{ent} losses due to the entrance effects. As expected, ΔP_{ent} is more significant for the contraction from the cartridge to the non-tapered cylindrical needle with a sharp entrance. On the other hand, ΔP_{ent} is much smaller, but is not negligible in the case of a conical needle with a wider connection to the cartridge. Pressure loss at the entrances into the capillary dies from the extruder, and capillary rheometer barrels have been investigated for polymer melts both experimentally and theoretically [252, 253]. The convergence flow at the entrance is analyzed in terms of its extensional and simple shear flow effects. Reorganization and aligning of the flow streams of the hydrogel while moving from the cartridge into the needle cause the pressure drop ΔP_{ent}. This result showed the importance of elastic effects, which were discussed in Section 2.2.

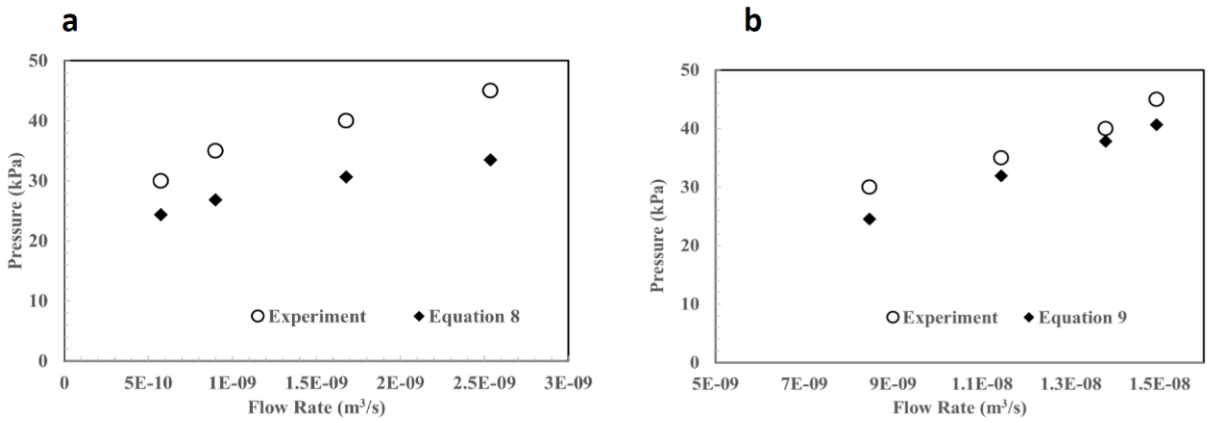

Figure 2.17 Applied experimental and calculated needle pressures vs. measured flow rate in (a) cylindrical geometry with needle length: 19.0 mm, needle diameter: 0.60 mm; (b) conical geometry with needle length: 19.0 mm, entrance diameter: 4.2 mm, exit diameter: 0.41 mm (unpublished results).

The maximum developed shear stresses in cylindrical and conical needle geometries were calculated for alginate sulfate-nanocellulose bioinks by flow visualization with COMSOL simulation [225]. Figure 2.18 shows the location of high shear areas. As expected, the cylindrical needle showed higher wall stresses than the converging conical needle. Similar to polymer melts [169], the shear stress at the sharp-edged entrance zone of the straight circular needle was higher than the shear stress at the tapered entrance of the conical entrance. The shear stress augments in the conical needle towards the exit of the tip. High pressures are needed to extrude the ink in the case of cylindrical needle geometries, which resulted in higher maximum shear stresses.

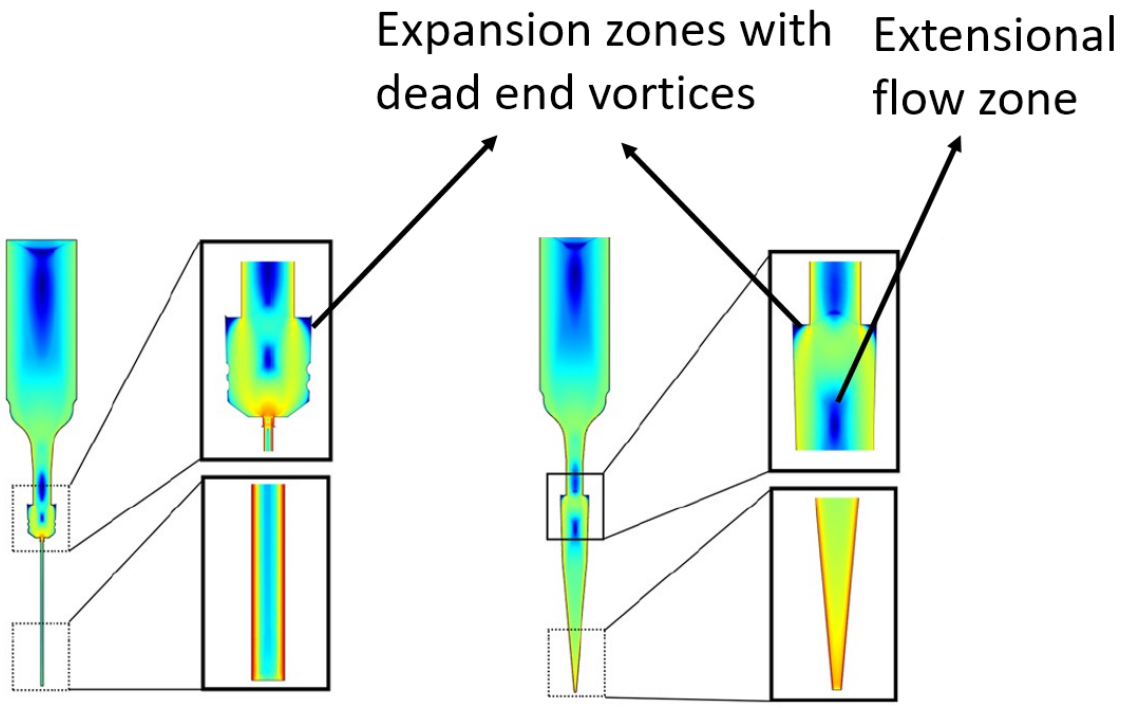

Figure 2.18 Computational fluid dynamic analysis of the printing setup. The red/orange colour indicates regions of high shear stress in the simulation with apparent differences between the straight and the conical needle geometries (adopted from *[225]*).

A few comments also can be added by closely inspecting Figure 2.18. It can be seen that expansion regions are present in the connector between the cartridge and the cylindrical needle, and at the connection between the cartridge and the conical needle. There are two possible pathways for the hydrogel (or any polymer melt) as it exits and expands from the narrow diameter cartridge end. It will either flow as a free jet through the expansion or stick to the wall and fill up the expansion. Here, the blue colour at the corners suggests the flow of that particular ink is a free jet which forms dead-end vortices. These vortices can lead to hydrodynamic instabilities and cell survival in the material that stays in the stagnant zones. In the converging conical needle, as discussed for the polymer melts[254], the flow can be visualized as being elongated by a squeezing mechanism from the sides of the conical needle. Therefore, the total pressure loss of the hydrogel

in the conical needle is the sum due to extension and that due to shear. The complicated governing equations involving the converging and extensional flow have often been deterrents to rigorous analysis. Most simulations on polymer melt flow in the converging flow, which is also applicable to hydrogels, are performed with integral type constitute equations or differential constitutive equations containing the derivative of the stress tensor [169]. Whether or not it plays a significant role, elasticity can be analyzed based on a dimensional analysis of rheological characteristics and flow conditions. According to the convected-Maxwell model, the Weissenberg number is defined as the ratio of elastic forces over the viscous forces [255]:

$$\mathrm{We} = \frac{\Psi_1(\dot{\gamma})\dot{\gamma}_{xy}}{\eta(\dot{\gamma})} \tag{10}$$

where $\frac{\Psi_1(\dot{\gamma})}{\eta(\dot{\gamma})}$ is the relaxation time λ, hence We=$\lambda\dot{\gamma}$. The relaxation time λ can also be obtained from the oscillatory shear flow. Another dimensionless number is the Deborah number, which is defined as the ratio of the fluid characteristic time (λ) to the residence time of the flow (t):

$$\mathrm{De} = \frac{\lambda}{t} \tag{11}$$

The relation between We and De can be written for the capillary flow for which the average residence time is Length/Velocity (L/V), and the shear rate is proportional to the velocity/radius (V/R). Combining Equations 12 and 13 gives:

$$We = De\frac{L}{R} \tag{12}$$

Deborah number, which includes hydrogels' viscoelastic properties and process conditions, are better suited to evaluate if elasticity plays a vital role in needle flow: If De >> 1, the hydrogel behavior is almost purely elastic; if De << 1, elasticity is not significant.

2.3.1.2 Filament Swell

Construction of a well-defined object by bioprinting requires a precise filament diameter control which depends not only on the exit diameter of the needle but also on the needle geometry and viscoelastic properties of the hydrogels and the polymer melts[154]. An extruded filament diameter, as in the case of any other polymer melt processing, exceeds the diameter of the needle (die) at the exit. Usually, the diameter of a filament cannot be smaller than 1.2 – 1.5 times the needle's diameter at the exit, as shown in Figure 2.19.

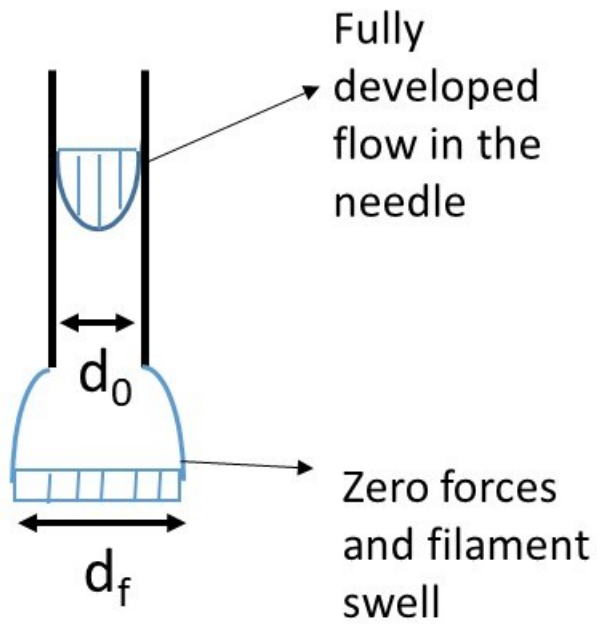

Figure 2.19 The likely streamline rearrangement of fluid after exiting from a capillary.

We call the extrudate swell a “filament swell,” also called a “die swell” in polymer processing. Within the narrow needle opening, the hydrogel is under stress, storing deformation material elastically. This stress is relaxed as the hydrogel leaves the needle and is released to a free surface, allowing the release of the elastically-stored material in the needle tip and subsequently resulting in radial expansion of the melt. The die (filament) swelling ratio χ, is defined as the ratio of the maximum diameter of the extruded material to the diameter of the die opening (d_f/d_0). The reported range is from ~1.05 to 1.3 for typical extrusion additive manufacturing processes [154, 155]. Hence, die swell is an elastic stress relaxation phenomenon and results from the combination of the recoil and normal stresses in the shear flow. Based on this understanding, Tanner has derived [256]: `

$$\chi = 0.12 + \left\{1 + \left(\left[\frac{\tau_{xx}-\tau_{yy}}{\tau_{xy}}\right]^2\right)^{1/6}\right\} \quad (15)$$

Here, we have shown that the first normal stress difference in collagen gels can predict the needle swell at that particular shear rate. However, we must emphasize that the relationship between filament swell and the rheological properties of collagen gels is not known yet. Another important point to note is the dependence of die swell in the capillary (needle) on L/d (the length to the diameter of the die) and the flow rate or the wall shear rate in the die. Like any other polymers, collagen hydrogels have a “memory” of the state in which they were in the die cartridge. The fluid memory stays intact in a short capillary, which results in a larger extrudate swell effect. For a long capillary, with a L/D ratio greater than 20, the effect of the capillary length can be negligible.

2.3.1.3 Filament Distortion

Bio-inks used for 3D bioprinting experience deformation by shear and elongation upon entering the conical or axial needle[257]. In a conventional 3D printing process, an extrudate distortion with a melt fracture often arises when the polymer is extruded freely out of a needle (die). There is a critical flow rate at which the extrudate surface is no longer smooth [171]. This type of flow also has been extensively studied in the polymer-processing industry. The extrudate diameter becomes rough and no longer uniform, exhibiting various distortions. Figure 2.20 shows the distortion of diameter and melt fracture as extrusion speeds increase.

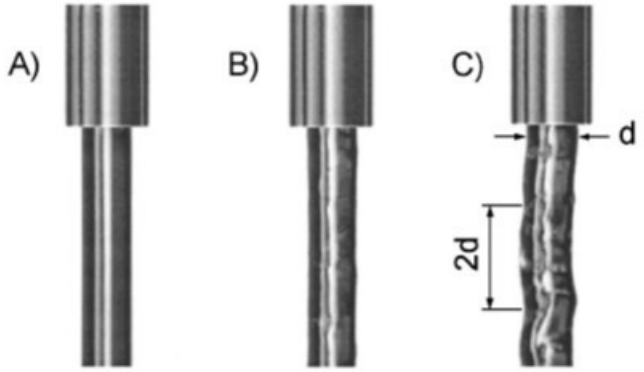

Figure 2.20 Extrusion of a 0.4% borax solution (A) smooth surface at the lowest speed (W_e=2.8, (B) development of a small roughness at intermediate speed (W_e=4.9), (C) well-developed melt fracture at the highest speed (W_e=8.4) (from [255]).

The surface instability often depends on the flow rate and viscoelasticity of the hydrogel. The amplitude of the distortions increases with increasing flow rate. As the flow rate is further increased, the extrudate exhibits chaotic distortion.

2.3.2 Layer-stacking, Bonding, and Shape integrity

Extruded hydrogel filaments are laid down on the software-controlled moving tray of the 3D printer, and stacked layer by layer to construct the desired piece (Figure 2.21). Construction of a three-dimensional piece from stacked filaments involves bonding (welding) of a fresh filament on top of a previously laid filament. Adequate bonding between the filament layers and the disappearance of weld lines are critical to attaining the desired mechanical properties for the constructed shape. Welding of two stacked layers is a growing interest not only for the 3D-bioprinting of hydrogels but also for the polymer melts. The research on interlayer bonding in the 3D printing process is still in its infancy. Nevertheless, interlayer fusion has been extensively investigated by polymer melt processors for pipe and film blowing die designs [169]. Welding efficiency depends on good contact between two layers of filament. Extrudate distortion and surface roughness, as shown in Figure 2.20, reduce the contact area between two layers of stacked filaments and result in poor bonding. Hence, the elasticity of hydrogels and needle design is extremely important for the filament extrusion quality and layer bonding. Once an adequate contact is established between the layers, polymer chains from two filaments have to connect by a diffusion mechanism. The movement of polymer chains is described by "reptation mechanism", which was developed by de Gennes [258] and Doi Edwards [259], and later applied to the theory of healing at the polymer-polymer interface [260]. In the case of rod-like collagen molecules, one has to consider the difference between the flexible and rod-like chains. In addition to the diffusion of collagen molecules, other factors such as hydrogen bonding and crystallization also play a role during the self-healing of hydrogels [261]. The adaptability of various bioprinting processes such as cryogenic printing, in-situ crosslinking, hybrid inks, and high-viscosity

collagen solutions on interlayer bonding needs to be investigated based on the self-healing of gels approach.

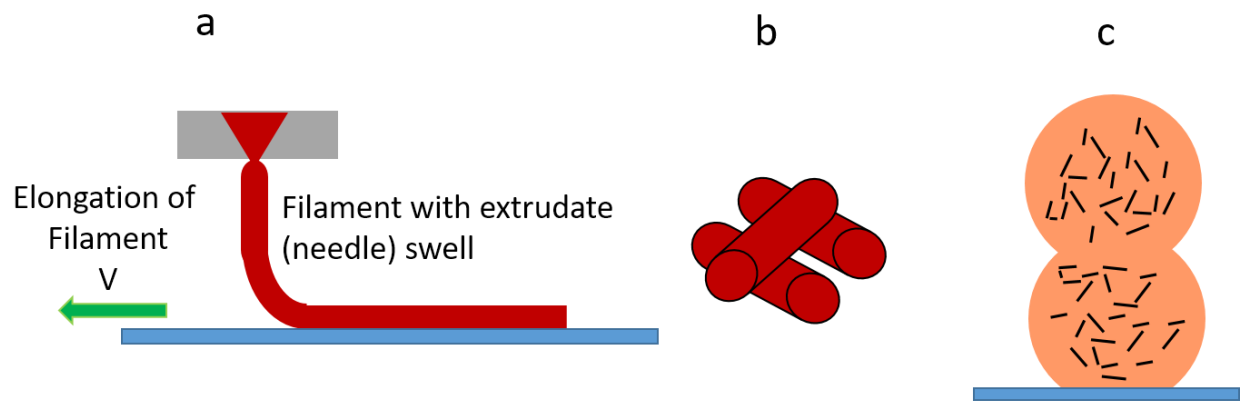

Figure 2.21 (a) Layer-stacking stage of bioprinting, (b) stacking of filament layers, (c) bonding of two filaments.

The state of gelation is also a determining factor for the shape integrity of the construct. Ouyang et al. [233] suggested three gelation states for a printed ink: under-gelation, proper-gelation and over-gelation, as shown in Figure 2.22. To investigate the printability under these three different states, the authors printed some grid constructs under different temperatures and various concentrations of gelatin and alginate gel. When the ink was in an under-gelation state, a droplet morphology was formed at the needle's tip. The extruded/printed filament is smooth but demonstrates a more liquid-like state, and the upper layer effortlessly fuses with the lower layer, creating circular holes that are different from the designed one. At this state, the time sweep shows that the loss modulus is greater than the storage modulus at a steady-state. For ideal gelation conditions, the interconnected channels of the construct would demonstrate a square shape that is similar to the designed one. The filament should be smooth and uniform during the extruding process, which results in a standard grid construct with distinguished layers. At this state, the

frequency sweep data shows that the loss modulus is close to the storage modulus of around 10 Pa. If the ink or the bioink was in the over-gelation condition, it would easily show fractured morphology, which results in irregular filaments and interconnected channels. Therefore, the bio-ink should be printed in a proper state to achieve optimum filament morphology and mechanical stability. Materials with higher *G'* facilitate stronger shape retention for the extruded parts despite the fact that *G'* may cause a poor extrusion [262]. Dynamic mechanical loss tangents (*tan δ =G''/G'*), which indicate predominately elastic or viscous behavior, can help judge shape integrity. In summary, a high *tan δ* value suggests that the material shows more fluid-like behavior, and a low *tan δ* value means more solid-like behavior with poor fluidity.

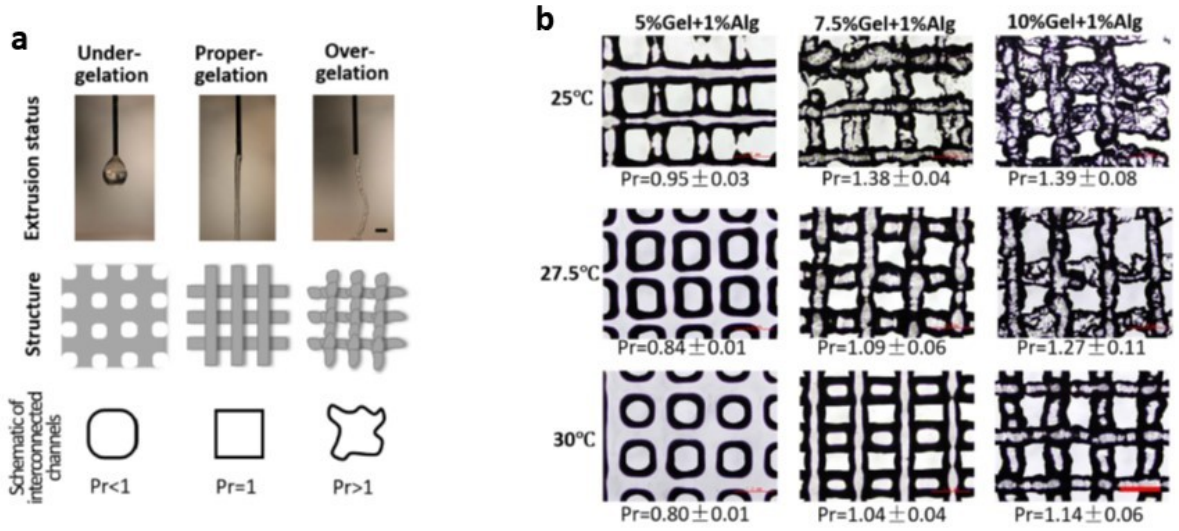

Figure 2.22 a) Evaluation of printability under three different states *[233]*, b) Printed construct at different concentrations. The printability parameter, Pr, is defined as $L^2/4A$ where the L and A is the filament perimeter and area, respectively (from *[233]*).

2.4 Cell Viability

The inevitability of shear stress in any dispensing process, including bioprinting via micro-extrusion of cell-laden hydrogels for the manufacturing of 3D tissue constructs for tissue engineering applications, has prompted much investigation into the factors that regulate it in all printing methodologies, and its effect on cell viability in bioprinting[149, 157, 223, 263, 264]. The level of shear stress has been reported to be directly influenced by printing parameters such as printing pressure, needle size and geometry, and non-Newtonian viscosity of the hydrogel in bioprinting. Moreover, shear stress has been identified as factors influencing cell behavior and the differentiation of stem cells. However, excessive shear stress and residence time have detrimental effects on cell membrane integrity. Striking a healthy balance between shear stress and cell viability is therefore crucial in bioprinting, particularly in the context of improving the resolution of bioprinting with high viscosity hydrogels and small diameter needles.

Live/dead assay is the predominant choice for assessing cell viability in the bioprinting of cell-laden hydrogels after gelation[149, 223, 263]. The assay is based on an assessment of cell membrane integrity. Cells with damaged cell membranes appear red under a fluorescence-based confocal microscope, and those alive appear green. Since studies on the cell viability of bioprinted collagens are limited, gelatin-based hydrogels are also reported[233]. The live/dead assay showed ESC viability increased exponentially by decreasing induced shear stress. Therefore, lower gelatin concentrations and higher printing temperatures increased the ESC viability by decreasing viscosity, which in turn demanded lower head pressure, needle shear rate and stress. Commonly reported lower cell viabilities at higher viscosities[265, 266] are due to a need to apply higher head pressures and resulting shear stresses in needles (see Equations 8 and 9).

Blaeser et al.[223] analyzed the viability of L929 mouse fibroblasts after exposure to a wide variety of needle shear stress (0.7-20 kPa) immediately after printing in alginate-based hydrogels. Their data were classified into three groups based on the applied needle shear stress: <5 kPa, 5-10 kPa and >10 kPa. The viability of the fibroblasts was unaffected at low needle shear stress (< 5kPa), with a reported 96% cell viability. In contrast, the fibroblasts' viability declined to 91% at medium needle shear stress (5-10 kPa), and 76% viability at high needle shear stress. While the data demonstrated that below a critical shear stress level, living cells could be dispensed without compromising cell membrane integrity, it also reveals that the applied needle shear stress is related to cell damage in the short-term.

The possible long-term effect of needle shear stress on cell viability has been demonstrated after seven days of printing human bone marrow mesenchymal stem cells (BM-MSCs)[223]. The printing of BM-MSCs in alginate-based hydrogels at three different needle shear stress levels of 4, 9 and 18 kPa, resulted in a 94% cell viability at 4 kPa, 92% viability at 9 kPa, and 86% viability at 18 kPa immediately after printing. After seven days of *in vitro* culture of the printed constructs, regardless of the needle shear stress level at the time of printing, the cell viability increased to 95-97%. However, it was noted that relative to the non-printed cell controls, the viability of the printed BM-MSCs was slightly but significantly lower. These findings are not only following the mouse data regarding the immediate effect of printing-induced shear stress but also reveal that the direct impact of printing shear stress on cell viability does not linger on to compromise the proliferative capacity of the BM-MSCs. It is, however, noteworthy that in another study, albeit with limited information on the actual bioprinting protocol and involving the dispensing of bovine meniscus fibrochondrocytes in a collagen-based hydrogel, that the cell

viability of the fibrochondrocytes remained unchanged at ~90% immediately post-printing, and after over ten days in an *in vitro* culture[263].

In addition to the needle shear stresses, due to the conical geometry of the dispensing needle, the effect of the extensional flow of the suspension biomaterials/bioinks on cell deformation is also responsible for cell membrane damage, leading to cell death at high flow rate conditions[213, 267-269]. For example, it has been shown that 3T3 fibroblasts can withstand up to 200 Pa of fluid stresses without cell damage. At low flow rates, the stress produced by shear flow (> 200 Pa) is prone to damage cells relative to stresses produced by extensional flow (> 200 Pa). However, as the flow rates increase, the extensional flow is enhanced, and the corresponding stress contributes to cell membrane damage[269].

2.5 Concluding Remarks and Future Directions

Collagen is the most preferred biomaterial for cell-laden 3D bioprinting due to its hydrophilic structure with natural binding sites, resulting in high cell viability and proliferation rates. 3D bioprinting offers precise control of the fabrication of tissue-engineered constructs, particularly in the context of the production of engineered tissues matching the anatomical shapes of the tissues to be repaired or replaced. While the extrusion of low viscosity collagen solutions is desirable for better cell viability, it requires carefully designed post-3D bioprinting crosslinking to preserve the shape integrity of the finished structures. Therefore, there needs to be a better understanding of the rheological properties of the bioprinting of collagen and their impact on extrusion, gelling, and crosslinking stages. It is important to note again that required properties at those stages do not often go hand-in-hand. More importantly, high cell viability under the

extrusion, gelling, crosslinking stages is necessary for the generation of functional tissue-engineered constructs that can be applied clinically to repair and replace damaged tissues.

In this review, the structures and rheological properties of collagen solutions are first discussed extensively, followed by a review of the micro-extrusion-based 3D-printing process. A rigorous evaluation and investigation of the 3D-printing process should encompass three separate components: 1) micro-extrusion of hydrogel (i.e. collagen), 2) layer-stacking, crosslinking, and building 3D constructs, and 3) integrity and applicability of the printed construct. To this end, the critical flow factors, including shear and extensional flow stresses should be considered during the bioprinting process to avoid cell damage. While Table 2.3 Summary of recent research (2017-2022) on collagen and its 3D-printing applications, the literatures also showed the lack of a complete and rigorous rheological characterization of 3D-bioprinting process with their impact on cell viability.

Rheological properties of hydrogels, including collagens, need to be measured to serve two objectives: 1) accurate rheological test and analysis, and 2) utilizing rheological results to predict the printability of the hydrogel during the 3D printing process.

First, rheological methods, especially measuring linear dynamic mechanical properties such as oscillatory strain, frequency, time sweeps, and viscosity as a function of temperature and concentration, are beneficial for the characterization of collagen gels and understanding the effect of crosslinking agents and strategies. Dynamic viscoelastic measurements are more suited to indicate collagens' structure and organization, fibrils' formation, and the crosslinking of collagen hydrogels. However, in most of the work in the literature, complex viscosity vs. oscillation frequency data under the linear deformation range have been used to represent steady shear

viscosity vs. shear rate data. The validity of this overlapping linear dynamic deformation vs. steady shear flow, or the Cox-Merz rule, may not hold true for specific collagen solutions. The validity of the Cox-Merz rule has to be verified to characterize the structures of collagen solutions. Before confirming the validity of the Cox-Merz rule, applying $|\eta^*|(\omega)$ vs. ω data in the place of $\eta(\dot{\gamma})$ vs. $\dot{\gamma}$ to model the 3D printing process can be erroneous.

Secondly, rheological measurements are used to obtain material functions such as shear viscosity, first normal stress coefficient, and extensional viscosity. These material functions can be used to predict the filament extrusion, swell, melt fractures, layer stacking, and shape integrity under different pressures, flow rates, residence times, and temperatures. Among these material functions, only shear-dependent viscosity has been widely used in the literature to evaluate the 3D printing of collagens. However, the roles of the first normal stress coefficient and extensional viscosity on the 3D printing process must not be underestimated. Most often, the shear rate-dependent characteristics has been described by using a two-parameter power-law equation, which is inadequate to describe the Newtonian plateau region. The full description of the viscosity vs. shear rate profile with the Carreau model or the viscosity vs. shear stress Ellis model is desirable for better characterization of collagen solutions and modelling their extrusion through the capillary needle of bioprinters.

This review also discussed a comprehensive rheological characterization strategy and the anticipated flow conditions during various stages of the 3D printing process. Our goal is to cover the critical aspects of collagen bioprinting for tissue engineers who are developing bioinks and bioprinting processes. With our discussion on the rheological properties of collagen as a

representative example, we emphasized that material functions should be used for the design of collagen and other non-Newtonian hydrogels for bioprinting.

How the hydrogel behaves during the various stages of 3D bioprinting also depends on the type of driving (pushing) systems, such as pneumatic, piston, or screw. It is also crucial to consider the capillary needle geometries while modelling the 3D bioprinting process. When modelling extrusion flow through the capillary needle, attention has to be given to pressure losses due to end effects. The role of rheological properties and process conditions on the filament-swell and distortion is best described by the dimensionless Deborah number.

Shear stresses in the needle due to the geometries of the dispensing needle affect shear viscosity and the extensional flow of the hydrogel. Extensional flow, in turn, may affect the cell deformation and be responsible for cell membrane damage leading to cell death at high flow rate conditions. Better characterizations of flow conditions and their effects on shear and extensional deformations in collagens and cell viabilities are needed.

Finally, we discussed the role of flow conditions and crosslinking on cell viability. While these discussions are focused on collagens, they are also valid on the 3D bioprinting of other hydrogels.

Table 2.3 Summary of recent research (2017-2022) on collagen and its 3D-printing applications

	Bioprinting material formulations	Collagen source	Rheological characterizations	Printer type	Gelation/crosslinking method	Other characterization	Application	Ref.
Vascular								
	Human collagen methacrylate (5mg/mL)	N/A	Amplitude sweep, time sweep (before and after crosslinking)	Micro-extrusion bioprinting using FRESH bioprinting method	UV crosslinking, thermo-gelation	Porosity, Mechanical property (compression), *in vivo* cultivation, histology, immunofluorescent, q-pcr,	Vascular tissue engineering	[270]
	Type I Collagen 0.015% (w/v) with alginate 2%	Rat tail	N/A	Micro-extrusion	$CaCl_2$ and Thermo-gelation	*In vivo* cultivation, histology, immunofluorescence	Vascular tissue engineering	[271]
	Type I collagen (around 2.1 mg/ml or 4.7mg/mL) with xanthan gum (4 – 10%)	Bovine	Amplitude sweep (as a function of steer strain)	Micro-extrusion	Thermo-gelation	Cell viability, cell proliferation, histology, printability	Vascular tissue engineering	[272]
	Methacrylate collagen (0.1%)	Bovine	Frequency sweep	Micro-extrusion	UV crosslinking, thermo-gelation	Cell viability, immunofluorescence	Vasculogenesis and neurite outgrowth	[273]
	Type I Collagen (0-3mg/mL) with sodium alginate (0-1.8%)	N/A	N/A	Coaxial extrusion printing	$CaCl_2$ and Thermo-gelation	Cell morphology, Live dead assay, immunofluorescence, q-PCR	Vascular tissue engineering	[274]
	Type I collagen (0.2, 0.5%), agarose (0.2-0.5%)	N/A	Strain sweep, shear modulus	Inkjet based printing	thermo-gelation	Swelling test, *in vitro* degradation, histology, angiogenesis evaluation	Angiogenesis potential	[275]
	Type I collagen (0.16-0.208%) with	N/A	Strain sweep, steady state flow	Micro-extrusion bioprinting	UV gelation	Cell viability, immunofluorescence	Promote angiogenesis	[276]

	Bioprinting material formulations	Collagen source	Rheological characterizations	Printer type	Gelation/crosslinking method	Other characterization	Application	Ref.
	methacrylate collagen (3-5%)		sweep, shear modulus					
Bone								
	Mineralized type I collagen (12mg/mL)	Blue shark	Temperature sweep, Steady state flow sweep,	Micro-extrusion bioprinting	Thermo-gelation	Porosity, Cell viability, Immunofluorescence, Metabolic activity,	Bone tissue engineering	[277]
	Type I collagen	Porcine	Temperature sweep, frequency sweep,	Micro-extrusion bioprinting	Thermo-gelation	Cell viability, mechanical test (compression), histology, immunofluorescence, q-pcr	Osteogenic Stimulators	[278]
	Type I collagen (0.06 – 0.18%) with methacrylate gelation (5%) and methacrylate hyaluronic acid (1%)	Rat tail	Steady state flow sweep, Temperature sweep, frequency sweep	Micro-extrusion bioprinting	UV crosslinking, thermo-gelation	Mechanical property (compression), printability, cell viability, immunofluorescence, q-pcr	Bone tissue engineering	[279]
	Mineralized Type I collagen (0-1%) and sodium alginate (6-12%)	Blue shark	Steady state flow sweep, frequency sweep	Micro-extrusion bioprinting	$CaCl_2$ and Thermo-gelation	Live/dead assay, cell morphology, metabolic actability, DNA assay	Bone tissue engineering	[280]
	Type I collagen (5.0mg/mL) and Tyramine derivative of hyaluronan (25mg/mL)	Rat tail	Steady state flow sweep, strain sweep	Micro-extrusion bioprinting	Enzymatic crosslinking initiated by H_2O_2 and light crosslinking, Thermo-gelation	Cell migration, fibril distribution, gene expression, histology, biochemistry assay, immunofluorescence	Bone tissue engineering	[281]
	Type I collagen (5%) with β-TCP (20%)	Porcine	Frequency sweep, temperature sweep,	Micro-extrusion bioprinting	Genipin, thermo-gelation	Cell viability, immunofluorescence, mechanical property	Bone tissue engineering	[120]

	Bioprinting material formulations	Collagen source	Rheological characterizations	Printer type	Gelation/crosslinking method	Other characterization	Application	Ref.
						(compression), histology, gene expression,		
	Type I collagen with hydroxyapatite or deproteinized bovine bone	Bovine	N/A	Micro-extrusion bioprinting	thermo-gelation	Mechanical property (compression property), gene expression, immunohistochemistry, cell proliferation, immunofluorescence	Bone tissue engineering	[282]
	Recombinant human Type I collagen (1%) with PLA (10%) and β-TCP (1%)	Nicotiana tabacum	N/A	Micro-extrusion bioprinting	Thermoplastic	Cell viability, mechanical property (compressive), *in vitro* degradation, printability, antibacterial property	Bone tissue engineering	[283]
	Type I collagen (2mg/mL)	Rat Tail	N/A	Laser-assisted bioprinting	Thermo-gelation	Printability, immunofluorescence,	Bone tissue engineering	[284]
	Type I collagen (6mg/mL) with alginate (25mg/mL) and fibrin (37.5mg/mL)	Rat tail	N/A	Reactive jet impingement bioprinting	Thermo-gelation, thrombin, $CaCl_2$	Gene expression, immunofluorescence, Live/Dead assay, Mechanical property (compression)	Bone tissue engineering	[285]
	Type I collagen (1, 2, 3 mg/mL) with Hydroxyapatite (1%)	Rat tail	Steady state shear viscosity, frequency sweep	Micro-extrusion bioprinting	thermo-gelation	Cell viability, cell proliferation, cell differentiation, *in vitro* degradation,	Bone tissue engineering	[286]
	Type I collagen (2mg/mL) with nano hydroxyapatite (1.2%)	Rat tail	N/A	In situ Laser-assisted bioprinting	thermo-gelation	Metabolic activity, *in vivo* cultivation, histology	Bone tissue engineering	[287]
Cartilage								

	Bioprinting material formulations	Collagen source	Rheological characterizations	Printer type	Gelation/crosslinking method	Other characterization	Application	Ref.
	Type I collagen (4%)	Porcine	N/A	Micro-extrusion	Thermo-gelation	*In vivo* cultivation, histology,	Cartilage tissue engineering	[288]
	Type I collagen (35mg/mL)	Bovine	Steady state flow sweep, Temperature sweep	Micro-extrusion bioprinting using FRESH bioprinting method	Thermo-gelation	Cell viability, cell proliferation, histology, immunofluorescent, q-pcr,	Cartilage tissue engineering	[215]
	Type I collagen (15mg/mL)	Rat tail	Time sweep (before and after gelation), steady state flow sweep, thixotropy	Micro-extrusion bioprinting	Thermo-gelation	Printability, cell viability, biochemistry assay,	Cartilage tissue engineering	[219]
	Type I collagen (0.1 – 0.2%) with agarose (0.5-1%)	N/A	N/A	Micro-extrusion bioprinting	Thermo-gelation	Mechanical property (compression), histology, biochemistry assay, immunofluorescence,	Cartilage tissue engineering	[289]
	Type I collagen (35mg/mL)	Bovine	N/A	Micro-extrusion bioprinting	Thermo-gelation	Live/dead assay	Meniscus tissue engineering	[290]
	Type I collagen (3, 3.75mg/mL) and alginate (75-80mg/mL)	N/A	N/A	Micro-extrusion bioprinting	$CaCl_2$, thermo-gelation	Swelling test, Mechanical property (compression, tensile), cell viability, immunofluorescence, histology, biochemistry, gene expression	Cartilage tissue engineering	[291]
Skin								
	Type I collagen (0.75%)	Porcine	Steady state flow sweep,	Inkjet printing	Thermo-gelation	Cell viability, histology, immunofluorescence	Skin tissue engineering	[292]

	Bioprinting material formulations	Collagen source	Rheological characterizations	Printer type	Gelation/crosslinking method	Other characterization	Application	Ref.
	Type I collagen (6mg/mL)	Bovine	N/A	Micro-extrusion bioprinting	1M sodium bicarbonate solution	Histology	Biomimetic skin	[293]
	Type I collagen (8%) and methacrylate gelatin (5%) doped by Tyrosinase (100-800U/mL)	N/A	Time sweep, temperature sweep	Micro-extrusion bioprinting	Enzyme crosslinking, UV crosslinking	*in vitro* degradation, Cell viability, histology, cell migration, *in vivo* wound closure analysis,	Skin tissue engineering	[294]
	Type I collagen (4mg/mL)	Rat tail	N/A	Micro-extrusion bioprinting	Thermo-gelation	Cell viability, printability, swelling test, immunofluorescence	Artificial skin model	[295]
	Type I collagen supported by PCL mesh	Porcine	N/A	Micro-extrusion bioprinting	Thermo-gelation	Contractility test, cell viability, histology, immunofluorescence	Skin tissue engineering	[296]
Wound Healing								
	Methacrylate collagen (0.3, 1.8, 2 mg/mL) with microfat	Bovine	N/A	Micro-extrusion	UV crosslinking, thermo-gelation	Cell metabolic activity, wound healing cytokines, printability	Wound healing	[297]
	Type I collagen (5mg/mL) and alginate (2%)	Rat tail	N/A	In situ extrusion bioprinting	$CaCl_2$, thermo-gelation	Cell viability, immunofluorescence, *in vivo* compatibility in porcine, histology, printability,	Wound healing	[298]
	Type I collagen (0.25%) with fibrinogen (1.25%) and hyaluronic acid (0.25%)				Thrombin, thermo-gelation			
Cornea								

	Bioprinting material formulations	Collagen source	Rheological characterizations	Printer type	Gelation/crosslinking method	Other characterization	Application	Ref.
	Type I collagen (0.3%) or Type I collagen (0.2%) and agarose (0.5%) blend	Bovine	Steady state flow sweep	Micro-extrusion bioprinting	Thermo-gelation	Cell viability, immunofluorescence, Mechanical property (compression property),	Corneal transplantation	[127]
	Human type I collagen (1.2mg/mL) with human plasma, thrombin, and hyaluronic acid	N/A	N/A	Laser-assisted bioprinting	N/A	Cell viability, cell proliferation, immunofluorescence, histology	Corneal tissue engineering	[299]
Heart								
	Type I collagen (17.5 mg/mL)	Bovine	N/A	Micro-extrusion bioprinting using FRESH bioprinting method	Thermo-gelation	Mechanical property (tensile property), histology, immunohistochemistry, immunofluorescence,	Heart valve scaffold	[125]
	Type I collagen (24mg/mL)	Bovine	Frequency sweep	Micro-extrusion bioprinting using FRESH bioprinting method	pH crosslinking and thermo-gelation	Printability, cell viability, histology, immunofluorescence,	Heart tissue engineering	[126]
Liver								
	Methacrylate Type I collagen with thiolate hyaluronic acid	Bovine	N/A	Micro-extrusion bioprinting	UV crosslinking, thermo-gelation, covalent bond	Printability, Cell Viability, Histology, immunofluorescence, Biochemistry assay,	Liver tissue engineering	[300]
Muscle								

	Bioprinting material formulations	Collagen source	Rheological characterizations	Printer type	Gelation/crosslinking method	Other characterization	Application	Ref.
	Type I collagen (5%)	Porcine	Frequency sweep, Temperature sweep, stress sweep	Micro-extrusion	Genipin, Thermo-gelation	Mechanical property (compression), myogenic differentiation, *in vitro* cellular activities, *in vivo* cultivation, histology, immunofluorescent, q-pcr,	Muscle tissue engineering	[301]
Others	Type I collagen (3 mg/mL) with glycidyl methacrylate hyaluronic acid (10 mg/mL) or methacrylic anhydride hyaluronic acid (10mg/mL)	Rat tail	Steady state flow sweep, temperature sweep	Micro-extrusion bioprinting	UV crosslinking, Thermo-gelation	Printability, Cell migration test, immunofluorescence,	Assessing neural cell response	[302]
	Methacrylate Type I collagen (4.5mg/mL) and Thiolate hyaluronic acid (1.5mg/mL)	Bovine	Strain sweep, thixotropy	Micro-extrusion bioprinting	UV crosslinking, thermo-gelation, covalent bond	Immunofluorescence, swelling test, proliferation assay, drug study,	Drug metabolism	[303]
	Type I collagen (0.2%) and agarose (0.5%)	N/A	Thixotropy	Micro-extrusion bioprinting	Thermo-gelation	Printability, histology, immunofluorescence, cell proliferation, gene expression	Cancer model	[304]
	Methacrylate collagen (0.5, 1.0. 1.5%)	N/A	Time sweep, frequency sweep	Micro-extrusion bioprinting	Blue light crosslinking, Thermo-gelation	Swelling ratio, *in vitro* degradation, Mechanical property (compression), Cell viability, *in*	Intrauterine Adhesion Prevention	[305]

Bioprinting material formulations	Collagen source	Rheological characterizations	Printer type	Gelation/crosslinking method	Other characterization	Application	Ref.
with methacrylate gelatin					*vivo* cultivation, histology		
Methacrylate collagen (5%)	Bovine	Flow sweep, storage and loss modulus before and after UV	Micro-extrusion bioprinting	UV crosslinking, Thermo-gelation	N/A	Compare the printability of Methacrylate collagen, gelatin, hyaluronic acid and alginate	[306]
collagen (1%) and Methacrylate hydroxybutyl chitosan (3%)	Fish Skin	Steady state flow sweep, Temperature sweep	Micro-extrusion	UV crosslinking, thermo-gelation	Mechanical property (compression), porosity, *in vitro* degradation, printability	N/A	[307]
Type I collagen (2mg/mL)	N/A	N/A	Micro-extrusion bioprinting using FRESH bioprinting method	Thermo-gelation	Cell infiltration, printability	N/A	[308]
Human collagen (0.5, 1, 3, and 6 mg/mL)	Human	N/A	Micro-extrusion bioprinting using FRESH bioprinting method	Thermo-gelation	Swelling ratio, mechanical property (compression), Live Dead assay	N/A	[309]
Norbornene-functionalized collagen with gelatin or alginate	Bovine	Time sweep (before and after UV)	Micro-extrusion bioprinting	UV crosslinking, Thermo-gelation	Mechanical property (compression), swelling test, cell viability, immunofluorescence, printability	N/A	[310]
Type I Collagen and chitosan	N/A	Steady state flow sweep, stain sweep, frequency sweep	Micro-extrusion bioprinting	pH crosslinking, Thermo-gelation	*In vitro* degradation, cytotoxicity assay	N/A	[311]

Bioprinting material formulations	Collagen source	Rheological characterizations	Printer type	Gelation/crosslinking method	Other characterization	Application	Ref.
Methacrylate Type I collagen (3mg/mL)	Bovine	N/A	Micro-extrusion bioprinting using FRESH bioprinting method	UV crosslinking, genipin crosslinking, thermo-gelation	Cell viability, cell metabolic assay, *in vitro* degradation, printability, Mechanical test (compression)	N/A	[312]
Type I collagen (6mg/mL) with or without Pluronic-F127 (60%)	Rat tail	Steady state flow sweep, Temperature sweep,	Micro-extrusion bioprinting	Thermo-gelation and thermo-crosslinking	Printability, Live/dead, immunofluorescence,	N/A	[313]
Type I collagen (20, 30, 40mg/mL)	Porcine	Frequency sweep, time sweep, temperature sweep	Micro-extrusion bioprinting	Thermo-gelation	Mechanical property, (compression), printability, cell viability,	N/A	[314]
Type I collagen (2mg/mL) coated with alginate	Rat tail	N/A	Coaxial extrusion printing	$CaCl_2$, thermo-gelation	Printability, Cell distribution, immunofluorescence	N/A	[315]
Type I collagen (0.5%) with gelatin and alginate	N/A	Steady state flow sweep	Micro-extrusion bioprinting	$CaCl_2$	Porosity, swelling test, mechanical property (compression), cell viability, immunofluorescence	N/A	[316]
Acidic Type I Collagen Hydrogel (35mg/Ml, cell seeded after printing)	Bovine	N/A	Micro-extruction bioprinting using FRESH bioprinting method	pH	Cell viability, printability, cell attachment	N/A	[317]
Type I collagen and starch blend (1.33mg/ml collagen with 1.5-12.5% starch)	Rat tail	Steady steady flow sweep, frequency sweep, thixotropy	Micro-extrusion	Thermo-gelation	Printability, porosity, cell viability,	N/A	[318]

	Bioprinting material formulations	Collagen source	Rheological characterizations	Printer type	Gelation/crosslinking method	Other characterization	Application	Ref.
	Type I collagen (3mg/mL), or Type II collagen (3, 6mg/mL)	Bovine	Dynamic viscosity	Aerosol jet printing	Thermo-gelation	Mechanical property, welling ratio,	N/A	[319]
	Type I collagen (4, 8, 12mg/mL) with riboflavin (0.5mM)	Rat tail	Time and frequency sweep (before and after UV crosslinking)	Micro-extrusion bioprinting	UV crosslinking, thermo-gelation	Printability, cell viability, pH effect for printability,	N/A	[212]

CHAPTER 3. Bioprinting of human nasoseptal chondrocytes-laden collagen hydrogel for cartilage tissue engineering

Contribution author: Xiaoyi Lan, Tianxing Gong, Yan Liang, Esra J.N. Erkut, Melanie Kunze, Aillette Mulet-Sierra, Martin Osswald, Khalid Ansari, Hadi Seikaly, Yaman Boluk Adetola B. Adesida

Chapter 3 has been published in parts as:

Xiaoyi Lan, Yan Liang, Esra JN Erkut, Melanie Kunze, Aillette Mulet-Sierra, Tianxing Gong, Martin Osswald, Khalid Ansari, Hadi Seikaly, Yaman Boluk, and Adetola B Adesida, "Bioprinting of human nasoseptal chondrocytes-laden collagen hydrogel for cartilage tissue engineering" The FASEB Journal, Journal vol.35, no. 3, p. e21191, 2021.

3.1 Introduction

Nasal reconstructive surgery, such as nasal airflow correction, fracture repair, septoplasty, and functional rhinoplasty, all require the modification of native nasal cartilages. The goals of nasal reconstruction are to restore not only physiological functions but also facial aesthetics. Since native cartilage tissues are poorly vascularized and have a poor regenerative ability, nasal reconstructive surgery often requires transplantation of cartilage grafts to replace the original tissues [320, 321]. The grafts must be mechanically robust to resist both static forces (e.g. gravity and wound healing contracture), and dynamic forces (cyclical nasal valve deformation and muscle contraction) [322, 323].Previously used cartilaginous grafts as nasal structural support include autografts, allografts, and cell-based tissue-engineered grafts [324-327]. Among these options, cell-based tissue-engineered grafts have the potential to mitigate donor-site morbidities and risk of infection issues associated with autografts and allografts usage [328-330]. Our group's previous work has demonstrated successful *in vitro* and *in vivo* chondrogenesis using human nasoseptal chondrocytes (NCs) seeded on clinically approved and commercially available semi-porous type I collagen and III hybrid membrane scaffold[64]. Despite promising results, the tissue-engineered nasal cartilages were limited to the shape and dimensions of the membrane scaffold and to inhomogeneous cell distribution facilitated by manual dispersion of the chondrocytes on to the membrane. These limitations may become bottlenecks for further advancements in clinical application. More recently, three-dimensional (3D) bioprinting approaches employing layer-by-layer additive technique allow the creation of custom anatomically shaped cell-laden engineered cartilages, which may be particularly impactful for patients with large nasal cartilage defect or absent cartilage structures[150, 331]. Using a computer-aided system (CAD), the 3D bioprinting process enables the precise dispensation of the cell-laden supporting biomaterial (also known as

"bioink") into printed biomimetic construct with a high spatial resolution and homogeneous cell distribution [83, 332].

Hydrogels have been identified as attractive materials for bioinks, due to the resemblance between hydrogel's water-swollen networks and cartilage's functional extracellular matrix (ECM)[264, 333, 334]. The most studied hydrogels for 3D-bioprinting are mostly natural polymers, such as collagen [80, 123, 263, 335], hyaluronic acid [80, 335, 336], chitosan [80, 337, 338], alginate [80, 130, 149, 225, 339, 340], cellulose [149, 225, 264, 339, 341], gelatin [80, 337, 340], and fibrin [80, 123]. Among these, collagen has been widely explored as a biomaterial for regenerating various tissues [175, 342-345]. As the predominant ECM component of cartilaginous tissues, collagen provides cell adhesion motifs, biochemical signals, and induce cellular differentiation and migration, therefore further promotes cartilage tissue regeneration [335]. Among the different types of collagen, type II collagen is primarily found in hyaline cartilage such as articular and nasoseptal cartilages, and is often considered the first choice as a cartilage substitute [346]. Unfortunately, type II collagen shows unwanted arthritogenic activities [347, 348]. In contrast, type I collagen does not elicit adverse immune reaction particularly in the absence of its telopeptides and lacks arthritogenic effects [349, 350]. Additionally, owing to its ubiquitous biocompatibility and vast clinical approval, type I collagen is used extensively in cartilage tissue engineering [351]. Therefore, in this study, a type I collagen hydrogel was explored as a scaffold to tissue engineer nasoseptal cartilagesvia 3D bioprinting. But type I collagen hydrogel cannot sustain the printed structure due to its low viscosity and elastic modulus, and slow gelation time, which greatly limits its application in 3D-bioprinting [352]. To circumvent this limitation in the absence of potentially toxic chemical crosslinking agents of any to augment collagen hydrogel strength [162], we adopted the freeform reversible embedding of suspended hydrogel (FRESH)

method [126, 353-355], to 3D bioprint nasal chondrocyte-laden type I collagen hydrogel for nasal cartilage tissue engineering for the first time.

In the FRESH method, cells can be pre-mixed with pH neutral type I collagen hydrogel and the desired anatomical structures can be printed and held within a secondary biocompatible gelatin support bath at room temperature. As the printed structure is transferred into a 37 °C incubator, the pH neutral type I collagen hydrogel undergoes thermo-induced fibril formation while the secondary gelatin support bath slowly melts at the same time. Then, chondrogenesis is induced *in vitro* by culture of the cell-laden printed structure in cell growth media supplemented with soluble chondrogenic factors. One key advantage of the *in vitro* cartilage tissue engineering is that the chondrogenic outcome is known based on several metrics of cartilage quality assessment before surgical implantation, making the engineered cartilage tissue surgery-ready [6].

In this work, we report a successful *in vitro* nasal cartilage tissue engineering method via the FRESH 3D-bioprinting. In brief, a commercially available type I collagen hydrogel was pre-mixed with monolayer-expanded human nasoseptal chondrocytes (NCs) to create a NCs-laden construct for the bio-fabrication of tissue engineered nasal cartilages. The effect of the addition of nasal chondrocytes on the hydrogel's rheological properties and printability were also investigated. The NCs-laden constructs were 3D printed, cultured in chondrogenic media, and the resulting engineered tissue's structural integrity was evaluated along with biochemical and molecular assessments.

3.2 Material and Methods

3.2.1 Human-derived Chondrocyte Isolation

Nasoseptal cartilage specimens were collected upon the approval of the University of Alberta's Health Research Ethics Board - Biomedical Panel (Study ID: Pro00018778). Human nasoseptal cartilage specimen was collected from 4 male donors receiving septoplasty or rhinospetoplasty procedures (age 23 to 28 years; Table S1). Male donors were the only available clinical specimens at the time of this study. Human nasal chondrocytes (NCs) were isolated enzymatically as previously described [64]. The primary NCs were then plated at a density of 10^4 cells/cm^2 and cultured in Dulbecco's Modified Eagle Medium (DMEM, Sigma Aldrich, Canada) supplemented with 10 v/v (%) fetal bovine serum (FBS), 1 ng/mL of Transforming growth factor-β1 (TGF-β1) and 5 ng/ml of basic fibroblast growth factor (FGF-2) at 37 °C under 5% CO_2 and 95% humidified atmosphere. Passage 2 (P2) cells were used for the bio-printing. The population doubling (PD) of the NCs for each donor were determined as PD = $\log_2$ (population final /population initial). The mean cumulative population doublings (CPD) by the end of P2 was 6.11 ± 0.47.

3.2.2 Chondrocyte-laden Bioink Preparation

NCs were trypsinized and then resuspended in a defined serum-free DMEM chondrogenic medium comprising of 100 U/mL antibiotics (penicillin and streptomycin), 2 mM L-glutamine, 100 mM 4-(2-hydroxyethyl)-1-piperazineethanesulfonic acid (HEPES), 0.1 μM dexamethasone, 0.1 mM L-Ascorbic acid 2-phosphate and 0.1 mM L-Proline. Subsequently, the cell suspension was mixed with bovine type I collagen gel (the bioink) (3.5 wt%, Lifeink® 200, Advanced BioMatrix, LOT:5202-1KIT, USA) to make the cell concentration of 1×10^7 cells/mL.

3.2.3 Rheological Characterization of Bioink and Printability Assessment

NCs-laden collagen bioink were analyzed for their rheological behaviors within 1 hour of preparation. The viscosities of bioinks were characterized on the rotatory rheometer (AR-G2, TA Instrument, USA) with a 25 mm parallel-plate geometry, and the shear rate was defined from 0.001 to 1000 s^{-1} at 20 ºC. The temperature sweep was conducted between 4 ºC and 45 ºC at a step of 1 ºC per minute. The strain and frequency were fixed at 1 % and 10 rad/s, respectively, within the linear region. The oscillatory frequency sweep was measured from 1 to 100 rad/s frequency at 20 ºC and 1% strain. The steady state flow sweep data were analyzed using TRIOS software (TA Instrument, USA).

In order to describe the shear thinning behavior, the two-parameter *Ostwald de Waele* relationship, also known as the Power Law, was used to fit the viscosity (η) versus shear rate ($\dot{\gamma}$) curve. In the Power Law model, the relation between viscosity and shear rate can be described in the following equation: $\eta = K\dot{\gamma}^{n-1}$, and the Power Law relationship between shear stress (σ) and shear rate can be described in the equation: $\sigma = K\dot{\gamma}^{n}$, where K is the flow consistency index, and n is the flow behavior index [171]. Flow model of power law fluid along the pipe were combined mechanical energy balance to predict the extrusion velocity of bioink through the printer nozzle and calculate the theoretical shear stress the bioink was subject to. The details of this theoretical model are given in the Supplementary material section 3.6.1.

3.2.4 3D Bioprinting of type I collagen Hydrogel

The bioprinted constructs were fabricated on a pneumatic microextrusion-based bioprinter (INKREDIBLE^{+}, Cellink, Sweden). The geometry and microstructure of the printed constructs were predefined in a commercial design software (Slic3r, USA) and the gelatin support bath

(Advanced BioMatrix, USA) was prepared according to manufacturer's instructions. A 20mm x 20mm x 3mm square block with 30% infill rate, a 16.04 mm x 20 mm x 9.29 mm human nose with 50% infill rate, and a 7 mm diameter, 3.5 mm height cylindrical disc with 70% infill rate were bioprinted inside the support bath using collagen hydrogel to show the printability of collagen hydrogel using FRESH method.

To investigate the cartilage formation of the bioprinted constructs after *in vitro* chondrogenic culture, a disc shape was selected as a model, NCs-laden type I collagen hydrogel are bioprinted into cylindrical shape (7 mm × 3.5 mm, diameter × height) with infill rate of 70%. After bioprinting, NCs-laden constructs were kept at 37 ºC for 30 minutes, and then placed in a defined serum-free chondrogenic medium containing 10 ng/mL TGF-β3 (4 mL/ construct) for 6 weeks under normoxia condition (21% O_2; 5% CO_2 and 95% humidity)[64].

3.2.5 Cell Viability Assay of Bioprinted Construct

Cell viability studies were conducted using a Live/Dead viability kit (Thermo Fisher Scientific, Canada). Bioprinted cartilages using 22G needle and 20G needle (after 3 days culture) were incubated in 1mL of 4 μM calcein AM and 2 μM ethidium homodimer-1 solution at room temperature in the dark for 30 minutes. The bioprinted cartilages were viewed under a Nikon confocal laser scanning microscope (Leica TCS SP5). The pictures were quantified using Fuji Image J software.

3.2.6 Structural Integrity and Microstructural Details Evaluation of Bioprinted Construct.

Scanning electron microscope (SEM, Model S-4800, Hitachi, Japan) was used to analyze the porosity of the bioprinted constructs as well as the NC morphologies in the bioink after 6-weeks of *in vitro* chondrogenic culture. All the reagents and accessories were obtained from Electron Microscope Science (Pennsylvania, USA). Each construct was fixed in sodium cacodylate trihydrate buffer containing 2% (v/v) glutaraldehyde and 2.5% (v/v) paraformaldehyde overnight at 4 ºC. Subsequently, samples were halved and washed twice with deionized water for 2 min. The samples were further fixed with osmium tetroxide and tannic acid prior to SEM observation.

3.2.7 Evaluations of the Effectiveness of Cartilage Tissue Formation

3.2.7.1 Sulfated glycosaminoglycan and DNA quantification

Total glycosaminoglycan (GAG) matrix content of engineered cartilaginous tissue were measured by 1,9-dimethylmethylene blue (DMMB, Sigma-Aldrich, Canada) assay with chondroitin sulfate (Sigma Aldrich, Canada) as the internal standard [356]. The engineered cartilage constructs were first rinsed twice with PBS and frozen at -80°C. The constructs were thawed and digested in Proteinase K (1 mg/mL) solution at 56 ˚C for overnight for 16 hours. Subsequently, total GAG content was evaluated on the V-max kinetic microplate reader (Molecular Devices, USA) at the wavelength of 530 nm. The DNA content from the Proteinase K digests was measured using the CyQUANT Cell Proliferation Assay Kit (Thermo Fisher Scientific). Measurements were taken according to the manufacturer's instruction. Calf thymus DNA (Sigma-Aldrich) was used as a standard. Fluorescence emission was measured at 530 nm (excitation 450

nm) on a CytoFluor II fluorescence multi-well plate reader (PerSeptive Biosystems). The quantity of GAG then was normalized to total DNA and wet weight.

The bioprinted engineered cartilaginous tissue were then compared with the 6 native human nasoseptal cartilage tissue, the average of GAG/DNA and GAG/wet-weight values measured from 6 male (age 19-28; see Table S2) donors' native human cartilage tissues served as the controls.

3.2.7.2 Histological and Immunolabeling

For histological analysis, samples were fixed in 10% (v/v) neutral buffered formalin at 4°C overnight and dehydrated through a series of alcohol washes before paraffin wax embedding. The embedded samples were sectioned into slices of 7 μm in thickness and deparaffinized by the xylene substitute. For histological assessment, the sliced sections were rehydrated through a graded series of ethanol (100%, 96% v/v, 70% v/v and 50% v/v), rinsed in distilled water and stained with Meyer's Hematoxylin, Green FCF, and Safranin-O. The Bern histological scoring of engineered cartilage that accounts for uniformity and intensity of matrix staining, cell density/matrix formation, and cellular morphologies was performed by 6 blinded observers [357].

The protein expression of *human* types I and II collagen were examined by immunofluorescence. In brief, micro-sectioned slices were first de-paraffinized, rehydrated and then subjected to antigen retrieval methods including the use of protease XXV (AP-9006-005 from Thermo Scientific) and hyaluronidase (H6254 from Sigma-Aldrich). After the antigen retriever steps, the rabbit anti-human type I collagen (CL50111AP-1, Cedarlane, Canada) and mouse anti-type II collagen (II-II6B3, Developmental Studies Hybridoma Bank (DSHB), USA) primary antibodies were used to detect types I and II collagen, respectively. The slices were subsequently incubated for 45 minutes with secondary antibodies; goat anti-rabbit IgG Alexa Fluor 594 (ab150080) and goat

anti-mouse IgG Alexa Fluor 488 (ab150117) from Abcam, USA, after initial treatment with the primary antibodies before inspection under a fluorescent microscope. In addition, the sectioned slices were also stained with 4',6-diamidino-2'- phenylindole (DAPI, Thermo Fisher Scientific) for 20 minutes at room temperature to examine the nuclei of NCs within each sample. Sections were mounted with 1:1 Glycerol: PBS and imaged on a Nikon Eclipse Ti-S microscope coupled to a DS-U3/Fi2 Color CCD camera using 100x and 200x objective lenses.

3.2.7.3 Real-time PCR

Real-time polymerase chain reaction (PCR) was used to analyze chondrogenic and fibrochondrogenic specific genes (*ACAN*, *COL1A2*, *COL2A1*, *SOX9*) and chondrocyte hypertrophy-related gene (*COL10A1)* expressions of the engineered cartilage tissue after *in vitro* chondrogenic culture for 42 days (6 weeks). The monolayer-expanded NCs devoid of *in vitro* chondrogenic culture from the 4 donors served as negative controls, and the native nasoseptal cartilage specimens from 6 donors (n=6) served as positive controls. Total RNA was extracted using Trizol (Life Technologies, USA) and examined on the Nanodrop One C (Thermo Fisher Scientific). Subsequently, the complementary DNA (cDNA) was synthesized from 100 ng of total RNA using GoScript, Reverse Transcriptase kit (Promega, USA) and 1 µg of oligo (dT) primer. Quantitative PCR was performed using Takyon DNA polymerase and SYBR Green detection (Eurogentec, USA) on a CFX connect Real-time PCR detection System (Bio-Rad Laboratories, USA). *YWHAZ*, a constitutively expressed protein, was used as a housekeeping gene in this study. *YWHAZ* presents in cells at relatively consistent level across different tissues and under different experimental conditions. Additionally, *YWHAZ* is not regulated by a variety of signaling pathways. The relative gene expressions in this study were calculated using the $2^{-\Delta\Delta Ct}$ method [358, 359]. Primer sequences were designed using Primer Express 3.0.1 (Thermo Fisher Scientific).

Primer sequences for *ACAN*, *COL1A2*, *COL2A1*, *COL10A1*, *SOX9*, and *YWHAZ* are shown in Table 3.1. Transcript levels for *ACAN*, *COL1A2*, *COL2A1*, *COL10A1* and *SOX9* were normalized to the housekeeping genes *YWHAZ* using the delta delta CT method ($2^{-\Delta\Delta CT}$)[358, 359].

Table 3.1 Primer sequences for real-time PCR

Genes	**Forward Primer (5′)**	**Reverse Primer (3′)**
Tyrosine 3 Monooxygenase/Tryptophan 5-Monooxygenase Activation Protein Zeta (*YWHAZ*)	TCTGTCTTGTCACCAACCATTCTT	TCATGCGGCCTTTTTCCA
Aggrecan (*ACAN*)	AGGGCGAGTGGAATGATGTT	GGTGGCTGTGCCCTTTTTAC
type I collagen (*COL1A2*)	GCTACCCAACTTGCCTTCATG	GCAGTGGTAGGTGATGTTCTGAGA
type II collagen (*COL2A1*)	CTGCAAAATAAAATCTCGGTGTTCT	GGGCATTTGACTCACACCAGT
SRY-Box 9 (*SOX9*)	CTTTGGTTTGTGTTCGTGTTTTG	AGAGAAAGAAAAAGGGAAAGGTAAGTTT
Collagen X (*COL1OA1*)	GAAGTTATAATTTACACTGAGGGTTTCAAA	GAGGCACAGCTTAAAAGTTTTAAACA

3.2.8 Statistics

The OriginLab Pro 2020 Education Edition (Massachusetts, USA) was used to perform statistical analysis. The unpaired two sample t-test was used to analyze the significance level between the sample group and control group ($p < 0.05$). The results are presented as the mean ± standard deviation (SD).

3.3 Results

3.3.1 Bioink Characterization and FRESH 3D Bioprinting

The rheological properties of the commercially available type I collagen hydrogel/ bioink were first studied to determine suitable 3D bioprinting parameters. As shown in Figure 3.1A, the measured rheological results for the cell free and NCs-laden hydrogels are plotted and fitted by Power Law (Power Law constants, *K* and *n* are provided in Table 3.2). Figure 3.1A showed that the shear thinning behavior of the collagen hydrogel was preserved despite the addition of the NCs. Using mechanical energy balance and power law fluid model, the printer needle was successfully modeled to allow the prediction of suitable printing parameters (see 3.6.1 supplementary information). From this model, the pneumatic pressure and nozzle diameter were identified to be the determining factors for extrusion velocity and shear stress. Two standard printer needle sizes were first evaluated, including a larger needle (20 Gauge; 20G, diameter = 603 μm), and a smaller needle (22 Gauge; 22G, diameter = 410 μm). As shown in Figure 3.1B, the predicted extrusion velocity was higher in the NCs-laden hydrogel than the NCs-free hydrogel. In addition, the larger needle yielded a higher extrusion velocity than the smaller one under the same pneumatic pressure. In Figure 3.1C, the wall shear stress experienced by the filament was found to be proportional to the extrusion velocity. Under the same velocity, the NCs -laden hydrogel bioink experienced lower wall shear stress than the NCs-free one. Additionally, the wall shear stress was slightly higher in the smaller nozzle under the same extrusion velocity. The data above indicated that the larger needle (20G) was more suitable for this application due to lower shear stress and higher extrusion velocity. To validate the mathematical model, the theoretical extrusion velocity was compared with experimental measured values using 20G needle and NCs-free collagen hydrogel. The measured extrusion velocity is calculated by measuring the weight of extruded

hydrogel ($v = \frac{Q}{A}$). The results showed that the model closely matched the measured results. Therefore, the wall shear stress experienced by the cell can be predicted by the model.

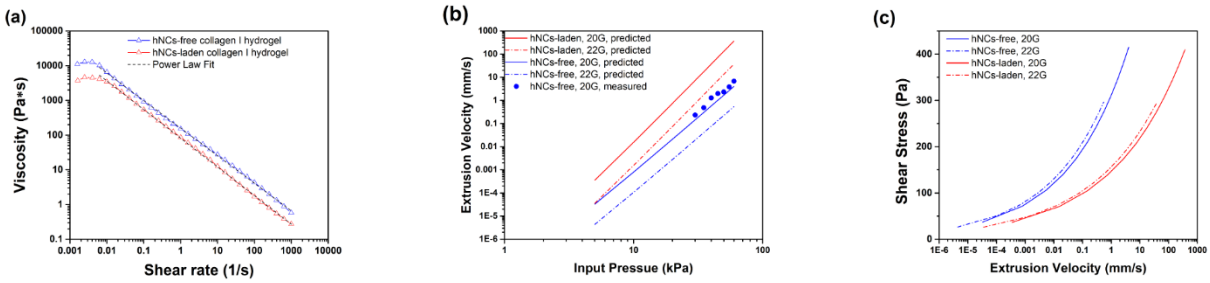

Figure 3.1 Printability characteristics of cell-free and cell-laden collagen hydrogel. (A) Steady state flow sweep from shear rate of 0.001 s -1 to 1000 s -1. The dash line represents the linear fit based on Power Law model; (B) The theoretical extrusion velocity as well as the measured extrusion velocity vs. input pressures; (C) The theoretical wall shear stress vs. the extrusion velocity.

Table 3.2 The Power Law fit of viscosity vs. shear rate curve

	K	*n*	R^2
Cell-free bioink	158.775	0.206	0.999
Cell-laden bioink	81.233	0.174	0.999

The changes of storage (G') and loss (G'') modulus with temperature are provided in Figure 3.2A. The storage modulus of NCs-free hydrogel remained constant at approximately 650 Pa from 4 ºC to 30 ºC and increased dramatically to 2746 Pa near 40 ºC. Similarly, the storage modulus curves of NC-laden bioink followed the same pattern; however, the initial and maximum storage modulus were much lower in NC-laden bioink comparing to the NCs-free one. In contrast, to the collagen hydrogel/ bioink, the G' of gelatin support bath remained constant up to 30 °C and decreased afterwards. In addition, both NCs-free and NC-laden hydrogels showed a sharp decline in storage modulus when the temperature was further increased above 40 °C. In Figure 3.2B, the moduli of the collagen hydrogel were closely related to the oscillatory frequency. G'' is initially higher than G' for NCs-free and NC-laden bioinks, as both storage and loss moduli increased with increasing oscillatory frequency, G' and G'' of both bioinks were crossed at the

frequency of 100 rad/s, implying that the type I collagen bioink demonstrated “weak-gel” behaviors. The results also indicate that the NCs-free collagen bioink showed much higher storage modulus than NCs-laden bioink.

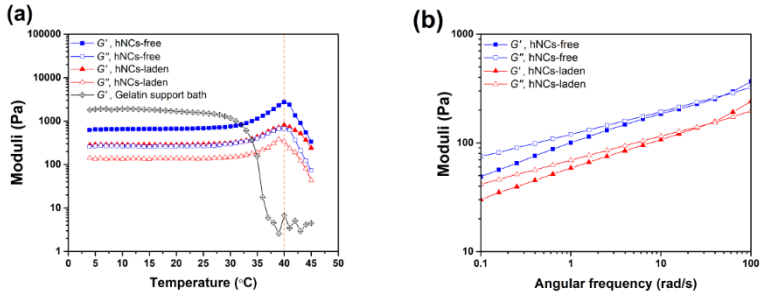

Figure 3.2 Rheological characterization of cell-free and cell-laden collagen hydrogel. (A) Oscillatory temperature sweep results of bioinks and gelatin bath at 1 Hz and 1% strain, from 4°C to 45 °C. G’ represents the storage modulus and G’’ stands for the loss modulus; (B) The frequency sweep results of NCs-laden and NCs-free bioinks from 1 rad/s to 100 rad/s at 1% strain and 20 °C.

Porous constructs were printed by the FRESH method in this study, the gelling and dissolution process of the type I collagen hydrogel as well as the gelatin support bath was captured by digital camera and depicted in Figure 3.3A. As shown in Figure 3.3A, designed structures were successfully bioprinted inside the gelatin bath using the FRESH method. As the temperature increased up to 37 °C, the gelatin support bath started to dissolve, and the bioprinted structure maintained its integrity after the gelatin support bath melted completely.

The LIVE/DEAD assay images (with respect to NCs from donor 1) after FRESH bioprinting using 20G and 22G needle are shown in Figure 3.3B, with a cell viability of 95±1%, and 81±3%, respectively. The LIVE/DEAD images from two additional donors are shown in Figure S3.3 and Figure S3.4. Therefore, the 20G needle was chosen for the remainder of the *in vitro* experiment. In the following *in vitro* cartilage tissue formation experiments, NCs-laden type I collagen hydrogel were bioprinted into cylindrical shapes. After 6-weeks of *in vitro* chondrogenic culture of the NC-laden type I collagen hydrogel cylindrical discs, originally of 7 mm in diameter showed

only 0.43% (~ 0.03 mm) diameter decrease. The bioprinted discs' appearance changed from semi-transparent to opaque, which perhaps indicates the formation and deposition of cartilaginous matrix by the inherent NCs under *in vitro* chondrogenic culture (Figure 3.3C).

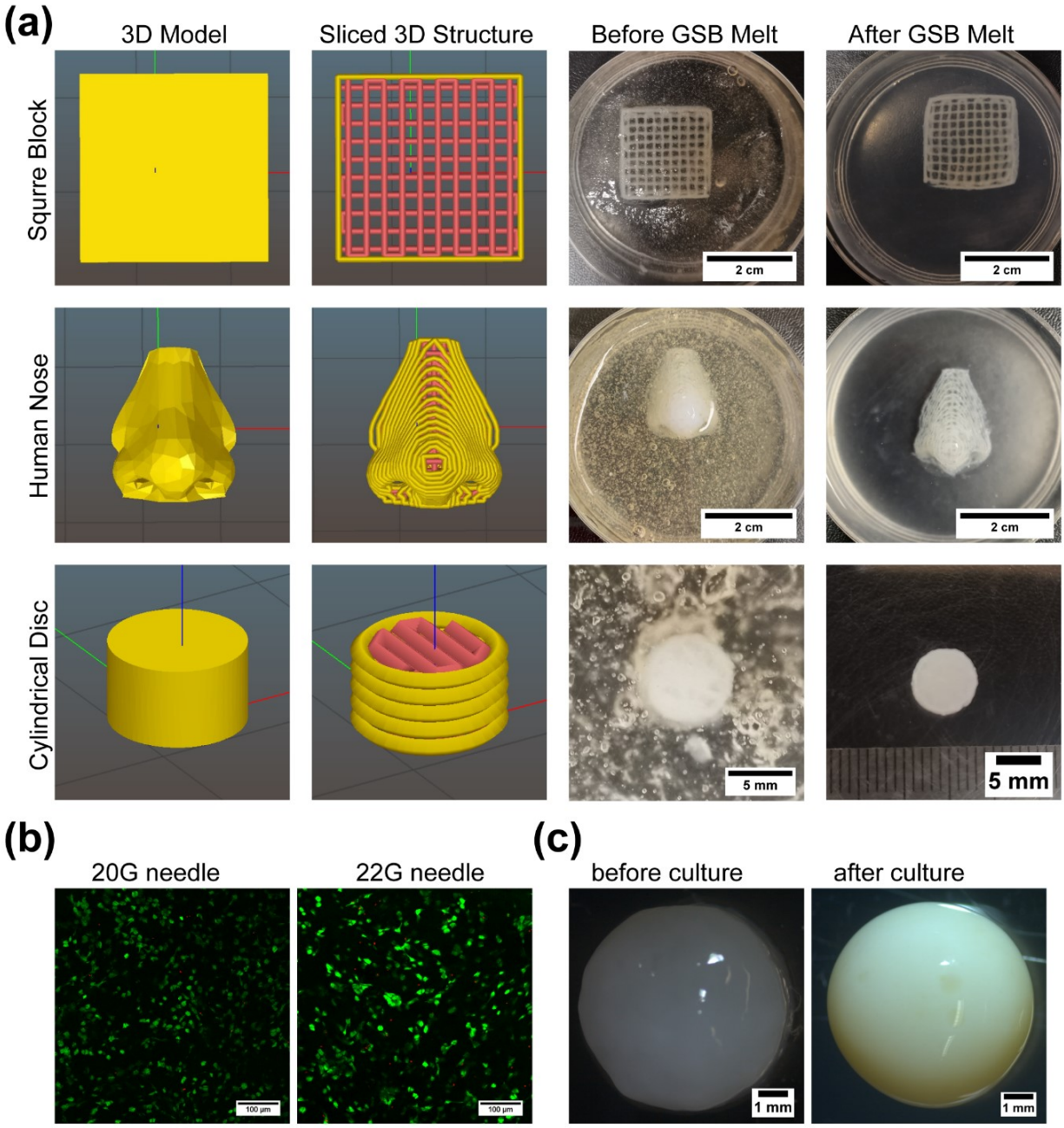

Figure 3.3 Gross appearance and cell-viability assessment of FRESH structures of (A) 3D model of the square block, human nose, and cylindrical disc parts are imported to Slic3r and the previews of the sliced parts are displayed. Image of 3D bioprinted structures in gelatin support bath (GSB)

captured before incubation. After 30 minutes of incubation, image of the 3D bioprinted structures. The support bath was carefully aspirated, and PBS was added. (B) LIVE/DEAD assay of 20G and 22G needles, after 3 days of chondrogenic culture. The green color represents the viable cells, red color represents the dead cells. (C) Gross morphology of FRESH bioprinted construct before and after 6 weeks of culture.

3.3.2 Assessment of Tissue Engineered Nasal Cartilage

The safranin-O staining results showed that most of NCs exhibited round-shaped chondrocyte morphology embedded within the lobules to form round lacuna structures(Figure 3.4). Comparing to the NCs-free constructs, the bioengineered cartilage stained intensely with safranin-O, signifying strong evidence of cartilage ECM formation and deposition by the NCs. This observation indicated that the monolayer-expanded NCs have been successfully re-differentiated into chondrocyte phenotype. As shown in Figure 3.4B-E, the safranin-O staining was uniform through the entirety of the cross-sections of samples engineered from all 4 donors of NCs, with their intensities resembling that of the native tissue. Furthermore, a semiquantitative histological scoring of engineered cartilage based on Safranin O staining of cartilage ECM, the Bern score ([357]; see Supplementary information 3.6.4), was performed by 6 blinded observers (

Table S3.3) The histological assessment results showed that the mean total score ± SD of the bi-oengineered nasal cartilage was statistically indifferent from that of the native tissue (Figure 3.4M).

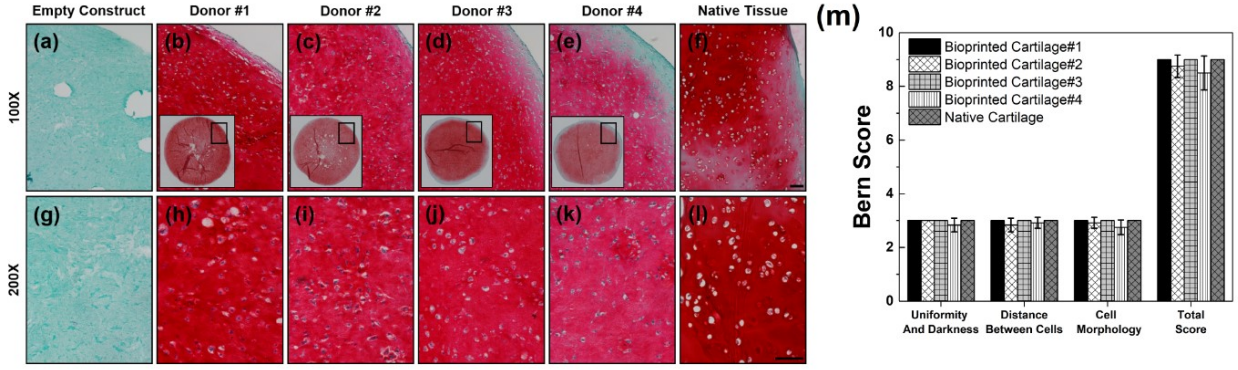

Figure 3.4 Safranin O histological assessment of native and bio-printed cartilage quality. The Safranin-O staining of NCs-free and NCs-laden constructs and the native cartilage tissue after 6-week *in vitro* culture (A – L); (M) The semi-quantitative analysis of cartilaginous tissue formation based upon the Bern Score. (n = 6 blinded individual observers). Scale bar = 100 µm.

To quantitatively analyze GAG formation after the 6-week culture, DMMB assay was performed to measure the GAG content, and DNA florescent assay was used to measure the DNA content for each bioprinted nasal cartilage sample. The GAG per DNA (GAG/DNA),GAG per wet weight (GAG/WW) and DNA per wet weight (DNA/WW) of both bioengineered cartilage and native tissue are presented in Figure 3.5A, Figure 3.5B, Figure 3.5C, respectively. Both GAG/DNA, GAG/WW, and DNA/WW values indicated no significant difference between the bioengineered cartilage and the native tissue. Therefore, the above results implied that the GAG of the bioengineered cartilage after 6-week culture closely resembled to that of the native tissue and the cellularity of the *in vitro* engineered nasal cartilage is similar to the one of native na-soseptal cartilage.

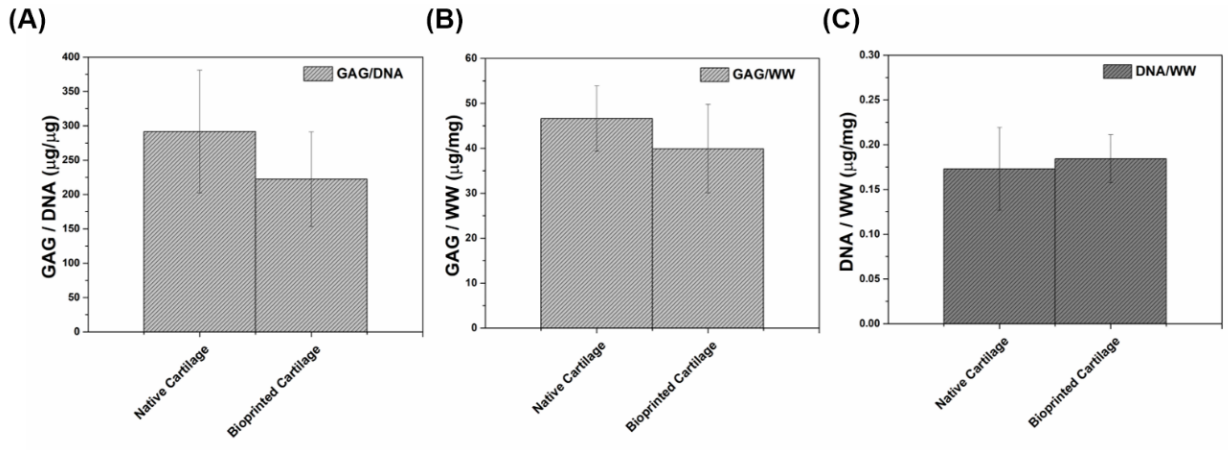

Figure 3.5 Wet weight and biochemical quantification of cartilage matrix production. The normalized values of GAG quantities between bioprinted scaffolds and the native cartilage tissue with respect to the total quantity of DNA (µg/µg) and the total wet weight of specimen (µg/mg). The asterisk symbol (*) indicates that values are significantly different at $p < 0.05$. ($n = 4$ donors for bioprinted scaffolds and 6 for native cartilage tissues)

The depositions of collagens I and II in the NCs-free constructs, bioprinted cartilage, as well as native cartilage tissue were examined by immunofluorescence (IF), as shown in Figure 3.6. The NCs-free constructs showed only faint type I collagen (COL1) staining (Figure 3.6G) and no type II collagen (COL2) was detected (Figure 3.6A). The bioprinted cartilages for all four donors stained for both collagens I and II but with type II collagen being much more evident (Figure 3.6H-K, Figure 3.6B-E), which exhibited similar IF characteristics as the native tissue (Figure 3.6F, I, R).

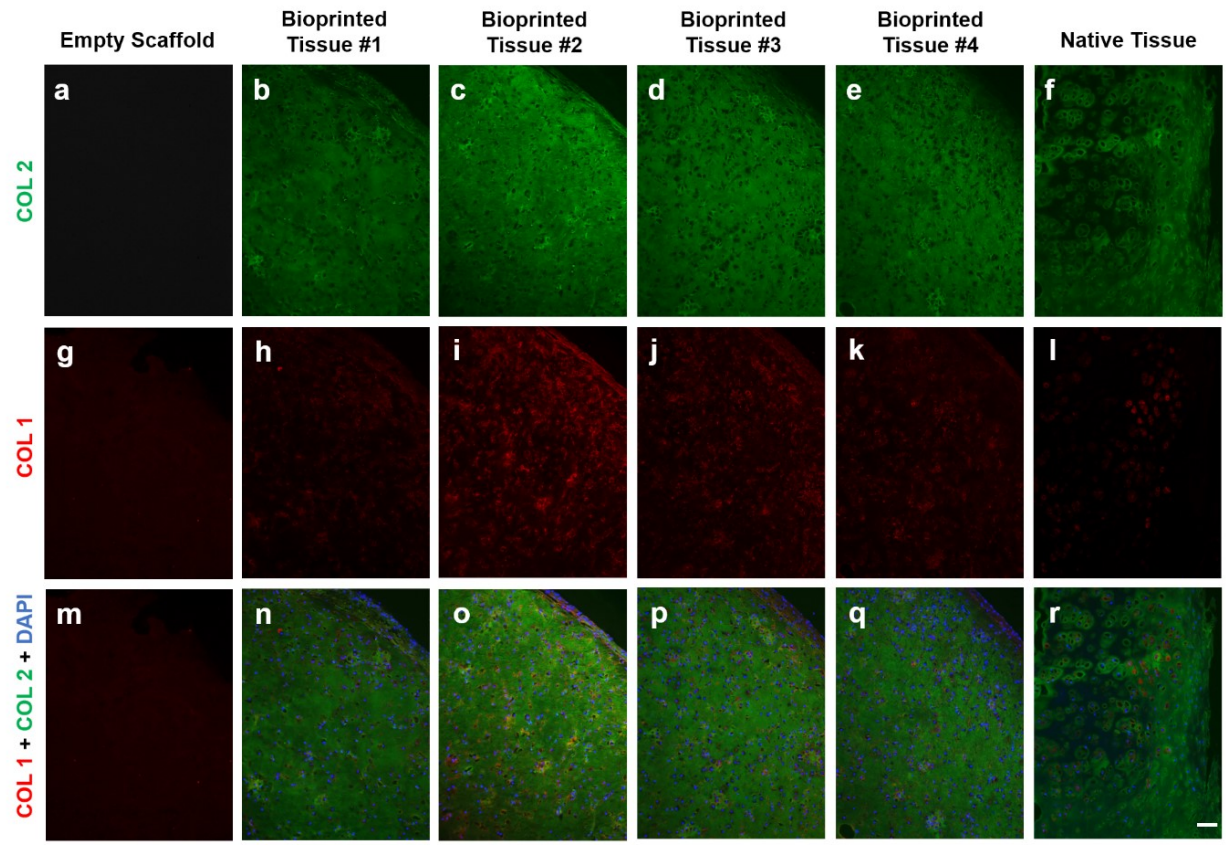

Figure 3.6 Type I and II collagen immunofluorescence of native and bio-printed cartilage. The immunofluorescence results of NCs-free, NCs-laden constructs and the native cartilage tissue after 6-week *in vitro* culture. The blue color from DAPI staining indicates cell nuclei, the red and green colors represent the presence of type I and type II collagens, respectively. Scale bar = 100 µm.

The SEM images of the cell free and NC-laden bioinks after 6 weeks of *in vitro* culture in chondrogenic media are depicted in Figure 3.7. Figure 3.7A and Figure 3.7B depict the surface SEM view of the cell free bionk's interwoven connectivity of collagen fibrils with variable spatial porous structures, while its cross-sectional SEM view in Figure 3.7C and Figure 3.7D display the 3D inter-connectivity of the fibrils alongside the spatial variable porous structure. In contrast, the SEM surface view of the NC-laden bioink displays large bundles of intercrossing collagen fibrils over round-shaped NCs and with little evidence of microporous structures within (Figure 3.7E and Figure 3.7F). Similarly, the cross-sectional SEM view of the NC-laden after the 6 weeks of

in vitro culture, revealed round chondrocyte-like morphology of NCs within small and large collagen fibril diameter connectivity with microporous implying the formation of extracellular matrix (ECM) after 6-week *in vitro* culture.

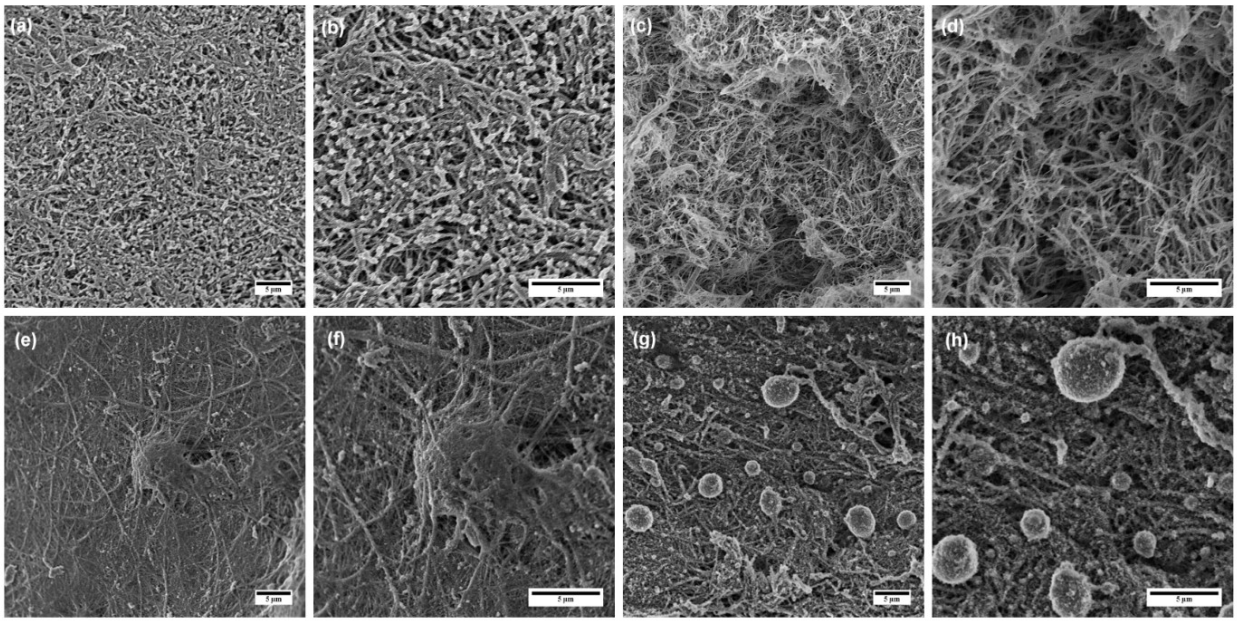

Figure 3.7 Ultrastructural characterization of bio-printed of cell-free and cell-laden collagen hydrogel. The microstructures of NCs-free (A-D) and NCs-laden (E-H) constructs after 6-week *in vitro* culture taken by SEM; (A, B, E & F) show the microstructure on the construct surface and (C, D, G & H) show the cross-section of the construct. Scale bar = 5 µm.

The fold changes of chondrogenesis-related (*ACAN*, *COL1A2*, *COL2A1* and *SOX9*) and hypertrophic chondrogenesis-associated gene (*COL10A1*) and their significant levels are depicted in Figure 3.8. In Figure 3.8A, all genes were significantly upregulated (≥ 2-fold change; $p < 0.05$) in the NCs-laden group as compared to the non-chondrogenically stimulated NCs monolayer control. However, the comparison of the NC-laden bionk after the 6 weeks of *in vitro* culture in chondrogenic media revealed a significant upregulation of *COL1A2, COL2A1*, and *COL10A1* with the exception of *SOX9* and *ACAN* which were downregulated and unchanged, respectively, relative to the native cartilage control group (Figure 3.8B).

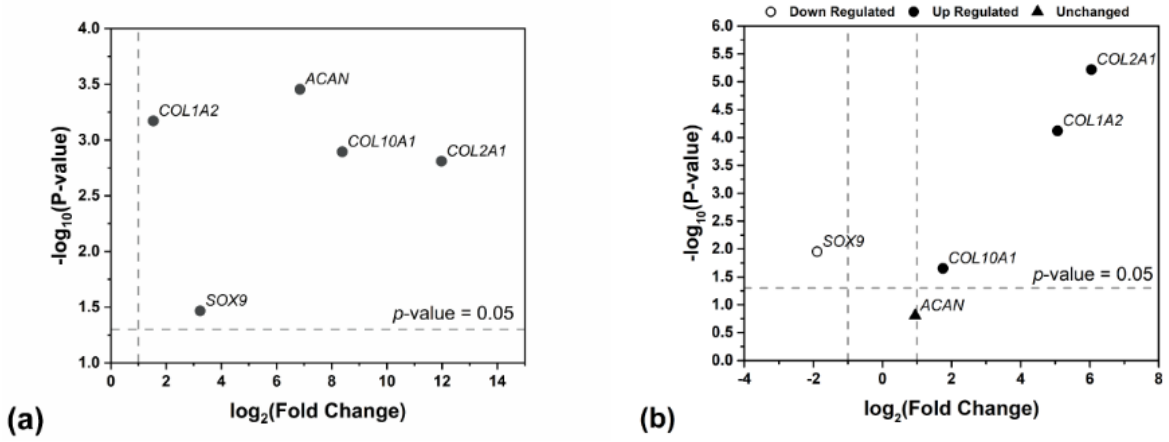

Figure 3.8 Molecular gene expression characteristics of native and bio-printed cartilage. (A) The fold changes of genes expressed in the bioengineered cartilage scaffold of 6-week *in vitro* culture as compared to the monolayer of NCs; (B) The fold changes of genes expressed in the bioengineered cartilage scaffold of 6-week *in vitro* culture as compared to the native cartilage tissue. Genes with fold changes increased by 2-fold or reduced by one-half are defined as significant upregulated or downregulated, respectively. ($p < 0.05$)

3.4 Discussion

In this present work, we report a novel method to biofabricate tissue engineered nasal cartilage with uniformly deposited cartilage ECM from *in vitro* expanded NCs-laden type I collagen hydrogel relative to nonuniformly distributed cartilage ECM in engineered nasal cartilage from NCs seeded porous collagen membrane scaffolds [360, 361].

In the steady-state flow sweep test (Figure 3.1A), both NCs-free and NCs-laden hydrogels showed shear-thinning properties which may be attributed to the break-down of hydrogen bonding between collagen molecules [362]. Based on the steady-state flow sweep result, we found that the presence of NCs in the hydrogel reduced the zero-shear viscosity, and enhanced shear-thinning effect. The decreased zero-shear viscosity may have resulted from the dilution of the collagen concentration by culture media. The increased shear thinning behavior may have been caused by the incorporation of the NCs, and thereby causing the disassembly of interconnected collagen fibril network at high shear rate.

Moreover, the temperature sweep results (Figure 3.2A) indicated that the collagen molecules were able to form collagen fibrils in both NCs-free and NCs-laden hydrogels [363]. However, when the temperature was above 40 °C, the denaturation of collagen occurred, and the storage modulus (G') reduced dramatically, implying that the hydrogel became viscous. The temperature-dependent viscoelastic behavior of collagen is attributed to the transition of the molecular arrangement of collagen triple helices [364, 365]. The collagen triple helices are in a random rod-like conformation at 10 °C in a dilute solution. This conformation starts to change when the temperature rises above 15 °C, and the formation of collagen fibrils [366] can be observed. With the temperature further increased above the physiological temperature (~37 °C), weak intermolecular bonding that holds collagen triple helices intact will be broken up, and individual collagen molecules exhibit the random coil conformation. Therefore, based on the type I collagen hydrogel's rheological characteristics, the optimal temperature window for 3D bioprinting should be between 4 ~ 28 °C.

A successful 3D bioprinted structure depends on the printability of bioink and, more importantly, the cell viability after printing. Sometimes, these two requirements are competing. A recent study [367], reported that controlling shear stress in 3D bioprinting process is a key factor to balance printing resolution and cell integrity. In this study, we characterized the rheological properties of the used collagen hydrogel in the presence and absence of NCs, then fitted it with the power law fluid model, and predicted the extrusion velocity and wall shear stress of these bioinks based on the mechanical energy balance and power law fluid equations.

A LIVE/DEAD assay was performed to further investigate the effect of shear stress on cell viability of the bioprinted construct using 20G and 22G needles. A relatively low printing speed (10mm/s) was selected as an input parameter, based on the fluid model, printing pressure of 30

kPa and 50kPa were used for 20G and 22G needle respectively, the cell viability result of 20G needle (95±1%) is significant higher than the cell viability results of 22G needle (81±3%), which further confirmed that the shear stress in 3D bioprinting process effect the cell viability. Due to the higher cell viability of the 20G needle, the 20G needle was chosen for the following *in vitro* experiment.

Comparing to our group's previous work, the bioprinted engineered nasal cartilage not only generated homogeneous distribution of cartilaginous tissue but also produced similar quantity of GAG matrix to native cartilage tissue (male, 39.87 ± 9.86 μg/mg in bioengineered cartilage *vs.* 46.62 ± 7.28 μg/mg of native nasal cartilage)[361]. The upregulated expression of *ACAN*, *COL1A2, COL2A1*, *SOX9* and *COL10A1* along with collagens I and II detection within the bioprinted engineered nasal cartilage after *in vitro* chondrogenic culture confirmed the redifferentiation of the dedifferentiated monolayer-expanded NCs and synthesis of nasal cartilage ECM. The *ACAN*, *COL1A2, COL2A1*, *SOX9* and *COL10A1* genes have been reported to be expressed and translated in engineered nasal cartilage from monolayer-expanded dedifferentiated NCs after *in vitro* chondrogenesis [361]. Moreover, the expression of these genes in the bio-printed engineered nasal with respect to their expression in native nasal cartilage confirmed the chondrogenic redifferentiation of the monolayer-expanded NCs to a phenotype that is characteristic of primary nasal chondrocytes. However, the notable upregulation of *COL1A2*, *COL2A1* and *COL10A1*, and downregulation of *SOX9* in the bio-printed engineered nasal cartilage relative to their expression in the native cartilage suggests that the performed *in vitro* chondrogenesis protocol and accompanying culture conditions may not have been optimal for chondrogenic redifferentiation. The critical role of *SOX9* in chondrogenesis as reported by several investigators [368-370] and its lowered expression in the bioprinted engineered nasal cartilage supports the suboptimal process of *in*

vitro chondrogenesis. Moreover, the expression of *COL10A1*, a marker of hypertrophic chondrocytes during endochondral ossification [371] also supports this view. It is probable that optimal cartilage formation may be achieved through transduction of *SOX9* [372] or through a combined transduction of the SOX trio; *SOX5*, *SOX6* and *SOX9*, which have been reported to form permanent cartilage [373]. Inclusion of parathyroid hormone-related protein (PTHrP) during *in vitro* chondrogenesis to suppress *COL10A1* may further enhance non-hypertrophic cartilage formation [374, 375]. While the induction of *COL10A1* in the bioprinted engineered cartilage may suggest the potential risk of bone-like tissue transformation after *in vivo* implantation as per the correlation of premature induction of chondrocyte hypertrophy markers with endochondral ossification [371], our previous work with *in vitro* expanded NCs on collagen membrane and with similar induction of *COL10A1* lacked evidence of such transformation after a 5-week subcutaneous implantation in immunodeficient nude [361].

For a successful mimic of native tissue, the microstructural resemblance is as important as the compositional similarity. Further analysis by SEM showed the ultrastructure of the engineered nasal cartilage particularly at high magnifications were consistent with high magnification images of native human nasoseptal cartilage reported by Holden et al [376]. Comparison of our data at a magnification of 2000x (Figure 3.7E, Figure 3.7G) as similarly reported by Holden et al revealed random thick collagen fibrils arranged linearly around lacunae as in native nasoseptal cartilage. Based upon the above observation from SEM and histology, our bioengineered nasal cartilage demonstrated a very close structural resemblance to native nasal cartilage. However, it is unclear how immature or mature the bioengineered nasal cartilage is as the degree of maturity has implications on how readily it will or otherwise integrate with surrounding tissue[377]. Further studies are therefore merited to determine the maturity of the bioengineered tissue.

Moreover, while the focus of our study is to replace nasal cartilage in skin cancer patients with lesions on their noses, it is noteworthy that bioengineered nasal cartilage as fabricated herein has utility in joint articular cartilage reconstruction[378, 379].

3.5 Conclusions

We have successfully used FRESH bioprinting method to generate engineered nasoseptal cartilage tissue with molecular, biochemical, histological and ultrastructural characteristics of native nasoseptal cartilage after a 6-week *in vitro* culture period. These results warrant future mechanical characterization and animal studies in which the bioprinted engineered nasal cartilage will be tested for flexural properties, implanted and their *in vivo* effectiveness as nasal cartilage substitutes will be further investigated. To this end, the combination of human nasoseptal chondrocytes with type I collagen hydrogel for FRESH-inspired bioprinting of engineered nasal cartilage is a promising strategy to explore further for the provision of autologous nasal cartilages for nasal cartilage reconstructive surgeries.

3.6 Supplementary material

3.6.1 Fluid Dynamic Modelling of Bioprinter

The fluid dynamic modeling of a micro-extrusion bioprinter was achieved by performing mechanical energy balance on a printer-head. The pressure loss in cartridge is assumed to be negligible. The geometry of the printer head is simplified to a pipe-flow with three sections: (1,2) syringe, and (3) needle, as shown in Figure S3.1.

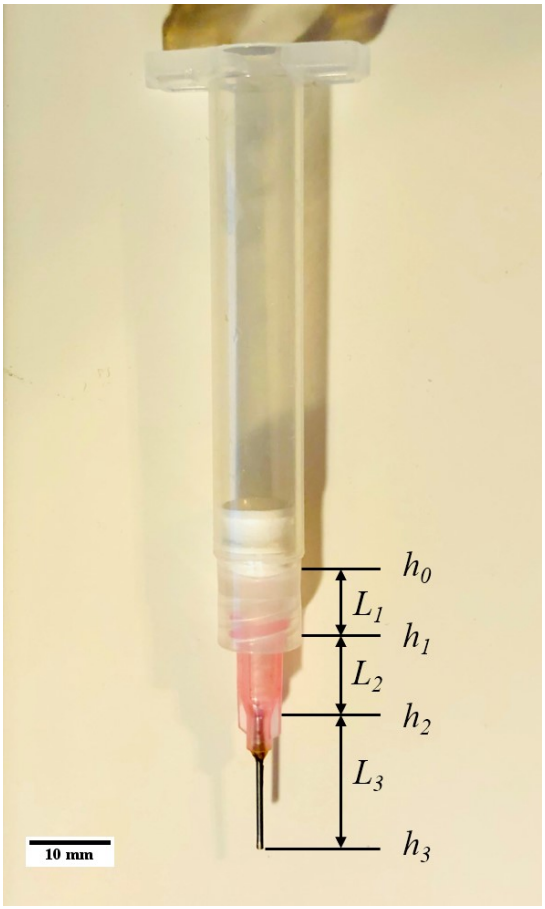

Figure S3.1 Schematic illustration of a printer head divided into four sections.

The two-printing needle were used for mathematical calculations are shown in Figure S3.2.

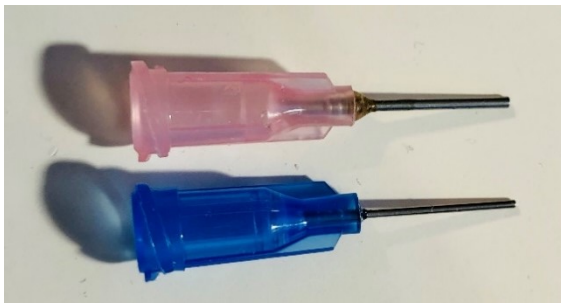

Figure S3.2 Needle tip geometries, Pink 20G, Blue 22G

Unsteady Bernoulli Equation for the pipe flow can be written as:

$$\int_1^2 \rho \frac{\partial v_s}{\partial t} ds + \left(p + \frac{1}{2}\rho {v_s}^2 + \rho g z\right)_2 - \left(p + \frac{1}{2}\rho {v_s}^2 + \rho g z\right)_1 = 0 \quad (1)$$

The flow in each section can be described by Unsteady-Bernoulli-Equation as follows:

$$p_o + \rho g h_0 + \frac{1}{2}\rho v_o^2 = p_1 + \rho g h_1 + \frac{1}{2}\rho v_1^2 + \rho \int_0^{L_1} \frac{\partial v_1}{\partial t} dL_1 + \Delta p_1(v_1, \eta) \quad (2)$$

$$p_1 + \rho g h_1 + \frac{1}{2}\rho v_1^2 = p_2 + \rho g h_2 + \frac{1}{2}\rho v_2^2 + \rho \int_0^{L_2} \frac{\partial v_2}{\partial t} dL_2 + \Delta p_2(v_2, \eta) \quad (3)$$

$$p_2 + \rho g h_2 + \frac{1}{2}\rho v_2^2 = p_3 + \rho g h_3 + \frac{1}{2}\rho v_3^2 + \rho \int_0^{L_3} \frac{\partial v_3}{\partial t} dL_3 + \Delta p_3(v_3, \eta) \quad (4)$$

where h_3 and p_3 is the outlet height and pressure with can be assume to 0. Then, combine Equation 2 to 4:

$$p_o + \rho g h_0 + \frac{1}{2}\rho v_o^2 = \frac{1}{2}\rho v_3^2 + \rho \int_0^{L_1} \frac{\partial v_1}{\partial t} dL_1 + \Delta p_1(v_1, \eta) + \rho \int_0^{L_2} \frac{\partial v_2}{\partial t} dL_2 + \Delta p_2(v_2, \eta) + \rho \int_0^{L_3} \frac{\partial v_3}{\partial t} dL_3 + \Delta p_3(v_3, \eta) \quad (5)$$

From continuity law (mass balance):

$$v_0 = \frac{A_3}{A_0} v_3 \quad (6)$$

$$v_1 = \frac{A_3}{A_1} v_3 \tag{7}$$

$$v_2 = \frac{A_3}{A_2} v_3 \tag{8}$$

By applying mass balance to the system, $\frac{\partial v_3}{\partial t}$ can be expressed as:

$$\frac{\partial v_3}{\partial t} = \frac{1}{\rho A_3 \left(\frac{L_1}{A_1} + \frac{L_2}{A_2} + \frac{L_3}{A_3}\right)} \left[p_0 + \rho g h_0 + \frac{1}{2} \left(\frac{A_3}{A_0}\right) \rho v_3^2 - \frac{1}{2} \rho v_3^2 - (\Delta p_1 + \Delta p_2 + \Delta p_3) \right] \tag{9}$$

The pressure drops across the syringe ($\Delta p_1, \Delta p_2, \Delta p_3$) can be predicted using Power Law fluid loss along a pipe [171]:

$$\Delta p_i = -\frac{dp_i}{dz} L = \frac{2^{n+2} \left(\frac{3n+1}{n}\right)^n L K v^n}{D^{n+1}} \tag{10}$$

Combine Equation 9 and 10:

$$\frac{\partial v_3}{\partial t} = \frac{1}{\rho A_3 \left(\frac{L_1}{A_1} + \frac{L_2}{A_2} + \frac{L_3}{A_3}\right)} \left[p_0 + \rho g h_0 + \frac{1}{2} \left(\frac{A_3}{A_0}\right)^2 \rho v_3^2 - \frac{1}{2} \rho v_3^2 - \left(\frac{2^{n+2} \left(\frac{3n+1}{n}\right)^n L_1 K \left(\frac{A_3}{A_1} v_3\right)^n}{{D_1}^{n+1}} + \right.\right.$$

$$\left.\left. \frac{2^{n+2} \left(\frac{3n+1}{n}\right)^n L_2 K \left(\frac{A_3}{A_2} v_3\right)^n}{{D_2}^{n+1}} + \frac{2^{n+2} \left(\frac{3n+1}{n}\right)^n L_3 K {v_3}^n}{{D_3}^{n+1}} \right] \tag{11}$$

Assuming an input pressures p_0, the steady-state extrusion velocity can be obtained by plotting Equation 14. By assuming varies input pressures, the extrusion velocity of the bioink can be plotted as Figure 3.1c. Then, using the steady-state extrusion velocity, the maximum shear stress at the printer nozzle can be calculated through Power Law model using the equation below:

$$\tau_w = -\frac{1}{2} R \frac{dp}{dz} = \frac{1}{2} R \left[\frac{2^{n+2} \left(\frac{3n+1}{n}\right)^n K {v_3}^n}{{D_3}^{n+1}} \right] \tag{12}$$

3.6.2 LIVE/DEAD results

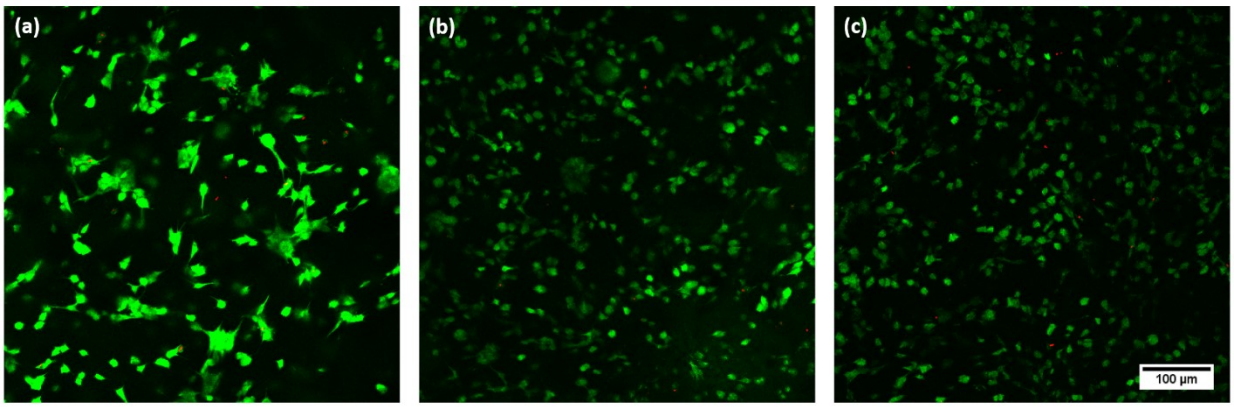

Figure S3.3 LIVE/DEAD images for bioprinted structures using 20G needle. NCs from: (a) donor 2 (age 26 years); (b) donor 3 (age 23 years); and (c) donor 1 (age 28 years).

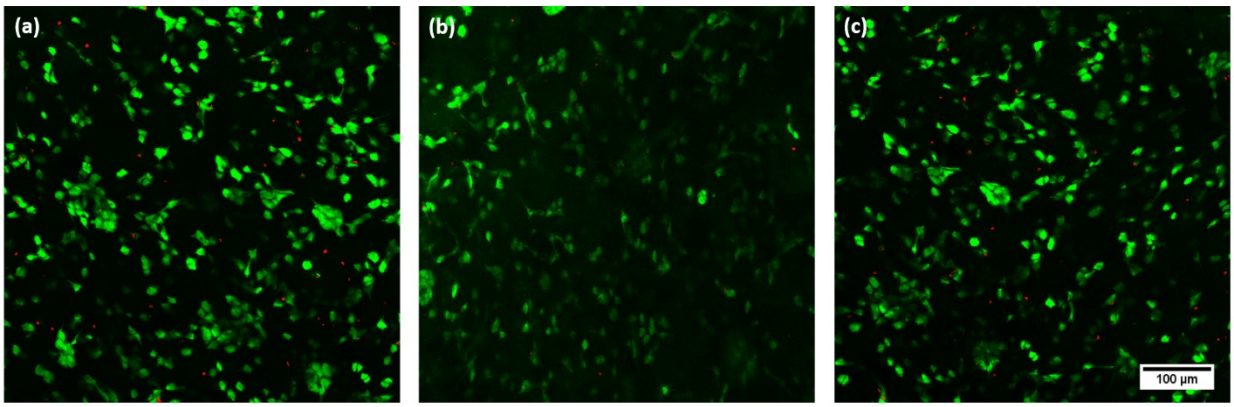

Figure S3.4 LIVE/DEAD images for bioprinted structures using 22G needle. NCs from: (a) donor 2 (age 26 years); (b) donor 3 (age 23 years); and (c) donor 1 (age 28 years).

3.6.3 Donor Information

Donor information of tissue engineered cartilage is shown in Table S3.1 . Donor information for the native cartilage control is shown in

Table S3.2

Table S3.1 Donor information for bioprinted cartilage

Donor	Biological sex	Age	Medical history	Days in P1	Days in P2
1	Male	28	Deviated septum, hypertrophied turbinate	5	4
2	Male	26	Deviated septum, hypertrophied turbinate	5	4
3	Male	23	Unknown	6	4
4	Male	28	Nasal obstruction	6	4

Table S3.2 Donor information for native nasal septal cartilage as positive controls

Donor	Biological sex	Age	Medical history
1	Male	29	Nasal obstruction
2	Male	26	Nasal obstruction
3	Male	18	Unknown
4	Male	28	Right chronic rhinosinusitis
5	Male	22	Deviated nasal septum
6	Male	19	Deviated nasal septum

3.6.4 Bern score – a semi-quantitative scale to evaluate neocartilage

Bern Score is a semi-quantitative scaling method to evaluate the Safranin O-Fast green stained neocartilage[357]. The Bern score was evaluated by 7 blinded observers: 2 trained lab technicians, 3 PhD trainees, 1 postdoc trainee, and 1 professor, all working in orthopedic basic research lab) are shown in Supplementary Table S3.

Table S3.3 Bern scores from 6 blinded observers

	Donor	**Uniformity and Darkness of Safranin O-fast green staining**	**Distance between cells of matrix accumulation**	**Cell morphology represented**	**Total Score**
Observer 1	Donor 1	3	3	3	9
	Donor 2	3	3	3	9
	Donor 3	3	3	3	9
	Donor 4	3	3	3	9
	Native Tissue	3	3	3	9
Observer 2	Donor 1	3	3	3	9
	Donor 2	3	3	3	9
	Donor 3	3	3	3	9
	Donor 4	2.5	3	2.5	8
	Native Tissue	3	3	3	9
Observer 3	Donor 1	3	3	3	9
	Donor 2	3	2.5	2.5	8
	Donor 3	3	3	3	9
	Donor 4	2.5	2.5	2.5	7.5
	Native Tissue	3	3	3	9
Observer 4	Donor 1	3	3	3	9
	Donor 2	3	2.5	3	8.5
	Donor 3	3	3	3	9
	Donor 4	3	3	3	9
	Native Tissue	3	3	3	9
Observer 5	Donor 1	3	3	3	9
	Donor 2	3	3	3	9
	Donor 3	3	3	3	9
	Donor 4	3	3	2.5	8.5
	Native Tissue	3	3	3	9
Observer 6	Donor 1	3	3	3	9
	Donor 2	3	3	3	9
	Donor 3	3	3	3	9
	Donor 4	3	3	3	9
	Native Tissue	3	3	3	9

CHAPTER 4. *In vitro* maturation and *in vivo* stability of bioprinted human nasal cartilage

Contributing authors: Xiaoyi Lan, Yan Liang, Margaret Vyhlidal, Esra J.N. Erkut, Melanie Kunze, Aillette Mulet-Sierra, Martin Osswald, Khalid Ansari, Hadi Seikaly, Yaman Boluk, Adetola B. Adesida

Chapter 4 has been published in parts as: Xiaoyi Lan, Yan Liang, Margaret Vyhlidal, Esra JN Erkut, Melanie Kunze, Aillette Mulet-Sierra, Martin Osswald, Khalid Ansari, Hadi Seikaly, Yaman Boluk, and Adetola B Adesida, "*In vitro* maturation and *in vivo* stability of bioprinted human nasal cartilage" Journal of Tissue Engineering, vol.13, p.20417314221086368, 2022.

4.1 Introduction

Non-melanoma skin cancers (NMSCs), including basal cell carcinoma (BCC) and squamous cell carcinoma (SCC), are the most frequent malignant skin cancers in the Caucasian population[380, 381]. Since 1960, it has been reported that there has been a 3-8% yearly increase in the incidence of NMSCs worldwide[380]. In the USA, it's estimated that the incidence of NMSCs is more than 1,000,000 cases per year[380]. Among the NMSCs cases, roughly 36% include the nasal alar lobule, which accounts for the highest regional frequency[6]. Therefore, it is not uncommon for the fibromuscular tissue around the alar lobule and nasal septal cartilage to be removed during tumor resection to establish clear margins[6]. After the tumor resection, nasal reconstructive surgery is usually necessary for restoring structural support and facial aesthetic[6, 322, 323, 382]. In particular, the critical structural support restoration step during nasal reconstruction is currently achieved by inserting an allogeneic, synthetic, or autologous cartilage graft[6]. Despite being clinically used; these materials have shown drawbacks that are yet to be resolved.

Allogeneic grafts are decellularized specimens that have been harvested from live or cadaveric donors. These grafts appear attractive since they are biocompatible and theoretically non-immunogenic[383]. However, the main drawback of allogeneic grafts is their high resorption rates. It was found that allogeneic costal cartilage grafts experienced a resorption rate of 31%[384] compared to 3% in the autologous tissue[385]. Synthetic grafts have also been explored due to their low immunogenicity and lack of donor-site morbidity. Materials that commonly have been used include silicon, porous high-density polyethylene (MedPor), or expanded polytetrafluoroethylene (Gore-tex)[386]. The drawbacks of synthetic materials, however, include infection, resorption, dislocation, and extrusion. For instance, the infection rate that has been associated with silicone, MedPor, and Gore-tex grafts are 3.9%, 20%, and 5.3% respectively[386]. Autologous grafts are

currently the golden standard used in nasal reconstructive surgery due to the absence of immunogenicity[6]. However, due to a lack of septal cartilage, sourcing cartilage from other body parts such as the ear and ribs, is common. Extracting cartilage from other areas presents the issue of donor-site morbidity. Also, some extracted tissues are considered to have inferior handling qualities and present the issue of warping (such as with costal cartilage)[387].

More recently, cell-based engineered cartilage grafts have shown the potential to overcome these drawbacks associated with the use of conventional cartilage grafts[3, 6]. Previous studies have shown that dedifferentiated NCs are a promising cell source with a redifferentiation capacity to generate hyaline-like cartilages[6, 23, 64, 388-390]. A large number of autologous NCs can be generated from a small cartilage biopsy taken from the nasal septum by expanding the cells in the presence of specific growth factors and autologous serum[3, 6]. Together with appropriate biomaterials, biochemical factors, and mechanical stimuli, it is possible to achieve cellular differentiation and thus, cartilage graft generation that can be subsequently implanted without an immune reaction[3, 6]. The first human trial implementations of engineered cartilage from NCs using the clinically approved collagen scaffold, Chondro-Gide, have already been successfully demonstrated[6]. However, despite these early successes, there are still some prominent drawbacks associated with the use of engineered constructs, such as the limited shapes of commercially available scaffolds and the inhomogeneous distribution of NCs during manual dispersion of NCs.

Three-dimensional (3D) bioprinting approaches allow a rapid additive fabrication of patient specific, anatomically, or surgical ready shaped engineered functional tissue by cooperate tissue engineering technique[79, 80]. Through computer aided design (CAD) tools, the 3D bioprinting process enables the precise dispensation of the hydrogels and living cells (known as bioink)

from a movable printing head into a biomimetic scaffold with homogeneous cell distribution[83, 332]. Bioink can be considered one of the most important aspects of the bioprinting process since an ideal bioink should satisfy both cell compatibility for tissue regeneration and printability to support the printing process. In 3D bioprinting of nasal cartilage, bioinks that are successfully used in 3D bioprinting application include natural polymers such as collagen[215], gelatin[391], alginate[130], cellulose[146, 149, 264, 392], agarose[393].

To this date, the results from recent research did not provide enough *in vivo* evidence that customized 3D bioprinted engineered nasal cartilage could achieve similar clinical promises to that of the commercial Chondro-Gide scaffold[146, 389, 392]. In the work of Yi et al., a 3D-printed PCL scaffold using human adipose stem cell-laden cartilage-derived hydrogels, was implanted subcutaneously in a nude mice model[389]. Unfortunately, the *in vivo* stability of the constructs, including calcification, vascularization, and bone formation, were not studied. Gatenholm's group utilized cellulose-based hydrogels with NCs to bioprint neocartilages which were implanted in a mice model[146, 392, 394]. Yet, the quantitative biochemical and biomechanical data, and *in vivo* stability were not reported in this study.

In our previous study, we successfully generated engineered nasal septal cartilage using type I collagen hydrogel via the freeform reversible embedding of suspended hydrogels (FRESH) bioprinting method, where the *in vitro* biochemical results highly resembled that of native tissue[215]. To further support its potential for clinical application and formation of patient-specific surgical - ready shapes, the mechanical characterization and *in vivo* stability of the engineered nasal cartilage substitutes is needed. Herein, we first demonstrated the ability to 3D bioprint patient-specific lower lateral cartilage from Computed tomography (CT) scans. We then investigated the effects of chondrogenic culture on the biochemical and mechanical properties of

bioprinted constructs of NCs *in vitro* and *in vivo* in nude mice. Engineered nasal cartilage from NCs seeded on clinically approved type I/III collagen membrane scaffolds (Chondro-Gide) served as a control.

4.2 Materials and Methods

4.2.1 Ethics

Human nasal septal cartilage specimens were collected from surgical discards of patients undergoing nasal reconstructive surgeries with the approval of the University of Alberta's health research ethics board – biomedical panel (Study ID: Pro00018778). The animal research work was conducted and approved in accordance with the protocol approved by the University of Alberta Animal Care User Committee (Study ID: AUP00001363).

4.2.2 Human nasal chondrocyte isolation

Human nasal septal cartilage specimens were collected from 6 male donors undergoing septoplasty or rhinoplasty. Donors ranged from 21 to 48 years old with a mean ± standard deviation (SD) of 32.83 ± 10.49 years (refer to Table 4.1 for donor information). The isolation and expansion of NCs were performed as previously described[395]. In brief, nasal cartilage specimens were digested with 0.15% (w/v) collagenase II solution (300 units/mg) for 22 hours at 37°C in an incubating shaker. NCs were then harvested and plated at a density of 10^4 cells/cm^2 and cultured in a standard medium: Dulbecco's Modified Eagle Medium (DMEM) supplemented with 10% (v/v) FBS, 1 ng/ml of transforming growth factor beta 1 (TGF-β1), and 5 ng/ml of fibroblast growth factor 2 (FGF-2) in a normoxic humidified incubator (21% O_2, 5% CO_2). The media was changed twice per week. The gross morphology of the nasal chondrocytes during the monolayer

expansion are shown in Figure S4.1. Passage 2 (P2) cells were used for bioprinting. The population doubling (PD) of NCs for each donor were calculated by the equation: $PD = \log_2 (population_{final} / population_{initial})$ for each passage. The cumulative PD (CPD) is the sum of PD at passage 1 and passage 2. The CPD reflects the total number of times primary NCs from the donors have doubled. The CPD and CPD/day for each donor is provided in Table S4.1.

Table 4.1. Donors Information

Donor	**Biological Sex**	**Age**	**Medical History**	***In vivo* Implantation**
1	Male	21	Asthma	Yes
2	Male	25	Deviated Septum	No
3	Male	30	N/A	Yes
4	Male	30	Deviated Septum	No
5	Male	43	Deviated Septum	No
6	Male	48	N/A	Yes

4.2.3 Nasal chondrocyte-laden bioink preparation

NCs were trypsinized and resuspended in a defined serum-free chondrogenic media (SFM) composed of DMEM, 100 U/ml penicillin and streptomycin with 2 mM L-glutamine (Life Technologies, all), 100 mM HEPES, insulin-transferrin-selenium (ITS) +1, 0.1 μM dexamethasone, 0.1 mM ascorbic acid 2-phosphate and 0.1 mM L-proline at a concentration of 0.875×10^7 cells/ml. The cell suspension was diluted in a 1:10 ratio with type I collagen gel (3.5wt%, Lifeink 200,

Advanced Biomatrix, LOT: 5202-1KIT, USA) to create a final concentration of 8.75x106 cells/ml. The resulting cell-laden bioink is a neutralized type I collagen solution that is thermo-responsive and can polymerize at 37 ºC.

4.2.4 3D bioprinting of type I collagen hydrogels and cell seeding of Chondro-Gide scaffolds

The bioink is then used to fabricate patient-specific lower lateral nasal cartilage shapes, using a micro-extrusion base bioprinter INKREDIBLE+ (CELLINK, Sweden). The sterile gelatin support bath (LifeSupport, Advanced Biomatrix, USA) was prepared according to the manufacturer's instructions. The filaments and the microstructures of the printed constructs were pre-defined in a 3D bioprinting software (Slic3r, USA). A CT-scanned patient-specific right lower lateral nasal cartilage with 90% infill rate, was first bioprinted inside support bath using type I collagen bioink, to show the printability of autologous cartilage. In order to compare the mechanical and *in vivo* behaviors of the bioprinted constructs with the cell-seeded clinically approved Chondro-Gide scaffolds, the collagen bioink was the bioprinted into a strip shape with a dimension of 25 mm length * 6 mm width * 2 mm height (same dimensions as Chondro-Gide). These 3D bioprinted cell-laden strip shaped constructs were then cultured in serum-free chondrogenic medium (4 ml per construct and changed twice per week) in normoxia for 3, 6, and 9 weeks.

Clinically approved type I/III collagen membrane scaffolds (Chondro-Gide, Geistlich Pharma, Wolhusen, Switzerland) served as the control group. Chondro-Gide scaffolds (25mm (length) x 6mm (width) x 2 mm (thickness)) were cut with scalpels from the same lot to control the lot-to-lot variability. 2.625 million NCs were seeded onto the porous side of the scaffolds (same cell

number as bioprinted scaffold) and then cultured in 4ml of defined serum-free chondrogenic medium with TGF-β3. The schematic experimental setup is shown in Figure 4.1.

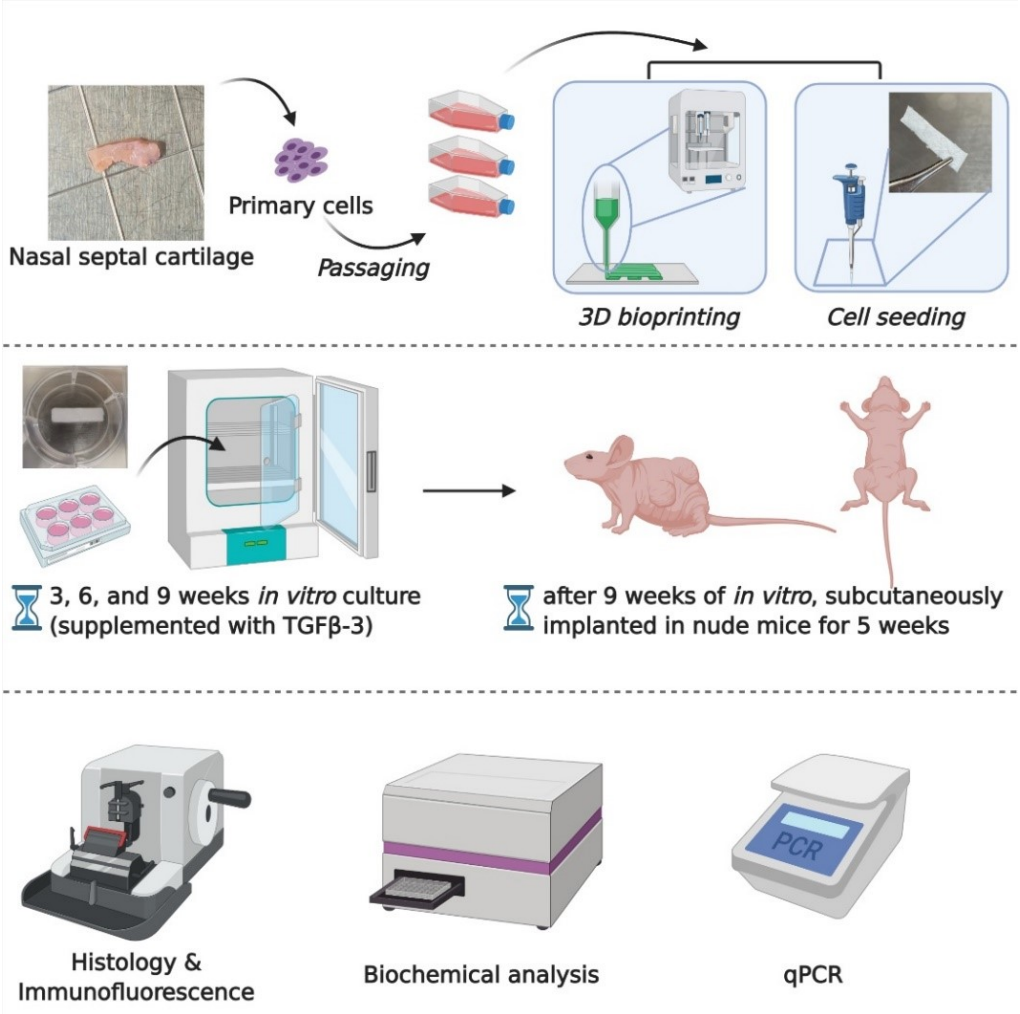

Figure 4.1. Schematic diagram of experimental design

4.2.5 Culture condition

4.2.5.1 *In vitro* culture condition

Both 3D bioprinted type I collagen hydrogel constructs and Chondro-Gide scaffolds (control group) were cultured in normoxic humidified incubators. Media changes were performed twice a

week (5mL per change). To provide sufficient time for the constructs and scaffolds to develop mechanical strength before *in vivo* culture, three culture periods were first evaluated, including 3 weeks, 6 weeks, and 9 weeks. Only the constructs and scaffolds cultured from one of the selected periods, which showed best mechanical strength and chondrogenic phenotype, were then subjected to further *in vivo* study.

4.2.5.2 *In vivo* culture condition

To study the *in vivo* behavior of engineered nasal cartilage, the *in vitro* cultured bioprinted type I collagen hydrogel constructs and Chondro-Gide scaffolds were divided into two experimental groups (n=3, three donors). Experimental group I involved five additional weeks of *in vivo* culture after being implanted subcutaneously in nude mice, whereas experimental group II involved five additional weeks of *in vitro* culture in chondrogenic media to serve as a comparison group.

For experimental group I, the *in vitro* cultured constructs and scaffold was first cut into smaller sizes to reduce the size of the implants. Then *in vitro* cultured constructs and scaffolds were implanted into the back of athymic CD-1 nude mice (n=7, seven mice, six-week-old, Charles River, Wilmington, USA) as previously described[64]. Each mouse received a pair of *in vitro* cultured bioprinted construct and Chondro-Gide scaffold, and the engineered cartilage from same experimental group were implanted in different mice. Six nude mice were implanted with the engineered nasal cartilages, with a total of 6 bioprinted constructs and 6 Chondro-Gide scaffolds. One additional mouse served as a control and received empty scaffolds (cultured bioprinted construct and Chondro-Gide scaffold without cells). Two small caudal subcutaneous incisions (4-5 mm) were dissected on the skin of each mouse. The constructs and scaffolds were then implanted in the subcutaneous pockets. Incisions were closed with suture and cyanoacrylate tissue

adhesive. No post-surgical complications were observed. Five weeks following the implantation, the mice were euthanized by CO_2 inhalation, and the constructs and scaffolds were macroscopically dissected from the murine subcutaneous tissues. Gross morphology pictures were taken before and after implantation.

4.2.6 Live/Dead Assay

Cell viability analysis was conducted using a live/dead viability kit (ThermoFisher, USA). The *in vitro* cultured constructs and scaffolds from 3 donors (at day 0, 3 weeks, 6 weeks, and 9 weeks of culture) were incubated in 1 ml of 4 μM Calcein AM and 1 ml of 2 μM ethidium homodimer-1 solution at room temperature in the dark for 30 minutes. They were then examined under a Nikon con-focal laser scanning microscope (Leica TCS SP5, German). The cell viability was quantified using Fuji Image J software.

4.2.7 Evaluation of cartilage formation

4.2.7.1 Sulfated glycosaminoglycans per DNA quantification

To measure the glycosaminoglycan (GAG) matrix content and the DNA content of the *in vitro* cultured engineered cartilages, the bioprinted constructs and Chondro-Gide scaffolds were weighed, cut into smaller pieces, and rinsed twice with Phosphate Buffered Saline (PBS), and then frozen at -80 °C. They were then thawed and digested in Proteinase K solution (1 mg/ml) at 56 °C overnight for 16 hours.

The GAG matrix content of the engineered cartilages was measured by a 1,9-dimethylmethylene blue (DMMB, Sigma Aldrich, Canada) assay with chondroitin sulfate (Sigma Aldrich, Canada)

used as the internal standard[396]. The GAG contents were evaluated on the V-max kinetic microplate reader (Molecular Devices, USA) at a wavelength of 530 nm.

The DNA contents were measured using the CyQUANT Cell Proliferation Assay Kit (Thermo Fisher). Calf thymus DNA (Sigma) was used as the standard. Fluorescence emission was measured at 580 nm (excitation 450 nm). The DNA contents were measured on a CytoFluor II fluorescence multi-well plate reader (PerSeptive Biosystems).

The quantity of GAG was then normalized to the total DNA content and wet weight of each engineered cartilage for the 6 donors.

4.2.7.2 Histology and Immunofluorescence

For both *in vitro* and *in vivo* engineered cartilages, the samples were fixed in 10% (v/v) neutral buffered formalin at 4°C overnight, dehydrated through a series of alcohol washes, and then embedded in paraffin wax. The embedded samples were sectioned into 5 um thick slices and deparaffinized by xylene substitute. The sliced sections were rehydrated through a graded series of ethanol (100%, 96%, 70% and 50% (v/v)), and rinsed in distilled water. Then, the prepared samples were evaluated for histology staining including Safranin-O/Fast Green, Masson Trichrome, and Alizarin Red, as well as immunofluorescence stains including type I and II collagen, type X collagen, CD31, Bone Sialoprotein (BSP), and F4/80 (BM8). Imaging was carried out using Nikon Eclipse Ti-S microscope coupled to a DS-U3/Fi2 Color CCD camera using 100x objective lenses.

For Safranin-O/Fast Green assessment, the prepared samples were stained with Meyer's Hematoxylin, Green FCF, and Safranin-O. For Masson Trichrome assessment (NovaUltra™ Masson

Trichrome Stain Kit, USA.), the samples were stained with Weigert's Iron Hematoxylin, Biebrich Scarlet-Acid Fuchsin, phosphomolybdic-phosphotungstic acid, aniline blue, and acetic acid solutions. For Alizarin red assessment, the samples were immersed in 2% (w/v), pH 4.1-4.3 Alizarin red (Sigma-Aldrich, Canada) solution for 2.5 minutes. After each of the histology staining, the stained slides were rinsed with distilled water and then dehydrated again with ethanol (95% (v/v) and 100%). The slides were mounted with mounting media (Richard-Allan Scientific, Thermo Scientific) to prepare for imaging.

Type I and II collagen protein expressions were examined by immunofluorescence. The slides were first de-paraffinized, rehydrated and then subjected to antigen retrieval methods including the use of protease XXV (AP-9006-005 from Thermo Scientific) and hyaluronidase (H6254 from Sigma-Aldrich). After antigen retrieval, slides were incubated with rabbit anti-type I collagen (CL50111AP-1, Cedarlane, Canada) and mouse anti-type II collagen, both primary antibodies are diluted in 1:200 ratio (II-II6B3, Developmental Studies Hydroma Band, USA.) overnight to allow for type I and II collagen bindings, respectively. Secondary antibodies (goat anti-rabbit IgG Alexa Fluor 594, ab150080; goat anti-mouse IgG Alexa Fluor 488, ab150117; Abcam, USA.) were incubated with the slides for 45 minutes, both secondary antibodies are diluted in 1:200 ratio. Sectioned slides were additionally stained with 4',6-diamidino-2p-phenylindole (DAPI, ThermoFisher, USA) for 20 minutes at room temperature to observe the nuclei of NCs within each sample. Sections were mounted with 1:1 Glycerol: PBS to prepare for imaging. The same DAPI staining and mounting methods applies to all immunofluorescence staining preparations.

The protein expression of type X collagen was also examined by immunofluorescence. The antigen retriever steps are similar as the type I/II immunofluorescence. Slides were incubated

overnight with rabbit anti-type X collagen antibodies in 1:100 dilution ratio (rabbit polyclonal to type X collagen, ab58632, Abcam, USA) to bind type X collagen and subsequently labeled by secondary antibody (goat anti-rabbit IgG Alexa Fluor 594, ab150080, Abcam, USA).

Immunofluorescence imaging was also used to assess the vascular invasion protein, CD31. For antigen retriever, the slides were incubated in the 0.01M of citric acid at a high temperature (around 90-100 °C) for 10 minutes. The primary antibody used was anti-mouse CD31 (CD31/PECAM Biotinylated Antibody, BAF3628, R&D systems, USA) in 1:100 dilution ratio, then Alexa Fluor 488 conjugated streptavidin in 1:100 dilution ratio (S32354, Life Technology, USA) was used to label the biotinylated primary antibody.

Immunofluorescence was further used to examine the bone associated protein, bone sialoprotein (BSP). The antigen retriever steps are similar as the type I/II immunofluorescence. The primary antibody was anti-bone sialoprotein, diluted in 1:100 ratio (ab195426, Abcam, USA), and was labeled by secondary antibody, goat anti-rabbit IgG Alexa Fluor 594 (ab150080, Abcam, USA) in 1:200 dilution ratio.

The F4/80 (BM8) molecule, solely expressed on the surface of macrophages, was examined by immunofluorescence. Following antigen retrieval described by Lee et al[397], slides were incubated with Biotinylated F4/80 (BM8) primary antibody (13-4801-82, ThermoFisher Scientific, Canada) in 1:100 dilution ratio. Slides were then incubated with streptavidin in 1:100 dilution ratio (S32354, Life Technology, USA), Alexa Fluor 488 conjugate in 1:200 dilution ratio (S32354, Life Technology, USA) prior to imaging.

4.2.7.3 Real-time RT-qPCR

RT-qPCR was used to measure relative gene expression of chondrogenic (e.g., *ACAN, COL2A1, SOX9*), fibrogenic (*e.g., COL1A2*), hypertrophic (e.g., *COL10A1, RUNX2*), and angiogenic markers (e.g., *PPARγ*), of NCs after 3, 6, and 9 weeks of culture. Expression of the collagen cross linking enzyme (*LOX*) was also analyzed by RT-qPCR at each of the culture times. Total RNA was extracted with Trizol reagent (Life Technologies) according to the manufacture instructions. RNA was immediately transferred to Trizol upon harvesting to prevent changes in gene expression. The purity and concentration of isolated RNA were examined with Nanodrop One C. 100ng total RNA was reverse transcribed to cDNA by GoScript reverse transcriptase (Promega Corporation, WI, USA.) with 1 μg of oligo (Dt) primers (Promega Corporation, WI, USA). RT-qPCR was performed as we have previously described[398] (primers sequences are presented in Table 4.2). The mRNA expression levels for each primer set were normalized to the housekeeping genes, β-actin (*ACTB*), Beta-2 microglobulin (*B2M*) and Tyrosine 3-Monooxygenase/Tryptophan 5-Monooxygenase Activation Protein Zeta (*YWHAZ*), using the $2^{-\Delta Ct}$ method. The use of multiple housekeeping genes helps to increase the accuracy and reliability of the results, as it allows researchers to confirm that the normalization of the data is not affected by the specific housekeeping gene chosen[399].

Table 4.2. Primer Sequences for Real-Time RT-qPCR

Genes	Forward Primer (5′)	Reverse Primer (3′)
Beta-actin (*ACTB*)	AAGCCACCCCACTTCTCTCTAA	AATGCTATCACCTCCCCTGTGT
Beta-2 microglobulin (*B2M*)	TGCTGTCTCCATGTTTGATGTATCT	TCTCTGCTCCCCACCTCTAAGT
Tyrosine 3-Monooxygenase/Tryptophan 5-monooxygenase activation	TCTGTCTTGTCACCAACCATTCTT	TCATGCGGCCTTTTTCCA

protein Zeta (*YWHAZ*)		
Aggrecan (*ACAN*)	AGGGCGAGTGGAATGATGTT	GGTGGCTGTGCCCTTTTTAC
type I collagen (*COL1A2*)	GCTACCCAACTTGCCTTCATG	GCAGTGGTAGGTGATGTTCTGAGA
type II collagen (*COL2A1*)	CTGCAAAATAAAATCTCGGTGTTCT	GGGCATTTGACTCACACCAGT
SRY-Box 9 (*SOX9*)	CTTTGGTTTGTGTTCGTGTTTTG	AGAGAAA-GAAAAAGGGAAAGGTAAGTTT
Collagen X (*COL10A1*)	GAAGTTATAATTTACAC-TGAGGGTTTCAAA	GAGGCACAGCTTAAAAGTTTTAAACA
Runt related transcription factor 2 (*RUNX2*)	GGAGTGGACGAGGCAAGAGTTT	AGCTTCTGTCTGTGCCTTCTGG
Peroxisome proliferative activated receptor gamma (*PPARγ*)	AAGCTGCTCCAGAAAATGACAGA	CGTCTTCTTGATCACCTGCAGTA
Lysyl Oxidase Like 2 (*LOXL2*)	ACGGCCACCGCATCTG	TCCGTCTCTTCGCTGAAGGA

4.2.8 Mechanical properties of cell seeded Chondro-Gide scaffolds and bioprinted constructs

After 3, 6, and 9 weeks of chondrogenic culture, suture tests were performed for both type of engineered cartilages at each time point. Briefly, to test the durability of the cartilages, a single 5-0 PROLENE suture was introduced through each engineered cartilage and a knot was tied. Subsequent knots were then made if the cartilages were strong enough.

Three-point bending results were measured by Dynamic Mechanical Analysis Q800 (TA instrument, USA). Small 5 mm three-point bending clamps were used for the test. Engineered cartilage tissues were placed on top of the 5mm stationary clamp, and a movable clamp moving 0.1N/s was used to measure the force responses. The bending modulus is determined by the Equation:

$$E = \frac{\Delta F}{\Delta d} \frac{l^3}{48 I^3}$$

where F is the applied force, and d is the bending deflection in the force direction. I is the second moment of area of the beam. The bioprinted cartilage and the Chondrogide scaffold were assumed as a rectangular section with width b and height d. The second moment of area is determined below:

$$I = \frac{bd^3}{12}$$

4.2.9 Microstructure of cell seeded Chondro-Gide scaffolds and bioprinted constructs

The ultrastructure of the 3D bioprinted constructs and Chondro-Gide scaffolds at each *in vitro* culture period (3, 6, and 9 weeks) were investigated by scanning electron microscopy (SEM, Hitachi, JA, Model S-4800). All reagents and accessories used were from Electron Microscope Science, PA, USA. Each construct and scaffold were fixed with 2 % (v/v) glutaraldehyde and 2.5% (v/v) paraformaldehyde in sodium cacodylate trihydrate buffer at 4 ºC overnight. Constructs and scaffolds were then cut in half using scalpels and washed with Milli-Q water twice for 2 minutes each the next day. The constructs and scaffolds were then post fixed in 2% (w/v) osmium tetroxide (OsO_4) and 2% (w/v) tannic acid. Post fixing and dehydration steps were as we have previously described[395]. The images of the engineered cartilages were captured using SEM (Zeiss Sigma 300 VP-FESEM).

4.2.10 Semi-quantitative Analysis

Safranin-O staining of *in vitro* engineering cartilages is evaluated using the Bern score semi-quantitative method, which accounts for uniformity and darkness of the staining, the distance

between cell and matrix, as well as cell morphology. In this study, the Bern scores are evaluated by four blinded observers [400].The immunofluorescence staining of Type I and II collagens is semi-quantified using python. The immunofluorescence intensities are normalized by cell number (DAPI).

4.2.11 Data Analysis and Statistical Methods

For biochemistry, gene expression, and mechanical test analysis, a repeated measures two-way analysis of variance (RM-ANOVA) test was used to assess for interaction between culture time and scaffold type. Culture time and scaffold type were treated as within-subject factors, the donors were treated as repeated measurements. If the interaction was non-significant, the main effects of culture time and scaffold type were reported. If the interaction was significant, the p-value was reported. Bonferroni post hoc tests were performed for the pairwise comparisons to compare within culture time and scaffold type. Cell viability was analyzed by pairwise comparisons between day 1 and 3 weeks, 3 weeks and 6 weeks, 6 weeks, and 9 weeks. Data are presented as mean $\pm$ SD. All analyses were performed using GraphPad Prism 8. A p-value of $p<0.05$ was considered statistically significant. A p-value between 0.05 and 0.1 was considered borderline significant.

4.3 Results

4.3.1 3D bioprinting of engineered cartilage with autologous shapes

A patient-specific right lower lateral nasal cartilage was bioprinted using the FRESH method to demonstrate the ability of fabricating autologous shaped cartilages. Figure 4.2A shows the STL image generated from CT, and the internal structure of the bioprinted cartilage in Figure 4.2B.

Figure 4.2C and Figure 4.2D show the 3D bioprinted nasal cartilage before and after the gelatin support bath melted, respectively. As temperature increased to 37°C, the construct printed in the FRESH support bath started to dissolve and caused the bioprinted collagen bioink to self-assemble and form a hydrogel to maintain its structural integrity.

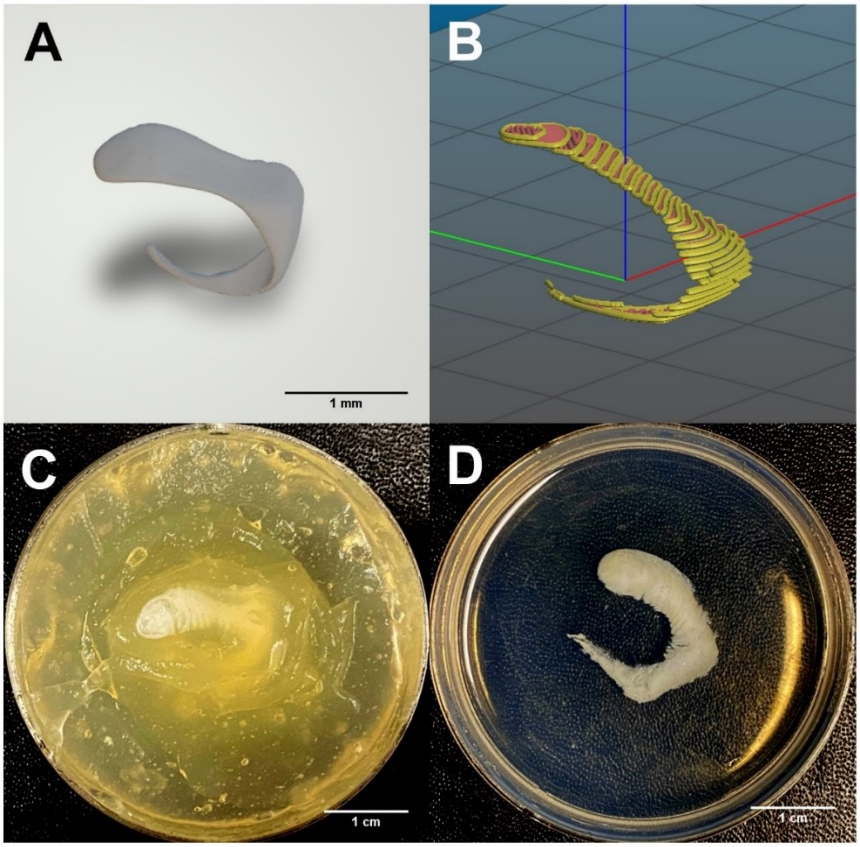

Figure 4.2. Gross morphology of the FRESH printed structure. (A) 3D model of a right lower lateral nasal cartilage from CT imaging and (B) the preview of the sliced nasal cartilage using Slic3r software. (C) 3D bioprinted lower lateral nasal cartilage in gelatin support bath before and (D) after 30 minutes incubation in 37 °C. Following the 30-minute incubation, the support bath was aspirated, and PBS was added.

4.3.2 Live/Dead analysis of bioprinted constructs

A Live/Dead fluorescent assay was used to assess the cell viability of the constructs following 3D bioprinting. The cell viability of constructs cultivated for 1 day, 3 weeks, 6 weeks, and 9 weeks were 85.5±3.9, 93.9±2.3, 93.8±3.1, 87.9±4.9, respectively (Figure 4.3). Post-hoc test for

the interested groups were conducted between day 1 and 3 weeks, 3 weeks and 6 weeks, and 6 weeks and 9 weeks. There was no significant difference in cell viability between 3 weeks and 6 weeks of culture (p=0.9765). Between 1 day and 3 weeks (p=0.0133), and 6 weeks and 9 weeks (*p=0.0370*), a significant increase and decrease in cell viability was observed, respectively.

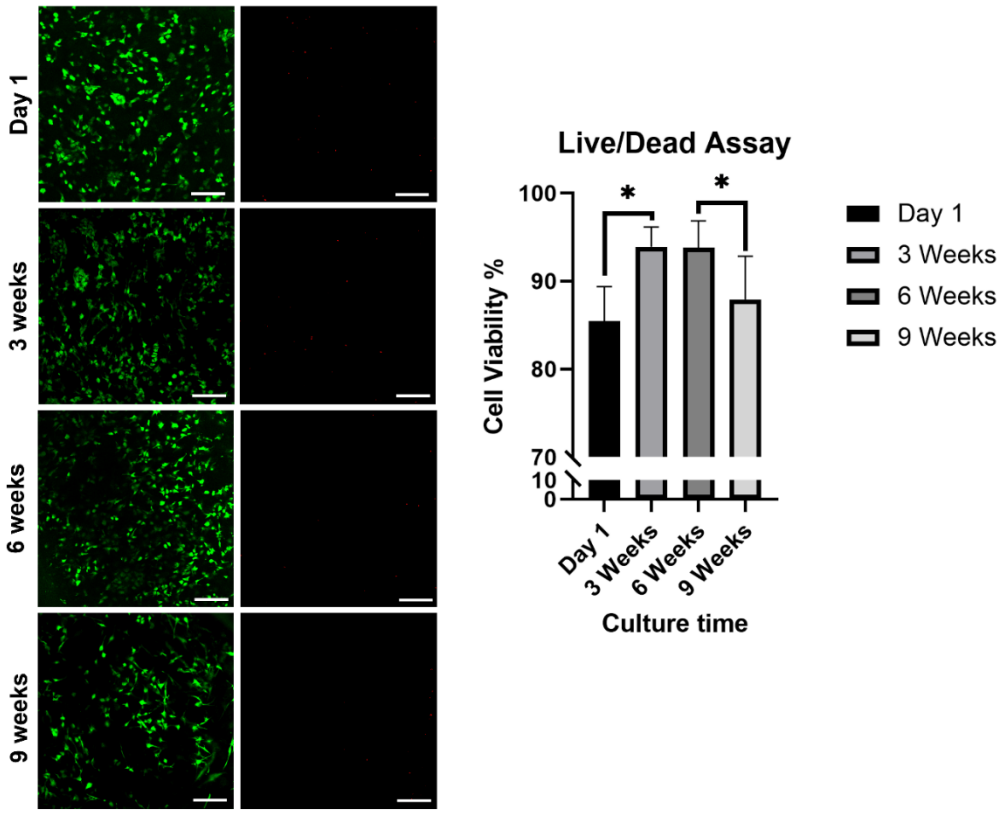

Figure 4.3. (a) Live/dead assay (b) cell viability over culture time. Paired t-tests were done to compare cell viability between Day 1 vs. 3 weeks, 3 weeks vs. 6 weeks, and 6 weeks vs. 9 weeks. * Represents 0.01<p <0.05. Scale bar: 100µm

4.3.3 Histological analysis of *in vitro* engineered cartilages

After 3, 6, and 9 weeks of chondrogenic culture, bioprinted, Chondro-Gide, and non-cellular cartilages, were processed, embedded in paraffin, cut, and then stained with Safranin-O/Fast Green staining and Masson Trichrome staining. Safranin-O was used to stain sulphated proteoglycans while Fast Green served as a counter stain for protein[401]. Weigert's Hematoxylin,

Aniline blue, and Biebrich scarlet-acid fuschin of the Masson Trichrome stain, were used to stain for nuclei, collagen, and cytoplasm/keratin, respectively[402]. Empty scaffolds did not show evidence of matrix synthesis, denoted by the absence of positive Safranin-O staining for proteoglycans. Only background staining for Fast Green was present in empty scaffolds. Chondro-Gide scaffolds were shown to have two different layers following Safranin-O/Fast Green staining, corresponding to the compact and porous layers. The porous layer was the cell seeding side. At 3 weeks of culture, both bioprinted constructs and Chondro-Gide scaffolds showed proteoglycan rich matrix deposition denoted by positive Safranin-O staining (Figure 4.4A). As culture time increased from 3 to 9 weeks, the intensity of Safranin-O staining increased in both engineered cartilages (Figure 4.4A, Safranin-O for all donors after 3, 6, 9 weeks culture are shown in Figure S4.2, Figure S4.3, and

Figure S4.4, respectively).

For the Masson Trichrome staining, the empty bioprinted constructs showed only faint blue staining for collagen. Chondro-Gide empty scaffolds, however, showed both Aniline blue and Scarlet red staining corresponding to collagen and cytoplasm/keratin, respectively. The layers staining red, and blue were the compact and cell seeding layers, respectively. Collagen deposition was consistent with Safranin-O staining and appeared at 3 weeks in both engineered cartilages (Figure 4.4B). The enhanced red staining and size of the Chondro-Gide scaffolds at 3 weeks, compared to the empty scaffold, was likely due to swelling of the scaffolds due to proteoglycan deposition. Bioprinted constructs overall, showed a more homogeneous distribution of ECM throughout the structure than Chondro-Gide. Since cells were only seeded on the porous surface of each Chondro-Gide scaffold, matrix deposition was limited to the porous surface. To characterize the collagen distribution, immunofluorescence for type I and II collagen

was performed. Type I and II collagens were observed in both bioprinted constructs and Chondro-Gide scaffolds across the three culture times (Figure 4.5A, and Figure S4.6A). Type II collagen was predominantly expressed in both engineered cartilages and was more homogeneous in bioprinted constructs. The intensity of type II collagen expression became more pronounced as culture time increased, which was consistent with Aniline blue (Figure S4.6B). The distribution of type II collagen expression was also like Aniline blue positive matrix formation in both the bioprinted constructs and Chondro-Gide scaffolds. Additionally, to assess for the presence of a bone forming phenotype, hypertrophic collagen marker, type X collagen, immunofluorescence was performed. Type X collagen was observed in both bioprinted constructs and Chondro-Gide scaffolds across the three culture times (Figure 4.5B, and Figure

S6a). Similarly, to type II collagen, the expression of type X collagen became more pronounced with culture time (Figure S4.6B).

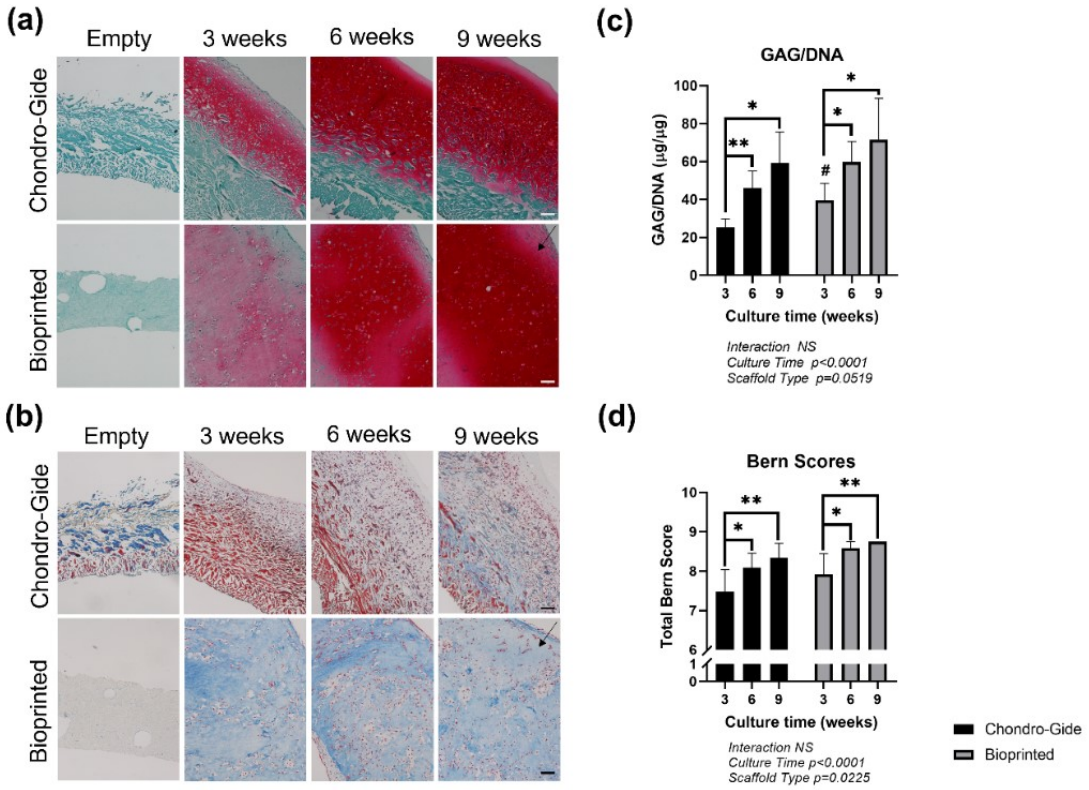

Figure 4.4. Histological and biochemical analysis of *in vitro* constructs across culture time. (a) Safranin-O/Fast green Staining, (b) Masson's Trichrome staining, and (c) GAG/DNA of *in vitro* constructs. Black arrows indicate tissue areas that have (a) positive Safranin-O staining for aggrecan or (b) positive aniline blue for collagen (b). Data were analyzed by two-way ANOVA and corrected with the Bonferroni *post hoc* test. GAG; glycosaminoglycan, NS; non-significant, WW; wet weight. Scale bar: 100µm. Star (*) represent the significant difference with regarding of culture time after Bonferroni *post hoc* correction: * represents 0.01<p <0.05, ** represents 0.001<p<0.01, *** represents 0.0001<p<0.001, **** represents p<0.00001. Pound (#) represent the significant difference with regarding of scaffold type after Bonferroni *post hoc* correction: # represents 0.01<p <0.05, ## represents 0.001<p<0.01, ### represents 0.0001<p<0.001, #### represents p<0.00001.

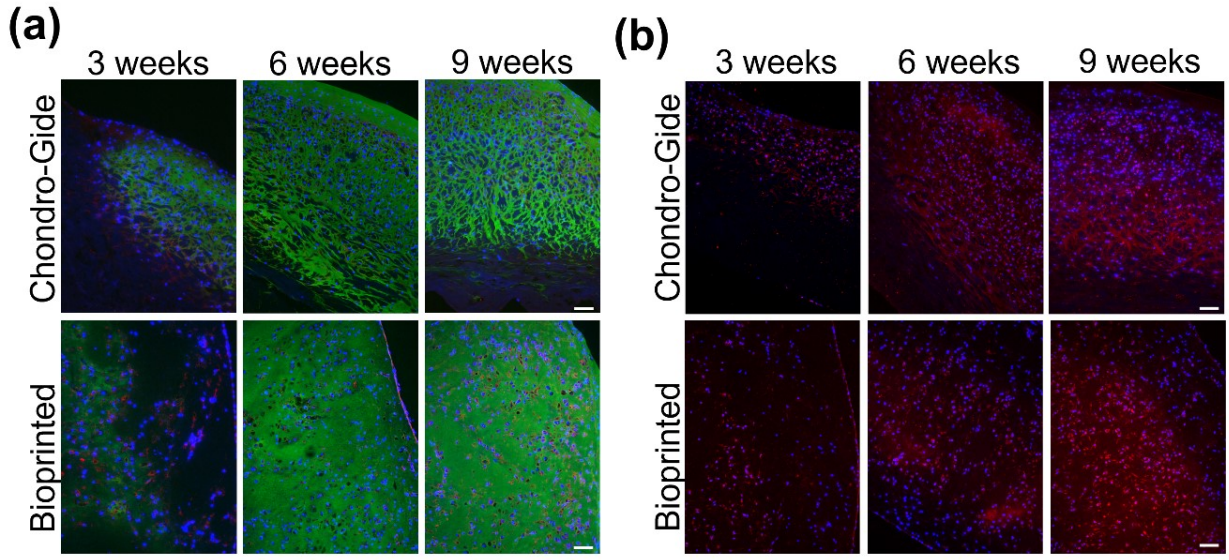

Figure 4.5. Immunofluorescence of in vitro constructs across culture time. (a) Type I (red) and II (green) collagen, and (b) Type X collagen (red). The blue color is from DAPI staining, which indicate cell nuclei. Scale bar: 100μm

4.3.4 GAG/DNA quantification of *in vitro* engineered cartilages

Biochemical analyses were performed in duplicates to quantify the GAG and DNA contents of scaffolds following each culture period (3, 6, and 9 weeks, n=6). The GAG/DNA ratios of Chondro-Gide scaffolds at 3, 6, and 9 weeks were 25.2±4.7, 46.0±9.0, and 59.2±16.4 respectively. GAG/DNA ratios of bioprinted constructs at 3, 6 and 9 weeks were 39.6±8.9, 59.8±10.8, and 71.7±21.7, respectively. Within both bioprinted and Chondro-Gide groups, culture time was shown to have a significant effect on GAG/DNA content ($p<0.0001$, Figure 4.4C). A significant difference in GAG/DNA ratios was observed between 3 weeks and 6 weeks ($p=0.0040$ for Chondro-Gide, $p=0.0113$ for bioprinted), and 3 weeks and 9 weeks ($p=0.0120$ for Chondro-Gide, $p=0.0168$ for bioprinted) for both scaffold types. However, there was no significant difference in GAG/DNA ratios between 6 and 9 weeks of culture ($p=0.1863$ for Chondro-Gide, $p=0.2718$ for bioprinted). There was a borderline significant difference in GAG/DNA content between scaffold types ($p=0.0519$), with bioprinted constructs showing higher GAG/DNA ratios

than Chondro-Gide scaffolds (significant higher at 3 weeks with *p=0.0269*). The Bern score evaluation is well correlated with the GAG/DNA assay (Figure 4.4D, Figure S4.5).

4.3.5 Mechanical properties of *in vitro* engineered cartilages

To assess the suturability of bioprinted constructs and Chondro-Gide scaffolds, a suture test was performed. A single 5-0 PROLENE suture was made on the edge of each construct and scaffold and then subsequently observed for damage. Chondro-Gide scaffolds were able to withstand suturing at all time points (Figure 4.6A). Bioprinted constructs, however, were only able to withstand suturing at 9 weeks of culture. To assess the bending modulus of the engineered cartilages, a Three-Point bending test was performed on the constructs and scaffolds at each culture time. Both bioprinted constructs and Chondro-Gide scaffolds became more robust overtime. The bending modulus of Chondro-Gide scaffolds at 3, 6, and 9 weeks of culture were 0.0675±0.00995, 0.213±0.0233, and 0.287±0.0513 MPa, respectively. For bioprinted constructs, the bending modulus was 0.0309±0.00704, 0.177±0.0557, and 0.298±0.0577 MPa at 3, 6, and 9 weeks, respectively. Bending modulus was found to increase significantly with increasing culture time for both scaffold types ($p<0.0001$, Figure 4.6B). The mean difference between Chondro-Gide and bioprinted bending modulus was 0.0366 MPa at 3 weeks, 0.0360 MPa at 6 weeks, and -0.0114 MPa at 9 weeks. Chondro-Gide scaffolds were almost twice that of bioprinted constructs at 3 weeks, but at 9 weeks, the bioprinted constructs showed a slightly higher bending modulus compared to Chondro-Gide. Due to non-sufficient donor numbers for bending modulus testing (n=3), no significant differences between scaffold types were observed. Bending modulus was also

shown to increase with culture time to a greater degree in bioprinted constructs than Chondro-Gide scaffolds.

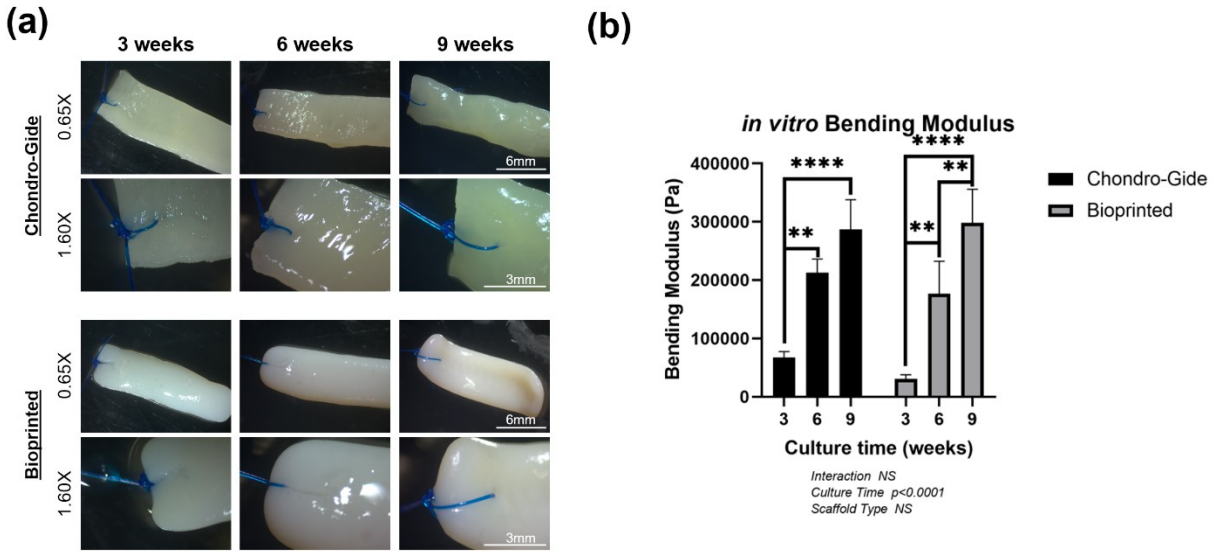

Figure 4.6. (a) Suturability of Chondro-Gide scaffolds and bioprinted constructs across culture time. Images are taken at 0.65x and 1.60x magnification. (b) Bending modulus of in vitro constructs across culture time. Data was analyzed by two-way ANOVA and corrected with the Bonferroni post-hoc test. NS; non-significant. Scale bars: 6 mm and 3 mm for 0.65x and 1.60x, respectively. Star (*) represent the significant difference with regarding of culture time after Bonferroni post hoc correction: * represents 0.01<p <0.05, ** represents 0.001<p<0.01, *** represents 0.0001<p<0.001, **** represents p<0.00001. Pound (#) represent the significant difference with regarding of scaffold type after Bonferroni post hoc correction: # represents 0.01<p <0.05, ## represents 0.001<p<0.01, ### represents 0.0001<p<0.001, #### represents p<0.00001.

4.3.6 SEM of *in vitro* engineered cartilages

SEM was used to visualize the ultrastructural differences between bioprinted constructs and Chondro-Gide scaffolds across the different cultivation times. At 3 weeks of culture, both bioprinted constructs and Chondro-Gide scaffolds showed evidence of remodelling, denoted by the presence of fibrous structures on the surface of the cartilages (Figure 4.7). Chondrocytes were also found inside the lacuna structures at 3 weeks in the bioprinted constructs. After 6 weeks of culture, the distribution of ECM fibers increased and became more even in both bioprinted constructs and Chondro-Gide scaffolds, and by 9 weeks, both engineered cartilages were completely

covered by a uniform layer of ECM. Bioprinted constructs at 3 weeks were shown to resemble native tissue most closely. This resemblance however was lost at 6 weeks as more ECM was deposited on the surface of the structures.

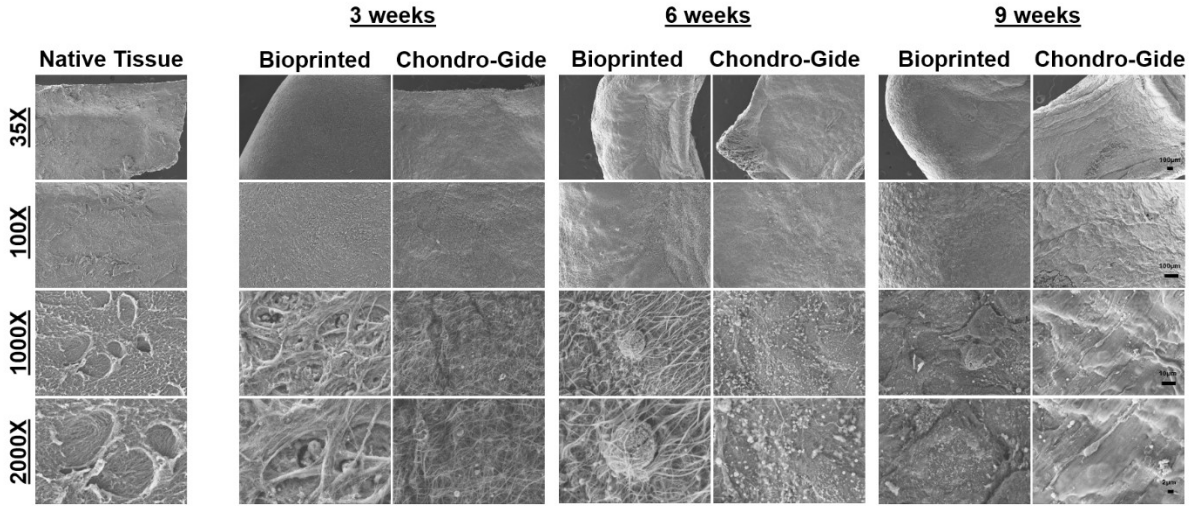

Figure 4.7. SEM imaging of in vitro constructs across culture time. Magnification of images is 35x, 100x, 1000x, and 2000x. Scale bars are 100µm, 10µm, and 2µm for 35x/100x, 1000x, and 2000x, respectively.

4.3.7 Gene expression of *in vitro* engineered cartilages

RT-qPCR was used to quantify the expression of chondrogenic (*ACAN*, *SOX9*, *COL2A1*, *CO1A2*), hypertrophic (*COL10A1*), osteogenic (*RUNX2*), and adipogenic genes (*PPARγ*), Additionally, the expression of the collagen cross linking enzyme (*LOX*) was quantified as well. The results were analyzed by two-way ANOVA and corrected with Bonferroni *post-hoc* tests.

The expression of chondrogenic-related genes was all found to be affected by culture time. Only *ACAN* expression was shown to have a significant interaction between scaffold type and culture time ($p=0.0088$, Figure 4.8). For bioprinted constructs, the expression of *ACAN* was found to increase with increasing culture time, with significant differences in expression between 3 and 6 weeks, 3 and 9 weeks. However, for Chondro-Gide scaffolds, *ACAN* expression was found to

increase only from 3 to 6 weeks and then decrease from 6 to 9 weeks (no significant differences). A significant difference was found at 9 weeks between bioprinted construct and Chondro-Gide ACAN expression. Both the expression of *COL2A1* and *SOX9* were significantly affected by culture time ($p<0.0001$ and $p=0.0006$, respectively), as the expression for both genes increased with increasing culture time. *COL1A2* expression was also significantly affected by culture time ($p=0.0004$), but instead, expression decreased with increasing culture time. There were no significant differences in *COL2A1*, *SOX9*, and *COL1A2* expressions between bioprinted constructs and Chondro-Gide scaffolds. The expression of *COL10A1* was significantly upregulated as the culture time increased ($p<0.0001$), with no significant differences between scaffold types. There was also a significant decrease in *PPARγ* expression ($p<0.0001$) with culture time, with no significant differences between scaffold types. A significant interaction was also found between scaffold type and culture time for *LOX* ($p=0.0006$). For bioprinted constructs and Chondro-Gide scaffolds, the expression of *LOX* was shown to increase and decrease significantly with culture time, respectively. The expression of *RUNX2* was not affected by either culture time or scaffold type.

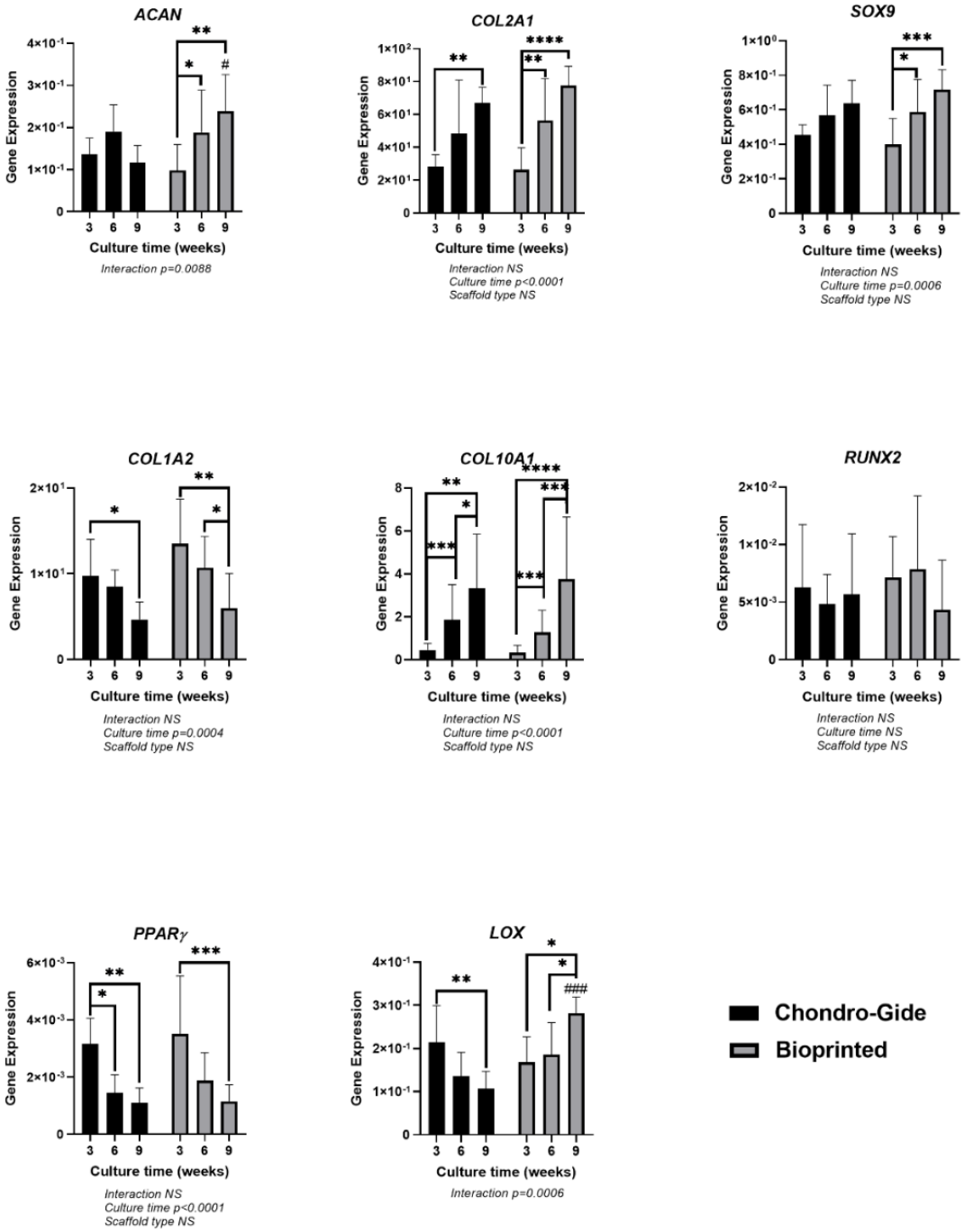

Figure 4.8. Gene expression of in vitro constructs. Values shown are 2-ΔCt values from RT-qPCR. Statistics were done using ΔCt values. Data was analyzed by two-way ANOVA and corrected with the Bonferroni post-hoc test. Housekeeping genes used were ACTB, B2M, and YWHAZ. n=6 donors (in duplicate). NS; non-significant. Star (*) represent the significant difference with regarding of culture time after Bonferroni post hoc correction: * represents 0.01<p <0.05, ** represents 0.001<p<0.01, *** represents 0.0001<p<0.001, **** represents p<0.00001. Pound (#) represent the significant difference with regarding of scaffold type after Bonferroni post hoc correction: # represents 0.01<p <0.05, ## represents 0.001<p<0.01, ### represents 0.0001<p<0.001, #### represents p<0.00001.

4.3.8 Gross morphology of engineered cartilages after *in vivo* implantation in nude mice

Following implantation in nude mice, the gross morphologies of the engineered cartilages were assessed for macroscopic differences. After 5 weeks of implantation, both bioprinted constructs and Chondro-Gide scaffolds maintained their original size and shape (Figure 4.9A). Both engineered cartilages were smooth and opaque following *in vivo* culture compared to the gluey and formless appearance of non-precultured engineered cartilages (empty scaffolds).

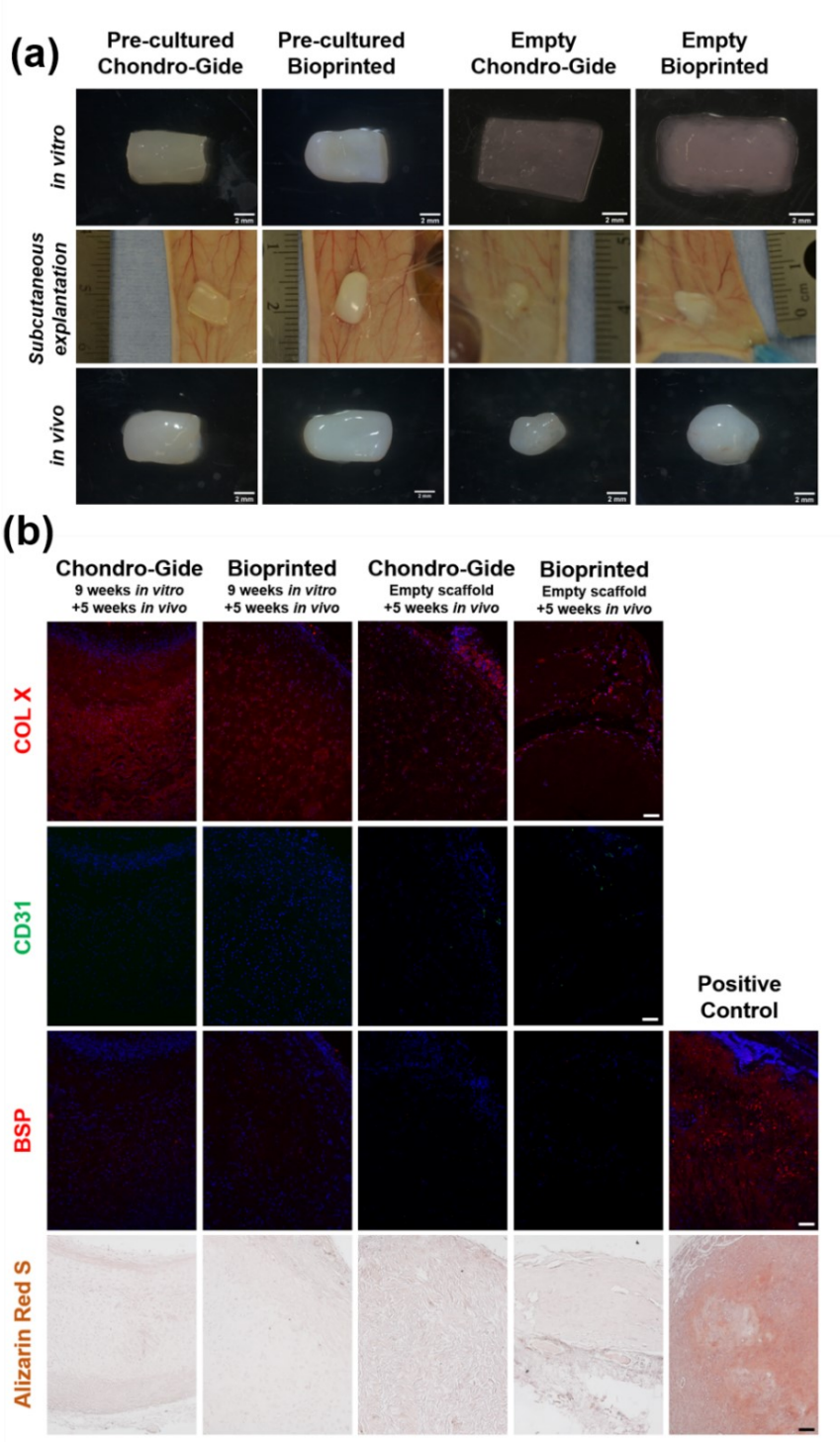

Figure 4.9. (a) Gross morphology of constructs and scaffolds before and after implantation (b) Histology and immunofluorescence of in vivo bone formation proteins, including type X collagen (red represents positive type X collagen, which is a marker of chondrocyte hypertrophy), CD31 (green represents positive CD31, CD31 is a marker of angiogenesis), BSP (red represents positive bone sialoprotein formation), and Alizarin Red (Orange color represents positive calcification). COL10; type X collagen, CD31; cluster of differentiation 31, BSP; bone sialoprotein. Scale bar: 100µm.

4.3.9 Histology and immunofluorescence after *in vivo* implantation

To characterize the nature of the ECM following implantation, Safranin-O and Masson's trichrome staining were performed to assess and compare the matrix composition of *in vivo* cultured engineered cartilages to *in vitro* controls. Following *in vivo* culture, both cell-laden bioprinted constructs and Chondro-Gide scaffolds showed peripheral loss of proteoglycan-rich matrix, denoted by the loss of Safranin-O staining (Figure 4.10, all the explanted donors are shown in Figure S4.7). The intensity of Safranin-O staining was overall fainter in the *in vivo* cartilages compared to the *in vitro* cartilages. No matrix deposition was observed in empty scaffolds. Collagen deposition, denoted by aniline blue, was slightly different between *in vitro* and *in vivo* cartilages. Engineered cartilages implanted *in vivo* appeared to have a more intense collagen staining in the periphery that contrasted Safranin-O staining, like native tissue. However, *in vitro* cartilages appeared to have a more diffuse and generalized distribution of collagen staining. Bioprinted constructs overall had more collagen staining than Chondro-Gide in both the *in vitro* and *in vivo* conditions. Collagen deposition that was observed in both empty scaffolds was most likely due to mouse skin cell infiltration, which is supported by the presence of cell nuclei and lack of human specific collagen expression detected by immunofluorescence (Figure 4.10). To characterize and compare the collagen deposition in the *in vivo* cultured engineered cartilages to those cultured *in vitro*, types I and II collagen immunofluorescence were performed. The expression of type I and II collagens were shown to be maintained in the cell-laden engineered cartilages following *in vivo* culture (all the explanted donors are shown in Figure S4.8), with type II collagen expression being the most pronounced. Type II collagen expression was also more intense in *in vivo* than *in vitro* cartilages. To determine whether macrophages contributed to the loss of the proteoglycan-rich matrix *in vivo*, BM8 immunofluorescence was performed (Figure

S4.10). Macrophages were observed in both *in vivo* cultured engineered cartilages, suggesting a phagocytic role of macrophages in proteoglycan loss. To assess the extent of bone formation in the *in vivo* cartilages, a few different analyses were performed. CD31, BSP, type X collagen immunofluorescence, and Alizarin Red S staining were performed to detect blood vessel invasion, bone ossification, chondrocyte hypertrophy, and calcium deposition in the *in vivo* cartilages, respectively. There was no evidence of blood vessel invasion, bone growth, or mineralization in either the cell-laden bioprinted constructs or Chondro-Gide scaffolds (Figure 4.9B, Alizarin Red S for explanted scaffolds and native tissue are shown in Figure S4.9). Empty scaffolds implanted *in vivo* showed some evidence of blood vessel invasion. *In vitro* parallel-cultured engineered cartilages served as a negative control for both BSP and Alizarin Red S staining. Type X collagen expression was observed in both bioprinted constructs and Chondro-Gide scaffolds *in vivo*, however, this staining was like *in vitro* controls.

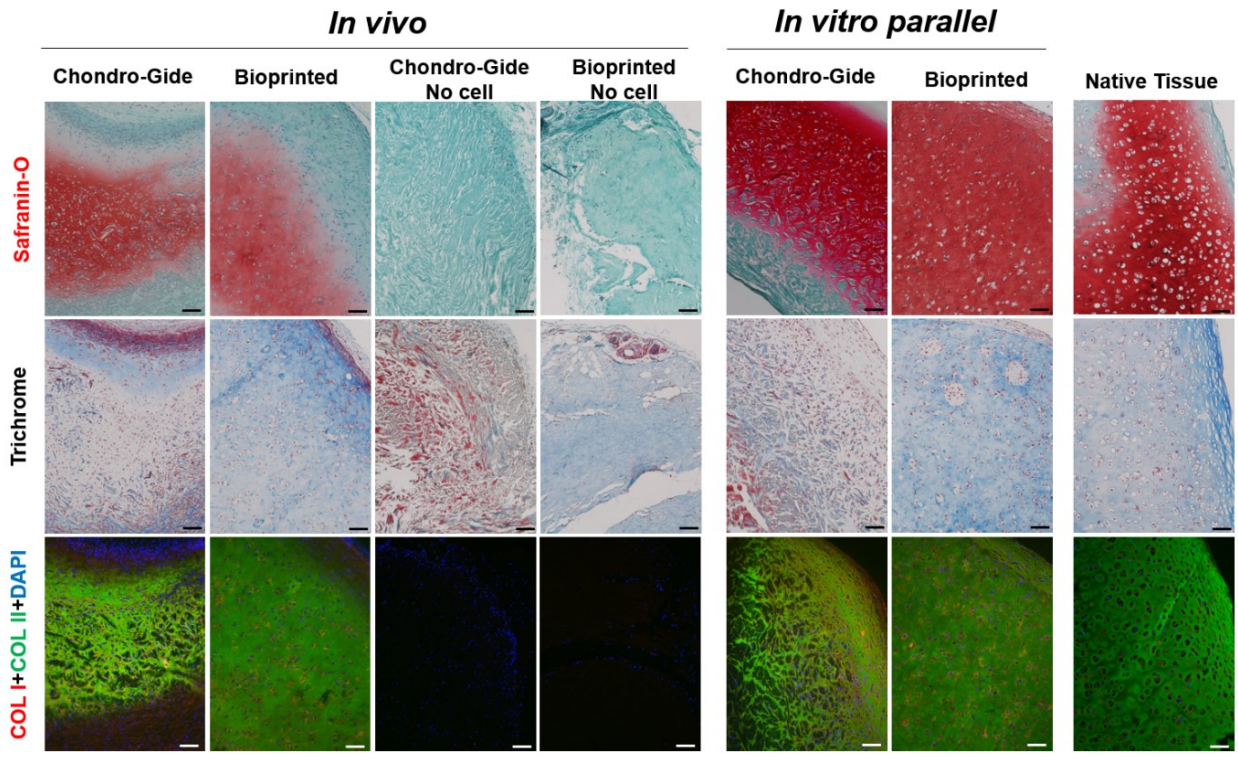

Figure 4.10. Histology and immunofluorescence of chondrogenic related proteins, including Safranin-O/Fast Green straining, Masson's Trichrome staining, and type I and II collagens immunofluorescence. Scale bar: 100μm

4.3.10 Mechanical property after *in vivo* implantation

To assess the effects of *in vivo* culture on the mechanical properties of engineered cartilages, a three-point bending test was performed before and after implantation in nude mice. Bending modulus was shown to increase from 0.287±0.0513 to 0.534±0.189 MPa in Chondro-Gide and from 0.298±0.577 to 0.582±0.0444 Pa in bioprinted constructs. All three donors showed an increase in bending modulus after implantation. The size of the implanted Donor #1 is untestable due to the size limitation.

Table 4.3. Bending modulus before and after implantation

Scaffold Type	Before implantation (Pa)			After implantation (Pa)		
	21/M Donor #1	30/M Donor#3	48/M Donor#6	21/M Donor #1	30/M Donor#3	48/M Donor#6
Chondro-Gide	227627	312329	320105	448666	751396	402828
Bioprinted	248587	284047	361490	N/A	549189	611978

4.4 Discussion

In this study, we have used human nasoseptal chondrocytes (NC)-laden bovine type I collagen hydrogel to 3D bioprint engineered nasal human cartilage. Our results supported the biofabrication of a robust and mechanically suturable engineered human nasal cartilage that is comparable if not better than engineered human nasal cartilage graft from NC-seeded porcine type I and III collagen membrane scaffold, Chondro-Gide. The bioprinted tissue was characterized by increased cellular viability from the time of biofabrication to the endpoint of 9 weeks of *in vitro* tissue development at which point there was a fall in the measured cellular viability relative to 3- and 6-weeks time points. The reason for the decline is unclear but the majority of the cells' morphology at 9 weeks seem to be consistent with the adhesive model of cell migration in 3D collagen lattices, suggesting that a number of cells may have migrated out of the engineered tissue construct after the 9 weeks long of ECM accumulation and matrix remodeling[403]. However, this would need to be verified in future studies.

Furthermore, our results emphasize the capacity of the extensively cell culture expanded NCs, up to six cell population doublings, in cell growth media supplemented with TGF-β1 and FGF-2 of been able to synthesize and organize cartilage ECM within the NCs-laden type I collagen hydrogel for bioprinting and within the type I/III collagen membrane scaffold. These results are

consistent with our previous works[64, 215] and Fulco et al's[6] work using the collagen membrane scaffold. Since the functional component of cartilage is its ECM[404], we evaluated the progression of tissue maturation over time. After 3, 6, and 9 weeks of chondrogenic culture, we first analyzed for cartilaginous ECM formation by visualizing sulfated proteoglycan via Safranin-O staining, collagen deposition via Masson Trichrome staining, human types I and II collagen via immunofluorescence (Figure 4.4A, Figure 4.3B). The bioprinted constructs showed a uniform distribution of Safranin O positive, collagen, and human types I/II collagen distribution relative to the same ECM distribution in the porcine-derived type I/III collagen membrane scaffolds. Thus, one benefit of the bioprinting approach for fabrication of the engineered nasal cartilage graft is that it allowed the NCs to be homogenously distributed within the bovine-derived type I collagen hydrogel before the 3D layer-by-layer deposition of the NCs-laden hydrogel. In contrast, the distribution of the NCs synthesized cartilaginous ECM appeared to be less uniformly distributed and restricted to the porous layer of the porcine-derived type I/III collagen membrane scaffold albeit with some evidence of the ECM extending into the smooth compact layer of the membrane over the course of the *in vitro* tissue maturation.

Quantitative measures of the chondrogenic capacity (i.e., GAG/DNA) of the NCs within the two matrices used in this study supports the superiority of the microenvironment of the hydrogel in facilitating the chondrogenic redifferentiation of the NCs. The GAG/DNA values for the bioprinted engineered nasal cartilage were higher than in the porcine-derived type I/III collagen membrane scaffolds with magnitudes of 14.38, 13.74, 12.48 μg/μg for 3, 6, and 9 weeks, respectively. This superiority is consistent with reports that the branched network of loose bundles of collagen fibers as found in collagen hydrogels as supposed to the membrane-like flatten wall internal structure of the fibers presented in the porous collagen sponges supports the round

chondrocytic phenotype of chondrocytes[405-407]. However, it is interesting to note that while the chondrogenic capacity of the NCs within the hydrogel matrix was superior relative to the collagen membrane scaffold, the gene expression of types I and X collagen were not different between the hydrogel and membrane scaffold as previously reported between the different internal structures of chitosan-based scaffold forms of sponges and hydrogels[405]. To that end, our finding seems to suggest that both the internal structure and composition of scaffolds play a role in the phenotypic expression of the cells in any given scaffold. The higher GAG/DNA contents in type I collagen bioink group may be attributed to a superior display of synthetic capacity of the NCs within the hydrogel microenvironment as well the entrapment of the synthesized ECM within the hydrogel matrix.

Given the fact that the mechanical strength of cartilaginous structures is by reason of their ECM's composition and organizational structure, it is no surprise that as the ECM synthesized by the NCs increased and accumulated with *in vitro* culture duration within the bioprinted constructs that it played a vital role in the development of its tensile properties (Figure 4.6A). As the images (Figure 4.6A) demonstrate, after 3 weeks of culture, the bioprinted constructs were unable to hold surgical sutures an indication of a weak tensile strength. However, it was not until after 9 weeks of *in vitro* culture that the bioprinted constructs' tensile properties was adequate to hold the surgical sutures without failure. In contrast, the high tensile strength of the collagen membrane was adequate to hold surgical sutures regardless of the *in vitro* culture duration of the due to the arrangement of its collagen fibres[6]. It is interesting to note that the ultrastructure of native human septal cartilage and that of the collagen membrane-derived engineered nasal cartilage looked very similar regardless of the *in vitro* culture maturation time with obvious tightly organized collagen fibres, while porous spaces are evident in the bioprinted constructs of

engineered cartilage at 3 and 6 weeks but not at the 9 weeks culture time when the ultrastructure looked similar to the ultrastructure of the native septal cartilage and collagen membrane-derived engineered cartilage. To that end, it is reasonable to speculate that the subsequent filling or re-modeling of the spaces contributed to the augmented tensile strength of the bioprinted construct after 9 weeks. The increased lysyl oxidase (*LOX*) expression which relatively peaked at 9 weeks coincided the improved tensile strength (Figure 4.8). Thus, given *LOX*'s functionality in cross-linking collagen and improving mechanical strength of engineered cartilage, we speculate that *LOX* contributed to the augmented tensile strength after the 9 weeks of maturation[408, 409]. The mechanism underlying the observed upregulation of *LOX* in the bioprinted constructs and its decline in the collagen membrane-derived constructs is unclear but may be associated with alterations in local hypoxia microenvironment as the cartilaginous ECM is deposited and remodeled within the cell-laden constructs. Makris *et al* has shown that *LOX* expression could be induced through hypoxia[408]. One possibility is a limited access of the NCs-media contact in the compact layer of the collagen membrane scaffold which may have led to a local hypoxic environment, resulting in a higher *LOX* gene expression at 3 weeks. However, as culture time increased, the *de novo* synthesized and deposited ECM by the NCs remodeled with extension into the compact layer leading to a disruption of the local hypoxic microenvironment with concomitant decline in *LOX* gene expression. In contrast, the NCs within the bioprinted hydrogel constructs had high initial cell-media contact that permitted a homogenous access of media dissolved oxygen to the NCs. But as the NCs within the bioprinted construct synthesized, deposited, and remodeled the *de novo* ECM during maturation local hypoxic microenvironments emerged leading to increased *LOX* expression.

In addition to the bioprinted engineered cartilage improved tensile characteristics as judged by its suturability, the bending modulus of the bioprinted cartilage experienced a larger increase with culture maturation time than the collagen membrane-derived engineered cartilage constructs. This finding further supports the concept that the gradual improvement in the tensile strength and suturability of the bioprinted engineered cartilage aligned with increased ECM production and accumulation within the hydrogel scaffold.

Monolayer expanded chondrocytes expressed adipogenic, chondrogenic and osteogenic markers genes and encoded proteins after respective inductions[410, 411]. Therefore, we investigated the expression of adipogenic, chondrogenic and osteogenic marker genes to assess *in vitro* phenotypic stability of the chondrogenically stimulated monolayer-expanded NCs. Our findings showed a gradual decline in adipogenic (*PPARγ*) and fibrogenic (*COL1A2*) marker gene expression regardless of whether the collagen membrane or hydrogel scaffold was used during *in vitro* maturation of the engineered cartilage constructs. In contrast, chondrogenic markers' gene expression (*COL2A1*, *SOX9*, *ACAN*) increased with culture time in the cell-laden hydrogel bioprinted constructs and to some extent similarly in the collagen membrane albeit with a notable drop in *ACAN* expression at 9 weeks. These results further reinforce the superiority of the hydrogel microenvironment in the enhancing the chondrogenic phenotype of the chondrogenically stimulated monolayer-expanded NCs.

The expression of *COL10A1*, a marker of hypertrophic chondrocyte has been shown to correlate with the propensity of chondrogenically induced bone marrow mesenchymal stem cells to undergo transformation akin to endochondral ossification[61]. As such, we investigated the expression of *COL10A1* and observed its upregulation with culture maturation time in both the cell-laden bioprinted and the collagen membrane constructs. Furthermore, its encoded protein, type X

collagen, was evident via immunofluorescence in the constructs (Figure 4.5B). To ensure that the engineered cartilage constructs were stable phenotypically *in vivo* without the risk of undergoing ossification, the constructs after 9 weeks of *in vitro* maturation were subcutaneously implanted in immunodeficient nude mice. There was no evidence of ossification regardless of whether the engineered cartilage construct was bioprinted or collagen membrane-derived after 5 weeks of implantation in the mice. This finding was consistent with our previous findings in regard to engineered cartilage in the collagen membrane scaffold[64]. Interestingly, Aksoy *et al* showed native nasal septal cartilage contain small amounts of Type X collagen[38]. Thus, it is reasonable to speculate that compositionally our engineered cartilage constructs resemble native nasoseptal cartilage.

In vivo preservation of the engineered cartilage constructs poses several challenges: the shrinkage and deformation of the construct due to the skin tension[412-414], the calcification of tissue-engineered cartilage[61, 64, 412, 415], and the preservation of cartilage-like ECM after implantation[388]. In this study, the bioprinted constructs were able to maintain their gross morphology even after 5 weeks of implantation. However, the gross morphology of the cell-free scaffolds deformed and shrunk suggesting some sort of remodeling or cell-mediated contraction had taken place (Figure 4.9). Following other histological and immunofluorescence assessments in addition to the above-mentioned assessment for bone formation after *in vivo* implantation, positive CD31 fluorescence were evident in the cell-free scaffolds suggesting an invasion of endothelial cells which may contributed to the observed shrinkage through cell-mediated contraction of the scaffold. Moreover, Safranin-O positive ECM staining was notably reduced after *in vivo* implantation, but the fluorescence of types I and II collagen remained unchanged as prior to *in vivo* implantation. These findings are consistent with previous studies of implanted engineered nasal

cartilages[64, 416]. But it is unclear the underlying mechanism of the decline of the Safranin O positive ECM. We reasoned it could be due to macrophage invasion from the nude mouse[417-419]. Thus, we assessed the presence of macrophage with anti-F4/80, a unique marker of murine macrophages in the explanted tissue engineered constructs[420], the F4/80 immunofluorescent results are shown in Figure S4.10. The assessment proved positive for the presence of macrophages and supported the mechanistic possibility that the decline of the Safranin O positive ECM may have been mediated by macrophage secreted matrix metalloproteinases as previously reported[419, 421, 422].

The mechanical strength of both engineered cartilage constructs increased almost 2-fold after *in vivo* implantation as shown in Table 4.3. Bending modulus before and after implantation. This finding suggested that the constructs underwent further remodeling or maturation *in vivo* after 9 weeks of *in vitro* maturation. This finding therefore raises the question; what is an adequate duration for *in vitro* maturation of engineered cartilage to achieve mechanical robustness for surgical handling prior to reconstructive surgery? Previous work, albeit in articular cartilage repair, indicated that 2 weeks of *in vitro* maturation of engineered cartilage resulted in better integrative repair relative to 6 weeks of *in vitro* maturation[423]. To this end, it is reasonable to suggest that a timeframe that enables suturability or mechanical handling during reconstructive surgery is appropriate given that further *in vivo* maturation is inevitable.

A potential limitation of our study was that only male donors were included which was due to the limited donor supply from the hospital. Previous research has not shown any significant differences between males and females in terms of nasal cartilage compositions and shapes[39, 424]. A pilot study might be worth future investigation to compare the effects of sex on the compositions of engineered cartilage tissues.

4.5 Conclusion

This study demonstrated the perspective of bioprinting engineered cartilage grafts with similar histological, molecular, and mechanical characteristics as those derived from the use of clinically approved type I/III collagen membrane scaffolds both *in vivo* and *in vitro*. Moreover, the mechanical characteristics of the bioprinted engineered grafts increased after *in vivo* implantation. Overall, this study showed strong evidence of the potential to engineer human nasal cartilage grafts for nasal reconstructive surgery via 3D bioprinting.

4.6 Supplementary Material

Table S4.1 Population Doubling for donors

Donor	Age/biological sex	Cumulative PD	PD/ day
1	21/M	6.610599	0.508508
2	25/M	6.888371	0.529875
3	30/M	6.541156	0.503166
4	30/M	6.517763	0.501366
5	43/M	6.613922	0.508763
6	48/M	6.57086	0.505451

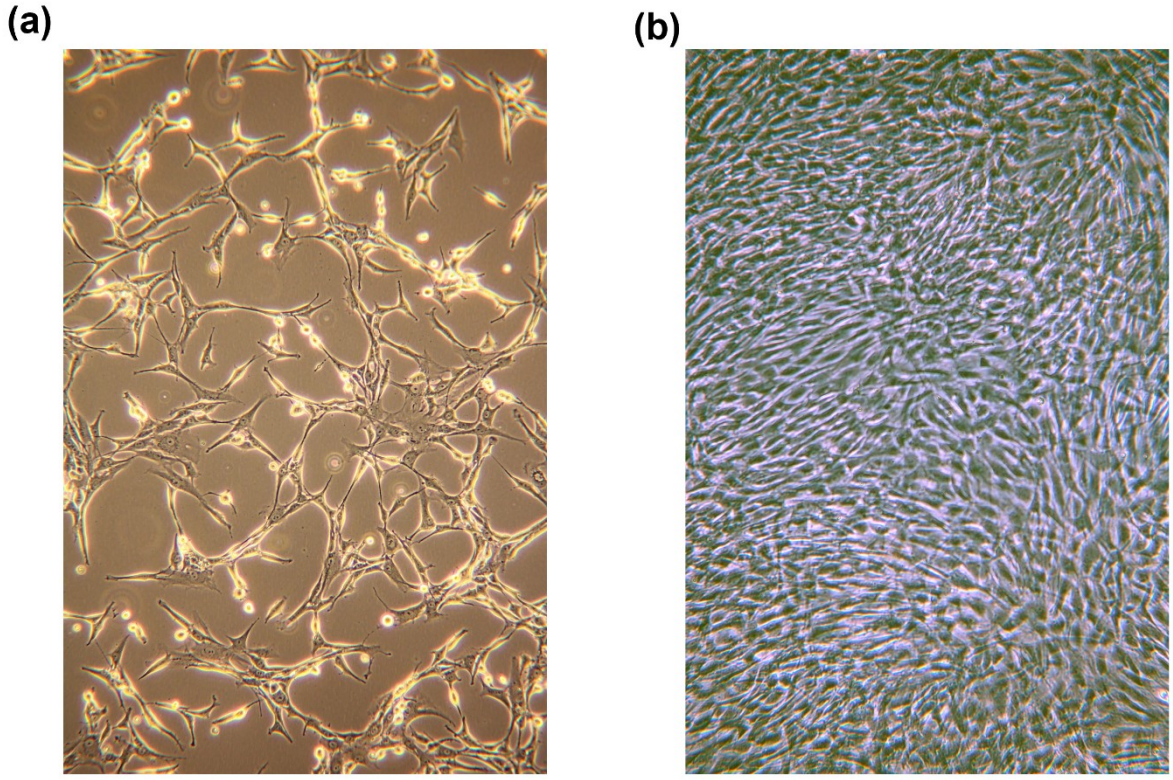

Figure S4.1 Gross morphology of the nasal chondrocytes (a) after one day of isolation, (b) after confluent

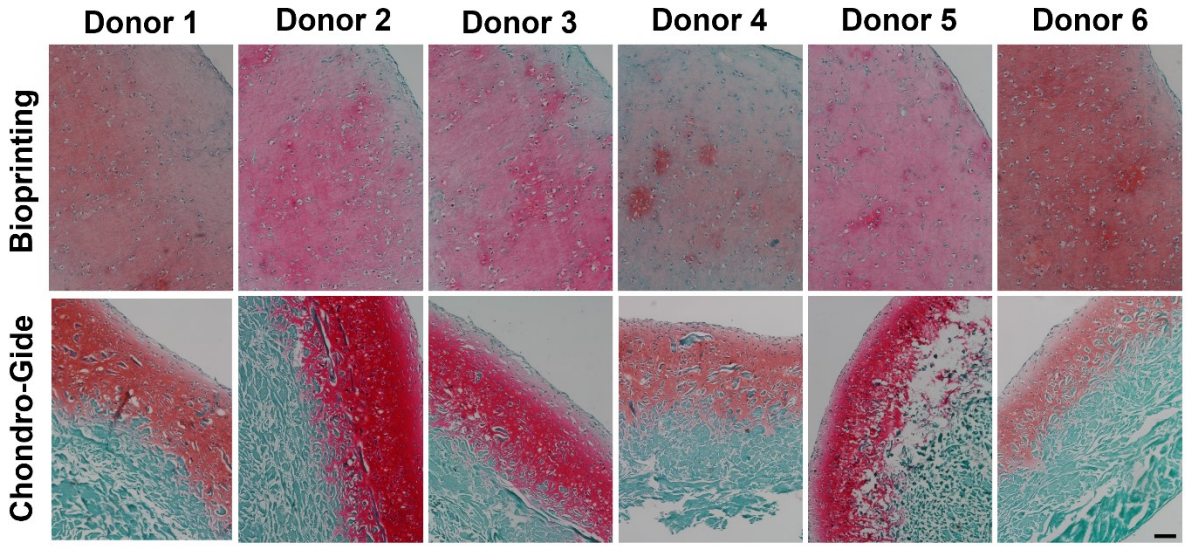

Figure S4.2 Safranin-O staining for proteoglycan (red) in all *in vitro* donors after 3 weeks implantation (n=6). Scale bar: 100µm

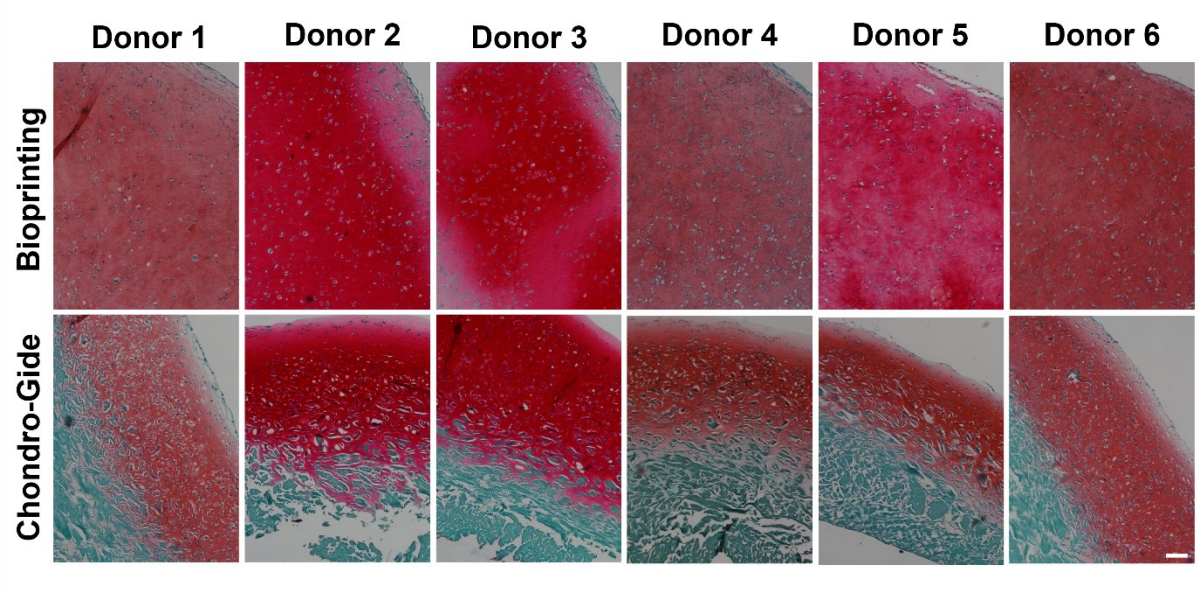

Figure S4.3 Safranin-O staining for proteoglycan (red) in all *in vitro* donors after 6 weeks implantation (n=6). Scale bar: 100µm

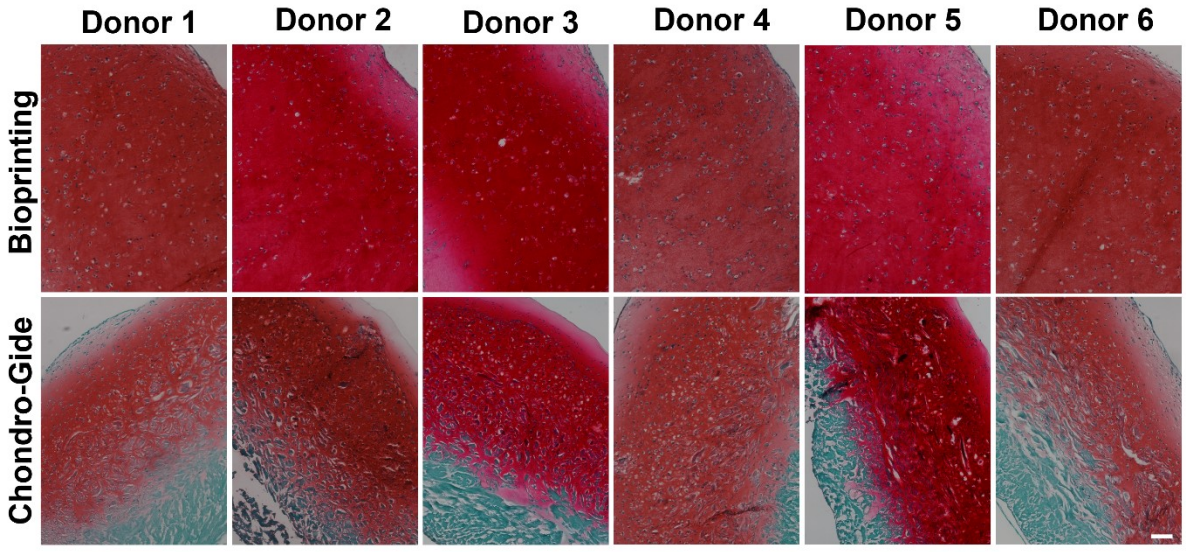

Figure S4.4 Safranin-O staining for proteoglycan (red) in all *in vitro* donors after 9 weeks implantation (n=6). Scale bar: 100µm

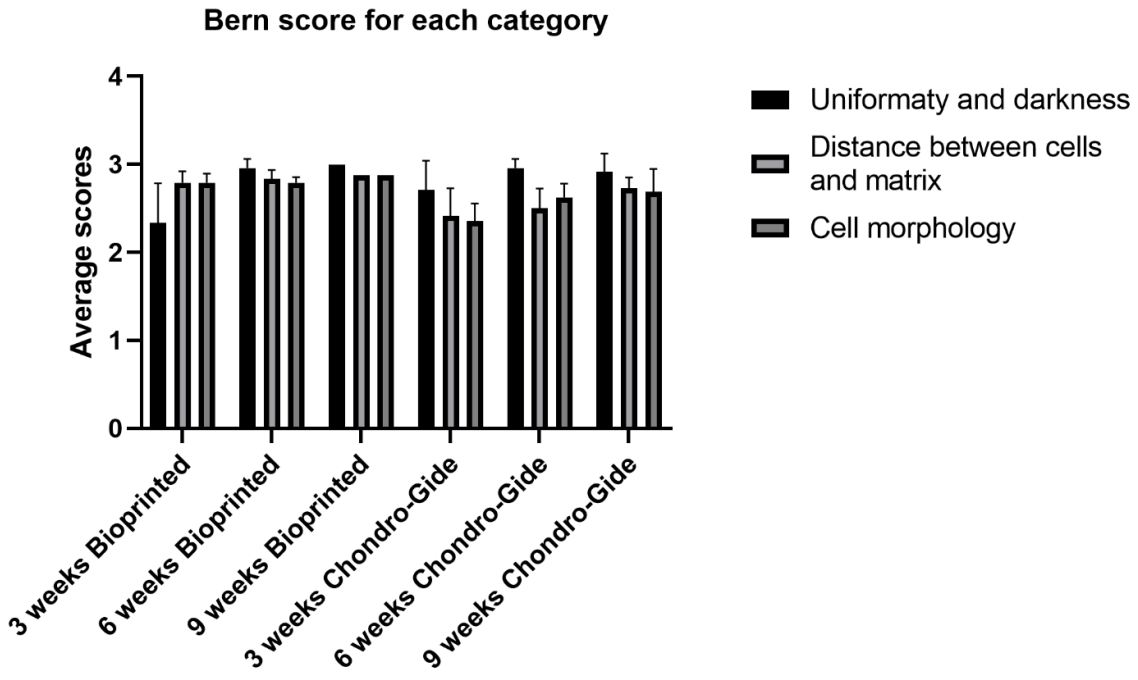

Figure S4.5 The semi-quantitative analysis of Bern Scores for each individual category (n=6). Bern scores are evaluated by 4 blinded individual observers.

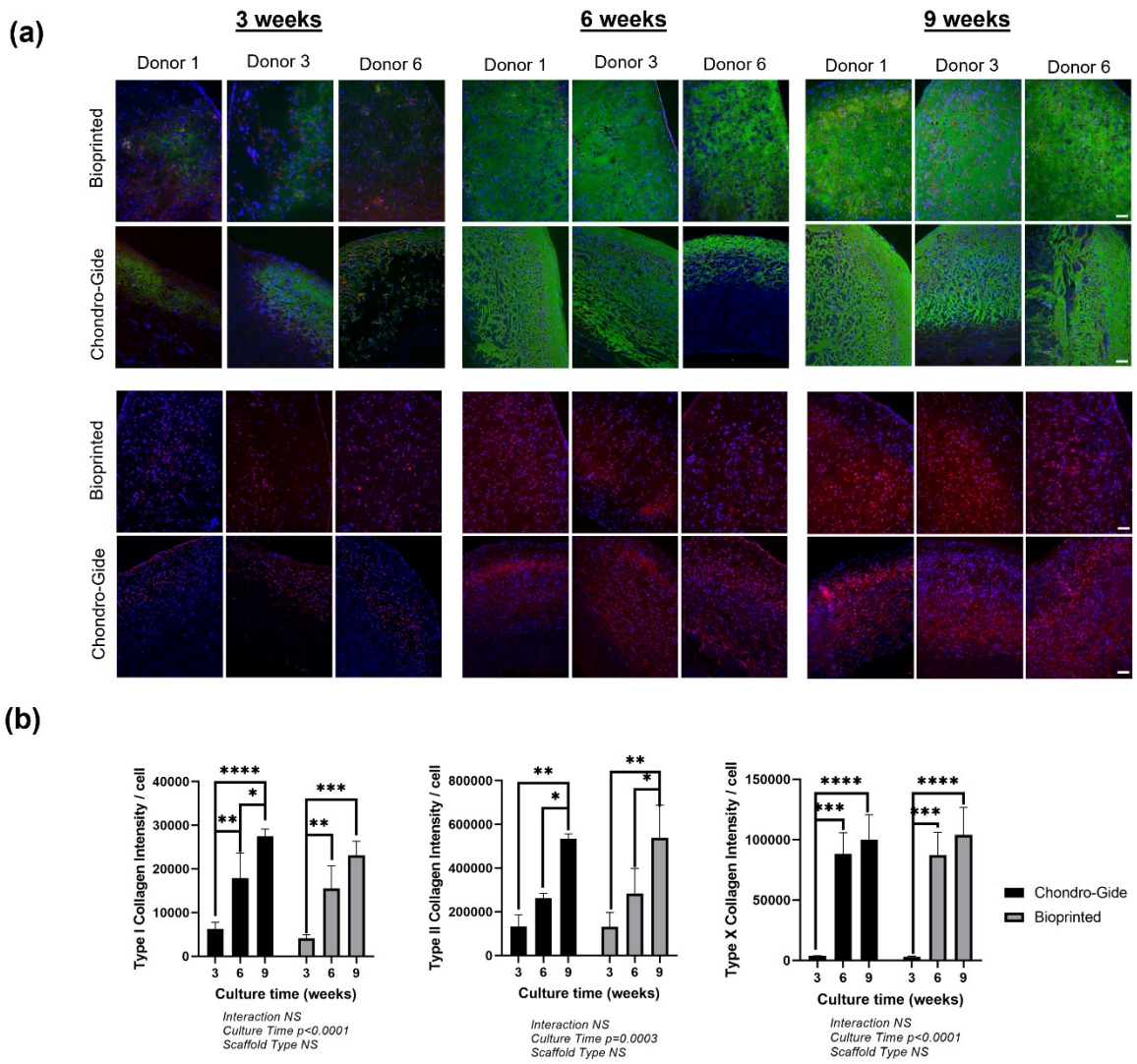

Figure S4.6 The semi-quantitative analysis of *in vitro* Types I, II and X collagens formation based upon immunofluorescence assay (n=3). Star (*) represent the significant difference with regarding of culture time after Bonferroni *post hoc* correction: * represents 0.01<p <0.05, ** represents 0.001<p<0.01, *** represents 0.0001<p<0.001, **** represents p<0.00001. Pound (#) represent the significant difference with regarding of scaffold type after Bonferroni *post hoc* correction: # represents 0.01<p <0.05, ## represents 0.001<p<0.01, ### represents 0.0001<p<0.001, #### represents p<0.00001.

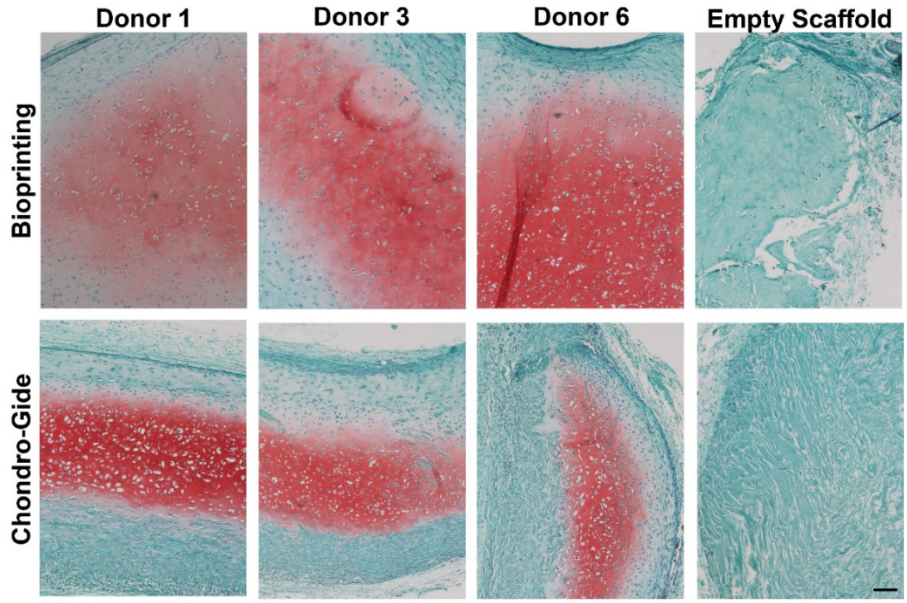

Figure S4.7 Safranin-O staining for proteoglycan (red) in all *in vivo* implanted donors (n=3). Scale bar: 100µm

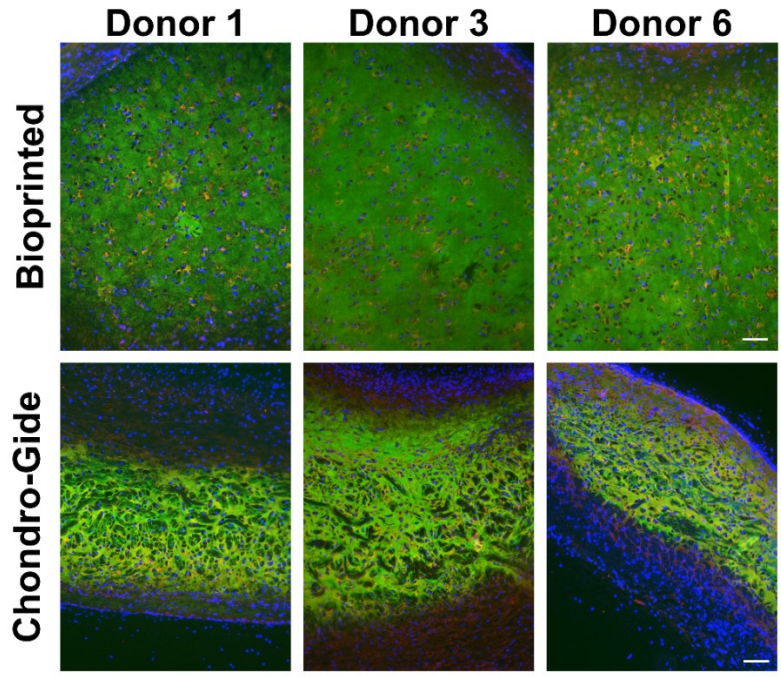

Figure S4.8 Immunofluorescences staining for Type I (red) and II (green) collagen in all *in vivo* implanted donors (n=3). Scale bar: 100µm

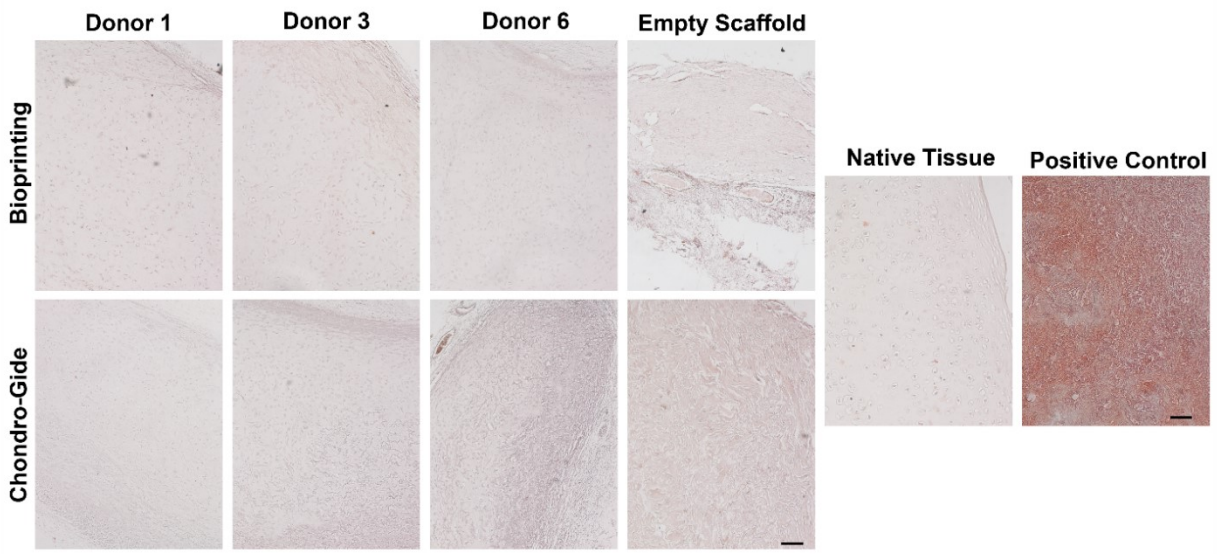

Figure S4.9 Alizarin Red S staining for calcium deposition (orange/red) in all *in vivo* implanted donors (n=3). Scale bar: 100µm

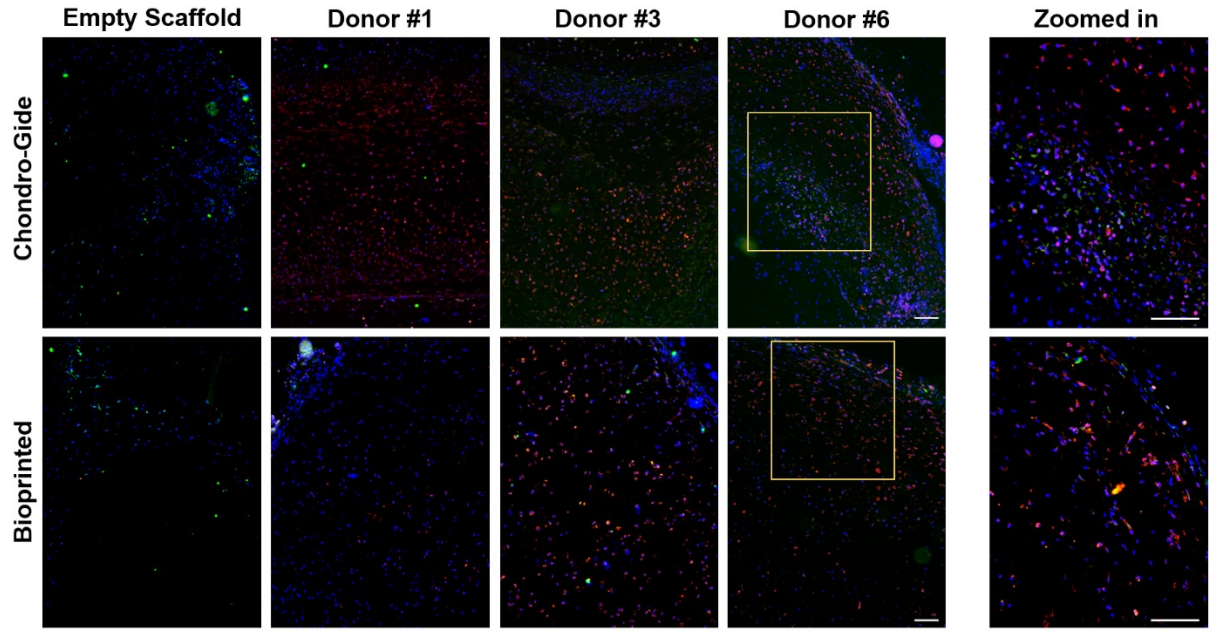

Figure S4.10 Immunofluorescence of F4/80 staining (green), aggrecan staining(red), and nuclei(blue) for all *in vivo* implanted constructs. Scale bar: 100µm

CHAPTER 5. Pre-crosslinked hyaluronic acid and collagen bio-ink for cartilage tissue engineering

5.1 Introduction

Hyaline cartilage is a dense connective tissue that can be found in rib, nose, articular cartilage, larynx, and trachea, and serves various structural or functional purposes to the human body. Unfortunately, hyaline cartilage defects occur in orthopedic (articular cartilage) and craniomaxillofacial (nasal cartilage) sites, caused by trauma, cancer removal, aging, or congenital disease. The most common cartilage defect in the craniomaxillofacial region is the deviated nasal septum, which has been observed in 80% of the general population[3]. The most common cartilage disease in orthopedic medicine is osteoarthritis (OA), which is a progressive and degenerative joint disease that leads to the loss of hyaline cartilage. Due to the avascular nature of the hyaline cartilage, damaged cartilage has limited spontaneous self-repair and regenerative capabilities[2]. The current treatment method for cartilage repair and regeneration includes autologous chondrocyte implantation (ACI), human mesenchymal stem cell (MSC) injection, and grafts (allograft, autograft, synthetic material)[4, 6, 425]. Although these treatment methods achieved some success, each method still showed some limitations, such as fibrocartilage formation, hypertrophic differentiation of MSC, lack of integration, donor-site morbidity, and unmatched mechanical properties of the repaired region[4, 425].

Recently, advancements in bioprinting enabled the straightforward extrusion of cell-laden biomaterials (known as “bioink”) and became the new solutions to tissue regeneration. Large numbers of autologous cells can be generated from a small tissue biopsy by monolayer cell expansion of the isolated primary cells *in vitro*. The expanded cells are then mixed with bioinks and bioprinted into specific geometry to form functional tissues to fit patients’ needs. Bioink is considered one of the most important aspects of the bioprinting process since an ideal bioink should be biocompatible and printable. Hydrogels have been used as bioinks to provide a biocompatible

environment to encapsulate cells and build 3D structures. A suitable hydrogel used in 3D bioprinting process need to be sufficiently viscous for bioprinting as well as crosslinkable to stabilize printed structure and encapsulate the cells. At the same time, to create a tissue-engineered construct, the bioink needs to have cell adhesive motifs for cells to migrate, attach, and differentiate. Commonly used bioinks include polysaccharide-based biomaterials, such as alginate, agarose, chitosan, and cellulose. These bioinks are biologically inert and non-adhesive for cells. Bioinks that are based on constituents of the ECM of cartilage, for example hyaluronic acid (HA) or type I collagen, have cell adhesion motifs which support cell growth and differentiation for cartilage formation [335]. Unfortunately, HA and type I collagen exhibit a poor rheological property, low storage modulus, and slow crosslinking behaviour that are not suitable for bioprinting. Recently, photocurable arylated collagen bioinks to enable fast crosslinking using long wavelength UV light have been explored[95, 276]. To mimic the native ECM environment and/or improve the mechanical property of methacrylated collagen, several studies have incorporated chemically modified thiolated HA (THA) for tissue engineering or drug screening applications[300, 303, 426-429].

In this study, methacrylate type I collagen (COLMA) is combined with THA to produce a functional bioink material for 3D bioprinting of nasal cartilage grafts. Poly (ethylene glycol) diacrylate (PEGDA) that contains two arylate bond, is used as an additional crosslinker and to augment the printability. As described in Figure 5.1, any of two (meth)acrylate functional groups on COLMA or PEGDA can form a covalent bond through chain-polymerization by UV curing, at the same time, the (meth)arylate groups can crosslink with thiolate moiety to form a thiol-ene bond through a step-grown click reaction spontaneously or by UV curing[430]. The thiolated group in THA can also be crosslinked via self-gelation at ambient conditions, which is the

disulfide bond crosslinking between two thiolated groups[431]. To improve zero-shear viscosity and storage modulus that is suitable for bioprinting, the methacrylate group of COLMA and PEGDA was first reacted with the THA spontaneously at room temperature for pre-crosslinking. We then compared COLMA-only bioink, COLMA+THA bioink, and COLMA+THA+PEGDA bioinks in terms of their printability and cell viability. Furthermore, a cartilage tissue model was cast using these three bioinks to assess their capacity to support *in vitro* cartilage formation.

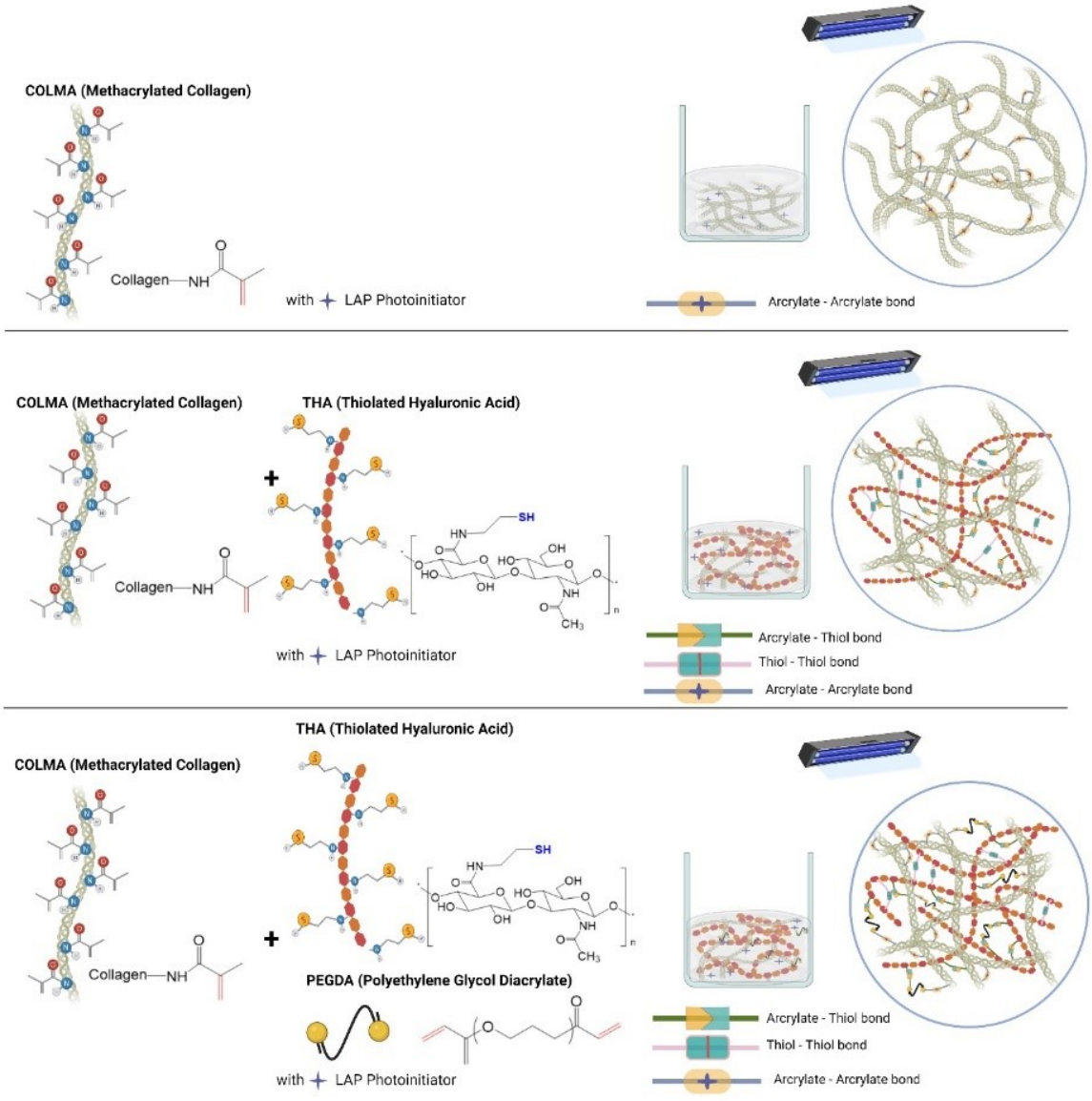

Figure 5.1 Reaction mechanism of the COLMA, COLMA+THA, COLMA+PEGDA bioinks

5.2 Materials and Methods

5.2.1 Human nasal chondrocyte isolation and expansion

Human nasal septal cartilage specimens were collected from surgical discards of . five (5) male donors with an age range from 20-56 years old undergoing nasal reconstructive surgery. The University of Alberta's health research ethics board – biomedical panel (Study ID: Pro00018778) approved the collection of the surgical discards. Nasal chondrocytes (NC) were isolated from the cartilage specimen and expanded in monolayer culture as previously described [42, 142]. Briefly, surgical discarded cartilages were digested in 0.15% (w/v) type II collagenase (300 units/mg solid) in Dulbecco's Modified Eagle Medium (DMEM) with 5% (v/v) FBS at 37 ℃ to extract the primary nasal chondrocytes. The primary nasal chondrocytes were expanded to passage 2 (P2) in DMEM-complete media (DMEM supplemented with 10 % (v/v) of fetal bovine serum, 100 U/mL penicillin, 100 μg/mL streptomycin, 2 mM L-glutamine, and 10 mM 4-(2-hydroxy-ethyl)-1-piperazineethanesulfonic acid (HEPES)) with 1ng/mL transforming growth factor β1 (TGF-β1) and 5 ng/mL of basic fibroblast growth factor 2 (FGF2).

Table 5.1.Donors Information

Donor	Biological Sex	Age	Medical History	Total PD	Total PD/day
1	Male	20	N/A	7.55	0.58
2	Male	24	Septoplasty	7.02	0.54
3	Male	32	Deviated nasal septum	7.90	0.61
4	Male	34	Deviated nasal septum	7.33	0.61
5	Male	56	Deviated nasal septum	7.31	0.56

The overview of the experimental setup is provided in Figure 5.2. Briefly, the expanded NC were mixed with each bioink. The rheology property was first determined, followed by 3D

bioprinting. The cell viability was tested after the bioprinting process. The bioinks were then cast into a 96-well plate for biological assessment including cell viability. After 6 weeks of *in vitro* chondrogenic culture, the engineered cartilage constructs were accessed under histology, immunofluorescence, biochemical assay, biomolecular assay, and mechanical testing.

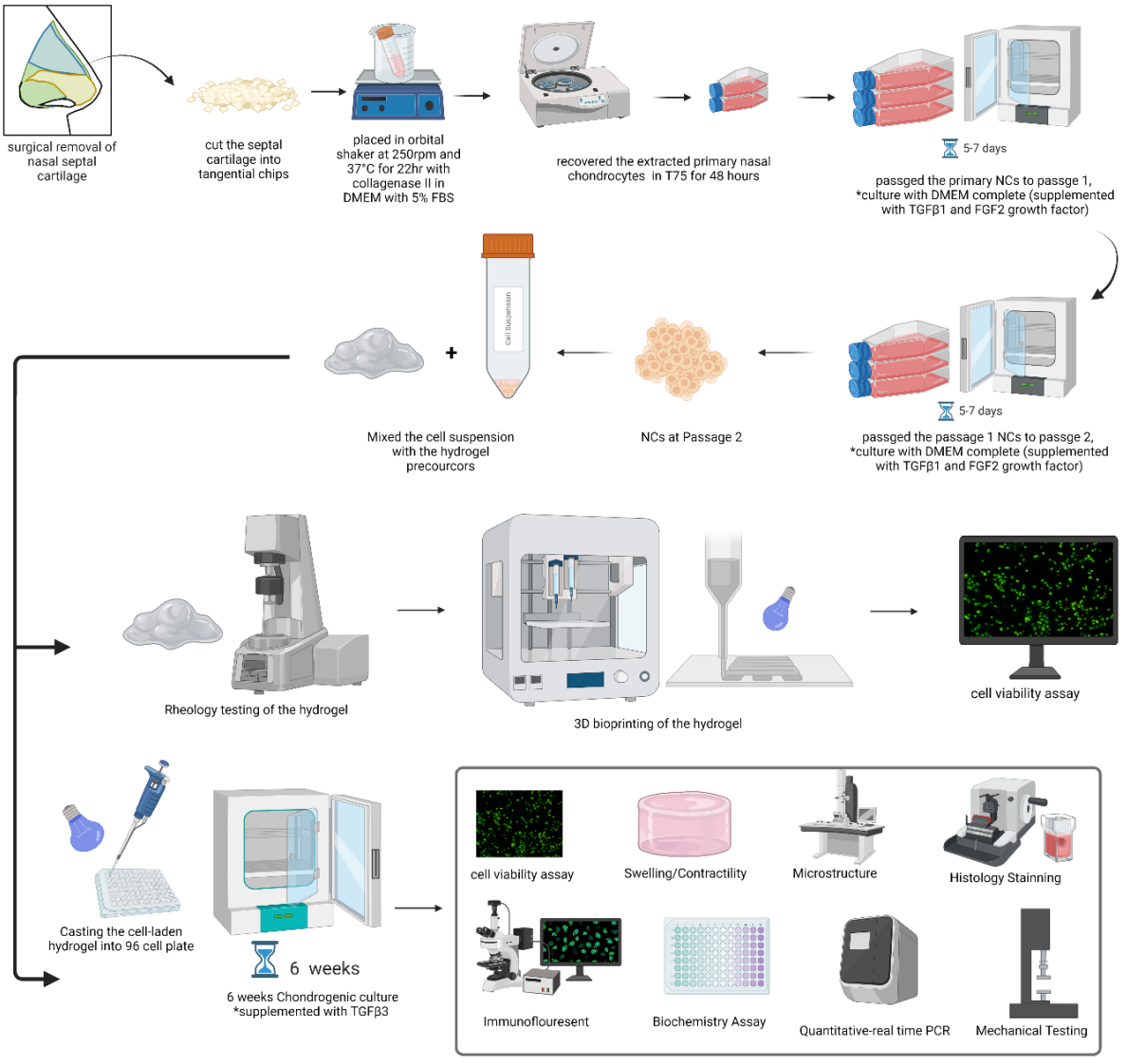

Figure 5.2 Schematic Diagram of the experimental setup

5.2.2 Nasal chondrocyte-laden bioink preparation

Bioink materials were prepared using the stock solutions of COLMA, THA, and PEGDA (illustrated in Figure 5.1) at 8 mg/mL under sterile conditions. The 8 mg/mL neutralized COLMA stock (CELLINK, USA) was dissolved in 20mM acetic acid, with 0.1% (w/v) of Lithium phenyl-2,4,6-trimethylbenzoylphosphinate (LAP) photo-initiator, and the pH was adjusted to around 7.5. The 8 mg/mL thiolated HA stock solution (Hystem, Advanced Biomatrix, USA) was prepared by dissolving with deionized water with 0.1% w/v of LAP photo-initiator. To prepare the COLMA+THA bioink, the COLMA was mixed with THA with a ratio of 1:1. To prepare the COLMA+THA+PEGDA solution, the solid PEGDA (Hystem, Advanced Biomatrix, USA) was first mixed with COLMA, then mixed with THA. The ink formulations for each group are summarized in Table 5.2.

Table 5.2 Formulation of each group of bioink

	COLMA : THA: PEGDA	COLMA concentration	THA concentration	PEGDA concentration	LAP concentration	Total biopolymer concentration	Total solid concentration
COLMA bioink	1:0:0	8mg/mL	0	0	0.1% w/v	8mg/mL	8mg/mL
COLMA+THA bioink	1:1:0	4mg/mL	4mg/mL	0	0.1% w/v	8mg/mL	8mg/mL
COLMA+THA+ PEGDA bioink	1:1:0.5	4mg/mL	4mg/mL	2mg/mL	0.1% w/v	8mg/mL	10mg/mL

5.2.3 Rheology characterization and 3D bioprinting process

A rotatory rheometer (AR-G2, TA Instrument, USA) with a 25 mm parallel plate was used to evaluate the rheology property of the bioinks. For steady-state flow sweep, shear rates were set at 10^{-3} to 10^{3} s^{-1} under 16 ℃. The temperature sweep was set between 16 ℃ and 40 ℃ with a ramp rate of 1 °C with fixed strain (1%, within the linear viscoelastic envelope) and frequency (10 rad/s). For oscillatory frequency sweep, a frequency of 1 to 100 rad/s with fixed strain (1%) was

used under 16 ℃. TRIOS software (TA Instruments, United States) was used to analyze the resulting data.

Micro-extrusion-based bioprinter, BIO X (CELLINK, Sweden), was used to print the construct into a petri-dish. The cells were first mixed with the bioink material with a cell concentration of 10 million/mL. The bioinks were then rested in the fumehood for 1 hour. The bioinks were then loaded into the cartridge. A 2 cm*2 cm*0.2cm constructs with a 30% infill rate were bioprinted in the petri-dish. The bioprinted constructs were then crosslinked by UV for 90 seconds.

5.2.4 Live/Dead Assay

The NCs cell viability after printing was assessed by Syto 13/Propidium iodide (PI) staining, Syto 13 (S7575, Thermo Fisher Scientific, Canada) stains the live-cell in green fluorescent, and PI (P3566, Thermo Fisher Scientific, Canada) stains the dead-cell in red fluorescent. After bioprinting, the constructs (before and after UV curing) were cultured in a chondrogenic medium(100 U/mL penicillin, 100 µg/mL streptomycin, 2 mM L-glutamine, 10 mM HEPES, ITS + 1 premix, 10 ng/mL transforming growth factor β3, 100 nM dexamethasone, 365 µg/mL ascorbic acid 2-phosphate, 125 µg/mL human serum albumin and 40 µg/mL L-proline) for 1 day, then incubated in 1mL PBS solution with 6.25 µM Syto 13 and 15 µM PI at room temperature in the dark for 30 minutes. A Nikon Eclipse TiS microscope coupled to a DS-U3/Fi2 Color CCD camera was used to view the viability of bioprinted constructs. Fuji Image J software was used to quantify.

5.2.5 Evaluation of cartilage formation

To compare and evaluate the cartilaginous ECM formation of each bioink material after *in vitro* culture, each of the three bioinks was mixed with NCs with a cell concentration of 10 million/mL and then cast in low attachment flat-bottom 96-well plates (Sarstedt, Germany). 75 µL of cell-laden bioink materials was added into each well. The chondrogenic medium containing 10 ng/mL of TGF-β3 was used for *in vitro* tissue culture for 6 weeks under normoxia condition (21% O_2). In the first two weeks, 250 µL/construct of the chondrogenic medium was used for tissue culture; the medium was changed every day in the first two weeks. The constructs were then transferred into 24 well plates in the following four weeks with 2 mL/constructs of the chondrogenic medium; the medium was changed twice per week.

5.2.5.1 Gross morphology pictures and the contraction/swelling ratio

After six weeks of chondrogenic culture, the shape and the size of the engineered cartilage constructs were recorded a Zeiss stereo microscope. The surface area of the constructs was measured through Image J software. As the initial cast area of the 96-well plate is 29 mm^2, the contraction/swelling ratio was calculated as

$$\frac{Contraction}{swelling} ratio\ (\%) = \frac{A_{\ after\ culture} - 29\ mm^2}{29\ mm^2}$$

The negative value indicates a contraction of the scaffold, and the positive value indicates a swelling of the scaffold.

5.2.5.2 Sulfated glycosaminoglycans per DNA quantification

A 1,9–dimethylmethylene blue (DMMB, Sigma-Aldrich, Canada) assay with chondroitin sulfate (Sigma Aldrich, Canada) as standard was used to measure the glycosaminoglycan (GAG) content of the bioprinted cartilage. Firstly, PBS was used to rinse the bioprinted cartilage twice. The bioprinted cartilage was then stored at - 80 ℃. Then, the constructs were thawed and digested in Proteinase K (1 mg/ml) solution for 16 hours at 56 ℃. The V-max kinetic microplate reader (Molecular Devices, USA) was used to evaluate the total GAG content at a wavelength of 530 nm.

To measure the DNA content of the constructs, a DNA assay was performed using the CyQUANT Cell Proliferation Assay Kit (Thermo Fisher Scientific). A standard curve was created using calf thymus DNA (Sigma-Aldrich). CytoFluor II fluorescence multi-well plate reader (PerSeptive Biosystems) was used to measure fluorescence emission at 530 nm (excitation 450 nm). Lastly, GAG content was normalized to total DNA and wet weight (WW) of the construct.

5.2.5.3 Histology and Immunofluorescence

After 6 weeks of *in vitro* culture, the engineered cartilage samples were fixed in 10% (v/v) neutral buffered formalin (Fisher Scientific, MA, USA) overnight at 4 ℃. The samples were then paraffin-embedded and sectioned into 5 μm thickness slices. To perform the staining, the sectioned slides were deparaffinized using a Ultraclear (xylene substitute) and rehydrated using a graded series of 100%, 96% v/v, 70% v/v, and 50% v/v alcohol and distilled water. Then the sections were stained for histology using Safranin-O/Fast Green and immunofluorescence using type I/ type II and type X collagen antibodies.

For Safranin-O/Fast green histology staining, sections were first stained by Haematoxylin (Sigma-Aldrich, United States) for cell morphology, then stained by Fast Green (Sigma-Aldrich, USA) stained for histones and proteins, and finally stained by Safranin-O (Sigma-Aldrich, USA) for sulfated glycosaminoglycan.

For immunofluorescence staining, the sections were first gone through antigen retriever step described previously[398]. Sections were then incubated with primary type I (Rabbit anti-human type I collagen, CL50111AP-1, Cedarlane, Canada), type II (mouse anti-type II collagen, II-II6B3, Developmental Studies Hybridoma Bank, USA), and type X collagen (rabbit anti-human collagen X, Abcam, UK, #ab58632) with 1:200 dilution overnight at 4°C. The secondary antibodies (goat anti-rabbit IgG Alexa Fluor 594 #ab150080; goat anti-mouse, IgG Alexa Fluor 488 #ab150117, Abcam, UK) with 1:200 dilution was incubated with the slides for 45 minutes to visualize the bound primary antibodies. The sections on the slides were stained with DAPI (4′, 6-diamidino-2-phenylindole, Cedarlane) to visualize the cell nuclei. Nikon Eclipse TI-S microscope was used to examine the stains and capture images.

5.2.5.4 Real-time qRT-PCR

Tissue constructs (n = 2 for each donor and N =10) were preserved in Trizol (Life Technologies, United States) immediately upon harvesting and stored at −80°C for RNA extraction. Total RNA was extracted with PuroSPIN Total DNA Purification KIT (Luna Nanotech, Canada) following the manufacturer's protocol. The purity and concentration of the extracted RNA were immediately examined using Nanodrop One C (Thermo Fisher Scientific). 100ng of total RNA was reversely transcribed into cDNA. The genes of interest were amplified by quantitative real-time polymerase chain reaction (RT-qPCR) using their specific primers (Table 5.3).

The mRNA expression level for genes of interest was normalized to the housekeeping genes β-actin (ACTB), Beta-2 microglobulin (B2M), and Tyrosine 3-Monooxygenase/Tryptophan 5-Monooxygenase Activation Protein Zeta (YWHAZ), using the $2^{-\Delta Ct}$ method.

Table 5.3 Primer Sequences for Real-Time qRT-PCR

Genes	Forward Primer (5′)	Reverse Primer (3′)
Beta-actin (*ACTB*)	AAGCCACCCCACTTCTCTCTAA	AATGCTATCACCTCCCCTGTGT
Beta-2 microglobulin (*B2M*)	TGCTGTCTCCATGTTTGATGTATCT	TCTCTGCTCCCCACCTCTAAGT
Tyrosine 3-Mono-oxygen-ase/Tryptophan 5-monooxygenase activation protein Zeta (*YWHAZ*)	TCTGTCTTGTCACCAACCATTCTT	TCATGCGGCCTTTTTCCA
Aggrecan (*ACAN*)	AGGGCGAGTGGAATGATGTT	GGTGGCTGTGCCCTTTTTAC
type I collagen (*COL1A2*)	GCTACCCAACTTGCCTTCATG	GCAGTGG-TAGGTGATGTTCTGAGA
type II collagen (*COL2A1*)	CTGCAAAATAAAATCTCGGTGTTCT	GGGCATTTGACTCACACCAGT
SRY-Box 9 (*SOX9*)	CTTTGGTTTGTGTTCGTGTTTTG	AGAGAAA-GAAAAAGGGAAAGGTAAGTTT
Collagen X (*COL10A1*)	GAAGTTATAATTTACAC-TGAGGGTTTCAAA	GAGGCACAGCTTAAAAGTTTTAA ACA
Runt related transcription factor 2 (*RUNX2*)	GGAGTGGACGAGGCAAGAGTTT	AGCTTCTGTCTGTGCCTTCTGG
Peroxisome proliferative activated receptor gamma (*PPARγ*)	AAGCTGCTCCAGAAAATGACAGA	CGTCTTCTTGATCACCTGCAGTA
Alpha smooth muscle Ac-tin (ACTA2)	CTATGCCTCTGGACGCACAACT	CAGATCCAGACGCATGATGGCA
Transgelin (TAGLN)	AGTGGGGGAGGCTGACAT	TCGCAGGAAGGAGTGAAGAC
Lysyl Oxidase Like 2 (*LOXL2*)	ACGGCCACCGCATCTG	TCCGTCTCTTCGCTGAAGGA

5.2.6 Mechanical properties of engineered cartilage tissue

A stepwise stress relaxation test was used to assess the unconfined compressive modulus of tissue constructs using the BioDynamic 5210 system (TA Instruments, USA). Constructs were first preconditioned by 15 cycles of sine wave dynamic loading with an amplitude of 5% tissue height at the frequency of 1 Hz. The following stress relaxation test consisted of 3 incremental strain

steps with a 10% strain ramp in each step at the rate of 50% strain/sec followed by 5 min relaxation to reach equilibrium under constant strain. The cross-section areas of tissue constructs were measured before mechanical tests. Stress at each step was calculated by normalizing the compressive force to the cross-section area. The peak modulus was calculated by dividing the peak stress at each strain step by the corresponding strain increment (10%). The equilibrium modulus was determined by utilizing the equilibrium stress value obtained at the conclusion of the relaxation period for each strain increment.

5.2.7 Data analysis and statistical method

One-way ANOVA (donor was treated as repeated measurements) was used to compare the GAG/DNA, wet weight, gene expression, change of area, and compressive modulus at each strain level. Tukey's post hoc test was performed for the pairwise comparisons in bioink types. Two-way ANOVA (donor was treated as repeated measurements) was performed to assess the cell viability before and after UV curing within the three bioink groups. Tukey's post hoc tests were performed for the pairwise comparisons to compare two variables. Data are presented as mean ± standard deviation (SD). All analyses were performed using GraphPad Prism 8. A p-value < 0.05 was considered statistically significant, and a p-value between 0.05 and 0.1 was considered borderline significant.

5.3 Results

5.3.1 Rheology characterization and 3D bioprinting of engineered cartilage with autologous shapes

The rheological property of each bioink group was studied to estimate the printability of the potential bioinks. After mixing, the bioinks were rested in the hood before printing to allow for any crosslinking reactions. The flow sweep (viscosity vs. shear rate) of all three bioinks is shown in Figure 5.3A. All three bioinks exhibited shear-thinning behavior, where the viscosity of the bioinks decreased as the shear rate increased. The COLMA demonstrated lower zero share viscosity than both COLMA+THA and COLMA+THA+PEGDA bioinks.

Collagen solutions exhibit thermo-induced fibril polymerization behavior as temperature increased. Since the tissue culture incubator has a temperature of 37°C, the temperature range of 16-40 °C was selected to measure the thermos-induced fibril polymerization profile of three bioinks. The changes in storage modulus (G') from a temperature range of 16-40 °C are shown in Figure 5.3B. All three bioinks displayed different polymerization profiles as the temperature increased. COLMA showed the least storage modulus at the lower temperature (16°C). As the temperature increased, a dramatic increase in storage modulus was shown from around 25 to 35°C, then gradually plateaued after 35°C. The COLMA+THA and COLMA+THA+PEGDA required a higher temperature to respond to the fibril polymerization. After the polymerization, the COLMA+THA and COLMA+THA+PEGDA showed a slower increase in storage modulus and smaller maximum storage modulus in the selected temperature range.

A frequency sweep is used to compare the bioink microstructure before and after cross-linking. Storage moduli (G') indicate the elastic behavior of the bioink, and loss moduli (G'') indicate the

viscous behavior. In Figure 5.3C, for all three bioinks, the G' is higher than the G'', meaning that all three bioinks showed a gel-like behavior before cross-linking. The difference between the storage and loss modulus of COLMA is less significant than in the COLMA+THA and COLMA+PEGDA, and both G' and G'' are smaller than the other two bioinks and are highly dependent on the frequency. COLMA+THA and COLMA+THA+PEGDA showed similar G' and G'' profiles under frequency sweep. COLMA+THA+PEGDA showed slightly higher G' than COLMA+THA. Figure 5.3D shows the G' and G'' of the bioinks after 90 seconds of UV cross-linking. The G' of COLMA, COLMA+THA and COLMA+THA+PEGDA increase around 17.5-fold, 10.1-fold, and 5.4-fold, respectively. Both G' and G'' are almost independent of frequency for all bioinks after the UV crosslinking.

Grid structures were then printed to demonstrate and compare the printability between each bio-ink group. The bioprinted constructs are shown in Figure 5.3E. Relative to COLMA, the COLMA+THA and COLMA+THA+PEGDA showed better printability regarding post-printing diameter. The COLMA+THA+PEGDA showed the best printing fidelity with the finest filament diameter after printing.

After bioprinting, the cell viabilities for COLMA, COLMA+THA, COLMA+THA+PEGDA was determined to be 90.9 ± 0.5%, 89.5% ± 1.5%, and 85.71% ± 0.6%, respectively (Figure 5.3F and Figure 5.3G). No significant difference was observed between COLMA vs. COLMA+THA groups and COLMA+THA vs. COLMA+THA+PEGDA group, while a significant difference was observed between COLMA and COLMA+THA+PEGDA group (adjusted p value = 0.0268). After UV curing, the cell viability for COLMA, COLMA+THA, and COLMA+THA+PEGDA were determined to be 62.3% ± 5.8%, 85.7% ± 1.2% and 83.3% ± 1.2%, respectively. A significant drop in cell viability was observed in the COLMA group (adjusted p value <0.0001) with a

mean difference of -23.4%. The other two groups observed no significant difference before and after UV curing. The cell viability after curing for COLMA is significantly lower than COLMA+THA and COLMA+THA+PEGDA (adjusted p value <0.0001 for both).

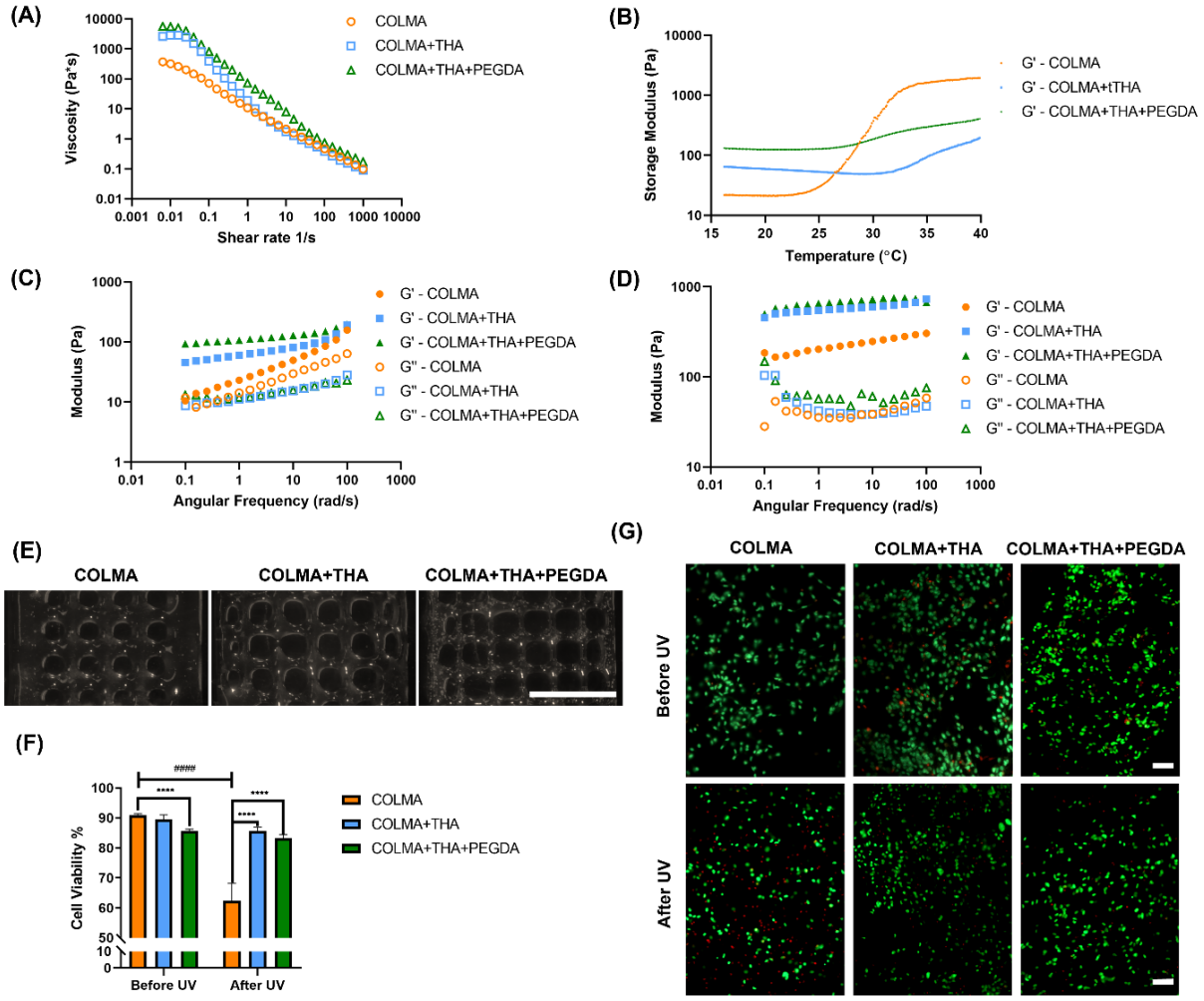

Figure 5.3 3D-bioprinting related rheological and cell viability characterization. (A) The steady state flow sweeps of three bioinks, strain rate from 0.001 to 1000 s^{-1}, at 16°C (without UV crosslinking) (B) The temperature ramp sweep of three bioinks from 16°C to 40°C at 10 rad/s (without UV crosslinking) (C) The frequency sweep of three bioinks, angular frequency from 1-100 rad/s (without UV crosslinking) at 16°C (D) The frequency sweep of three bioinks, angular frequency from 1-100 rad/s (after UV crosslinking) at 16°C (E) 3D bioprinted mesh structure using three bioinks. Scale bar: 1 cm (F) Quantified cell viability of bioprinted constructs before and after UV crosslinking (n=4), Star (*) represent the significant difference with regarding of types of bioink after Tukey's post hoc correction: * represents 0.01<p <0.05, ** represents 0.001<p<0.01, *** represents 0.0001<p<0.001, **** represents p<0.0001. Pound (#) represent the significant difference with regarding of the effect of UV curing after Tukey's post hoc correction: # represents 0.01<p <0.05, ## represents 0.001<p<0.01, ### represents 0.0001<p<0.001, #### represents

p<0.0001. (G) Live/dead images after bioprinting, with and without UV crosslinking, live cell appears green and dead cell appears red, Scale bar: 100µm

5.3.2 Gross morphology and contractility of *in vitro* engineered cartilage

To investigate the potential of the bioinks to support in vitro chondrogenesis of the encapsulated nasal chondrocytes, the bioinks with cell content were cast into 96-well plates and cultured under normoxia conditions for 6 weeks. The size of the casted scaffold varied between donors (Figure 5.4A). In general, the addition of crosslinker (PEGDA) resulted in no contraction, which was observed for all 5 donors after 6 weeks of *in vitro* chondrogenic culture. The COLMA+THA+PEGDA also swelled more compared to the other groups, with an average swelling ratio of 27.7% (Figure 5.4B). For the COLMA only group, all the constructs were significantly contracted with a contraction ratio of 49.7% (Figure 5.4B). For COLMA+THA group, the contraction/swelling of the constructs was highly dependent on the nasal chondrocytes' donor: three constructs swelled, and two contracted. The average change area (absolute value) was 31.4% (Figure 5.4C). In general, the COLMA+THA+PEGDA retained the casted morphology, displayed a predictable swelling pattern, and was the least unchanged in surface area regardless of donor variability.

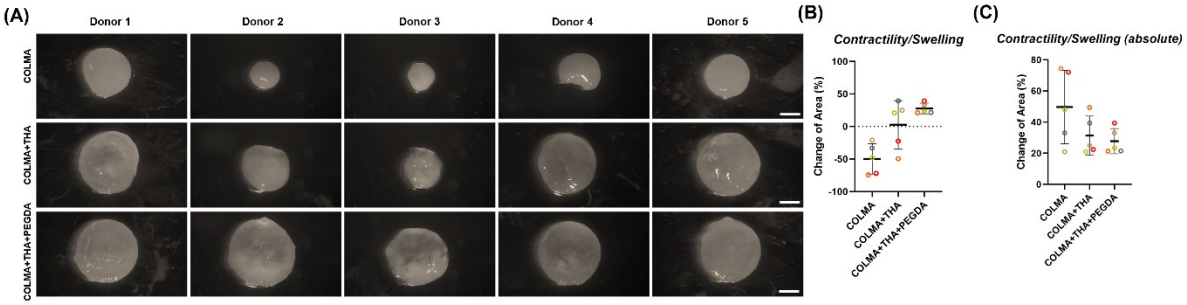

Figure 5.4 (A) Gross morphology of engineered cartilage using COLMA, COLMA+THA, COLMA+THA+PEGDA bioink materials with nasal chondrocytes after 6 weeks of *in vitro* chondrogenic culture. Scale bar: 2mm (B) The contractility (negative -) and the swelling (positive +) of the construct

compared to the initial casting area (29mm2). (C) the absolute area changes of the constructs before and after *in vitro* culture.

5.3.3 Histological analysis of *in vitro* engineered cartilages

The empty bioink showed positive Fast Green staining, but no positive Safranin-O or type I collagen stained (data not shown).

After 6 weeks of chondrogenic culture, all constructs showed positive Safranin-O staining throughout the construct (Figure 5.5A). Most NCs exhibited round chondrocyte morphology within the bioink to form round lacuna structures in all three groups. Type I collagen (red) and II (green) immunofluorescence was performed for each group, as shown in Figure 5.5A. All constructs show positive type I and II collagen staining, with type II collagen being much for evident throughout the construct and type I collagen is mainly on the paraffin of the tissue. A variation was observed between the donors. No type X collagen was stained for all three groups.

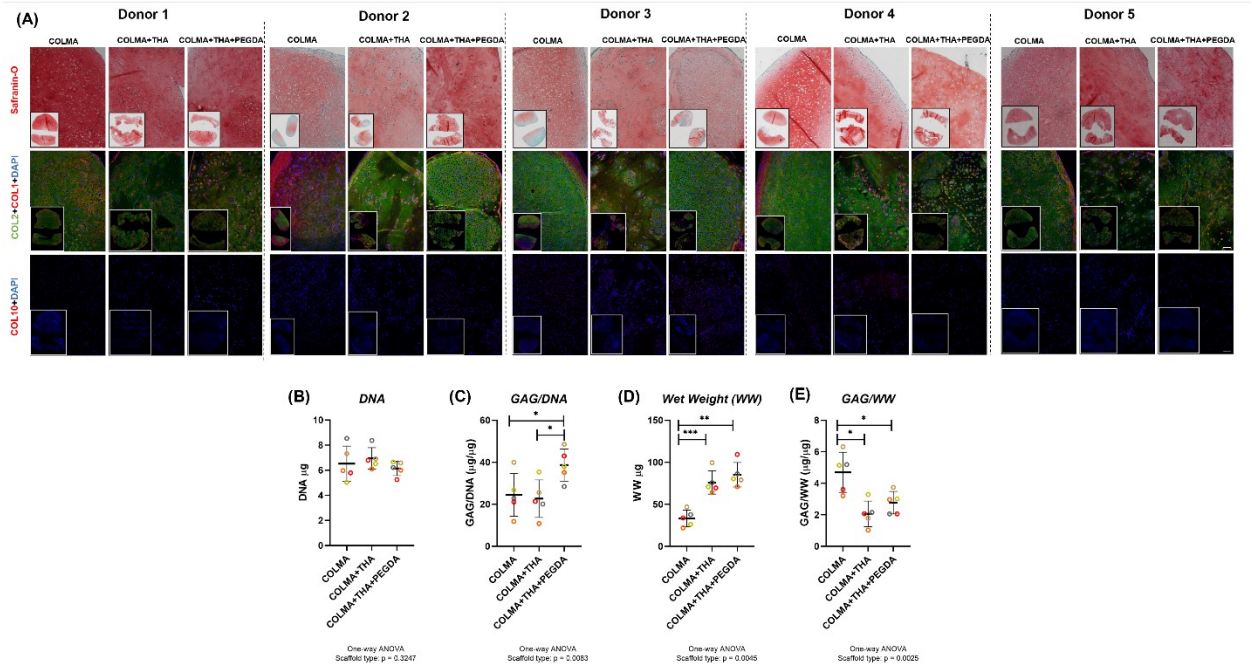

Figure 5.5 Qualitative histology and immunofluorescence investigation of cartilaginous ECM for engineered cartilages (A) Safranin-O staining (red or pink represents proteoglycan, green represents collagen-

based protein), type I collagen and II staining (red represents type I collagen, green represents type II collagen, blue represents DAPI), Collagen X staining (red represents collagen X, blue represents DAPI). Quantitative physical and biochemical analysis of engineered cartilages (B) DNA content in the constructs (C) GAG/DNA (D) Weight wet (WW) (E) GAG/WW. p values are from one-way ANOVA with Tukey's post hoc test. Star (*) represent the significant difference with regarding of types of bioink after Tukey's post hoc correction: * represents $0.01<p<0.05$, ** represents $0.001<p<0.01$, *** represents $0.0001<p<0.001$, **** represents $p<0.0001$.

5.3.4 GAG/DNA quantification of *in vitro* engineered cartilages

To quantitatively analyze GAG formation for each bioinks after 6 weeks of chondrogenic culture, a DMMB blue assay was performed to measure the GAG content, and CyQuant DNA assay was performed to measure the DNA content for each group. The DNA content, GAG per DNA (GAG/DNA), weight wet (WW), GAG per WW (GAG/WW) are presented in Figure 5.5B, C, D and E, respectively.

The DNA content was measured to investigate the cell amount and proliferation. The DNA content is generally constant throughout all three groups (One-way ANOVA $p=0.3247$). The accumulated GAG content was measured and normalized to DNA content for each engineered cartilage construct to assess the ability of the nasal chondrocytes to produce GAG in the different bioinks. The COLMA+THA+PEGDA group showed significantly higher GAG/DNA than the COLMA and COLMA+THA (Tukey's adjusted $p=0.0362$, $p=0.0473$ respectively), while no significant difference was observed between COLMA and COLMA+THA group.

The total wet weight (WW) of the engineered constructs includes the ECM and water. COLMA group showed a significantly lower WW compared to COLMA+THA and COLMA+THA+PEGDA (adjusted $p=0.0003$, $p=0.0038$, respectively). The GAG contents were then normalized by WW for each engineered cartilage. COLMA showed the highest GAG/WW

among the groups (adjusted p=0.0177 compared to COLMA+THA, p=0.0379 compared to COLMA+THA+PEGDA).

5.3.5 Mechanical properties of *in vitro* engineered cartilages

The compressive modulus (peak) for each experimental group was measured by an unconfined compression test. Figure 5.6 shows the compressive modulus of the engineered cartilage constructs. COLMA group showed a significantly higher compressive modulus compared to the COLMA+THA and COLMA+THA+PEGDA at 10% (adjusted p = 0.0386, 0.0225 respectively), 20% (adjusted p = 0.0353, 0.0222 respectively) and 30% (adjusted p = 0.0148, 0.0090 respectively) stain levels. No significant difference was observed between COLMA+THA and COLMA+THA+PEGDA groups.

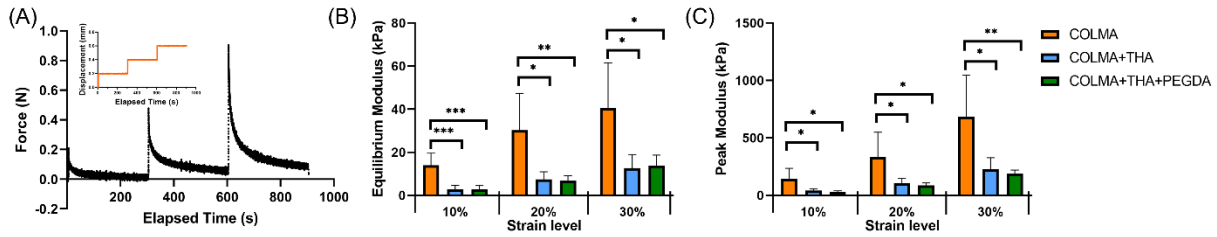

Figure 5.6 Mechanical property of the bioinks, (A) Example of strain steps and data acquisition of the unconfined compression test (B) Equilibrium modulus as a function of the cumulative strain (n=5) (c) Peak modulus as a function of the cumulative strain (n=5). Star (*) represent the significant difference with regarding of types of bioink after Tukey's post hoc correction: * represents 0.01<p <0.05, ** represents 0.001<p<0.01, *** represents 0.0001<p<0.001, **** represents p<0.0001.

5.3.6 Gene expression of *in vitro* engineered cartilage

The gene expression data of the engineered cartilage is shown in Figure 5.7A. The engineered cartilage in the different bioinks significantly differed in chondrogenic gene expression (*ACAN*, *COL2A1*, *SOX9*) and hypertrophic gene expression (*COL10A1*, *RUNX2*). COLMA demonstrated the highest expression of selected chondrogenic genes (*ACAN*, *COL2A1*, and *SOX9*) among all

three groups, with statistically significant results.At the same time, COLMA showed a relatively high hypertrophic gene expression (*COL10A1*, *RUNX2*) among all three groups with borderline significance. No significant difference was observed in the fibrocartilage-related gene (*COL1A2*) and adipogenic-related gene (*PPARγ*). To investigate the contractility/swelling of the tissue, the expression of *ACTA2* and *TAGLN* as genes known to be associated with the contractile phenotype of dedifferentiated chondrocytes were measured. However, there was no significant difference in the expression of these genes between the three bioinks. Similarly, there was no significant difference in the expression of the collagen cross-linking enzyme (*LOX*) between the three bioinks.

To better understand the difference between these three different bioinks, a Pearson correlation heatmap was generated for the three bioinks cohort with all factors of interest (Figure 5.7B). For all three bioinks, the area of the constructs positively correlated with the GAG/DNA and WW. For COLMA and COLMA+THA, the size of the constructs was negatively correlated with the contractile genes *ACTA2* and *TAGLN*. On the other hand, by adding the additional crosslinker to the bioink, COLMA+THA+PEGDA did not show this correlation. For COLMA and COLMA+THA groups, the area of the construct showed a strong negative correlation with the compressive modulus, which means the more the construct contracted, the higher the compressive modulus of the engineered cartilage, while this is not observed in the COLMA+THA+PEG. The GAG/DNA value of the COLMA and COLMA+THA are positively correlated with the chondrogenic gene expression, while the COLMA+THA+PEGDA did not. Overall, the correlation analysis yielded different patterns among each bioink cohort.

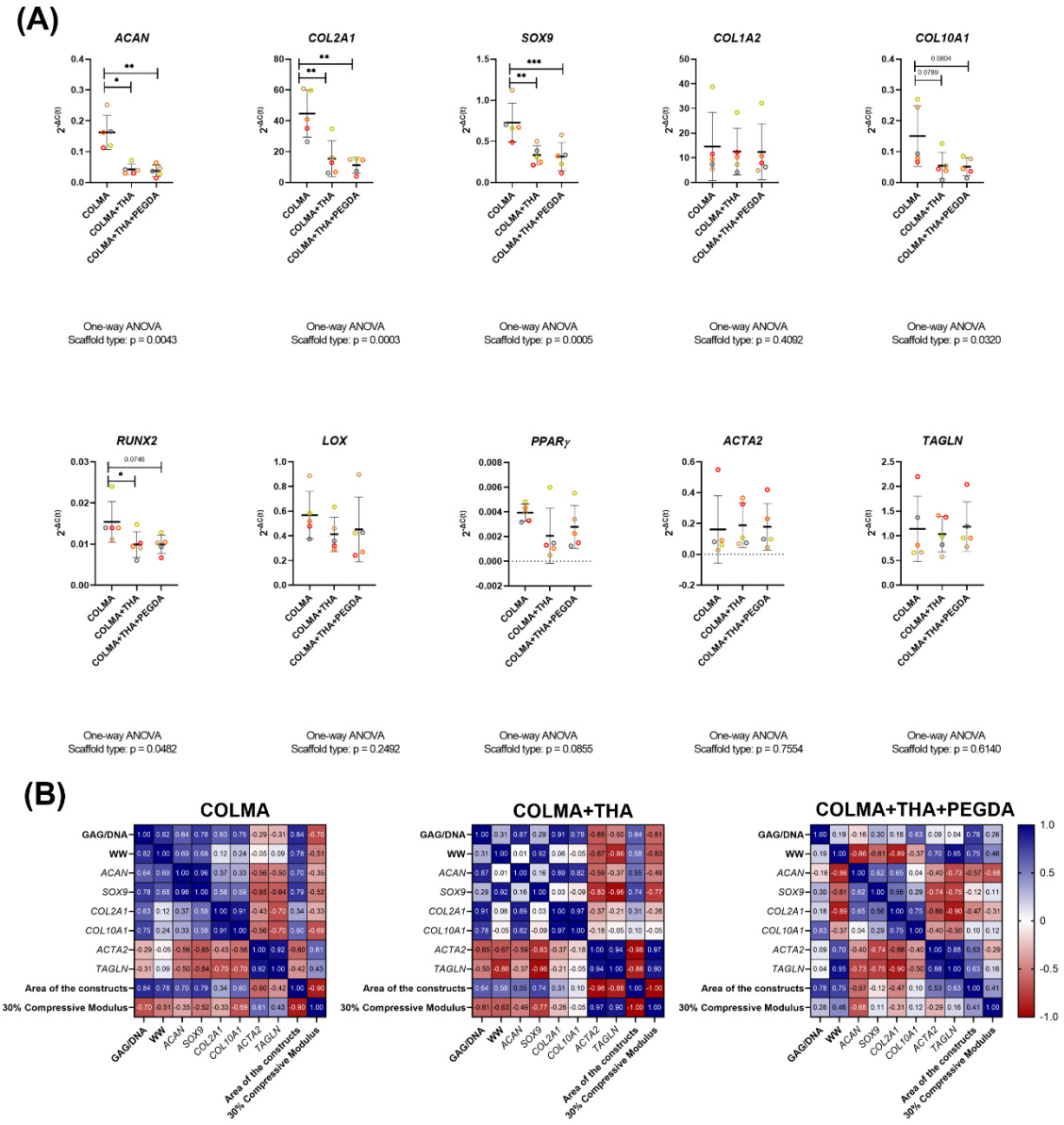

Figure 5.7 (a) Hyaline cartilage related gene expression of the engineered cartilage after 6 weeks of *in vitro* chondrogenic culture (n=5). (b) Pearson correlation heatmap of analyzed factors. Star (*) represent the significant difference with regarding of types of bioink after Tukey's post hoc correction: * represents 0.01<p <0.05, ** represents 0.001<p<0.01, *** represents 0.0001<p<0.001, **** represents p<0.0001.

5.4 Discussion

In this present work, we did a proof-of-concept study by preparing a pre-crosslinked (arylate – arylate, arylate – thiol, thiol - thiol) collagen – hyaluronic acid – PEGDA bioink for cartilage tissue engineering. Three groups of bioinks, including COLMA-only, COLMA+THA, and COLMA+THA+PEGDA, were compared regarding support for *in vitro* cartilage ECM formation, gross morphology, gene expression and mechanical property.

The arylate-thiol reaction could happen slowly without any crosslinker, and the disulphide-linked network (thiol-thiol) can result from the oxidation of the thiols in THA to molecular oxygen in ambient air (Figure 5.1). These two reactions increase the solid-like behavior of the COLMA+THA and COLMA+THA+PEGDA bioinks. The frequency sweep test without UV curing (Figure 5.3C) further validates the gel formation. Even all bioinks showed a predominance of G' over G'' (G'>G''), indicating gel-like behavior. The G' and G'' for COLMA+THA and COLMA+THA+PEGDA are more frequency independent than the COLMA bioink, and the G' of these two bioinks are much higher than COLMA. The frequency independence of G' and G'' indicates a large relaxation time, which characterizes more solid-like behavior [432]. Therefore, the COLMA showed weaker gel behavior compared to the other two bioinks. The stronger-gel behavior in COLMA+THA and COLMA+THA+PEGDA gave better dimensional stability of the printed structure and more precise filament diameter than COLMA bioink, which allows the bioink to hold its shape for some time following printing and before UV crosslinking (Figure 5.3E).

Shear-thinning property can alleviate shear stresses acting on the cells during the flow through in the printing nozzle. Therefore, this is an important property for bioinks used in extrusion-based

bioprinting[432]. In the steady state flow sweep test (Figure 5.3A), all three bioinks exhibited a shear-thinning behavior – decreasing viscosity as the shear rate increased. Both collagen and HA are long-chain biopolymers. The shear thinning behavior may be attributed to the biopolymer chain's disentanglement and the break of structured chain-chain interactions during flow. As the shear rate increases, the entanglement, as well as the interactions of the hydrogel network, is weakened, and the entrapped liquid that resists the flow is released, and therefore the viscosity decreases.

As collagen exhibits a thermosensitive property, a temperature sweep test was used to investigate the behavior of thermo-responsive G. The pre-crosslinking increased the initial G' at a low-temperature range but flattened the sol-gel transition of the bioink and yielded a weaker thermosensitive network. This may be due to the dilution of the collagen concentration by THA since the collagen concentration is known to affect the fibrillogenesis process[188]. For COLMA-only bioink, collagen concentration was 8 mg/mL, while by adding the HA biopolymer in a 1:1 ratio, the collagen concentration was diluted into 4 mg/mL for COLMA+THA and COLMA+THA+PEGDA.

After 90 seconds of UV crosslinking, the G' of COLMA increased about 17.5-fold, while the G' of COLMA+THA and COLMA+THA+PEGDA increased about 10.1-fold and 5.4-fold, respectively. This may be attributed to the pre-crosslinking of COLMA+THA and COLMA+THA+PEGDA. Even though UV curing can accelerate the thiol-ene click reaction, some binding sites (acylate and thiol) for the structure assembly have been consumed in the pre-crosslinking stage before UV curing. The COLMA+THA+PEGDA still showed the highest G' among all three bioinks after UV curing at 16 °C.

In addition to printability, cell viability after printing and crosslinking also plays a vital role in the success of 3D bioprinting. A LIVE/DEAD assay was performed to investigate the cell viability after bioprinting and after UV curing. COLMA showed the highest cell viability after bioprinting (without UV curing) compared to the other two bioinks. As the COLMA bionk is the least viscous among the three groups, it generated the smallest shear stress during the printing process and leading to higher cell viability. However, COLMA showed a significantly reduced cell viability after the UV crosslinking process, while no significant difference was observed for COLMA+THA and COLMA+THA+PEGDA. Through UV crosslinking, (meth)acrylate groups were photo-crosslinked through radical chain-growth reaction to from arylate-arylate bond, while the UV crosslinking can also accelerate thiol-ene radical step-growth reaction between the (meth)acrylate group and thiol group. This means that there are different polymerization reaction models in these three bioinks. Both COLMA+THA and COLMA+THA+PEGDA achieve the gelation by a mixed model of chain-growth and step-growth reaction, while the COLMA group only involved the chain-growth reaction. Previous research has reported the influence of chain-growth and step-growth polymerization reactions on cell viability and protein activity after *in situ* UV cross-linking. Lin et al. showed that the step-growth thiol-ene photo-click gelation in a PEG-based hydrogel showed more cytocompatibility than chain-growth polymerization for *in situ* pancreatic β-cells[433]. Monoz et al. reported that the thiol-ene reaction showed significantly higher cell viability for *in situ* human mesenchymal stem cells (MSC) encapsulation than the chain-growth arylate reaction [434]. Mũnoz et al suggests that propagating acrylate chain growth reactions are more reactive than the thiol-ene step growth, which may lead to damaging reactions with protein and/or lipids in the cell membrane[435]. Previous studies have also confirmed that arylate chain growth reaction may cause lipid peroxidation of the cell membrane in

chondrocytes, which leads to intracellular reactive oxygen species (ROS) generation[436]. We, therefore, hypothesize that the significant decrease in cell viability in COLMA group may be due to the propagation of acrylate-based radical attack of the chondrocytes during crosslinking, leading to upregulation of intracellular ROS, further causing the increase in cell death in the COLMA bioink [437].

The spreading of cells will generate a traction force in hydrogel, and as the mechanical strength of the hydrogel network cannot resist the force, a cell mediated contraction can occur[438]. Chondrocytes exhibit a contractile property in collagen hydrogel, which is considered one of the significant obstacles to the application in cartilage tissue engineering[439]. In COLMA only group, a significant contraction was observed, while partial contraction was observed in COLMA+THA group, and no contraction was observed in the COLMA+THA+PEGDA group. This may be attributed to two reasons n: 1) differences in the polymerization model may contribute to the difference in contractile properties for the engineered cartilage constructs; 2) specific ECM components with different ECM ligands may contribute to the different contractile properties in each bioink. The step-growth polymerization can form a more homogeneous and structured polymer network compared to chain-growth polymerization, which leads to a less contractile property[440]. By adding a thiol crosslinker, PEGDA, a higher crosslinking density in step-growth hydrogel can be achieved. The higher crosslinking density will further enhance the polymer structured network, making the network more stable and improving restriction on the spreading of the chondrocytes, thereby reducing the contraction [441]. Biologically, the cell adhesion motif in COLMA includes the GxOGER and RGD peptide, with which chondrocytes can interact through integrin receptors, while for COLMA+THA and COLMA+THA+PEGDA bioinks, the chondrocytes are able to recognize both collagen and hyaluronic acid through integrin

and CD44 receptors, respectively. This observation aligns well with previous literature. Yang et al. found that HA showed no shrinkage, while the type I collagen hydrogel showed significant contraction under in vitro chondrogenic culture of bone marrow stem cells (BM-MSC)[438]. By adding hyaluronic acid to the collagen I hydrogel, there was a significant reduction in contraction [442]. A study with bovine chondrocytes demonstrated that β1 integrin plays an essential role in collagen gel contraction by mediating signals leading to matrix metalloproteinase (MMP) production and collagen remodeling [443]. The entrapment of water by the negatively charged HA may also be a reason that resists the contraction by the cell[444]. In addition, as the cell surface is negatively charged, the negatively charged HA may cause electrostatic repulsion to cells, which was not conducive to spreading, therefore leading to a weaker cell traction force.

All three bioinks showed positive cartilaginous ECM staining (sulphated GAG and type II collagen) without hypertrophic protein formation (type X collagen) throughout the constructs. This indicates that all three bioink supported cartilaginous tissue formation. COLMA+THA+PEGDA showed the highest GAG/DNA, which meant that the nasal chondrocytes in the COLMA+THA+PEGDA bioink had a better GAG synthetic capacity. The GAG/DNA result matched well with the gross appearance of the safranin-O stained sections, where the staining of the sections from the COLMA+THA+PEGDA engineered cartilage constructs were homogenously evident throughout the whole constructs developed from the nasal chondrocytes of all five donors. It is highly probable that the homogenous deposition of the GAG matrix within the COLMA+THA+PEGDA bioink was in part due to the bioink's capacity to resist cell-mediated contraction which allowed them to maintain a more porous microstructure that was beneficial for nutrient transport.

The wet weight of both COLMA+THA and COLMA+THA+PEGDA were significantly higher than COLMA while the GAG/WW of COLMA was significantly higher than COLMA+THA and COLMA+THA+PEGDA. This may be due to the presence of HA in the bioink since the abundant carboxyl groups in HA can easily interact with water to form hydrogen bonds, making it a super hydrophilic molecule that can absorb large amounts of water. HA can significantly increase the wet weight, leading to a lower GAG/WW for the THA-incorporated bioniks[444]. The higher GAG/WW results in more GAG molecules in unit mass of engineered cartilage tissue, with a denser GAG distribution, which agrees with the contractile gross morphology of the COLMA bioink.

The higher compressive modulus of the engineered cartilages via COLMA bioink relative to the engineered cartilage in the COLMA+THA and COLMA+THA+PEGDA bionks is most likely due to the significant cell-mediated contraction in the COLMA bioink. The compressive moduli for COLMA and COLMA+THA are strongly negatively correlated to the area of the scaffold (Pearson r = -0.9 and -1, respectively), meaning that the more the scaffold contracts, the higher the compressive modulus. This further proved that the contraction led to a denser tissue formation, further increasing mechanical properties.

ACTA2 and *TAGLN* are characteristics of the contractile phenotype in dedifferentiated articular chondrocytes, in which their activity is associated with cytoskeletal composition and structure[445, 446]. *ACTA2* and *TAGLN* expression negatively correlated with the area of engineered cartilage constructs and positively correlated with the compressive modulus in both COLMA and COLMA+THA bioinks. These correlations suggests that the expression of *ACTA2* and *TAGLN* are associated with the contractile phenotype of the nasal chondrocytes in the COLMA and COLMA+THA bioinks. Furthermore, it is probable that the myocardin-related transcription

factor-a (MRTF-A) is involved in regulating this contractile phenotype. MRTF-A has been shown to upregulate ACTA2 and TAGLN expression in the acquisition of the contractile phenotype articulated chondrocytes[446]. For the enhanced crosslinking group, COLMA+THA+PEGDA, since no contraction of the engineered cartilage was observed, there are no correlations between the mechanical property and the contractile gene expression. To further improve the mechanical property of COLMA+THA+PEGDA for bioprinting, low cytotoxic crosslinkers such as genipin, transglutaminase, and lysl oxidase can be used to further improve the mechanical property of engineered cartilage after bioprinting or during the culture period.

Even though the GAG/DNA of the COLMA+THA+PEGDA are significantly higher than the other two bioink groups, the COLMA group showed the highest gene expression in all chondrogenic-related genes of interest (*ACAN*, *COL2A1*, and *SOX9*). The reason for the unmatched gene expression profile with the GAG/DNA is unclear and will require future investigation. But a similar observation was reported by Yang et al [438]. Yang and co-authors found that *in vitro* chondrogenic culture of BM-MSC in HA hydrogel displayed the lowest *SOX9* and *COL2A1* expression relative to their in type I collagen hydrogel, but with similar GAG content. It is probable that the cell-mediated contraction in the type I collagen hydrogel recapitulated to some extent the cellular condensation during the early stages of chondrogenic differentiation. While the minimal or lack of cell-mediated contraction in the HA hydrogel enabled space for the chondrogenically induced BM-MSC to secrete cartilage-related ECM. Therefore, we speculate that the extensive cell-mediated contraction of the COLMA bioinks enable cellular condensation leading to an increase of chondrogenic gene expression. However, the contracted bio-ink resulted in a limited volumetric space for the accumulation of GAG matrix. A future time course study can be conducted to investigate the chondrogenic potential of these three bioinks in gene expression and

cartilage ECM secretion at different time points, and this can give us more information on the cartilaginous development in these bioinks.

5.5 Conclusion

In this work, we developed a novel strategy to enhance collagen-based biomaterial using THA and PEGDA. Overall, the COLMA+THA+PEGDA showed better printability, cell viability and cartilaginous ECM production (GAG/DNA), with no contraction after chondrogenic culture *in vitro*, compared to the other two bioinks. These results warrant future animal studies where the bioprinted engineered hyaline cartilage could be implanted, and the *in vivo* effectiveness as hyaline cartilage substitutes will be further investigated. A formulation study can also be conducted to determine the optimal ratio of COLMA:THA:PEGDA bioink to yield the best printability and cartilaginous tissue formation. To this end, the 3D bioprinting of pre-crosslinked COLMA+THA+PEGDA bioink with nasal chondrocytes can be explored further as a substitute for autologous cartilage sources for hyaline cartilage defects.

CHAPTER 6. Conclusion and Future Work

6.1 Major Conclusions and Contributions

This thesis was focused on exploring strategies to allow the bioprinting of soft collagen bioink to create functional neocartilage tissue. The focus of this thesis was on investigating methods to enable the bioprinting of soft collagen bioink for the purpose of creating functional neocartilage tissue. The study aimed at exploring strategies to overcome the challenges that arise when utilizing collagen as a bioink, with regards to the creation of soft tissue constructs that mimic the extracellular matrix of native cartilage. The major conclusions and original contributions are listed below:

(I) Chapter 3 study have successfully demonstrated the generation of engineered nasoseptal cartilage tissue with molecular, biochemical, histological and ultrastructural characteristics of native nasoseptal cartilage after a 6-week *in vitro* culture period using FRESH bioprinting method. These results warrant future mechanical characterization and animal studies in which the bioprinted engineered nasal cartilage will be tested for flexural properties, implanted and their *in vivo* effectiveness as nasal cartilage substitutes will be further investigated. The combination of human nasoseptal chondrocytes with type I collagen hydrogel for FRESH-inspired bioprinting of engineered nasal cartilage is a promising strategy to explore further for the provision of autologous nasal cartilages for nasal cartilage reconstructive surgeries.

(II) Chapter 4 study demonstrated the perspective of bioprinting engineered cartilage grafts with similar histological, molecular, and mechanical characteristics as those derived from the use of clinically approved type I/III collagen membrane scaffolds both *in vivo* and *in vitro*. No *in vivo* calcification was observed. Moreover, the mechanical characteristics of the bioprinted

engineered grafts increased after *in vivo* implantation. Overall, this study showed strong evidence of the potential to engineer human nasal cartilage grafts for nasal reconstructive surgery via 3D bioprinting.

(III) Chapter 5 study demonstrated a novel bioink, which combines methacrylate type I collagen with thiolate hyaluronic acid and PEGDA, can resist contraction, have better printability and cell viability compared to the methacrylate type I collagen-only bioink. This work demonstrated that the 3D bioprinting of pre-crosslinked COLMA+THA+PEGDA bioink with nasal chondrocytes can be to explore further as a substitute of autologous cartilage source for hyaline cartilage defects.

6.2 Future Work

There are still several challenges associated with the translation of bioprinted cartilage into the clinic. First, creating bioprinted neocartilage that mimicking the properties of native cartilage is challenging. It is difficult to reproduce mechanical properties, such as stiffness and elasticity of nature cartilage. Second, manufacturing bioprinted cartilage at scale for clinical use is challenging. It requires the development of automated and efficient manufacturing process that can produce large numbers of functional structures. Third, obtaining regulatory approval for the use of bioprinted cartilage in humans is a lengthy and complex process, and it requires extensive preclinical testing and clinical trials to demonstrate safety and efficacy. Lastly, there is limited knowledge about the long-term effects of bioprinted cartilage on human body. Addressing these challenges is crucial for the widespread adoption of 3D bioprinting in the clinical setting.

To advance the 3D bioprinted cartilage for clinical use, it is important to improve mechanical property of the bioprinted cartilage graft to further shorten the culture period. In Chapter 4,

despite the bioprinted engineered cartilage graft shows similar mechanical property as those derived from clinical approved scaffold (Chondro-Gide), it required 9 weeks of culture for the grafts to be strong enough to hold sutures, compared to the 3 weeks of culture for Chondro-Gide. To accelerate the maturation and shorten the required culture time of the bioprinted nasal cartilage grafts, an adequate crosslinker with good biocompatibility and less *in vivo* toxicity can be used. The potential crosslinkers can be used in future are discussed in Chapter 1 and 2.

As collagen hydrogel has relatively low zero-shear viscosity and elastic modulus, a FRESH printing method (Chapter 3 and Chapter 4), or crosslinking (Chapter 5) is required for a successful bioprinting. To improve the printability and retain the filament diameter and the post-printing shape of the collagen hydrogel, a viscous contributor material can be used to combine with collagen bioink, such as cellulose nanofiber (CNF), sodium alginate (ALG) etc. A proof-of-concept study using CNF/ALG bioink showed excellent printability are shown in Appendix A.

Additionally, an optimum culture condition, cell seeding density and stimulation method can be determined in future studies. In Chapter 3 and Chapter 4, a higher cell concentration (10 million/mL vs. 8.75 million/mL, respectively) and more medium (29 mL/million per week vs. 3.8 mL/million per week, respectively) was used in these two different studies, the GAG/DNA value at 6 weeks of *in vitro* culture showed a significant difference (~225ug/ug vs. ~45ug/ug, respectively). As the TGFβ-3 supplemented chondrogenic medium volume increase, the GAG production per cell increase. The effect of nutrient consumption and cell sending density in articular chondrocytes has been well studied and reported in the literature[447-449]. However, such study has not been investigated in the nasal chondrocytes. Therefore, the effects of cell density or chondrogenic medium consumption on neocartilage formation can be studied in the future.

Despite advancements in the development of bioinks and printing methods that aim to create functional tissue constructs with improved mechanical properties and enhanced cell viability, a significant challenge remains in the lack of standardization in the production of functional and viable tissue at a scale suitable for clinical application. This lack of standardization poses challenges in ensuring consistency and reproducibility in bioprinted tissue. To overcome this challenge, adherence to Current Good Manufacturing Practices (cGMP) is critical in ensuring the quality control of manufactured biological entities, including the use of clinically acceptable biomaterials, cross-linkers, and culture media.

Additionally, extensive preclinical testing to demonstrate the long-term safety, efficacy, and reproducibility of 3D bioprinted cartilages need to be conducted to advance 3D bioprinting into clinical setting. This includes in vivo studies in mice and large animals such as porcine or Non-human primates. Once preclinical testing is complete, researcher must obtain regulatory approval for clinical use by submitting data to regulatory bodies such as the FDA or the European Medicines Agency. The clinical trials must be conducted to test the safety and efficacy of 3D bioprinted cartilage in humans, at the same time, establishing manufacture and distribution processes to produce the 3D bioprinted structures at scales for clinical use. The process required collaboration between researchers, clinicians, regulatory agencies, and industry.

Other than hyaline cartilage, 3D bioprinting technique can also be implemented for other cartilage cell sources, such as meniscus fibrochondrocytes, mesenchymal stem cells, and auricular chondrocytes. Daly et al. has showed that the type of encapsulated cell and biomaterial in the bioink has a potent effect on the cartilaginous tissue formation[450]. Future studies can be focused on discovering the optimal bioinks formations for the engineering of other cartilage tissues.

References

[1] S. Grässel, A. Aszódi, Cartilage, Springer2016.
[2] A.C. Daly, F.E. Freeman, T. Gonzalez-Fernandez, S.E. Critchley, J. Nulty, D.J.J.A.H.M. Kelly, 3D bioprinting for cartilage and osteochondral tissue engineering, 6(22) (2017) 1700298.
[3] L. Lavernia, W.E. Brown, B.J. Wong, J.C. Hu, K.A. Athanasiou, Toward Tissue-engineering of Nasal Cartilages, Acta biomaterialia (2019).
[4] Y. Liu, G. Zhou, Y.J.E. Cao, Recent progress in cartilage tissue engineering—our experience and future directions, 3(1) (2017) 28-35.
[5] T.D. Bornes, A.B. Adesida, N.M. Jomha, Mesenchymal stem cells in the treatment of traumatic articular cartilage defects: a comprehensive review, Arthritis research & therapy 16(5) (2014) 432.
[6] I. Fulco, S. Miot, M.D. Haug, A. Barbero, A. Wixmerten, S. Feliciano, F. Wolf, G. Jundt, A. Marsano, J. Farhadi, Engineered autologous cartilage tissue for nasal reconstruction after tumour resection: an observational first-in-human trial, The Lancet 384(9940) (2014) 337-346.
[7] V. Cervelli, D.J. Bottini, P. Gentile, L. Fantozzi, A. Arpino, C. Cannatà, L. Fiumara, C.U.J.A.o.p.s. Casciani, Reconstruction of the nasal dorsum with autologous rib cartilage, 56(3) (2006) 256-262.
[8] A. Sajjadian, R. Rubinstein, N.J.P. Naghshineh, r. surgery, Current status of grafts and implants in rhinoplasty: part I. Autologous grafts, 125(2) (2010) 40e-49e.
[9] D. Bottini, P. Gentile, A. Donfrancesco, L. Fiumara, V.J.A.p.s. Cervelli, Augmentation rhinoplasty with autologous grafts, 32(1) (2008) 136-142.
[10] A.M. Read-Fuller, D.M. Yates, A. Radwan, A.M. Schrodt, R.A.J.J.o.O. Finn, M. Surgery, The use of allogeneic cartilage for grafting in functional and reconstructive rhinoplasty, 76(7) (2018) 1560. e1-1560. e7.
[11] M. Steinwachs, T. Guggi, P.J.I. Kreuz, Marrow stimulation techniques, 39(1) (2008) 26-31.
[12] M. Brittberg, A. Lindahl, A. Nilsson, C. Ohlsson, O. Isaksson, L.J.N.e.j.o.m. Peterson, Treatment of deep cartilage defects in the knee with autologous chondrocyte transplantation, 331(14) (1994) 889-895.
[13] F. Migliorini, N. Maffulli, A. Baroncini, J. Eschweiler, M. Knobe, M. Tingart, H.J.T.A.J.o.S.M. Schenker, Allograft versus autograft osteochondral transplant for chondral defects of the talus: systematic review and meta-analysis, (2021) 03635465211037349.
[14] A. Pareek, P.J. Reardon, T.G. Maak, B.A. Levy, M.J. Stuart, A.J.J.A.T.J.o.A. Krych, R. Surgery, Long-term outcomes after osteochondral autograft transfer: a systematic review at mean follow-up of 10.2 years, 32(6) (2016) 1174-1184.
[15] T.J. Levingstone, A. Ramesh, R.T. Brady, P.A. Brama, C. Kearney, J.P. Gleeson, F.J.J.B. O'Brien, Cell-free multi-layered collagen-based scaffolds demonstrate layer specific regeneration of functional osteochondral tissue in caprine joints, 87 (2016) 69-81.
[16] T. Gotterbarm, W. Richter, M. Jung, S.B. Vilei, P. Mainil-Varlet, T. Yamashita, S.J.J.B. Breusch, An in vivo study of a growth-factor enhanced, cell free, two-layered collagen–tricalcium phosphate in deep osteochondral defects, 27(18) (2006) 3387-3395.
[17] S. Wakitani, T. Mitsuoka, N. Nakamura, Y. Toritsuka, Y. Nakamura, S.J.C.t. Horibe, Autologous bone marrow stromal cell transplantation for repair of full-thickness articular cartilage defects in human patellae: two case reports, 13(5) (2004) 595-600.
[18] R.M. Frank, E.J. Cotter, I. Nassar, B.J.S.M. Cole, A. Review, Failure of bone marrow stimulation techniques, 25(1) (2017) 2-9.

[19] K. Pelttari, B. Pippenger, M. Mumme, S. Feliciano, C. Scotti, P. Mainil-Varlet, A. Procino, B. Von Rechenberg, T. Schwamborn, M.J.S.t.m. Jakob, Adult human neural crest–derived cells for articular cartilage repair, 6(251) (2014) 251ra119-251ra119.
[20] A. Shafiee, M. Kabiri, N. Ahmadbeigi, S.O. Yazdani, M. Mojtahed, S. Amanpour, M.J.S.c. Soleimani, development, Nasal septum-derived multipotent progenitors: a potent source for stem cell-based regenerative medicine, 20(12) (2011) 2077-2091.
[21] C. Candrian, D. Vonwil, A. Barbero, E. Bonacina, S. Miot, J. Farhadi, D. Wirz, S. Dickinson, A. Hollander, M.J.A. Jakob, Rheumatism, Engineered cartilage generated by nasal chondrocytes is responsive to physical forces resembling joint loading, 58(1) (2008) 197-208.
[22] K. Pelttari, M. Mumme, A. Barbero, I.J.C.o.i.b. Martin, Nasal chondrocytes as a neural crest-derived cell source for regenerative medicine, 47 (2017) 1-6.
[23] M. Mumme, A. Barbero, S. Miot, A. Wixmerten, S. Feliciano, F. Wolf, A.M. Asnaghi, D. Baumhoer, O. Bieri, M. Kretzschmar, Nasal chondrocyte-based engineered autologous cartilage tissue for repair of articular cartilage defects: an observational first-in-human trial, The Lancet 388(10055) (2016) 1985-1994.
[24] F.N. Ghadially, Structure and function of articular cartilage, Clinics in rheumatic diseases 7(1) (1981) 3-28.
[25] Y. Xu, H.-J. Sun, Y. Lv, J.-C. Zou, B.-L. Liu, T.-C.J.C. Hua, Effects of freezing rates and cryoprotectant on thermal expansion of articular cartilage during freezing process, 34(4) (2013) 313-323.
[26] L. Zhang, J. Hu, K.A. Athanasiou, The role of tissue engineering in articular cartilage repair and regeneration, Critical Reviews™ in Biomedical Engineering 37(1-2) (2009).
[27] A.J. Sophia Fox, A. Bedi, S.A.J.S.h. Rodeo, The basic science of articular cartilage: structure, composition, and function, 1(6) (2009) 461-468.
[28] T. Li, S. Chen, M. Pei, Contribution of neural crest-derived stem cells and nasal chondrocytes to articular cartilage regeneration, Cellular and Molecular Life Sciences 77(23) (2020) 4847-4859.
[29] A.D. Pearle, R.F. Warren, S.A.J.C.i.s.m. Rodeo, Basic science of articular cartilage and osteoarthritis, 24(1) (2005) 1-12.
[30] K. Anderson, M. Henneberg, R. Norris, Anatomy of the nasal profile, Journal of anatomy 213(2) (2008) 210-216.
[31] A.T.J.W.j.o.p.s. Ashrafi, Management of upper lateral cartilages (ULCs) in rhinoplasty, 3(2) (2014) 129.
[32] M. Popko, R. Bleys, J. De Groot, E.H.J.R. Huizing, Histological structure of the nasal cartilages and their perichondrial envelope I. The septal and lobular cartilage, 45(2) (2007) 148.
[33] E. Kheir, D.J.O. Shaw, Trauma, Hyaline articular cartilage, 23(6) (2009) 450-455.
[34] Y. Gao, S. Liu, J. Huang, W. Guo, J. Chen, L. Zhang, B. Zhao, J. Peng, A. Wang, Y. Wang, The ECM-cell interaction of cartilage extracellular matrix on chondrocytes, BioMed research international 2014 (2014).
[35] N.P. Cohen, R.J. Foster, V.C.J.J.o.O. Mow, S.P. Therapy, Composition and dynamics of articular cartilage: structure, function, and maintaining healthy state, 28(4) (1998) 203-215.
[36] J.-J. Wu, M.A. Weis, L.S. Kim, D.R.J.J.o.B.C. Eyre, Type III collagen, a fibril network modifier in articular cartilage, 285(24) (2010) 18537-18544.
[37] D.J.A.R. Eyre, Therapy, Articular cartilage and changes in arthritis: collagen of articular cartilage, 4(1) (2001) 1-6.

[38] F. Aksoy, Y. Yildirim, H. Demirhan, O. Özturan, S. Solakoglu, Structural characteristics of septal cartilage and mucoperichondrium, The Journal of Laryngology & Otology 126(1) (2012) 38-42.
[39] M.R. Homicz, K.B. McGowan, L.M. Lottman, G. Beh, R.L. Sah, D. Watson, A compositional analysis of human nasal septal cartilage, Archives of facial plastic surgery 5(1) (2003) 53-58.
[40] M.K. Neuman, K.K. Briggs, K. Masuda, R.L. Sah, D.J.T.L. Watson, A compositional analysis of cadaveric human nasal septal cartilage, 123(9) (2013) 2120-2124.
[41] N. Rotter, G. Tobias, M. Lebl, A.K. Roy, M.C. Hansen, C.A. Vacanti, L.J. Bonassar, Age-related changes in the composition and mechanical properties of human nasal cartilage, Archives of biochemistry and biophysics 403(1) (2002) 132-140.
[42] X. Lan, Y. Liang, E.J. Erkut, M. Kunze, A. Mulet-Sierra, T. Gong, M. Osswald, K. Ansari, H. Seikaly, Y.J.T.F.J. Boluk, Bioprinting of human nasoseptal chondrocytes-laden collagen hydrogel for cartilage tissue engineering, 35(3) (2021) e21191.
[43] F. Boschetti, G. Pennati, F. Gervaso, G.M. Peretti, G.J.B. Dubini, Biomechanical properties of human articular cartilage under compressive loads, 41(3-4) (2004) 159-166.
[44] D. Shepherd, B.J.R. Seedhom, The'instantaneous' compressive modulus of human articular cartilage in joints of the lower limb, 38(2) (1999) 124-132.
[45] J. Jurvelin, M. Buschmann, E.J.P.o.t.I.o.M.E. Hunziker, Part H: Journal of Engineering in Medicine, Mechanical anisotropy of the human knee articular cartilage in compression, 217(3) (2003) 215-219.
[46] T. Franz, E. Hasler, R. Hagg, C. Weiler, R. Jakob, P.J.O. Mainil-Varlet, Cartilage, In situ compressive stiffness, biochemical composition, and structural integrity of articular cartilage of the human knee joint, 9(6) (2001) 582-592.
[47] D. Bader, G.J.B.-m.m. Kempson, engineering, The short-term compressive properties of adult human articular cartilage, 4(3) (1994) 245-256.
[48] S. Grad, D. Eglin, M. Alini, M.J.J.C.O. Stoddart, R. Research®, Physical stimulation of chondrogenic cells in vitro: a review, 469(10) (2011) 2764-2772.
[49] E.Y. Salinas, J.C. Hu, K.J.T.E.P.B.R. Athanasiou, A guide for using mechanical stimulation to enhance tissue-engineered articular cartilage properties, 24(5) (2018) 345-358.
[50] M.J. Glasgold, Y.P. Kato, D. Christiansen, J.A. Hauge, A.I. Glasgold, F.H. Silver, Mechanical Properties of Septai Cartilage Homografts, Otolaryngology—Head and Neck Surgery 99(4) (1988) 374-379.
[51] M. Griffin, Y. Premakumar, A. Seifalian, M. Szarko, P. Butler, Biomechanical characterisation of the human nasal cartilages; implications for tissue engineering, Journal of Materials Science: Materials in Medicine 27(1) (2016) 11.
[52] J.D. Richmon, A. Sage, V.W. Wong, A.C. Chen, R.L. Sah, D.J.A.j.o.r. Watson, Compressive biomechanical properties of human nasal septal cartilage, 20(5) (2006) 496-501.
[53] J.D. Richmon, A.B. Sage, V.W. Wong, A.C. Chen, C. Pan, R.L. Sah, D.J.A.j.o.r. Watson, Tensile biomechanical properties of human nasal septal cartilage, 19(6) (2005) 617-622.
[54] R.W. Westreich, H.-W. Courtland, P. Nasser, K. Jepsen, W.J.A.o.F.P.S. Lawson, Defining nasal cartilage elasticity: biomechanical testing of the tripod theory based on a cantilevered model, 9(4) (2007) 264-270.
[55] J.P. Caffrey, A.M. Kushnaryov, M.S. Reuther, V.W. Wong, K.K. Briggs, K. Masuda, R.L. Sah, D.J.O.-.-H. Watson, N. Surgery, Flexural properties of native and tissue-engineered human septal cartilage, 148(4) (2013) 576-581.

[56] B.K. Hall, J.A.J.J.o.a. Gillis, Incremental evolution of the neural crest, neural crest cells and neural crest-derived skeletal tissues, 222(1) (2013) 19-31.
[57] S. Dash, P.A.J.B. Trainor, The development, patterning and evolution of neural crest cell differentiation into cartilage and bone, 137 (2020) 115409.
[58] M. Salamone, S. Rigogliuso, A. Nicosia, M. Tagliavia, S. Campora, P. Cinà, C. Bruno, G.J.C. Ghersi, Neural crest-derived chondrocytes isolation for tissue engineering in regenerative medicine, 9(4) (2020) 962.
[59] T.D. Bornes, A.B. Adesida, N.M.J.A.r. Jomha, therapy, Mesenchymal stem cells in the treatment of traumatic articular cartilage defects: a comprehensive review, 16(5) (2014) 1-19.
[60] C. De Bari, F. Dell'Accio, F.P. Luyten, Failure of in vitro–differentiated mesenchymal stem cells from the synovial membrane to form ectopic stable cartilage in vivo, Arthritis & Rheumatism: Official Journal of the American College of Rheumatology 50(1) (2004) 142-150.
[61] K. Pelttari, A. Winter, E. Steck, K. Goetzke, T. Hennig, B.G. Ochs, T. Aigner, W.J.A. Richter, R.O.J.o.t.A.C.o. Rheumatology, Premature induction of hypertrophy during in vitro chondrogenesis of human mesenchymal stem cells correlates with calcification and vascular invasion after ectopic transplantation in SCID mice, 54(10) (2006) 3254-3266.
[62] S. Rahman, A.R.A. Szojka, Y. Liang, M. Kunze, V. Goncalves, A. Mulet Sierra, N.M. Jomha, A.B.J.F.i.c. Adesida, d. biology, Inability of Low Oxygen Tension to Induce Chondrogenesis in Human Infrapatellar Fat Pad-Mesenchymal Stem Cells, 9 (2021) 1780.
[63] A. Aung, G. Gupta, G. Majid, S.J.A. Varghese, Rheumatism, Osteoarthritic chondrocyte–secreted morphogens induce chondrogenic differentiation of human mesenchymal stem cells, 63(1) (2011) 148-158.
[64] S.H. Andrews, M. Kunze, A. Mulet-Sierra, L. Williams, K. Ansari, M. Osswald, A.B. Adesida, Strategies to Mitigate Variability in Engineering Human Nasal Cartilage, Scientific reports 7(1) (2017) 6490.
[65] J.A. Liu, M.J.D.b. Cheung, Neural crest stem cells and their potential therapeutic applications, 419(2) (2016) 199-216.
[66] V. Mayo, Y. Sawatari, C.-Y.C. Huang, F.J.J.o.D. Garcia-Godoy, Neural crest-derived dental stem cells—where we are and where we are going, 42(9) (2014) 1043-1051.
[67] P.T.J.D. Sharpe, Dental mesenchymal stem cells, 143(13) (2016) 2273-2280.
[68] F.C. Ferré, H. Larjava, L.-S. Loison-Robert, T. Berbar, G.R. Owen, A. Berdal, H. Chérifi, B. Gogly, L. Häkkinen, B.P.J.S.c. Fournier, development, Formation of cartilage and synovial tissue by human gingival stem cells, 23(23) (2014) 2895-2907.
[69] A. Moshaverinia, X. Xu, C. Chen, K. Akiyama, M.L. Snead, S.J.A.b. Shi, Dental mesenchymal stem cells encapsulated in an alginate hydrogel co-delivery microencapsulation system for cartilage regeneration, 9(12) (2013) 9343-9350.
[70] N. Rotter, L.J. Bonassar, G. Tobias, M. Lebl, A.K. Roy, C.A.J.B. Vacanti, Age dependence of biochemical and biomechanical properties of tissue-engineered human septal cartilage, 23(15) (2002) 3087-3094.
[71] W.e. Kafienah, M. Jakob, O. Démarteau, A. Frazer, M.D. Barker, I. Martin, A.P. Hollander, Three-dimensional tissue engineering of hyaline cartilage: comparison of adult nasal and articular chondrocytes, Tissue engineering 8(5) (2002) 817-826.
[72] K. El Sayed, U. Marzahn, T. John, M. Hoyer, H. Zreiqat, A. Witthuhn, B. Kohl, A. Haisch, G.J.J.o.T.E. Schulze-Tanzil, R. Medicine, PGA-associated heterotopic chondrocyte cocultures: implications of nasoseptal and auricular chondrocytes in articular cartilage repair, 7(1) (2013) 61-72.

[73] C. Scotti, A. Osmokrovic, F. Wolf, S. Miot, G.M. Peretti, A. Barbero, I. Martin, Response of human engineered cartilage based on articular or nasal chondrocytes to interleukin-1β and low oxygen, Tissue engineering Part A 18(3-4) (2011) 362-372.
[74] K. Chua, B. Aminuddin, N. Fuzina, B. Ruszymah, Insulin-transferrin-selenium prevent human chondrocyte dedifferentiation and promote the formation of high quality tissue engineered human hyaline cartilage, Eur Cell Mater 9(9) (2005) 58-67.
[75] C. Scotti, A. Osmokrovic, F. Wolf, S. Miot, G.M. Peretti, A. Barbero, I.J.T.E.P.A. Martin, Response of human engineered cartilage based on articular or nasal chondrocytes to interleukin-1β and low oxygen, 18(3-4) (2012) 362-372.
[76] M. Mumme, A. Steinitz, K.M. Nuss, K. Klein, S. Feliciano, P. Kronen, M. Jakob, B. von Rechenberg, I. Martin, A.J.T.E.P.A. Barbero, Regenerative potential of tissue-engineered nasal chondrocytes in goat articular cartilage defects, 22(21-22) (2016) 1286-1295.
[77] J. Farhadi, I. Fulco, S. Miot, D. Wirz, M. Haug, S.C. Dickinson, A.P. Hollander, A.U. Daniels, G. Pierer, M.J.A.o.s. Heberer, Precultivation of engineered human nasal cartilage enhances the mechanical properties relevant for use in facial reconstructive surgery, 244(6) (2006) 978.
[78] I. Fulco, S. Miot, M.D. Haug, A. Barbero, A. Wixmerten, S. Feliciano, F. Wolf, G. Jundt, A. Marsano, J.J.T.L. Farhadi, Engineered autologous cartilage tissue for nasal reconstruction after tumour resection: an observational first-in-human trial, 384(9940) (2014) 337-346.
[79] S.V. Murphy, A. Atala, 3D bioprinting of tissues and organs, Nature biotechnology 32(8) (2014) 773.
[80] S.V. Murphy, A. Skardal, A. Atala, Evaluation of hydrogels for bio-printing applications, Journal of Biomedical Materials Research Part A 101(1) (2013) 272-284.
[81] S. Gupta, A. Bit, 3D bioprinting in tissue engineering and regenerative medicine, Cell and Tissue Banking (2021) 1-14.
[82] A. Jiao, N.E. Trosper, H.S. Yang, J. Kim, J.H. Tsui, S.D. Frankel, C.E. Murry, D.-H. Kim, Thermoresponsive nanofabricated substratum for the engineering of three-dimensional tissues with layer-by-layer architectural control, ACS nano 8(5) (2014) 4430-4439.
[83] C. Mandrycky, Z. Wang, K. Kim, D.-H. Kim, 3D bioprinting for engineering complex tissues, Biotechnology advances 34(4) (2016) 422-434.
[84] Z. Gu, J. Fu, H. Lin, Y. He, Development of 3D bioprinting: From printing methods to biomedical applications, Asian Journal of Pharmaceutical Sciences 15(5) (2020) 529-557.
[85] E.M. Sánchez, J.C. Gómez-Blanco, E.L. Nieto, J.G. Casado, A. Macías-García, M.A.D. Díez, J.P. Carrasco-Amador, D.T. Martín, F.M. Sánchez-Margallo, J.B. Pagador, Hydrogels for Bioprinting: A Systematic Review of Hydrogels Synthesis, Bioprinting Parameters, and Bioprinted Structures Behavior, Frontiers in Bioengineering and Biotechnology 8 (2020).
[86] L. Shi, Y. Hu, M.W. Ullah, H. Ou, W. Zhang, L. Xiong, X. Zhang, Cryogenic free-form extrusion bioprinting of decellularized small intestinal submucosa for potential applications in skin tissue engineering, Biofabrication 11(3) (2019) 035023.
[87] T. Hiller, J. Berg, L. Elomaa, V. Röhrs, I. Ullah, K. Schaar, A.-C. Dietrich, M.A. Al-Zeer, A. Kurtz, A.C. Hocke, Generation of a 3D liver model comprising human extracellular matrix in an alginate/gelatin-based bioink by extrusion bioprinting for infection and transduction studies, International journal of molecular sciences 19(10) (2018) 3129.
[88] E. Davoodi, E. Sarikhani, H. Montazerian, S. Ahadian, M. Costantini, W. Swieszkowski, S.M. Willerth, K. Walus, M. Mofidfar, E. Toyserkani, Extrusion and Microfluidic-Based

Bioprinting to Fabricate Biomimetic Tissues and Organs, Advanced Materials Technologies 5(8) (2020) 1901044.
[89] C. Xu, W. Chai, Y. Huang, R.R. Markwald, Scaffold-free inkjet printing of three-dimensional zigzag cellular tubes, Biotechnol Bioeng 109(12) (2012) 3152-60.
[90] E. Masaeli, V. Forster, S. Picaud, F. Karamali, M.H. Nasr-Esfahani, C. Marquette, Tissue engineering of retina through high resolution 3-dimensional inkjet bioprinting, Biofabrication 12(2) (2020) 025006.
[91] A.M. Compaan, K. Christensen, Y. Huang, Inkjet bioprinting of 3D silk fibroin cellular constructs using sacrificial alginate, ACS Biomaterials Science & Engineering 3(8) (2017) 1519-1526.
[92] D. Hakobyan, O. Kerouredan, M. Remy, N. Dusserre, C. Medina, R. Devillard, J.-C. Fricain, H. Oliveira, Laser-assisted bioprinting for bone repair, 3D Bioprinting, Springer2020, pp. 135-144.
[93] F. Kawecki, W.P. Clafshenkel, F.A. Auger, J.-M. Bourget, J. Fradette, R. Devillard, Self-assembled human osseous cell sheets as living biopapers for the laser-assisted bioprinting of human endothelial cells, Biofabrication 10(3) (2018) 035006.
[94] M.E. Cooke, D.H. Rosenzweig, The rheology of direct and suspended extrusion bioprinting, APL bioengineering 5(1) (2021) 011502.
[95] M.T. Tavares, V.M. Gaspar, M.V. Monteiro, J.P.S. Farinha, C. Baleizão, J.F. Mano, GelMA/bioactive silica nanocomposite bioinks for stem cell osteogenic differentiation, Biofabrication 13(3) (2021) 035012.
[96] H.A.-D.M.A. Awwad, L. Thiagarajan, J.M. Kanczler, M.H. Amer, G. Bruce, S. Lanham, R.M. Rumney, R.O. Oreffo, J.E. Dixon, Genetically-programmed, mesenchymal stromal cell-laden & mechanically strong 3D bioprinted scaffolds for bone repair, Journal of Controlled Release 325 (2020) 335-346.
[97] L. De Moor, S. Fernandez, C. Vercruysse, L. Tytgat, M. Asadian, N. De Geyter, S. Van Vlierberghe, P. Dubruel, H. Declercq, Hybrid bioprinting of chondrogenically induced human mesenchymal stem cell spheroids, Frontiers in Bioengineering and Biotechnology 8 (2020) 484.
[98] A. Perez-Valle, C. Del Amo, I.J.I.J.o.M.S. Andia, Overview of current advances in extrusion bioprinting for skin applications, 21(18) (2020) 6679.
[99] A. Tijore, J.-M. Behr, S.A. Irvine, V. Baisane, S. Venkatraman, Bioprinted gelatin hydrogel platform promotes smooth muscle cell contractile phenotype maintenance, Biomedical microdevices 20(2) (2018) 1-10.
[100] K.T. Lawlor, J.M. Vanslambrouck, J.W. Higgins, A. Chambon, K. Bishard, D. Arndt, P.X. Er, S.B. Wilson, S.E. Howden, K.S. Tan, Cellular extrusion bioprinting improves kidney organoid reproducibility and conformation, Nature materials 20(2) (2021) 260-271.
[101] N.I. Moldovan, Three-Dimensional Bioprinting of Anatomically Realistic Tissue Constructs for Disease Modeling and Drug Testing, Tissue Engineering Part C: Methods 27(3) (2021) 225-231.
[102] A. Gebeyehu, S.K. Surapaneni, J. Huang, A. Mondal, V.Z. Wang, N.F. Haruna, A. Bagde, P. Arthur, S. Kutlehria, N. Patel, Polysaccharide hydrogel based 3D printed tumor models for chemotherapeutic drug screening, Scientific reports 11(1) (2021) 1-15.
[103] X. Cui, D. Dean, Z.M. Ruggeri, T. Boland, Cell damage evaluation of thermal inkjet printed Chinese hamster ovary cells, Biotechnology and bioengineering 106(6) (2010) 963-969.

[104] J.S. Mandelli, J. Koepp, A. Hama, S. Sanaur, G.A. Rae, C.R. Rambo, Cell viability and cytotoxicity of inkjet-printed flexible organic electrodes on parylene C, Biomedical Microdevices 23(1) (2021) 1-12.
[105] J. Guo, A.E. Niaraki Asli, K.R. Williams, P.L. Lai, X. Wang, R. Montazami, N.N. Hashemi, Viability of neural cells on 3D printed graphene bioelectronics, Biosensors 9(4) (2019) 112.
[106] S. Derakhshanfar, R. Mbeleck, K. Xu, X. Zhang, W. Zhong, M.J.B.m. Xing, 3D bioprinting for biomedical devices and tissue engineering: A review of recent trends and advances, 3(2) (2018) 144-156.
[107] L. Koch, O. Brandt, A. Deiwick, B. Chichkov, Laser-assisted bioprinting at different wavelengths and pulse durations with a metal dynamic release layer: A parametric study, International Journal of Bioprinting 3(1) (2017).
[108] V. Keriquel, H. Oliveira, M. Rémy, S. Ziane, S. Delmond, B. Rousseau, S. Rey, S. Catros, J. Amédée, F. Guillemot, In situ printing of mesenchymal stromal cells, by laser-assisted bioprinting, for in vivo bone regeneration applications, Scientific reports 7(1) (2017) 1-10.
[109] O. Kérourédan, J.-M. Bourget, M. Rémy, S. Crauste-Manciet, J. Kalisky, S. Catros, N.B. Thébaud, R. Devillard, Micropatterning of endothelial cells to create a capillary-like network with defined architecture by laser-assisted bioprinting, Journal of Materials Science: Materials in Medicine 30(2) (2019) 28.
[110] L. Koch, A. Deiwick, S. Schlie, S. Michael, M. Gruene, V. Coger, D. Zychlinski, A. Schambach, K. Reimers, P.M. Vogt, Skin tissue generation by laser cell printing, Biotechnology and bioengineering 109(7) (2012) 1855-1863.
[111] B. Wang, P.J. Díaz-Payno, D.C. Browe, F.E. Freeman, J. Nulty, R. Burdis, D.J. Kelly, Affinity-bound growth factor within sulfated interpenetrating network bioinks for bioprinting cartilaginous tissues, Acta Biomaterialia (2021).
[112] G. Irmak, M. Gümüşderelioğlu, Photo-activated platelet-rich plasma (PRP)-based patient-specific bio-ink for cartilage tissue engineering, Biomedical Materials 15(6) (2020) 065010.
[113] T. Lam, T. Dehne, J.P. Krüger, S. Hondke, M. Endres, A. Thomas, R. Lauster, M. Sittinger, L. Kloke, Photopolymerizable gelatin and hyaluronic acid for stereolithographic 3D bioprinting of tissue-engineered cartilage, Journal of Biomedical Materials Research Part B: Applied Biomaterials 107(8) (2019) 2649-2657.
[114] Y.P. Singh, A. Bandyopadhyay, B.B. Mandal, 3D Bioprinting Using Cross-Linker-Free Silk–Gelatin Bioink for Cartilage Tissue Engineering, ACS applied materials & interfaces 11(37) (2019) 33684-33696.
[115] J.M. Townsend, E.C. Beck, S.H. Gehrke, C.J. Berkland, M.S.J.P.i.p.s. Detamore, Flow behavior prior to crosslinking: The need for precursor rheology for placement of hydrogels in medical applications and for 3D bioprinting, 91 (2019) 126-140.
[116] M. Zhou, B.H. Lee, Y.J. Tan, L.P.J.B. Tan, Microbial transglutaminase induced controlled crosslinking of gelatin methacryloyl to tailor rheological properties for 3D printing, 11(2) (2019) 025011.
[117] K. Song, A.M. Compaan, W. Chai, Y.J.A.a.m. Huang, interfaces, Injectable gelatin microgel-based composite ink for 3D bioprinting in air, 12(20) (2020) 22453-22466.
[118] K. Weadock, R.M. Olson, F.H.J.B. Silver, medical devices,, a. organs, Evaluation of collagen crosslinking techniques, 11(4) (1983) 293-318.
[119] K. Adamiak, A.J.I.J.o.B.M. Sionkowska, Current methods of collagen cross-linking, 161 (2020) 550-560.

[120] W. Kim, G.J.B. Kim, Collagen/bioceramic-based composite bioink to fabricate a porous 3D hASCs-laden structure for bone tissue regeneration, 12(1) (2019) 015007.
[121] N. Diamantides, L. Wang, T. Pruiksma, J. Siemiatkoski, C. Dugopolski, S. Shortkroff, S. Kennedy, L.J.J.B. Bonassar, Correlating rheological properties and printability of collagen bioinks: the effects of riboflavin photocrosslinking and pH, 9(3) (2017) 034102.
[122] W. Lee, J. Pinckney, V. Lee, J.-H. Lee, K. Fischer, S. Polio, J.-K. Park, S.-S.J.N. Yoo, Three-dimensional bioprinting of rat embryonic neural cells, 20(8) (2009) 798-803.
[123] Y.-B. Lee, S. Polio, W. Lee, G. Dai, L. Menon, R.S. Carroll, S.-S. Yoo, Bio-printing of collagen and VEGF-releasing fibrin gel scaffolds for neural stem cell culture, Experimental neurology 223(2) (2010) 645-652.
[124] J.-H. Shim, J.Y. Kim, M. Park, J. Park, D.-W.J.B. Cho, Development of a hybrid scaffold with synthetic biomaterials and hydrogel using solid freeform fabrication technology, 3(3) (2011) 034102.
[125] E.L. Maxson, M.D. Young, C. Noble, J.L. Go, B. Heidari, R. Khorramirouz, D.W. Morse, A.J.B. Lerman, In vivo remodeling of a 3D-Bioprinted tissue engineered heart valve scaffold, 16 (2019) e00059.
[126] A. Lee, A. Hudson, D. Shiwarski, J. Tashman, T. Hinton, S. Yerneni, J. Bliley, P. Campbell, A. Feinberg, 3D bioprinting of collagen to rebuild components of the human heart, Science 365(6452) (2019) 482-487.
[127] D.F. Duarte Campos, M. Rohde, M. Ross, P. Anvari, A. Blaeser, M. Vogt, C. Panfil, G.H.F. Yam, J.S. Mehta, H.J.J.o.B.M.R.P.A. Fischer, Corneal bioprinting utilizing collagen-based bioinks and primary human keratocytes, 107(9) (2019) 1945-1953.
[128] P. Rastogi, B.J.B. Kandasubramanian, Review of alginate-based hydrogel bioprinting for application in tissue engineering, 11(4) (2019) 042001.
[129] A. Fatimi, O.V. Okoro, D. Podstawczyk, J. Siminska-Stanny, A.J.G. Shavandi, Natural Hydrogel-Based Bio-Inks for 3D Bioprinting in Tissue Engineering: A Review, 8(3) (2022) 179.
[130] J. Kundu, J.H. Shim, J. Jang, S.W. Kim, D.W. Cho, An additive manufacturing-based PCL–alginate–chondrocyte bioprinted scaffold for cartilage tissue engineering, Journal of tissue engineering and regenerative medicine 9(11) (2015) 1286-1297.
[131] Y. Sun, Y. You, W. Jiang, Z. Zhai, K.J.T. Dai, 3D-bioprinting a genetically inspired cartilage scaffold with GDF5-conjugated BMSC-laden hydrogel and polymer for cartilage repair, 9(23) (2019) 6949.
[132] L. Jia, Y. Hua, J. Zeng, W. Liu, D. Wang, G. Zhou, X. Liu, H.J.B.m. Jiang, Bioprinting and regeneration of auricular cartilage using a bioactive bioink based on microporous photocrosslinkable acellular cartilage matrix, 16 (2022) 66-81.
[133] R. Choe, E. Devoy, B. Kuzemchak, M. Sherry, E. Jabari, J.D. Packer, J.P.J.B. Fisher, Computational investigation of interface printing patterns within 3D printed multilayered scaffolds for osteochondral tissue engineering, 14(2) (2022) 025015.
[134] J. Yu, S. Lee, S. Choi, K.K. Kim, B. Ryu, C.-Y. Kim, C.-R. Jung, B.-H. Min, Y.-Z. Xin, S.A.J.P. Park, Fabrication of a polycaprolactone/alginate bipartite hybrid scaffold for osteochondral tissue using a three-dimensional bioprinting system, 12(10) (2020) 2203.
[135] S. Critchley, E.J. Sheehy, G. Cunniffe, P. Diaz-Payno, S.F. Carroll, O. Jeon, E. Alsberg, P.A. Brama, D.J.J.A.B. Kelly, 3D printing of fibre-reinforced cartilaginous templates for the regeneration of osteochondral defects, 113 (2020) 130-143.
[136] J. Hauptstein, T. Böck, M. Bartolf-Kopp, L. Forster, P. Stahlhut, A. Nadernezhad, G. Blahetek, A. Zernecke-Madsen, R. Detsch, T.J.A.H.M. Jüngst, Hyaluronic Acid-Based Bioink

Composition Enabling 3D Bioprinting and Improving Quality of Deposited Cartilaginous Extracellular Matrix, 9(15) (2020) 2000737.
[137] S.R. Moxon, M.J. Ferreira, P.d. Santos, B. Popa, A. Gloria, R. Katsarava, D. Tugushi, A.C. Serra, N.M. Hooper, S.J.J.P. Kimber, A Preliminary Evaluation of the Pro-Chondrogenic Potential of 3D-Bioprinted Poly (ester Urea) Scaffolds, 12(7) (2020) 1478.
[138] R. Schipani, S. Scheurer, R. Florentin, S.E. Critchley, D.J.J.B. Kelly, Reinforcing interpenetrating network hydrogels with 3D printed polymer networks to engineer cartilage mimetic composites, 12(3) (2020) 035011.
[139] L. Ruiz-Cantu, A. Gleadall, C. Faris, J. Segal, K. Shakesheff, J.J.M.S. Yang, E. C, Multi-material 3D bioprinting of porous constructs for cartilage regeneration, 109 (2020) 110578.
[140] S. Stichler, T. Böck, N. Paxton, S. Bertlein, R. Levato, V. Schill, W. Smolan, J. Malda, J. Teßmar, T.J.B. Blunk, Double printing of hyaluronic acid/poly (glycidol) hybrid hydrogels with poly (ε-caprolactone) for MSC chondrogenesis, 9(4) (2017) 044108.
[141] A.C. Daly, S.E. Critchley, E.M. Rencsok, D.J.J.B. Kelly, A comparison of different bioinks for 3D bioprinting of fibrocartilage and hyaline cartilage, 8(4) (2016) 045002.
[142] X. Lan, Y. Liang, M. Vyhlidal, E.J. Erkut, M. Kunze, A. Mulet-Sierra, M. Osswald, K. Ansari, H. Seikaly, Y.J.J.o.T.E. Boluk, In vitro maturation and in vivo stability of bioprinted human nasal cartilage, 13 (2022) 20417314221086368.
[143] P. Apelgren, M. Amoroso, K. Säljö, M. Montelius, A. Lindahl, L.S. Orrhult, P. Gatenholm, L.J.B. Kölby, Vascularization of tissue engineered cartilage-Sequential in vivo MRI display functional blood circulation, 276 (2021) 121002.
[144] P. Apelgren, M. Amoroso, K. Säljö, A. Lindahl, C. Brantsing, L. Stridh Orrhult, K. Markstedt, P. Gatenholm, L. Kölby, Long-term in vivo integrity and safety of 3D-bioprinted cartilaginous constructs, Journal of Biomedical Materials Research Part B: Applied Biomaterials 109(1) (2021) 126-136.
[145] P. Apelgren, E. Karabulut, M. Amoroso, A. Mantas, H.c. Martínez Ávila, L. Kölby, T. Kondo, G. Toriz, P. Gatenholm, In vivo human cartilage formation in three-dimensional bioprinted constructs with a novel bacterial nanocellulose bioink, ACS Biomaterials Science & Engineering 5(5) (2019) 2482-2490.
[146] P. Apelgren, M. Amoroso, A. Lindahl, C. Brantsing, N. Rotter, P. Gatenholm, L.J.P.O. Kölby, Chondrocytes and stem cells in 3D-bioprinted structures create human cartilage in vivo, 12(12) (2017) e0189428.
[147] H.M. Ávila, S. Schwarz, N. Rotter, P.J.B. Gatenholm, 3D bioprinting of human chondrocyte-laden nanocellulose hydrogels for patient-specific auricular cartilage regeneration, 1 (2016) 22-35.
[148] M.H. Lim, J.H. Jeun, S.H. Park, W. Lee, S.H. Park, M.Y. Kwon, S.H. Hwang, S.W. Kim, Evaluation of polycaprolactone-associated human nasal chondrocytes as a therapeutic agent for cartilage repair, Tissue engineering and regenerative medicine 16(6) (2019) 605-614.
[149] K. Markstedt, A. Mantas, I. Tournier, H.c. Martínez Ávila, D. Hägg, P. Gatenholm, 3D bioprinting human chondrocytes with nanocellulose–alginate bioink for cartilage tissue engineering applications, Biomacromolecules 16(5) (2015) 1489-1496.
[150] S. Schwarz, S. Kuth, T. Distler, C. Gögele, K. Stölzel, R. Detsch, A.R. Boccaccini, G. Schulze-Tanzil, 3D printing and characterization of human nasoseptal chondrocytes laden dual crosslinked oxidized alginate-gelatin hydrogels for cartilage repair approaches, Materials Science and Engineering: C (2020) 111189.

[151] P.S. Thayer, L.S. Orrhult, H. Martínez, Bioprinting of cartilage and skin tissue analogs utilizing a novel passive mixing unit technique for bioink precellularization, Journal of visualized experiments: JoVE (131) (2018).
[152] T. Jungst, W. Smolan, K. Schacht, T. Scheibel, J.r. Groll, Strategies and molecular design criteria for 3D printable hydrogels, Chemical reviews 116(3) (2015) 1496-1539.
[153] J. Malda, J. Visser, F.P. Melchels, T. Jüngst, W.E. Hennink, W.J. Dhert, J. Groll, D.W. Hutmacher, 25th anniversary article: engineering hydrogels for biofabrication, Advanced materials 25(36) (2013) 5011-5028.
[154] B. N. Turner, R. Strong, S. A. Gold, A review of melt extrusion additive manufacturing processes: I. Process design and modeling, Rapid Prototyping Journal 20(3) (2014) 192-204.
[155] B.N. Turner, S.A. Gold, A review of melt extrusion additive manufacturing processes: II. Materials, dimensional accuracy, and surface roughness, Rapid Prototyping Journal 21(3) (2015) 250-261.
[156] J.M. Lee, S.K.Q. Suen, W.L. Ng, W.C. Ma, W.Y. Yeong, Bioprinting of Collagen: Considerations, Potentials, and Applications, Macromolecular Bioscience 21(1) (2021) 2000280.
[157] N. Paxton, W. Smolan, T. Böck, F. Melchels, J. Groll, T. Jungst, Proposal to assess printability of bioinks for extrusion-based bioprinting and evaluation of rheological properties governing bioprintability, Biofabrication 9(4) (2017) 044107.
[158] D.M. Kirchmajer, R. Gorkin Iii, An overview of the suitability of hydrogel-forming polymers for extrusion-based 3D-printing, Journal of Materials Chemistry B 3(20) (2015) 4105-4117.
[159] K. Almdal, J. Dyre, S. Hvidt, O. Kramer, Towards a phenomenological definition of the term ‘gel’, Polymer gels and networks 1(1) (1993) 5-17.
[160] J. Groll, J. Burdick, D. Cho, B. Derby, M. Gelinsky, S. Heilshorn, T. Jüngst, J. Malda, V. Mironov, K. Nakayama, A definition of bioinks and their distinction from biomaterial inks, Biofabrication 11(1) (2018) 013001.
[161] M. Hospodiuk, M. Dey, D. Sosnoski, I.T. Ozbolat, The bioink: a comprehensive review on bioprintable materials, Biotechnology advances 35(2) (2017) 217-239.
[162] Y.B. Kim, H. Lee, G.H. Kim, Strategy to achieve highly porous/biocompatible macroscale cell blocks, using a collagen/genipin-bioink and an optimal 3D printing process, ACS applied materials & interfaces 8(47) (2016) 32230-32240.
[163] N.C. Hunt, L.M. Grover, Cell encapsulation using biopolymer gels for regenerative medicine, Biotechnology letters 32(6) (2010) 733-742.
[164] D.F. Duarte Campos, A. Blaeser, A. Korsten, S. Neuss, J. Jäkel, M. Vogt, H. Fischer, The stiffness and structure of three-dimensional printed hydrogels direct the differentiation of mesenchymal stromal cells toward adipogenic and osteogenic lineages, Tissue Engineering Part A 21(3-4) (2014) 740-756.
[165] J.-H. Shim, J.Y. Kim, M. Park, J. Park, D.-W. Cho, Development of a hybrid scaffold with synthetic biomaterials and hydrogel using solid freeform fabrication technology, Biofabrication 3(3) (2011) 034102.
[166] E.O. Osidak, V.I. Kozhukhov, M.S. Osidak, S.P. Domogatsky, Collagen as Bioink for Bioprinting: A Comprehensive Review, International Journal of Bioprinting 6(3) (2020).
[167] M. Askari, M.A. Naniz, M. Kouhi, A. Saberi, A. Zolfagharian, M. Bodaghi, Recent progress in extrusion 3D bioprinting of hydrogel biomaterials for tissue regeneration: a comprehensive review with focus on advanced fabrication techniques, Biomaterials science 9(3) (2021) 535-573.

[168] A.B. Dababneh, I.T. Ozbolat, Bioprinting technology: a current state-of-the-art review, Journal of Manufacturing Science and Engineering 136(6) (2014) 061016.
[169] J. Agassant, P. Avenas, J. Sergent, P. Carreau, Polymer processing: principles and modeling'; 1991, Munich, Hanser.
[170] S. Middleman, flow of high polymers; continuum and molecular rheology, (1968).
[171] S. Middleman, Fundamentals of polymer processing, McGraw-Hill College1977.
[172] R.B. Bird, R.C. Armstrong, O. Hassager, Dynamics of polymeric liquids. Vol. 1: Fluid mechanics, (1987).
[173] R. Joshi, Introduction to Drug Delivery, Collagen Biografts for Tunable Drug Delivery, Springer2021, pp. 1-8.
[174] J. Engel, H.P. Bächinger, Structure, stability and folding of the collagen triple helix, Collagen, Springer2005, pp. 7-33.
[175] R. Parenteau-Bareil, R. Gauvin, F. Berthod, Collagen-based biomaterials for tissue engineering applications, Materials 3(3) (2010) 1863-1887.
[176] M.J. Buehler, Nature designs tough collagen: explaining the nanostructure of collagen fibrils, Proceedings of the National Academy of Sciences 103(33) (2006) 12285-12290.
[177] V.R. Sherman, W. Yang, M.A. Meyers, The materials science of collagen, Journal of the mechanical behavior of biomedical materials 52 (2015) 22-50.
[178] D.R. Eyre, J.-J. Wu, Collagen Cross-Links, in: J. Brinckmann, H. Notbohm, P.K. Müller (Eds.), Collagen: Primer in Structure, Processing and Assembly, Springer Berlin Heidelberg, Berlin, Heidelberg, 2005, pp. 207-229.
[179] M.D. Shoulders, R.T. Raines, Collagen structure and stability, Annual review of biochemistry 78 (2009) 929-958.
[180] G. Beier, J. Engel, The renaturation of soluble collagen. Products formed at different temperatures, Biochemistry 5(8) (1966) 2744-2755.
[181] R. Dash, M. Foston, A.J. Ragauskas, Improving the mechanical and thermal properties of gelatin hydrogels cross-linked by cellulose nanowhiskers, Carbohydrate polymers 91(2) (2013) 638-645.
[182] N. Rajan, J. Habermehl, M.-F. Coté, C.J. Doillon, D. Mantovani, Preparation of ready-to-use, storable and reconstituted type I collagen from rat tail tendon for tissue engineering applications, Nature protocols 1(6) (2006) 2753-2758.
[183] R. Timpl, R.W. Glanville, H. Nowack, H. Wiedemann, P.P. Fietzek, K. Kühn, Isolation, chemical and electron microscopical characterization of neutral-salt-soluble type III collagen and procollagen from fetal bovine skin, (1975).
[184] K.E. Kadler, D.F. Holmes, J.A. Trotter, J.A. Chapman, Collagen fibril formation, Biochemical Journal 316(1) (1996) 1-11.
[185] J. Parkinson, K.E. Kadler, A. Brass, Simple physical model of collagen fibrillogenesis based on diffusion limited aggregation, Journal of molecular biology 247(4) (1995) 823-831.
[186] G. Wood, M.K. Keech, The formation of fibrils from collagen solutions 1. The effect of experimental conditions: kinetic and electron-microscope studies, Biochemical Journal 75(3) (1960) 588.
[187] G. Wood, The formation of fibrils from collagen solutions. 2. A mechanism for collagen-fibril formation, Biochemical Journal 75(3) (1960) 598.
[188] F. Gobeaux, G. Mosser, A. Anglo, P. Panine, P. Davidson, M.-M. Giraud-Guille, E. Belamie, Fibrillogenesis in dense collagen solutions: a physicochemical study, Journal of molecular biology 376(5) (2008) 1509-1522.

[189] F.H. Silver, D.E. Birk, Kinetic analysis of collagen fibrillogenesis: I. Use of turbidity-time data, Collagen and related research 3(5) (1983) 393-405.
[190] F. Gobeaux, E. Belamie, G. Mosser, P. Davidson, S. Asnacios, Power law rheology and strain-induced yielding in acidic solutions of type I-collagen, Soft Matter 6(16) (2010) 3769-3777.
[191] D.E. Birk, J. Fitch, J.P. Babiarz, K.J. Doane, T. Linsenmayer, Collagen fibrillogenesis in vitro: interaction of types I and V collagen regulates fibril diameter, Journal of cell science 95(4) (1990) 649-657.
[192] V. Magno, J. Friedrichs, H.M. Weber, M.C. Prewitz, M.V. Tsurkan, C. Werner, Macromolecular crowding for tailoring tissue-derived fibrillated matrices, Acta biomaterialia 55 (2017) 109-119.
[193] S. Ranamukhaarachchi, R. Modi, A. Han, D. Velez, A. Kumar, A. Engler, S. Fraley, Macromolecular crowding tunes 3D collagen architecture and cell morphogenesis, Biomaterials science 7(2) (2019) 618-633.
[194] C. Lee, A. Grodzinsky, M. Spector, The effects of cross-linking of collagen-glycosaminoglycan scaffolds on compressive stiffness, chondrocyte-mediated contraction, proliferation and biosynthesis, Biomaterials 22(23) (2001) 3145-3154.
[195] D. Veríssimo, R. Leitão, R. Ribeiro, S. Figueiró, A. Sombra, J. Góes, G. Brito, Polyanionic collagen membranes for guided tissue regeneration: Effect of progressive glutaraldehyde cross-linking on biocompatibility and degradation, Acta Biomaterialia 6(10) (2010) 4011-4018.
[196] Z. Tian, W. Liu, G. Li, The microstructure and stability of collagen hydrogel cross-linked by glutaraldehyde, Polymer Degradation and Stability 130 (2016) 264-270.
[197] Z. Tian, L. Duan, L. Wu, L. Shen, G. Li, Rheological properties of glutaraldehyde-crosslinked collagen solutions analyzed quantitatively using mechanical models, Materials Science and Engineering: C 63 (2016) 10-17.
[198] A. Sionkowska, J. Skopinska-Wisniewska, M. Gawron, J. Kozlowska, A. Planecka, Chemical and thermal cross-linking of collagen and elastin hydrolysates, International journal of biological macromolecules 47(4) (2010) 570-577.
[199] S.-N. Park, J.-C. Park, H.O. Kim, M.J. Song, H. Suh, Characterization of porous collagen/hyaluronic acid scaffold modified by 1-ethyl-3-(3-dimethylaminopropyl) carbodiimide cross-linking, Biomaterials 23(4) (2002) 1205-1212.
[200] D. Liu, X. Dong, B. Han, H. Huang, M. Qi, Cellulose nanocrystal/collagen hydrogels reinforced by anisotropic structure: shear viscoelasticity and related strengthening mechanism, Composites Communications 21 (2020) 100374.
[201] E. Tsekoura, A. Helling, J. Wall, Y. Bayon, D. Zeugolis, Battling bacterial infection with hexamethylene diisocyanate cross-linked and Cefaclor-loaded collagen scaffolds, Biomedical Materials 12(3) (2017) 035013.
[202] N. Bryan, H. Ashwin, N. Smart, Y. Bayon, N. Scarborough, J.A. Hunt, The innate oxygen dependant immune pathway as a sensitive parameter to predict the performance of biological graft materials, Biomaterials 33(27) (2012) 6380-6392.
[203] N. Gostynska, G.S. Krishnakumar, E. Campodoni, S. Panseri, M. Montesi, S. Sprio, E. Kon, M. Marcacci, A. Tampieri, M. Sandri, 3D porous collagen scaffolds reinforced by glycation with ribose for tissue engineering application, Biomedical Materials 12(5) (2017) 055002.
[204] H. Dandia, K. Makkad, P. Tayalia, Glycated collagen–a 3D matrix system to study pathological cell behavior, Biomaterials science 7(8) (2019) 3480-3488.

[205] G.S. Krishnakumar, N. Gostynska, E. Campodoni, M. Dapporto, M. Montesi, S. Panseri, A. Tampieri, E. Kon, M. Marcacci, S. Sprio, Ribose mediated crosslinking of collagen-hydroxyapatite hybrid scaffolds for bone tissue regeneration using biomimetic strategies, Materials Science and Engineering: C 77 (2017) 594-605.
[206] B.N. Mason, A. Starchenko, R.M. Williams, L.J. Bonassar, C.A. Reinhart-King, Tuning three-dimensional collagen matrix stiffness independently of collagen concentration modulates endothelial cell behavior, Acta biomaterialia 9(1) (2013) 4635-4644.
[207] Y.-J. Hwang, J. Larsen, T.B. Krasieva, J.G. Lyubovitsky, Effect of genipin crosslinking on the optical spectral properties and structures of collagen hydrogels, ACS applied materials & interfaces 3(7) (2011) 2579-2584.
[208] D. Macaya, K.K. Ng, M. Spector, Injectable collagen–genipin gel for the treatment of spinal cord injury: in vitro studies, Advanced Functional Materials 21(24) (2011) 4788-4797.
[209] J. Chen, Z. Cai, Q. Wei, D. Wang, J. Wu, Y. Tan, J. Lu, H. Ai, Proanthocyanidin-crosslinked collagen/konjac glucomannan hydrogel with improved mechanical properties and MRI trackable biodegradation for potential tissue engineering scaffolds, Journal of Materials Chemistry B 8(2) (2020) 316-331.
[210] H. Yang, L. Duan, Q. Li, Z. Tian, G. Li, Experimental and modeling investigation on the rheological behavior of collagen solution as a function of acetic acid concentration, Journal of the mechanical behavior of biomedical materials 77 (2018) 125-134.
[211] L. Brazdaru, M. Micutz, T. Staicu, M. Albu, D. Sulea, M. Leca, Structural and rheological properties of collagen hydrogels containing tannic acid and chlorhexidine digluconate intended for topical applications, Comptes Rendus Chimie 18(2) (2015) 160-169.
[212] N. Diamantides, L. Wang, T. Pruiksma, J. Siemiatkoski, C. Dugopolski, S. Shortkroff, S. Kennedy, L.J. Bonassar, Correlating rheological properties and printability of collagen bioinks: the effects of riboflavin photocrosslinking and pH, Biofabrication 9(3) (2017) 034102.
[213] G. Lai, Y. Li, G. Li, Effect of concentration and temperature on the rheological behavior of collagen solution, International Journal of Biological Macromolecules 42(3) (2008) 285-291.
[214] K.K. Moncal, V. Ozbolat, P. Datta, D.N. Heo, I.T. Ozbolat, Thermally-controlled extrusion-based bioprinting of collagen, Journal of Materials Science: Materials in Medicine 30(5) (2019) 1-14.
[215] X. Lan, Y. Liang, E.J. Erkut, M. Kunze, A. Mulet-Sierra, T. Gong, M. Osswald, K. Ansari, H. Seikaly, Y. Boluk, Bioprinting of human nasoseptal chondrocytes-laden collagen hydrogel for cartilage tissue engineering, The FASEB Journal 35(3) (2021) e21191.
[216] M.G. Haugh, M.J. Jaasma, F.J. O'Brien, The effect of dehydrothermal treatment on the mechanical and structural properties of collagen-GAG scaffolds, Journal of Biomedical Materials Research Part A: An Official Journal of The Society for Biomaterials, The Japanese Society for Biomaterials, and The Australian Society for Biomaterials and the Korean Society for Biomaterials 89(2) (2009) 363-369.
[217] K.S. Weadock, E.J. Miller, L.D. Bellincampi, J.P. Zawadsky, M.G.J.J.o.b.m.r. Dunn, Physical crosslinking of collagen fibers: comparison of ultraviolet irradiation and dehydrothermal treatment, 29(11) (1995) 1373-1379.
[218] Q. Zhang, Q. Tang, Y. Yang, J. Yi, W. Wei, Y. Hong, X. Zhang, F. Zhou, X. Yao, H.J.A.M.T. Ouyang, Wound dressing gel with resisted bacterial penetration and enhanced re-epithelization for corneal epithelial-stromal regeneration, 24 (2021) 101119.

[219] N. Diamantides, C. Dugopolski, E. Blahut, S. Kennedy, L.J. Bonassar, High density cell seeding affects the rheology and printability of collagen bioinks, Biofabrication 11(4) (2019) 045016.
[220] T. Nishihara, P. Doty, The sonic fragmentation of collagen macromolecules, Proceedings of the National Academy of Sciences of the United States of America 44(5) (1958) 411.
[221] H. Oguzlu, C. Danumah, Y. Boluk, Colloidal behavior of aqueous cellulose nanocrystal suspensions, Current opinion in colloid & interface science 29 (2017) 46-56.
[222] H. Gudapati, D. Parisi, R.H. Colby, I.T. Ozbolat, Rheological investigation of collagen, fibrinogen, and thrombin solutions for drop-on-demand 3D bioprinting, Soft matter 16(46) (2020) 10506-10517.
[223] A. Blaeser, D.F. Duarte Campos, U. Puster, W. Richtering, M.M. Stevens, H. Fischer, Controlling shear stress in 3D bioprinting is a key factor to balance printing resolution and stem cell integrity, Advanced healthcare materials 5(3) (2016) 326-333.
[224] J. Mewis, N.J. Wagner, Colloidal suspension rheology, Cambridge university press2012.
[225] M. Müller, E. Öztürk, Ø. Arlov, P. Gatenholm, M. Zenobi-Wong, Alginate sulfate–nanocellulose bioinks for cartilage bioprinting applications, Annals of biomedical engineering 45(1) (2017) 210-223.
[226] C.A. Cathey, G.G. Fuller, Uniaxial and biaxial extensional viscosity measurements of dilute and semi-dilute solutions of rigid rod polymers, Journal of non-newtonian fluid mechanics 30(2-3) (1988) 303-316.
[227] G. Batchelor, The stress generated in a non-dilute suspension of elongated particles by pure straining motion, Journal of Fluid Mechanics 46(4) (1971) 813-829.
[228] J.A. Paten, S.M. Siadat, M.E. Susilo, E.N. Ismail, J.L. Stoner, J.P. Rothstein, J.W. Ruberti, Flow-induced crystallization of collagen: a potentially critical mechanism in early tissue formation, ACS nano 10(5) (2016) 5027-5040.
[229] G. Forgacs, S.A. Newman, B. Hinner, C.W. Maier, E. Sackmann, Assembly of collagen matrices as a phase transition revealed by structural and rheologic studies, Biophysical journal 84(2) (2003) 1272-1280.
[230] W. Friess, M. Schlapp, Effects of processing conditions on the rheological behavior of collagen dispersions, European journal of pharmaceutics and biopharmaceutics 51(3) (2001) 259-265.
[231] J. Lee, M. Yeo, W. Kim, Y. Koo, G.H. Kim, Development of a tannic acid cross-linking process for obtaining 3D porous cell-laden collagen structure, International journal of biological macromolecules 110 (2018) 497-503.
[232] A.D. Nocera, R. Comín, N.A. Salvatierra, M.P. Cid, Development of 3D printed fibrillar collagen scaffold for tissue engineering, Biomedical microdevices 20(2) (2018) 26.
[233] L. Ouyang, R. Yao, Y. Zhao, W. Sun, Effect of bioink properties on printability and cell viability for 3D bioplotting of embryonic stem cells, Biofabrication 8(3) (2016) 035020.
[234] S.A. Madbouly, J.U. Otaigbe, Kinetic analysis of fractal gel formation in waterborne polyurethane dispersions undergoing high deformation flows, Macromolecules 39(12) (2006) 4144-4151.
[235] H. Yoon, J.-S. Lee, H. Yim, G. Kim, W. Chun, Development of cell-laden 3D scaffolds for efficient engineered skin substitutes by collagen gelation, RSC advances 6(26) (2016) 21439-21447.
[236] R. Gelman, B.R. Williams, K. Piez, Collagen fibril formation. Evidence for a multistep process, Journal of Biological Chemistry 254(1) (1979) 180-186.

[237] A.W. Pederson, J.W. Ruberti, P.B. Messersmith, Thermal assembly of a biomimetic mineral/collagen composite, Biomaterials 24(26) (2003) 4881-4890.
[238] M.R. Kamal, H. Nyun, Capillary viscometry: a complete analysis including pressure and viscous heating effects, Polymer Engineering & Science 20(2) (1980) 109-119.
[239] A. Bellini, S. Guceri, M. Bertoldi, Liquefier dynamics in fused deposition, Journal of Manufacturing Science and Engineering 126(2) (2004) 237-246.
[240] B. Han, J. Jaurequi, B.W. Tang, M.E. Nimni, Proanthocyanidin: a natural crosslinking reagent for stabilizing collagen matrices, Journal of Biomedical Materials Research Part A: An Official Journal of The Society for Biomaterials, The Japanese Society for Biomaterials, and The Australian Society for Biomaterials and the Korean Society for Biomaterials 65(1) (2003) 118-124.
[241] D.T. Cheung, D. Tong, N. Perelman, D. Ertl, M.E. Nimni, Mechanism of crosslinking of proteins by glutaraldehyde IV: In Vitro and In Vivo stability of a crosslinked collagen matrix, Connective Tissue Research 25(1) (1990) 27-34.
[242] M.E. Nimni, D. Cheung, B. Strates, M. Kodama, K. Sheikh, Chemically modified collagen: a natural biomaterial for tissue replacement, Journal of biomedical materials research 21(6) (1987) 741-771.
[243] V. Perez-Puyana, A. Romero, A. Guerrero, Influence of collagen concentration and glutaraldehyde on collagen-based scaffold properties, Journal of Biomedical Materials Research Part A 104(6) (2016) 1462-1468.
[244] K. Hyun, M. Wilhelm, C.O. Klein, K.S. Cho, J.G. Nam, K.H. Ahn, S.J. Lee, R.H. Ewoldt, G.H. McKinley, A review of nonlinear oscillatory shear tests: Analysis and application of large amplitude oscillatory shear (LAOS), Progress in Polymer Science 36(12) (2011) 1697-1753.
[245] R.H. Ewoldt, A. Hosoi, G.H. McKinley, New measures for characterizing nonlinear viscoelasticity in large amplitude oscillatory shear, Journal of Rheology 52(6) (2008) 1427-1458.
[246] J.R. McKee, S. Hietala, J. Seitsonen, J. Laine, E. Kontturi, O. Ikkala, Thermoresponsive nanocellulose hydrogels with tunable mechanical properties, ACS Macro Letters 3(3) (2014) 266-270.
[247] K. Hyun, S.H. Kim, K.H. Ahn, S.J. Lee, Large amplitude oscillatory shear as a way to classify the complex fluids, Journal of Non-Newtonian Fluid Mechanics 107(1-3) (2002) 51-65.
[248] J. Stolz, H. Oguzlu, Z. Khalili, Y. Boluk, Exploring the gelation of aqueous cellulose nanocrystals (CNCs)-hydroxyethyl cellulose (HEC) mixtures, Rheologica Acta 60(9) (2021) 483-495.
[249] S. Nam, K.H. Hu, M.J. Butte, O. Chaudhuri, Strain-enhanced stress relaxation impacts nonlinear elasticity in collagen gels, Proceedings of the National Academy of Sciences 113(20) (2016) 5492-5497.
[250] S.W. Kim, D.Y. Kim, H.H. Roh, H.S. Kim, J.W. Lee, K.Y. Lee, Three-dimensional bioprinting of cell-laden constructs using polysaccharide-based self-healing hydrogels, Biomacromolecules 20(5) (2019) 1860-1866.
[251] H.M. Laun, Polymer melt rheology with a slit die, Rheologica Acta 22(2) (1983) 171-185.
[252] F. Cogswell, Converging flow of polymer melts in extrusion dies, Polymer Engineering & Science 12(1) (1972) 64-73.
[253] E. Bagley, End corrections in the capillary flow of polyethylene, Journal of Applied Physics 28(5) (1957) 624-627.
[254] D. Huang, R. Shroff, Converging flow of polymer melts, Journal of Rheology 25(6) (1981) 605-617.

[255] V. Bertola, B. Meulenbroek, C. Wagner, C. Storm, A. Morozov, W. van Saarloos, D. Bonn, Experimental evidence for an intrinsic route to polymer melt fracture phenomena: a nonlinear instability of viscoelastic Poiseuille flow, Physical review letters 90(11) (2003) 114502.
[256] J.-F. Agassant, P. Avenas, P.J. Carreau, B. Vergnes, M. Vincent, Polymer processing: principles and modeling, Carl Hanser Verlag GmbH Co KG2017.
[257] M.E. Mackay, The importance of rheological behavior in the additive manufacturing technique material extrusion, Journal of Rheology 62(6) (2018) 1549-1561.
[258] P.-G. de Gennes, Reptation of a polymer chain in the presence of fixed obstacles, The journal of chemical physics 55(2) (1971) 572-579.
[259] M. Doi, S. Edwards, Dynamics of concentrated polymer systems. Part 2.—Molecular motion under flow, Journal of the Chemical Society, Faraday Transactions 2: Molecular and Chemical Physics 74 (1978) 1802-1817.
[260] Y.H. Kim, R.P. Wool, A theory of healing at a polymer-polymer interface, Macromolecules 16(7) (1983) 1115-1120.
[261] Z. Wei, J.H. Yang, J. Zhou, F. Xu, M. Zrínyi, P.H. Dussault, Y. Osada, Y.M. Chen, Self-healing gels based on constitutional dynamic chemistry and their potential applications, Chemical Society Reviews 43(23) (2014) 8114-8131.
[262] Z. Liu, M. Zhang, B. Bhandari, C. Yang, Impact of rheological properties of mashed potatoes on 3D printing, Journal of Food Engineering 220 (2018) 76-82.
[263] S. Rhee, J.L. Puetzer, B.N. Mason, C.A. Reinhart-King, L.J. Bonassar, 3D bioprinting of spatially heterogeneous collagen constructs for cartilage tissue engineering, ACS Biomaterials Science & Engineering 2(10) (2016) 1800-1805.
[264] H.M. Ávila, S. Schwarz, N. Rotter, P. Gatenholm, 3D bioprinting of human chondrocyte-laden nanocellulose hydrogels for patient-specific auricular cartilage regeneration, Bioprinting 1 (2016) 22-35.
[265] T. Billiet, E. Gevaert, T. De Schryver, M. Cornelissen, P. Dubruel, The 3D printing of gelatin methacrylamide cell-laden tissue-engineered constructs with high cell viability, Biomaterials 35(1) (2014) 49-62.
[266] E. Rizzuto, A. Musarò, A. Catizone, Z. Del Prete, Measuring tendon properties in mdx mice: cell viability and viscoelastic characteristics, Journal of biomechanics 42(14) (2009) 2243-2248.
[267] T. Tanzeglock, M. Soos, G. Stephanopoulos, M. Morbidelli, Induction of mammalian cell death by simple shear and extensional flows, Biotechnology and bioengineering 104(2) (2009) 360-370.
[268] B.A. Aguado, W. Mulyasasmita, J. Su, K.J. Lampe, S.C. Heilshorn, Improving viability of stem cells during syringe needle flow through the design of hydrogel cell carriers, Tissue Engineering Part A 18(7-8) (2011) 806-815.
[269] M. Li, X. Tian, J.A. Kozinski, X. Chen, D.K. Hwang, Modeling mechanical cell damage in the bioprinting process employing a conical needle, Journal of Mechanics in Medicine and Biology 15(05) (2015) 1550073.
[270] A.A. Szklanny, M. Machour, I. Redenski, V. Chochola, I. Goldfracht, B. Kaplan, M. Epshtein, H. Simaan Yameen, U. Merdler, A.J.A.M. Feinberg, 3D Bioprinting of Engineered Tissue Flaps with Hierarchical Vessel Networks (VesselNet) for Direct Host-To-Implant Perfusion, 33(42) (2021) 2102661.

[271] L. Dogan, R. Scheuring, N. Wagner, Y. Ueda, S. Schmidt, P. Wörsdörfer, J. Groll, S.J.B. Ergün, Human iPSC-derived mesodermal progenitor cells preserve their vasculogenesis potential after extrusion and form hierarchically organized blood vessels, 13(4) (2021) 045028.
[272] S. Muthusamy, S. Kannan, M. Lee, V. Sanjairaj, W.F. Lu, J.Y. Fuh, G. Sriram, T.J.B. Cao, Bioengineering, 3D bioprinting and microscale organization of vascularized tissue constructs using collagen-based bioink, (2021).
[273] H. Oliveira, C. Médina, M.-L. Stachowicz, B.P. dos Santos, L. Chagot, N. Dusserre, J.-C.J.B. Fricain, Extracellular matrix (ECM)-derived bioinks designed to foster vasculogenesis and neurite outgrowth: Characterization and bioprinting, 22 (2021) e00134.
[274] T.T. Dang, C.H. Hwang, S.H. Back, K.-i.J.B. Koo, Coaxial printing of double-layered and free-standing blood vessel analogues without ultraviolet illumination for high-volume vascularised tissue, 12(4) (2020) 045033.
[275] F. Kreimendahl, M. Köpf, A.L. Thiebes, D.F. Duarte Campos, A. Blaeser, T. Schmitz-Rode, C. Apel, S. Jockenhoevel, H.J.T.E.P.C.M. Fischer, Three-dimensional printing and angiogenesis: tailored agarose-type I collagen blends comprise three-dimensional printability and angiogenesis potential for tissue-engineered substitutes, 23(10) (2017) 604-615.
[276] H. Stratesteffen, M. Köpf, F. Kreimendahl, A. Blaeser, S. Jockenhoevel, H.J.B. Fischer, GelMA-collagen blends enable drop-on-demand 3D printablility and promote angiogenesis, 9(4) (2017) 045002.
[277] G.S. Diogo, C.F. Marques, S. Freitas-Ribeiro, C.G. Sotelo, R.I. Pérez-Martin, R.P. Pirraco, R.L. Reis, T.H.J.M.S. Silva, E. C, Mineralized collagen as a bioactive ink to support encapsulation of human adipose stem cells: A step towards the future of bone regeneration, (2021) 112600.
[278] W.S. Yang, W.J. Kim, J.Y. Ahn, J. Lee, D.W. Ko, S. Park, J.Y. Kim, C.H. Jang, J.M. Lim, G.H.J.A.A.M. Kim, Interfaces, New Bioink Derived from Neonatal Chicken Bone Marrow Cells and Its 3D-Bioprinted Niche for Osteogenic Stimulators, 12(44) (2020) 49386-49397.
[279] Y. Yang, M. Wang, S. Yang, Y. Lin, Q. Zhou, H. Li, T.J.B. Tang, Bioprinting of an osteocyte network for biomimetic mineralization, 12(4) (2020) 045013.
[280] G.S. Diogo, C.F. Marques, C.G. Sotelo, R.I. Pérez-Martín, R.P. Pirraco, R.L. Reis, T.H.J.A.B.S. Silva, Engineering, Cell-laden biomimetically mineralized shark-skin-collagen-based 3D printed hydrogels for the engineering of hard tissues, 6(6) (2020) 3664-3672.
[281] A. Schwab, C. Hélary, R. Richards, M. Alini, D. Eglin, M.J.M.T.B. d'Este, Tissue mimetic hyaluronan bioink containing collagen fibers with controlled orientation modulating cell migration and alignment, 7 (2020) 100058.
[282] Q. Li, X. Lei, X. Wang, Z. Cai, P. Lyu, G.J.T.E.P.A. Zhang, Hydroxyapatite/collagen three-dimensional printed scaffolds and their osteogenic effects on human bone marrow-derived mesenchymal stem cells, 25(17-18) (2019) 1261-1271.
[283] M.O. Aydogdu, E.T. Oner, N. Ekren, G. Erdemir, S.E. Kuruca, E. Yuca, M.S. Bostan, M.S. Eroglu, F. Ikram, M.J.B. Uzun, Comparative characterization of the hydrogel added PLA/β-TCP scaffolds produced by 3D bioprinting, 13 (2019) e00046.
[284] O. Kérourédan, J.-M. Bourget, M. Rémy, S. Crauste-Manciet, J. Kalisky, S. Catros, N.B. Thébaud, R.J.J.o.M.S.M.i.M. Devillard, Micropatterning of endothelial cells to create a capillary-like network with defined architecture by laser-assisted bioprinting, 30(2) (2019) 28.
[285] R. da Conceicao Ribeiro, D. Pal, A.M. Ferreira, P. Gentile, M. Benning, K.J.B. Dalgarno, Reactive jet impingement bioprinting of high cell density gels for bone microtissue fabrication, 11(1) (2018) 015014.

[286] L. Benning, L. Gutzweiler, K. Tröndle, J. Riba, R. Zengerle, P. Koltay, S. Zimmermann, G.B. Stark, G.J.J.o.B.M.R.P.A. Finkenzeller, Cytocompatibility testing of hydrogels toward bioprinting of mesenchymal stem cells, 105(12) (2017) 3231-3241.
[287] V. Keriquel, H. Oliveira, M. Rémy, S. Ziane, S. Delmond, B. Rousseau, S. Rey, S. Catros, J. Amédée, F.J.S.r. Guillemot, In situ printing of mesenchymal stromal cells, by laser-assisted bioprinting, for in vivo bone regeneration applications, 7(1) (2017) 1-10.
[288] E.E. Beketov, E.V. Isaeva, N.D. Yakovleva, G.A. Demyashkin, N.V. Arguchinskaya, A.A. Kisel, T.S. Lagoda, E.P. Malakhov, V.I. Kharlov, E.O.J.I.J.o.M.S. Osidak, Bioprinting of Cartilage with Bioink Based on High-Concentration Collagen and Chondrocytes, 22(21) (2021) 11351.
[289] D.F.D. Campos, M.A. Philip, S. Gürzing, C. Melcher, Y.Y. Lin, J. Schöneberg, A. Blaeser, B. Theek, H. Fischer, M.J.D.P. Betsch, A. Manufacturing, Synchronized dual bioprinting of bioinks and biomaterial inks as a translational strategy for cartilage tissue engineering, 6(2) (2019) 63-71.
[290] G. Filardo, M. Petretta, C. Cavallo, L. Roseti, S. Durante, U. Albisinni, B.J.B. Grigolo, j. research, Patient-specific meniscus prototype based on 3D bioprinting of human cell-laden scaffold, 8(2) (2019) 101-106.
[291] X. Yang, Z. Lu, H. Wu, W. Li, L. Zheng, J.J.M.S. Zhao, E. C, Collagen-alginate as bioink for three-dimensional (3D) cell printing based cartilage tissue engineering, 83 (2018) 195-201.
[292] H.-R. Lee, J.A. Park, S. Kim, Y. Jo, D. Kang, S.J.B. Jung, 3D microextrusion-inkjet hybrid printing of structured human skin equivalents, 22 (2021) e00143.
[293] D. Min, W. Lee, I.H. Bae, T.R. Lee, P. Croce, S.S.J.E.d. Yoo, Bioprinting of biomimetic skin containing melanocytes, 27(5) (2018) 453-459.
[294] Y. Shi, T. Xing, H. Zhang, R. Yin, S. Yang, J. Wei, W.J.B.M. Zhang, Tyrosinase-doped bioink for 3D bioprinting of living skin constructs, 13(3) (2018) 035008.
[295] X. Hou, S. Liu, M. Wang, C. Wiraja, W. Huang, P. Chan, T. Tan, C.J.S.T.T.L.S.I. Xu, Layer-by-layer 3D constructs of fibroblasts in hydrogel for examining transdermal penetration capability of nanoparticles, 22(4) (2017) 447-453.
[296] B.S. Kim, J.-S. Lee, G. Gao, D.-W.J.B. Cho, Direct 3D cell-printing of human skin with functional transwell system, 9(2) (2017) 025034.
[297] T. Schmitt, N. Katz, V.J.F.i.B. Kishore, Biotechnology, A Feasibility Study on 3D Bioprinting of Microfat Constructs Towards Wound Healing Applications, 9 (2021).
[298] N. Hakimi, R. Cheng, L. Leng, M. Sotoudehfar, P.Q. Ba, N. Bakhtyar, S. Amini-Nik, M.G. Jeschke, A.J.L.o.a.C. Günther, Handheld skin printer: in situ formation of planar biomaterials and tissues, 18(10) (2018) 1440-1451.
[299] A. Sorkio, L. Koch, L. Koivusalo, A. Deiwick, S. Miettinen, B. Chichkov, H.J.B. Skottman, Human stem cell based corneal tissue mimicking structures using laser-assisted 3D bioprinting and functional bioinks, 171 (2018) 57-71.
[300] A. Mazzocchi, M. Devarasetty, R. Huntwork, S. Soker, A.J.B. Skardal, Optimization of collagen type I-hyaluronan hybrid bioink for 3D bioprinted liver microenvironments, 11(1) (2018) 015003.
[301] W. Kim, C.H. Jang, G.J.C.E.J. Kim, Bioprinted hASC-laden structures with cell-differentiation niches for muscle regeneration, 419 (2021) 129570.
[302] T.B. Ngo, B.S. Spearman, N. Hlavac, C.E.J.A.B.S. Schmidt, Engineering, Three-Dimensional Bioprinted Hyaluronic Acid Hydrogel Test Beds for Assessing Neural Cell Responses to Competitive Growth Stimuli, 6(12) (2020) 6819-6830.

[303] C.C. Clark, J. Aleman, L. Mutkus, A.J.B. Skardal, A mechanically robust thixotropic collagen and hyaluronic acid bioink supplemented with gelatin nanoparticles, 16 (2019) e00058.
[304] D.F. Duarte Campos, A. Bonnin Marquez, C. O'Seanain, H. Fischer, A. Blaeser, M. Vogt, D. Corallo, S.J.C. Aveic, Exploring cancer cell behavior in vitro in three-dimensional multicellular bioprintable collagen-based hydrogels, 11(2) (2019) 180.
[305] M. Feng, S. Hu, W. Qin, Y. Tang, R. Guo, L.J.A.o. Han, Bioprinting of a Blue Light-Cross-Linked Biodegradable Hydrogel Encapsulating Amniotic Mesenchymal Stem Cells for Intrauterine Adhesion Prevention, 6(36) (2021) 23067-23075.
[306] H. Jongprasitkul, S. Turunen, V.S. Parihar, S. Annurakshita, M.J.B. Kellomäki, Photocross-linkable Methacrylated Polypeptides and Polysaccharides for Casting, Injecting, and 3D Fabrication, 22(2) (2020) 481-493.
[307] Y. Liu, X. Luo, W. Wu, A. Zhang, B. Lu, T. Zhang, M.J.I.J.o.B.M. Kong, Dual cure (thermal/photo) composite hydrogel derived from chitosan/collagen for in situ 3D bioprinting, 182 (2021) 689-700.
[308] Y. Zhang, S.T. Ellison, S. Duraivel, C.D. Morley, C.R. Taylor, T.E.J.B. Angelini, 3D printed collagen structures at low concentrations supported by jammed microgels, 21 (2021) e00121.
[309] T. Schmitt, N. Kajave, H.H. Cai, L. Gu, M. Albanna, V.J.J.o.B.A. Kishore, In vitro characterization of xeno-free clinically relevant human collagen and its applicability in cell-laden 3D bioprinting, 35(8) (2021) 912-923.
[310] K. Guo, H. Wang, S. Li, H. Zhang, S. Li, H. Zhu, Z. Yang, L. Zhang, P. Chang, X.J.A.A.M. Zheng, Interfaces, Collagen-Based Thiol–Norbornene Photoclick Bio-Ink with Excellent Bioactivity and Printability, 13(6) (2021) 7037-7050.
[311] A.C. Heidenreich, M. Pérez-Recalde, A.G. Wusener, É.B.J.P.T. Hermida, Collagen and chitosan blends for 3D bioprinting: A rheological and printability approach, 82 (2020) 106297.
[312] N.S. Kajave, T. Schmitt, T.-U. Nguyen, V.J.M.S. Kishore, E. C, Dual crosslinking strategy to generate mechanically viable cell-laden printable constructs using methacrylated collagen bioinks, 107 (2020) 110290.
[313] K.K. Moncal, V. Ozbolat, P. Datta, D.N. Heo, I.T.J.J.o.M.S.M.i.M. Ozbolat, Thermally-controlled extrusion-based bioprinting of collagen, 30(5) (2019) 1-14.
[314] E.O. Osidak, P.A. Karalkin, M.S. Osidak, V.A. Parfenov, D.E. Sivogrivov, F.D. Pereira, A.A. Gryadunova, E.V. Koudan, Y.D. Khesuani, V.A.J.J.o.M.S.M.i.M. Kasyanov, Viscoll collagen solution as a novel bioink for direct 3D bioprinting, 30(3) (2019) 1-12.
[315] J. He, J. Shao, X. Li, Q. Huang, T.J.B. Xu, Bioprinting of coaxial multicellular structures for a 3D co-culture model, 11 (2018) e00036.
[316] A. Bandyopadhyay, V.K. Dewangan, K.Y. Vajanthri, S. Poddar, S.K.J.B. Mahto, B. Engineering, Easy and affordable method for rapid prototyping of tissue models in vitro using three-dimensional bioprinting, 38(1) (2018) 158-169.
[317] A. Engberg, C. Stelzl, O. Eriksson, P. O'Callaghan, J.J.S.r. Kreuger, An open source extrusion bioprinter based on the E3D motion system and tool changer to enable FRESH and multimaterial bioprinting, 11(1) (2021) 1-11.
[318] P. Zhuang, Z. Greenberg, M.J.A.M.T. He, Biologically Enhanced Starch Bio-Ink for Promoting 3D Cell Growth, (2021) 2100551.
[319] R. Gibney, E.J.F.i.b. Ferraris, biotechnology, Bioprinting of collagen type I and II via aerosol jet printing for the replication of dense collagenous tissues, (2021) 1068.

[320] G.K. Austin, W.W. Shockley, Reconstruction of nasal defects: contemporary approaches, Curr Opin Otolaryngol Head Neck Surg 24(5) (2016) 453-60.
[321] C. Vinatier, J. Guicheux, Cartilage tissue engineering: From biomaterials and stem cells to osteoarthritis treatments, Ann Phys Rehabil Med 59(3) (2016) 139-144.
[322] G.C. Burget, F.J. Menick, The subunit principle in nasal reconstruction, Plast Reconstr Surg 76(2) (1985) 239-247.
[323] F.J. Menick, Nasal reconstruction, Plast Reconstr Surg 125(4) (2010) 138e-150e.
[324] D.M. Toriumi, Autogenous grafts are worth the extra time, Arch Otolaryngol Head Neck Surg 126(4) (2000) 562-4.
[325] T. Romo, 3rd, A.P. Sclafani, P. Sabini, Reconstruction of the major saddle nose deformity using composite allo-implants, Facial Plast Surg 14(2) (1998) 151-7.
[326] D.W. Raimer, A.R. Group, M.S. Petitt, N. Nosrati, M.L. Yamazaki, N.A. Davis, B.C. Kelly, B.R. Gibson, R.D. Montilla, R.F. Wagner, Jr., Porcine xenograft biosynthetic wound dressings for the management of postoperative Mohs wounds, Dermatol Online J 17(9) (2011) 1.
[327] M. Ansari, M. Eshghanmalek, Biomaterials for repair and regeneration of the cartilage tissue, Bio-Design and Manufacturing 2(1) (2019) 41-49.
[328] P.H. Chao, S. Yodmuang, X. Wang, L. Sun, D.L. Kaplan, G. Vunjak-Novakovic, Silk hydrogel for cartilage tissue engineering, J Biomed Mater Res B Appl Biomater 95(1) (2010) 84-90.
[329] N. Gupta, M.A. Cruz, P. Nasser, J.D. Rosenberg, J.C. Iatridis, Fibrin-Genipin Hydrogel for Cartilage Tissue Engineering in Nasal Reconstruction, Ann Otol Rhinol Laryngol 128(7) (2019) 640-646.
[330] S.H. Park, J.Y. Seo, J.Y. Park, Y.B. Ji, K. Kim, H.S. Choi, S. Choi, J.H. Kim, B.H. Min, M.S. Kim, An injectable, click-crosslinked, cytomodulin-modified hyaluronic acid hydrogel for cartilage tissue engineering, Npg Asia Mater 11(1) (2019) 1-16.
[331] X. Cui, K. Breitenkamp, M. Finn, M. Lotz, D.D. D'Lima, Direct human cartilage repair using three-dimensional bioprinting technology, Tissue Engineering Part A 18(11-12) (2012) 1304-1312.
[332] M. Nakamura, S. Iwanaga, C. Henmi, K. Arai, Y. Nishiyama, Biomatrices and biomaterials for future developments of bioprinting and biofabrication, Biofabrication 2(1) (2010) 014110.
[333] B. Balakrishnan, R. Banerjee, Biopolymer-based hydrogels for cartilage tissue engineering, Chemical reviews 111(8) (2011) 4453-4474.
[334] J. Kopeček, Hydrogel biomaterials: a smart future?, Biomaterials 28(34) (2007) 5185-5192.
[335] J.Y. Park, J.-C. Choi, J.-H. Shim, J.-S. Lee, H. Park, S.W. Kim, J. Doh, D.-W. Cho, A comparative study on collagen type I and hyaluronic acid dependent cell behavior for osteochondral tissue bioprinting, Biofabrication 6(3) (2014) 035004.
[336] L. Pescosolido, W. Schuurman, J. Malda, P. Matricardi, F. Alhaique, T. Coviello, P.R. van Weeren, W.J. Dhert, W.E. Hennink, T. Vermonden, Hyaluronic acid and dextran-based semi-IPN hydrogels as biomaterials for bioprinting, Biomacromolecules 12(5) (2011) 1831-1838.
[337] W.L. Ng, W.Y. Yeong, M.W. Naing, Polyelectrolyte gelatin-chitosan hydrogel optimized for 3D bioprinting in skin tissue engineering, International Journal of Bioprinting 2(1) (2016).
[338] T.T. Demirtaş, G. Irmak, M. Gümüşderelioğlu, A bioprintable form of chitosan hydrogel for bone tissue engineering, Biofabrication 9(3) (2017) 035003.

[339] D. Nguyen, D.A. Hägg, A. Forsman, J. Ekholm, P. Nimkingratana, C. Brantsing, T. Kalogeropoulos, S. Zaunz, S. Concaro, M. Brittberg, Cartilage tissue engineering by the 3D bioprinting of iPS cells in a nanocellulose/alginate bioink, Scientific reports 7(1) (2017) 658.
[340] T. Gao, G.J. Gillispie, J.S. Copus, Y.-J. Seol, A. Atala, J.J. Yoo, S.J. Lee, Optimization of gelatin–alginate composite bioink printability using rheological parameters: A systematic approach, Biofabrication 10(3) (2018) 034106.
[341] P. Gatenholm, H. Martinez, E. Karabulut, M. Amoroso, L. Kölby, K. Markstedt, E. Gatenholm, I. Henriksson, Development of nanocellulose-based bioinks for 3d bioprinting of soft tissue, 3D Printing and Biofabrication (2018) 331-352.
[342] L. Cen, W. Liu, L. Cui, W. Zhang, Y. Cao, Collagen tissue engineering: development of novel biomaterials and applications, Pediatric research 63(5) (2008) 492.
[343] J. Glowacki, S. Mizuno, Collagen scaffolds for tissue engineering, Biopolymers: Original Research on Biomolecules 89(5) (2008) 338-344.
[344] B. Chevallay, D. Herbage, Collagen-based biomaterials as 3D scaffold for cell cultures: applications for tissue engineering and gene therapy, Medical and Biological Engineering and Computing 38(2) (2000) 211-218.
[345] D.G. Wallace, J. Rosenblatt, Collagen gel systems for sustained delivery and tissue engineering, Advanced drug delivery reviews 55(12) (2003) 1631-1649.
[346] N.S. Gudmann, M.A. Karsdal, Type II Collagen, in: M.A. Karsdal (Ed.), Biochemistry of Collagens, Laminins and Elastin, Academic Press2016, pp. 13-20.
[347] D.E. Trentham, A.S. Townes, A.H. Kang, Autoimmunity to type II collagen an experimental model of arthritis, J Exp Med 146(3) (1977) 857-68.
[348] T.J. Yoo, J.M. Stuart, T. Takeda, N. Sudo, R.A. Floyd, T. Ishibe, G. Olson, D. Orchik, J.J. Shea, A.H. Kang, Induction of Type-Ii Collagen Autoimmune Arthritis and Ear Disease in Monkey, Ann. N.Y. Acad. Sci. 475 (1986) 341-342.
[349] A.K. Lynn, I.V. Yannas, W. Bonfield, Antigenicity and immunogenicity of collagen, J Biomed Mater Res B Appl Biomater 71(2) (2004) 343-54.
[350] S. Radhakrishnan, S. Nagarajan, M. Bechelany, S.N. Kalkura, Collagen Based Biomaterials for Tissue Engineering Applications: A Review, Springer International Publishing, Cham, 2020, pp. 3-22.
[351] V. Irawan, T.C. Sung, A. Higuchi, T. Ikoma, Collagen Scaffolds in Cartilage Tissue Engineering and Relevant Approaches for Future Development, Tissue Eng Regen Med 15(6) (2018) 673-697.
[352] T.J. Hinton, Q. Jallerat, R.N. Palchesko, J.H. Park, M.S. Grodzicki, H.J. Shue, M.H. Ramadan, A.R. Hudson, A.W. Feinberg, Three-dimensional printing of complex biological structures by freeform reversible embedding of suspended hydrogels, Sci Adv 1(9) (2015) e1500758.
[353] N.S. Kajave, T. Schmitt, T.U. Nguyen, V. Kishore, Dual crosslinking strategy to generate mechanically viable cell-laden printable constructs using methacrylated collagen bioinks, Mater Sci Eng C Mater Biol Appl 107 (2020) 110290.
[354] T.J. Hinton, A. Hudson, K. Pusch, A. Lee, A.W. Feinberg, 3D printing PDMS elastomer in a hydrophilic support bath via freeform reversible embedding, ACS biomaterials science & engineering 2(10) (2016) 1781-1786.
[355] T.J. Hinton, Q. Jallerat, R.N. Palchesko, J.H. Park, M.S. Grodzicki, H.-J. Shue, M.H. Ramadan, A.R. Hudson, A.W. Feinberg, Three-dimensional printing of complex biological

structures by freeform reversible embedding of suspended hydrogels, Science advances 1(9) (2015) e1500758.
[356] R.W. Farndale, D.J. Buttle, A.J. Barrett, Improved quantitation and discrimination of sulphated glycosaminoglycans by use of dimethylmethylene blue, Biochimica et Biophysica Acta (BBA)-General Subjects 883(2) (1986) 173-177.
[357] S.P. Grogan, A. Barbero, V. Winkelmann, F. Rieser, J.S. Fitzsimmons, S. O'driscoll, I. Martin, P. Mainil-Varlet, Visual histological grading system for the evaluation of in vitro–generated neocartilage, Tissue engineering 12(8) (2006) 2141-2149.
[358] K.J. Livak, T.D. Schmittgen, Analysis of relative gene expression data using real-time quantitative PCR and the 2− ΔΔCT method, methods 25(4) (2001) 402-408.
[359] T.D. Schmittgen, K.J. Livak, Analyzing real-time PCR data by the comparative C T method, Nature protocols 3(6) (2008) 1101.
[360] I. Fulco, S. Miot, M.D. Haug, A. Barbero, A. Wixmerten, S. Feliciano, F. Wolf, G. Jundt, A. Marsano, J. Farhadi, M. Heberer, M. Jakob, D.J. Schaefer, I. Martin, Engineered autologous cartilage tissue for nasal reconstruction after tumour resection: an observational first-in-human trial, The Lancet (2014).
[361] S.H.J. Andrews, M. Kunze, A. Mulet-Sierra, L. Williams, K. Ansari, M. Osswald, A.B. Adesida, Strategies to Mitigate Variability in Engineering Human Nasal Cartilage, Scientific Reports 7(1) (2017) 6490.
[362] M. Guvendiren, H.D. Lu, J.A. Burdick, Shear-thinning hydrogels for biomedical applications, Soft Matter 8(2) (2012) 260-272.
[363] D.G. Wallace, A. Thompson, Description of collagen fibril formation by a theory of polymer crystallization, Biopolymers 22(7) (1983) 1793-811.
[364] B. Brodsky, J.A. Ramshaw, The collagen triple-helix structure, Matrix Biology 15(8-9) (1997) 545-554.
[365] Y.-l. Yang, L.J. Kaufman, Rheology and confocal reflectance microscopy as probes of mechanical properties and structure during collagen and collagen/hyaluronan self-assembly, Biophysical journal 96(4) (2009) 1566-1585.
[366] D.G. Wallace, A. Thompson, Description of collagen fibril formation by a theory of polymer crystallization, Biopolymers: Original Research on Biomolecules 22(7) (1983) 1793-1811.
[367] N. Paxton, W. Smolan, T. Bock, F. Melchels, J. Groll, T. Jungst, Proposal to assess printability of bioinks for extrusion-based bioprinting and evaluation of rheological properties governing bioprintability, Biofabrication 9(4) (2017) 044107.
[368] W. Bi, J.M. Deng, Z. Zhang, R.R. Behringer, B. de Crombrugghe, Sox9 is required for cartilage formation, Nat Genet 22(1) (1999) 85-9.
[369] H. Akiyama, M.C. Chaboissier, J.F. Martin, A. Schedl, B. de Crombrugghe, The transcription factor Sox9 has essential roles in successive steps of the chondrocyte differentiation pathway and is required for expression of Sox5 and Sox6, Genes Dev 16(21) (2002) 2813-28.
[370] V. Lefebvre, R.R. Behringer, B. de Crombrugghe, L-Sox5, Sox6 and Sox9 control essential steps of the chondrocyte differentiation pathway, Osteoarthritis Cartilage 9 Suppl A (2001) S69-75.
[371] K. Pelttari, A. Winter, E. Steck, K. Goetzke, T. Hennig, B.G. Ochs, T. Aigner, W. Richter, Premature induction of hypertrophy during in vitro chondrogenesis of human mesenchymal stem cells correlates with calcification and vascular invasion after ectopic transplantation in SCID mice, Arthritis Rheum 54(10) (2006) 3254-66.

[372] S.R. Tew, Y. Li, P. Pothacharoen, L.M. Tweats, R.E. Hawkins, T.E. Hardingham, Retroviral transduction with SOX9 enhances re-expression of the chondrocyte phenotype in passaged osteoarthritic human articular chondrocytes, Osteoarthritis Cartilage 13(1) (2005) 80-9.
[373] T. Ikeda, S. Kamekura, A. Mabuchi, I. Kou, S. Seki, T. Takato, K. Nakamura, H. Kawaguchi, S. Ikegawa, U.I. Chung, The combination of SOX5, SOX6, and SOX9 (the SOX trio) provides signals sufficient for induction of permanent cartilage, Arthritis Rheum 50(11) (2004) 3561-73.
[374] J. Fischer, A. Dickhut, M. Rickert, W. Richter, Human articular chondrocytes secrete parathyroid hormone-related protein and inhibit hypertrophy of mesenchymal stem cells in coculture during chondrogenesis, Arthritis Rheum 62(9) (2010) 2696-706.
[375] W. Kafienah, S. Mistry, S.C. Dickinson, T.J. Sims, I. Learmonth, A.P. Hollander, Three-dimensional cartilage tissue engineering using adult stem cells from osteoarthritis patients, Arthritis & Rheumatism 56(1) (2007) 177-187.
[376] P.K. Holden, L.H. Liaw, B.J. Wong, Human nasal cartilage ultrastructure: characteristics and comparison using scanning electron microscopy, Laryngoscope 118(7) (2008) 1153-6.
[377] S. Miot, W. Brehm, S. Dickinson, T. Sims, A. Wixmerten, C. Longinotti, A.P. Hollander, P. Mainil-Varlet, I. Martin, Influence of in vitro maturation of engineered cartilage on the outcome of osteochondral repair in a goat model, Eur Cell Mater 23 (2012) 222-36.
[378] M. Mumme, A. Barbero, S. Miot, A. Wixmerten, S. Feliciano, F. Wolf, A.M. Asnaghi, D. Baumhoer, O. Bieri, M. Kretzschmar, G. Pagenstert, M. Haug, D.J. Schaefer, I. Martin, M. Jakob, Nasal chondrocyte-based engineered autologous cartilage tissue for repair of articular cartilage defects: an observational first-in-human trial, Lancet 388(10055) (2016) 1985-1994.
[379] K.E. Sayed, A. Haisch, T. John, U. Marzahn, A. Lohan, R.D. Müller, B. Kohl, W. Ertel, K. Stoelzel, G. Schulze-Tanzil, Heterotopic autologous chondrocyte transplantation—a realistic approach to support articular cartilage repair?, Tissue Engineering Part B: Reviews 16(6) (2010) 603-616.
[380] V. Madan, J.T. Lear, R.-M. Szeimies, Non-melanoma skin cancer, The lancet 375(9715) (2010) 673-685.
[381] A. Lomas, J. Leonardi-Bee, F. Bath-Hextall, A systematic review of worldwide incidence of nonmelanoma skin cancer, British Journal of Dermatology 166(5) (2012) 1069-1080.
[382] G.K. Austin, W.W. Shockley, Reconstruction of nasal defects: contemporary approaches, Current opinion in otolaryngology & head and neck surgery 24(5) (2016) 453.
[383] A. Sajjadian, N. Naghshineh, R.J.P. Rubinstein, r. surgery, Current status of grafts and implants in rhinoplasty: Part II. Homologous grafts and allogenic implants, 125(3) (2010) 99e-109e.
[384] D.J. Menger, G.J.N. Trenité, Irradiated homologous rib grafts in nasal reconstruction, Archives of facial plastic surgery 12(2) (2010) 114-118.
[385] J.H. Wee, S.J. Mun, W.S. Na, H. Kim, J.H. Park, D.-K. Kim, H.-R. Jin, Autologous vs irradiated homologous costal cartilage as graft material in rhinoplasty, JAMA facial plastic surgery 19(3) (2017) 183-188.
[386] K. Patel, K. Brandstetter, Solid implants in facial plastic surgery: potential complications and how to prevent them, Facial Plastic Surgery 32(05) (2016) 520-531.
[387] J.P. Farkas, M.R. Lee, C. Lakianhi, R.J. Rohrich, Effects of carving plane, level of harvest, and oppositional suturing techniques on costal cartilage warping, Plast Reconstr Surg 132(2) (2013) 319-325.

[388] J. Farhadi, I. Fulco, S. Miot, D. Wirz, M. Haug, S.C. Dickinson, A.P. Hollander, A.U. Daniels, G. Pierer, M. Heberer, Precultivation of engineered human nasal cartilage enhances the mechanical properties relevant for use in facial reconstructive surgery, Annals of surgery 244(6) (2006) 978.
[389] H.-G. Yi, Y.-J. Choi, J.W. Jung, J. Jang, T.-H. Song, S. Chae, M. Ahn, T.H. Choi, J.-W. Rhie, D.-W.J.J.o.t.e. Cho, Three-dimensional printing of a patient-specific engineered nasal cartilage for augmentative rhinoplasty, 10 (2019) 2041731418824797.
[390] C. Vinatier, O. Gauthier, M. Masson, O. Malard, A. Moreau, B.H. Fellah, M. Bilban, R. Spaethe, G. Daculsi, J. Guicheux, Nasal chondrocytes and fibrin sealant for cartilage tissue engineering, J Biomed Mater Res A 89(1) (2009) 176-85.
[391] L. Ruiz-Cantu, A. Gleadall, C. Faris, J. Segal, K. Shakesheff, J. Yang, Multi-material 3D bioprinting of porous constructs for cartilage regeneration, Materials Science and Engineering: C 109 (2020) 110578.
[392] P. Apelgren, M. Amoroso, K. Säljö, A. Lindahl, C. Brantsing, L.S. Orrhult, P. Gatenholm, L. Kölby, Skin grafting on 3D bioprinted cartilage constructs in vivo, Plastic and Reconstructive Surgery Global Open 6(9) (2018).
[393] Y. Gu, B. Schwarz, A. Forget, A. Barbero, I. Martin, V.P. Shastri, Advanced Bioink for 3D Bioprinting of Complex Free-Standing Structures with High Stiffness, Bioengineering 7(4) (2020) 141.
[394] T. Möller, M. Amoroso, D. Hägg, C. Brantsing, N. Rotter, P. Apelgren, A. Lindahl, L. Kölby, P. Gatenholm, In vivo chondrogenesis in 3D bioprinted human cell-laden hydrogel constructs, Plastic and reconstructive surgery global open 5(2) (2017).
[395] Y. Liang, E. Idrees, A.R. Szojka, S.H. Andrews, M. Kunze, A. Mulet-Sierra, N.M. Jomha, A.B. Adesida, Chondrogenic differentiation of synovial fluid mesenchymal stem cells on human meniscus-derived decellularized matrix requires exogenous growth factors, Acta biomaterialia 80 (2018) 131-143.
[396] P. Sabiston, M. Adams, Y. Ho, Automation of 1, 9-dimethylmethylene blue dye-binding assay for sulfated glycosaminoglycans with application to cartilage microcultures, Analytical biochemistry 149(2) (1985) 543-548.
[397] A.S. Lee, J. Rusch, A.C. Lima, A. Usmani, N. Huang, M. Lepamets, K.A. Vigh-Conrad, R.E. Worthington, R. Mägi, X. Wu, Rare mutations in the complement regulatory gene CSMD1 are associated with male and female infertility, Nature communications 10(1) (2019) 1-16.
[398] Y. Liang, E. Idrees, S.H. Andrews, K. Labib, A. Szojka, M. Kunze, A.D. Burbank, A. Mulet-Sierra, N.M. Jomha, A.B. Adesida, Plasticity of human meniscus fibrochondrocytes: A study on effects of mitotic divisions and oxygen tension, Scientific reports 7(1) (2017) 12148.
[399] J. Vandesompele, K. De Preter, F. Pattyn, B. Poppe, N. Van Roy, A. De Paepe, F.J.G.b. Speleman, Accurate normalization of real-time quantitative RT-PCR data by geometric averaging of multiple internal control genes, 3(7) (2002) 1-12.
[400] S.P. Grogan, A. Barbero, V. Winkelmann, F. Rieser, J.S. Fitzsimmons, S. O'driscoll, I. Martin, P.J.T.e. Mainil-Varlet, Visual histological grading system for the evaluation of in vitro–generated neocartilage, 12(8) (2006) 2141-2149.
[401] R.E. Allen, K.C. Masak, P.K. McAllister, Staining protein in isoelectric focusing gels with fast green, Analytical biochemistry 104(2) (1980) 494-498.
[402] P. Dey, Connective Tissue Stain: Principle and Procedure, Basic and Advanced Laboratory Techniques in Histopathology and Cytology, Springer2018, pp. 99-108.

[403] P. Friedl, K.S. Zänker, E.B. Bröcker, Cell migration strategies in 3-D extracellular matrix: differences in morphology, cell matrix interactions, and integrin function, Microscopy research and technique 43(5) (1998) 369-378.
[404] P. Fisch, N. Broguière, S. Finkielsztein, T. Linder, M. Zenobi-Wong, Bioprinting of Cartilaginous Auricular Constructs Utilizing an Enzymatically Crosslinkable Bioink, (2020).
[405] J. Zhang, Z. Yang, C. Li, Y. Dou, Y. Li, T. Thote, D.-a. Wang, Z. Ge, Cells behave distinctly within sponges and hydrogels due to differences of internal structure, Tissue Engineering Part A 19(19-20) (2013) 2166-2175.
[406] P.H.G. Chao, S. Yodmuang, X. Wang, L. Sun, D.L. Kaplan, G. Vunjak-Novakovic, Silk hydrogel for cartilage tissue engineering, Journal of biomedical materials research part B: applied biomaterials 95(1) (2010) 84-90.
[407] P.D. Benya, J.D. Shaffer, Dedifferentiated chondrocytes reexpress the differentiated collagen phenotype when cultured in agarose gels, Cell 30(1) (1982) 215-224.
[408] E.A. Makris, D.J. Responte, N.K. Paschos, J.C. Hu, K.A. Athanasiou, Developing functional musculoskeletal tissues through hypoxia and lysyl oxidase-induced collagen cross-linking, Proceedings of the National Academy of Sciences 111(45) (2014) E4832-E4841.
[409] E. Makris, J. Hu, K. Athanasiou, Hypoxia-induced collagen crosslinking as a mechanism for enhancing mechanical properties of engineered articular cartilage, Osteoarthritis and cartilage 21(4) (2013) 634-641.
[410] E. Vinod, U. Kachroo, S.M. Amirtham, B. Ramasamy, S.J.A.h. Sathishkumar, Comparative analysis of fresh chondrocytes, cultured chondrocytes and chondroprogenitors derived from human articular cartilage, 122(1) (2020) 151462.
[411] A. Barbero, S. Ploegert, M. Heberer, I. Martin, Plasticity of clonal populations of dedifferentiated adult human articular chondrocytes, Arthritis & Rheumatism 48(5) (2003) 1315-1325.
[412] A.v. Bomhard, J. Veit, C. Bermueller, N. Rotter, R. Staudenmaier, K. Storck, H.N. The, Prefabrication of 3D cartilage contructs: towards a tissue engineered auricle–a model tested in rabbits, PloS one 8(8) (2013) e71667.
[413] L. Zhou, I. Pomerantseva, E.K. Bassett, C.M. Bowley, X. Zhao, D.A. Bichara, K.M. Kulig, J.P. Vacanti, M.A. Randolph, C.A. Sundback, Engineering ear constructs with a composite scaffold to maintain dimensions, Tissue Engineering Part A 17(11-12) (2011) 1573-1581.
[414] H.T. Liao, R. Zheng, W. Liu, W.J. Zhang, Y. Cao, G. Zhou, Prefabricated, ear-shaped cartilage tissue engineering by scaffold-free porcine chondrocyte membrane, Plast Reconstr Surg 135(2) (2015) 313e-321e.
[415] B.E. Pippenger, M. Ventura, K. Pelttari, S. Feliciano, C. Jaquiery, A. Scherberich, X.F. Walboomers, A. Barbero, I. Martin, Bone-forming capacity of adult human nasal chondrocytes, Journal of cellular and molecular medicine 19(6) (2015) 1390-1399.
[416] M. Anderson-Baron, Y. Liang, M. Kunze, A. Mulet-Sierra, M. Osswald, K. Ansari, H. Seikaly, A.B. Adesida, Suppression of Hypertrophy During in vitro Chondrogenesis of Cocultures of Human Mesenchymal Stem Cells and Nasal Chondrocytes Correlates With Lack of in vivo Calcification and Vascular Invasion, Frontiers in bioengineering and biotechnology 8 (2021) 1483.
[417] C.D. Bucana, A. Fabra, R. Sanchez, I.J. Fidler, Different patterns of macrophage infiltration into allogeneic-murine and xenogeneic-human neoplasms growing in nude mice, The American journal of pathology 141(5) (1992) 1225.

[418] Y. Fujihara, Y. Asawa, T. Takato, K. Hoshi, Tissue reactions to engineered cartilage based on poly-L-lactic acid scaffolds, Tissue Engineering Part A 15(7) (2009) 1565-1577.
[419] M. Janusz, M. Hare, S. Durham, J. Potempa, W. McGraw, R. Pike, J. Travis, S. Shapiro, Cartilage proteoglycan degradation by a mouse transformed macrophage cell line is mediated by macrophage metalloelastase, Inflammation research 48(5) (1999) 280-288.
[420] A. dos Anjos Cassado, F4/80 as a major macrophage marker: the case of the peritoneum and spleen, Macrophages (2017) 161-179.
[421] V.B. Kraus, G. McDaniel, J.L. Huebner, T.V. Stabler, C.F. Pieper, S.W. Shipes, N.A. Petry, P.S. Low, J. Shen, T.A. McNearney, Direct in vivo evidence of activated macrophages in human osteoarthritis, Osteoarthritis and cartilage 24(9) (2016) 1613-1621.
[422] H. Raghu, C.M. Lepus, Q. Wang, H.H. Wong, N. Lingampalli, F. Oliviero, L. Punzi, N.J. Giori, S.B. Goodman, C.R. Chu, CCL2/CCR2, but not CCL5/CCR5, mediates monocyte recruitment, inflammation and cartilage destruction in osteoarthritis, Annals of the rheumatic diseases 76(5) (2017) 914-922.
[423] S. Miot, W. Brehm, S. Dickinson, T. Sims, A. Wixmerten, C. Longinotti, A. Hollander, P. Mainil-Varlet, I. Martin, Influence of in vitro maturation of engineered cartilage on the outcome of osteochondral repair in a goat model, Eur Cell Mater 23 (2012) 222-236.
[424] I.-S. Kim, M.-Y. Lee, K.-I. Lee, H.-Y. Kim, Y.-J.J.C. Chung, e. otorhinolaryngology, Analysis of the development of the nasal septum according to age and gender using MRI, 1(1) (2008) 29.
[425] X. Huang, R. Das, A. Patel, T.J.R.e. Duc Nguyen, t. medicine, Physical stimulations for bone and cartilage regeneration, 4(4) (2018) 216-237.
[426] S.S. Rao, J. DeJesus, A.R. Short, J.J. Otero, A. Sarkar, J.O.J.A.a.m. Winter, interfaces, Glioblastoma behaviors in three-dimensional collagen-hyaluronan composite hydrogels, 5(19) (2013) 9276-9284.
[427] E. Maloney, C. Clark, H. Sivakumar, K. Yoo, J. Aleman, S.A. Rajan, S. Forsythe, A. Mazzocchi, A.W. Laxton, S.B.J.M. Tatter, Immersion bioprinting of tumor organoids in multi-well plates for increasing chemotherapy screening throughput, 11(2) (2020) 208.
[428] B. Carrion, M.F. Souzanchi, V.T. Wang, G. Tiruchinapally, A. Shikanov, A.J. Putnam, R.M.J.A.H.M. Coleman, The synergistic effects of matrix stiffness and composition on the response of chondroprogenitor cells in a 3D precondensation microenvironment, 5(10) (2016) 1192-1202.
[429] K.G. Nairon, T.J. DePalma, J.M. Zent, J.L. Leight, A.J.I. Skardal, Tumor cell-conditioned media drives collagen remodeling via fibroblast and pericyte activation in an in vitro premetastatic niche model, 25(7) (2022) 104645.
[430] C.J.P.i.p.s. Decker, Photoinitiated crosslinking polymerisation, 21(4) (1996) 593-650.
[431] K. Goodarzi, S.S.J.J.o.M.C.B. Rao, Hyaluronic acid-based hydrogels to study cancer cell behaviors, 9(31) (2021) 6103-6115.
[432] P.A. Amorim, M. d'Ávila, R. Anand, P. Moldenaers, P. Van Puyvelde, V.J.B. Bloemen, Insights on shear rheology of inks for extrusion-based 3D bioprinting, 22 (2021) e00129.
[433] C.-C. Lin, A. Raza, H.J.B. Shih, PEG hydrogels formed by thiol-ene photo-click chemistry and their effect on the formation and recovery of insulin-secreting cell spheroids, 32(36) (2011) 9685-9695.
[434] Z. Mũnoz, H. Shih, C.-C.J.B.S. Lin, Gelatin hydrogels formed by orthogonal thiol–norbornene photochemistry for cell encapsulation, 2(8) (2014) 1063-1072.

[435] J.D. McCall, K.S.J.B. Anseth, Thiol–ene photopolymerizations provide a facile method to encapsulate proteins and maintain their bioactivity, 13(8) (2012) 2410-2417.
[436] N. Farnsworth, C. Bensard, S.J.O. Bryant, Cartilage, The role of the PCM in reducing oxidative stress induced by radical initiated photoencapsulation of chondrocytes in poly (ethylene glycol) hydrogels, 20(11) (2012) 1326-1335.
[437] J.J. Roberts, S.J.J.B. Bryant, Comparison of photopolymerizable thiol-ene PEG and acrylate-based PEG hydrogels for cartilage development, 34(38) (2013) 9969-9979.
[438] J. Yang, Z. Tang, Y. Liu, Z. Luo, Y. Xiao, X.J.I.J.o.B.M. Zhang, Comparison of chondro-inductivity between collagen and hyaluronic acid hydrogel based on chemical/physical microenvironment, 182 (2021) 1941-1952.
[439] G.-Z. Jin, H.-W.J.T.E. Kim, R. Medicine, Effects of type I collagen concentration in hydrogel on the growth and phenotypic expression of rat chondrocytes, 14(4) (2017) 383-391.
[440] S. Lee, X. Tong, F.J.B.s. Yang, Effects of the poly (ethylene glycol) hydrogel crosslinking mechanism on protein release, 4(3) (2016) 405-411.
[441] M. Keeney, J.H. Lai, F.J.C.o.i.b. Yang, Recent progress in cartilage tissue engineering, 22(5) (2011) 734-740.
[442] R. Mohan, N. Mohan, D.J.T.E.P.A. Vaikkath, Hyaluronic acid dictates chondrocyte morphology and migration in composite gels, 24(19-20) (2018) 1481-1491.
[443] L. Galois, S. Hutasse, D. Cortial, C.F. Rousseau, L. Grossin, M.-C. Ronziere, D. Herbage, A.-M.J.B. Freyria, Bovine chondrocyte behaviour in three-dimensional type I collagen gel in terms of gel contraction, proliferation and gene expression, 27(1) (2006) 79-90.
[444] V.K. Lai, D.S. Nedrelow, S.P. Lake, B. Kim, E.M. Weiss, R.T. Tranquillo, V.H.J.A.o.b.e. Barocas, Swelling of collagen-hyaluronic acid co-gels: an in vitro residual stress model, 44(10) (2016) 2984-2993.
[445] Z. Ma, D. Li, M. Kunze, A. Mulet Sierra, L. Westover, A.B.J.F.i.b. Adesida, biotechnology, Engineered human meniscus in modeling sex differences of knee osteoarthritis in vitro, (2022) 126.
[446] J. Parreno, S. Raju, P.-h. Wu, R.A.J.M.B. Kandel, MRTF-A signaling regulates the acquisition of the contractile phenotype in dedifferentiated chondrocytes, 62 (2017) 3-14.
[447] R. Mauck, C.-B. Wang, E. Oswald, G. Ateshian, C.J.O. Hung, cartilage, The role of cell seeding density and nutrient supply for articular cartilage tissue engineering with deformational loading, 11(12) (2003) 879-890.
[448] A.A. Khan, J.M. Suits, R.A. Kandel, S.D.J.B.p. Waldman, The effect of continuous culture on the growth and structure of tissue-engineered cartilage, 25(2) (2009) 508-515.
[449] R. Tarantino, L.L. Chiu, J.F. Weber, M. Yat Tse, D.D. Bardana, S.C. Pang, S.D.J.B. Waldman, Bioengineering, Effect of nutrient metabolism on cartilaginous tissue formation, 118(10) (2021) 4119-4128.
[450] A.C. Daly, S.E. Critchley, E.M. Rencsok, D.J. Kelly, A comparison of different bioinks for 3D bioprinting of fibrocartilage and hyaline cartilage, Biofabrication 8(4) (2016) 045002.
[451] D.C. Fithian, M.A. Kelly, V.C. Mow, Material properties and structure-function relationships in the menisci, Clinical orthopaedics and related research (252) (1990) 19-31.
[452] B. Leslie, D. Gardner, J. McGeough, R. Moran, Anisotropic response of the human knee joint meniscus to unconfined compression, Proceedings of the Institution of Mechanical Engineers, Part H: Journal of Engineering in Medicine 214(6) (2000) 631-635.

[453] E.A. Makris, P. Hadidi, K.A.J.B. Athanasiou, The knee meniscus: structure–function, pathophysiology, current repair techniques, and prospects for regeneration, 32(30) (2011) 7411-7431.
[454] D.C. Fithian, M.A. Kelly, V.C.J.C.o. Mow, r. research, Material properties and structure-function relationships in the menisci, (252) (1990) 19-31.
[455] A.B. Adesida, L.M. Grady, W.S. Khan, S.J. Millward-Sadler, D.M. Salter, T.E. Hardingham, Human meniscus cells express hypoxia inducible factor-1α and increased SOX9 in response to low oxygen tension in cell aggregate culture, Arthritis research & therapy 9(4) (2007) 1-9.
[456] J. Sanchez-Adams, K.A. Athanasiou, The knee meniscus: a complex tissue of diverse cells, Cellular and Molecular Bioengineering 2(3) (2009) 332-340.
[457] A. Chevrier, M. Nelea, M.B. Hurtig, C.D. Hoemann, M.D. Buschmann, Meniscus structure in human, sheep, and rabbit for animal models of meniscus repair, Journal of orthopaedic research 27(9) (2009) 1197-1203.
[458] K. Nakata, K. Shino, M. Hamada, T. Mae, T. Miyama, H. Shinjo, S. Horibe, K. Tada, T. Ochi, H. Yoshikawa, Human meniscus cell: characterization of the primary culture and use for tissue engineering, Clinical Orthopaedics and Related Research® 391 (2001) S208-S218.
[459] S.P. Arnoczky, R.F. Warren, Microvasculature of the human meniscus, The American journal of sports medicine 10(2) (1982) 90-95.
[460] D. King, The healing of semilunar cartilages, JBJS 18(2) (1936) 333-342.
[461] A.R. Szojka, C.N. Moore, Y. Liang, S.H. Andrews, M. Kunze, A. Mulet-Sierra, N.M. Jomha, A.B. Adesida, Engineered human meniscus' matrix-forming phenotype is unaffected by low strain dynamic compression under hypoxic conditions, PloS one 16(3) (2021) e0248292.
[462] T. Fairbank, Knee joint changes after meniscectomy, The Journal of bone and joint surgery. British volume 30(4) (1948) 664-670.
[463] J.S. Cox, C.E. Nye, W.W. Schaefer, I.J. Woodstein, The degenerative effects of partial and total resection of the medial meniscus in dogs' knees, Clinical orthopaedics and related research (109) (1975) 178-183.
[464] P.T. Paradowski, L.S. Lohmander, M. Englund, Osteoarthritis of the knee after meniscal resection: long term radiographic evaluation of disease progression, Osteoarthritis and cartilage 24(5) (2016) 794-800.
[465] C. Ibarra, J.A. Koski, R.F. Warren, Tissue engineering meniscus: cells and matrix, The Orthopedic clinics of North America 31(3) (2000) 411-418.
[466] A.C. Daly, F.E. Freeman, T. Gonzalez-Fernandez, S.E. Critchley, J. Nulty, D.J. Kelly, 3D bioprinting for cartilage and osteochondral tissue engineering, Advanced Healthcare Materials 6(22) (2017) 1700298.
[467] C. Di Bella, A. Fosang, D.M. Donati, G.G. Wallace, P.F. Choong, 3D bioprinting of cartilage for orthopedic surgeons: reading between the lines, Frontiers in surgery 2 (2015) 39.
[468] A. Skardal, M. Devarasetty, H.-W. Kang, I. Mead, C. Bishop, T. Shupe, S.J. Lee, J. Jackson, J. Yoo, S. Soker, A hydrogel bioink toolkit for mimicking native tissue biochemical and mechanical properties in bioprinted tissue constructs, Acta biomaterialia 25 (2015) 24-34.
[469] J. Göhl, K. Markstedt, A. Mark, K. Håkansson, P. Gatenholm, F. Edelvik, Simulations of 3D bioprinting: predicting bioprintability of nanofibrillar inks, Biofabrication 10(3) (2018) 034105.

[470] P. Erkoc, I. Uvak, M.A. Nazeer, S.R. Batool, Y.N. Odeh, O. Akdogan, S.J.M.B. Kizilel, 3D Printing of Cytocompatible Gelatin-Cellulose-Alginate Blend Hydrogels, 20(10) (2020) 2000106.
[471] E.B. Heggset, B.L. Strand, K.W. Sundby, S. Simon, G. Chinga-Carrasco, K. Syverud, Viscoelastic properties of nanocellulose based inks for 3D printing and mechanical properties of CNF/alginate biocomposite gels, Cellulose 26(1) (2019) 581-595.
[472] Z.M. Jessop, A. Al-Sabah, N. Gao, S. Kyle, B. Thomas, N. Badiei, K. Hawkins, I.S. Whitaker, Printability of pulp derived crystal, fibril and blend nanocellulose-alginate bioinks for extrusion 3D bioprinting, Biofabrication 11(4) (2019) 045006.
[473] M. Ojansivu, A. Rashad, A. Ahlinder, J. Massera, A. Mishra, K. Syverud, A. Finne-Wistrand, S. Miettinen, K.J.B. Mustafa, Wood-based nanocellulose and bioactive glass modified gelatin–alginate bioinks for 3D bioprinting of bone cells, 11(3) (2019) 035010.
[474] Y. Wu, Z.Y.W. Lin, A.C. Wenger, K.C. Tam, X.S.J.B. Tang, 3D bioprinting of liver-mimetic construct with alginate/cellulose nanocrystal hybrid bioink, 9 (2018) 1-6.
[475] X. Yang, Z. Lu, H. Wu, W. Li, L. Zheng, J. Zhao, Collagen-alginate as bioink for three-dimensional (3D) cell printing based cartilage tissue engineering, Materials Science and Engineering: C 83 (2018) 195-201.
[476] L. Li, Y. Fang, R. Vreeker, I. Appelqvist, E. Mendes, Reexamining the egg-box model in calcium− alginate gels with X-ray diffraction, Biomacromolecules 8(2) (2007) 464-468.
[477] E.S. Abdul Rashid, N. Muhd Julkapli, W.A.J.P.f.A.T. Yehye, Nanocellulose reinforced as green agent in polymer matrix composites applications, 29(6) (2018) 1531-1546.
[478] T. Abitbol, A. Rivkin, Y. Cao, Y. Nevo, E. Abraham, T. Ben-Shalom, S. Lapidot, O. Shoseyov, Nanocellulose, a tiny fiber with huge applications, Current opinion in biotechnology 39 (2016) 76-88.
[479] A. Dufresne, Nanocellulose: a new ageless bionanomaterial, Materials Today 16(6) (2013) 220-227.
[480] X. Wang, Q. Wang, C. Xu, Nanocellulose-based inks for 3D bioprinting: Key Aspects in research development and challenging perspectives in applications—a mini review, Bioengineering 7(2) (2020) 40.
[481] N. Lin, C.c. Bruzzese, A. Dufresne, TEMPO-oxidized nanocellulose participating as crosslinking aid for alginate-based sponges, ACS applied materials & interfaces 4(9) (2012) 4948-4959.
[482] V.R. Herrera Millar, L. Mangiavini, U. Polito, B. Canciani, V.T. Nguyen, F. Cirillo, L. Anastasia, G.M. Peretti, S.C. Modina, A. Di Giancamillo, Hypoxia as a Stimulus for the Maturation of Meniscal Cells: Highway to Novel Tissue Engineering Strategies?, International Journal of Molecular Sciences 22(13) (2021) 6905.
[483] A.R. Szojka, B.D. Lyons, C.N. Moore, Y. Liang, M. Kunze, E. Idrees, A. Mulet-Sierra, N.M. Jomha, A.B. Adesida, Hypoxia and TGF-β3 synergistically mediate inner meniscus-like matrix formation by fibrochondrocytes, Tissue Engineering Part A 25(5-6) (2019) 446-456.
[484] M. El Bakkari, V. Bindiganavile, J. Goncalves, Y. Boluk, Preparation of cellulose nanofibers by TEMPO-oxidation of bleached chemi-thermomechanical pulp for cement applications, Carbohydrate polymers 203 (2019) 238-245.
[485] R.E. Abouzeid, R. Khiari, D. Beneventi, A. Dufresne, Biomimetic mineralization of three-dimensional printed alginate/TEMPO-oxidized cellulose nanofibril scaffolds for bone tissue engineering, Biomacromolecules 19(11) (2018) 4442-4452.

[486] T. Gao, G.J. Gillispie, J.S. Copus, A.K. Pr, Y.-J. Seol, A. Atala, J.J. Yoo, S.J. Lee, Optimization of gelatin–alginate composite bioink printability using rheological parameters: a systematic approach, Biofabrication 10(3) (2018) 034106.
[487] L. Li, Y. Fang, R. Vreeker, I. Appelqvist, E.J.B. Mendes, Reexamining the egg-box model in calcium− alginate gels with X-ray diffraction, 8(2) (2007) 464-468.
[488] I. Braccini, S.J.B. Pérez, Molecular basis of Ca2+-induced gelation in alginates and pectins: the egg-box model revisited, 2(4) (2001) 1089-1096.
[489] J. Wang, S. Roberts, J.H. Kuiper, W. Zhang, J. Garcia, Z. Cui, K.J.S.r. Wright, Characterization of regional meniscal cell and chondrocyte phenotypes and chondrogenic differentiation with histological analysis in osteoarthritic donor-matched tissues, 10(1) (2020) 1-14.
[490] D. Bosnakovski, M. Mizuno, G. Kim, S. Takagi, M. Okumura, T. Fujinaga, Chondrogenic differentiation of bovine bone marrow mesenchymal stem cells (MSCs) in different hydrogels: influence of collagen type II extracellular matrix on MSC chondrogenesis, Biotechnology and bioengineering 93(6) (2006) 1152-1163.
[491] M. Mizuno, R. Fujisawa, Y. Kuboki, Type I collagen-induced osteoblastic differentiation of bone-marrow cells mediated by collagen-α2β1 integrin interaction, Journal of cellular physiology 184(2) (2000) 207-213.
[492] E.A. Makris, J.C. Hu, K.A. Athanasiou, Hypoxia-induced collagen crosslinking as a mechanism for enhancing mechanical properties of engineered articular cartilage, Osteoarthritis Cartilage 21(4) (2013) 634-41.

Appendix A. TEMPO-oxidized cellulose nanofiber-alginate hydrogel as a bioink for human meniscus tissue engineering

Appendix A has been published in parts as: Xiaoyi Lan, Zhiyao Ma, Alexander R. A. Szojka, Melanie Kunze, Aillette Mulet-Sierra, Margaret Vyhlidal, Yaman Boluk and Adetola B Adesida, “TEMPO-Oxidized Cellulose Nanofiber-Alginate Hydrogel as a Bioink for Human Meniscus Tissue Engineering” Frontiers in bioengineering and biotechnology, p.1033, 2021.

A.1 Introduction

The menisci are a pair of C-shaped fibrocartilages that withstand compressive and tensile forces [395, 451, 452]. They are essential for mechanical load distribution and transmission, lubrication, and stability of the knee joint [395, 453, 454]. The biomechanical properties are attributed to the presence of functional extracellular matrix (ECM) [395, 451, 452, 455]. The menisci exhibit regional and zonal variations in their ECM and cellular compositions, reparative capacities, and vascularity with age [456-459]. Type I collagen is found throughout the entire meniscus; type II collagen and aggrecan are usually only found in the inner regions of the meniscus [458, 460, 461]. The outer region of the meniscus are contain of type I collagen fibre bundles that aligned in the circumferential direction, exhibiting a fibrous connective tissue (ligament and tendon-like) phenotype and a peripheral blood supply (1/3 or less in adults) that provides some healing capacity [458, 460, 461]. The cell population in the outer meniscus is predominantly fibroblast-like. In contrast, the middle and inner regions (2/3 or more) of the meniscus have a fibrocartilage phenotype that is avascular and non-healing [458, 460, 461]. The cell population for the inner region of the meniscus are human fibrochondrocytes (hMFC), which are a mix of fibroblast and chondrocyte-like cells [458, 460, 461].

Due to the limited healing capacities of meniscus, patients with meniscus defects or injuries often undergo partial or total meniscectomy, which is known to cause biomechanical changes to joint function with a risk for early knee osteoarthritis development [462-464]. Cell-based meniscus tissue engineering is a promising technology to circumvent this challenge by creating meniscus tissue replacements [465]. 3D bioprinting with a “bioink” composed of a biomaterial and cells, can create patient-specific tissues for reconstructive surgery [79, 466, 467]. 3D bioprinting can spatially control the placement of cells, biomaterial, and growth factors in a construct.

Therefore, it has the potential to accurately mimic the structure and morphology of tissues and organs [79, 83]. Natural hydrogel precursors are attractive for bioinks because of their favourable biocompatible properties and high-water content like human ECM [149, 264, 468]. To be suitable for printing, the rheological behaviour of the bioink is critical [94, 367]. The bioink must have shear thinning properties, which allows extrusion through small orifices with a decrease in shear to maintain cell viability. The bioink also needs a high zero-shear viscosity to retain its shape during and after printing [94, 367]. Beyond rheological properties, the bioink needs to be crosslinkable to retain 3D structures and provide appropriate mechanical properties to the bioprinted constructs [149, 367]. Alginate has been proven as a promising crosslinkable material for 3D bioprinting [87, 149, 150, 225, 339, 341, 469-475]. It can form a stable hydrogel in the presence of divalent cations such as Ca^{2+} and Ba^{2+} due to the ionic interaction between the cation and the carboxyl functional group by forming "egg-box"-calcium linked junctions [476]. Alginate is usually mixed with other biomaterials to achieve higher printing resolution [149, 225, 339, 470-472].

Cellulose, the most abundant renewable biopolymer found in nature, is a linear polysaccharide composed of β (1→4) linked D-glucose units [477-479]. The term nanocellulose refers to processed cellulose extract with one dimension in the nanometer range [341, 478, 479]. Depending on the sources and the preparation method, nanocellulose materials can be categorized into three main groups: bacteria cellulose (BC), cellulose nanofiber (CNF), and cellulose nanocrystal (CNC) [480]. The most common nanocellulose used in 3D bioprinting applications is CNF [480]. CNFs exhibit shear-thinning behaviour and a high zero shear viscosity, making them useful as a viscous contributor for the bioink. CNFs can be extracted from raw materials by a combination of chemical (e.g., acid hydrolysis, enzymatic reaction, TEMPO oxidation) and mechanical

treatments (e.g., high-pressure homogenization and grinding) [480]. TEMPO-oxidized CNFs (TCNFs) exhibit a high concentration of carboxyl groups and the new TEMPO-induced carboxyl groups in TCNFs are able to support alginate in the construction of crosslinked network, which enhances the scaffold mechanical strength, porosity, water absorption, and structural integrity [481].

This study incorporates hMFCs with TEMPO-oxidized CNF and alginate (TCNF/ALG) precursors to create tissue-engineered meniscus constructs. First, we evaluated the printability and the rheology properties of various formulations of TCNF/ALG precursors as potential bioinks. Then, we evaluated the biological functionality of 3D bioprinted meniscus-like tissue constructs using the optimal formulations, followed by 6 weeks of *in vitro* chondrogenic culture in low oxygen tension (i.e., hypoxia of 3% O_2). type I collagen, the major component of the meniscus fibrocartilage's ECM served as a reference biomaterial. Hypoxia was used since it has been proven as a stimulus for the maturation of meniscus fibrochondrocytes [482]. Our previous research has found that hypoxia and TGF-β3 synergistically mediated the inner meniscus-like tissue matrix formation [483]. The schematic diagram of the experimental design is shown in Figure A.1.

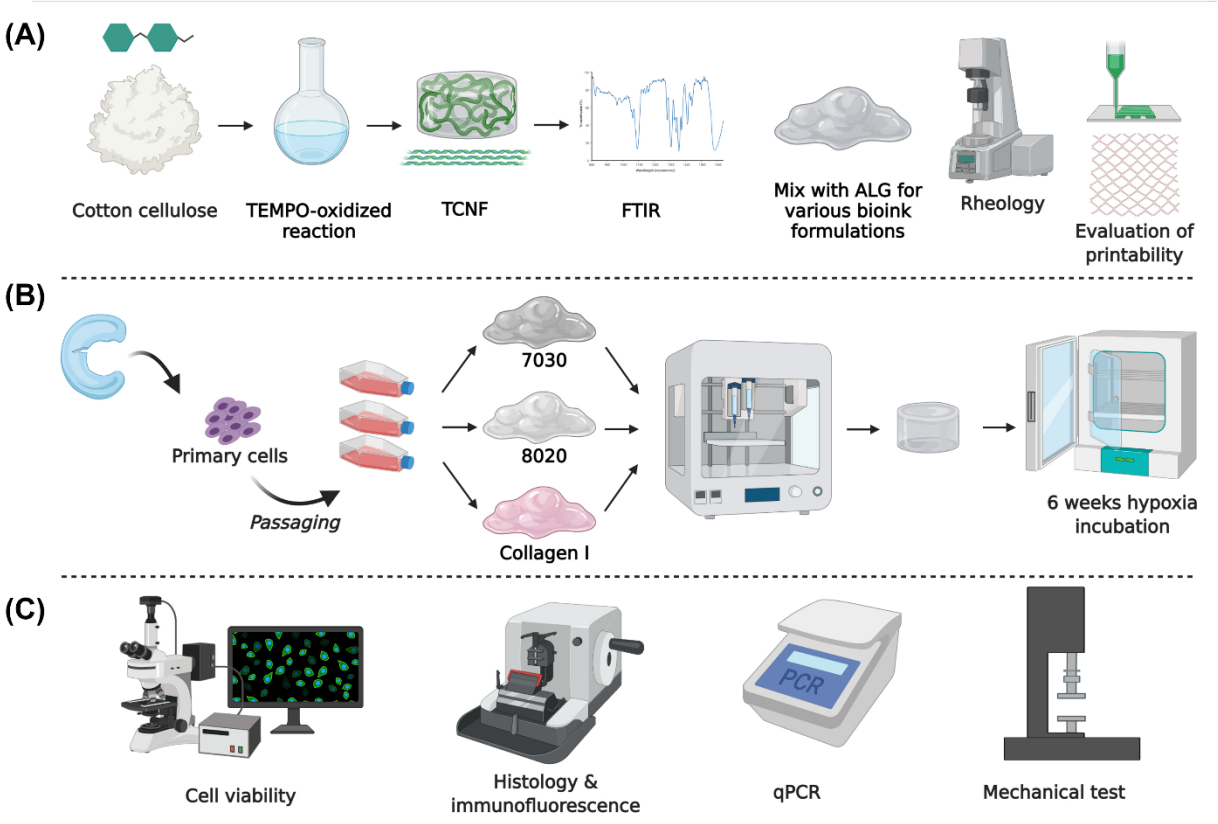

Figure A.1 Schematic diagram of the experimental design. (A) Biomaterial formation and characterization, (B) engineered tissue formation, and (C) evaluation of engineered tissues.

A.2 Materials and Methods

A.2.1 TCNF Synthesis and Preparation of TCNF/ALG Precursors

Cotton cellulose (10 g, Whatman No.1 filter paper) was cut into small pieces and immersed in deionized water (DI) water to make 1 liter of 1% w/w cellulose pulp slurry. 0.189 g of TEMPO (Sigma Aldrich, Canada), 1.178 g NaBr (Sigma Aldrich, Canada), 50 mL of 1.8 M NaClO (Sigma Aldrich, Canada) were added into the cellulose slurry under continuous stirring until dissolved. The pH of the reactants in the flask was maintained at pH=10.5 by adding 0.5 M NaOH until the pH of the reactant were stable at 10. The TEMPO-oxidized cellulose was then washed

with DI water for 15 times until the conductivity for supernatant was constant (~ 12.5 μs/cm). The TEMPO-oxidized cellulose nanofiber (TCNF) was prepared by blending the TEMPO-oxidized cellulose for 7 minutes. The carboxylate content for the TCNF was 0.84 mmol/g. The TCNF was centrifuged and adjusted to 3.5% w/v solid content. Freeze-dried cellulose pulp slurry (pure cellulose) and TCNF were characterized by Fourier Transform Infrared spectroscopy (FTIR).

Sodium alginate (ALG, Alfa Aesar, J61887, USA) was prepared into a 3.5% w/v solution. The concentrated TCNF and the ALG solution were sterilized by autoclave. The TCNF and ALG are mixed into various printing formulations (Table A.1) with a final solid content of 3.5% w/v.

Table A.1 TCNF/ALG precursor formulations

Precursors	Composition	Formulation (% w/v)	Solid content (% w/v)
0100	100% of ALG solution	ALG: 3.5	3.5
2080	20% TCNF 80% ALG	TCNF: 0.7 ALG: 2.8	3.5
5050	50% TCNF 50% ALG	TCNF: 1.75 ALG: 1.75	3.5
6040	60% TCNF 40% ALG	TCNF: 2.1 ALG: 1.4	3.5
7030	70% TCNF 30% ALG	TCNF: 2.45 ALG: 1.05	3.5
8020	80% TCNF 20% ALG	TCNF: 2.8 ALG: 0.7	3.5
9010	90% TCNF 10% ALG	TCNF: 3.15 ALG: 0.35	3.5

A.2.2 Rheological Characterization of TCNF/ALG Precursors as Potential Bioink Materials

The rheological properties of all the TCNF/ALG precursors were characterized using a rotatory rheometer (AR-G2, TA Instrument, USA) with a 25 mm parallel-plate geometry. The steady-

state flow sweep was characterized under the shear rate from 0.001 to 1000 s^{-1} at room temperature. The oscillatory frequency sweep was measured under 1% strain (within the linear viscoelastic region) and 1 to 100 rad/s frequency. The thixotropy tests were done by first fixing the shear rate at 0.001 s^{-1} for 100 s, followed by a sudden increase in the shear rate to 1000 s^{-1}, and then a sudden drop in the shear rate to the initial state (0.001 s^{-1}). The rheology data was analyzed using TRIOS software (TA Instruments, USA).

A.2.3 Assessment of Printing Fidelity Before and After Crosslinking

To assess the printability of the TCNF/ALG precursors, 20 mm x 20 mm x 3 mm blocks with a 30% infill were bioprinted using an extrusion-based bioprinter (INKREDIBLE+, CELLINK, Sweden). The geometry and printing parameters of the printed constructs were predefined in commercial design software (Slic3r, U.S.A.). The needle inner diameter was 0.413 cm (22G). The printing speed was 10 mm/s with each layer height of 0.5 mm (6 layers in total). After bioprinting, a 100 mM $CaCl_2$ solution was added over the bioprinted TCNF/ALG constructs for 3 minutes followed by a phosphate buffered saline (PBS) rinse. After crosslinking, the precursors with the best printing fidelity were used for further biological functionality evaluation. A commercially available bovine type I collagen gel with similar solid content to the TCNF/ALG precursors was used as a control (3.5% w/v, Advanced Biomatrix, USA). The type I collagen gel was printed at room temperature and spontaneously polymerized at 37°C. The fidelity parameter (side length of the square blocks (L) before and after the crosslinking, filament diameter) were quantified using Image J (Fiji, USA). The contractility from the crosslinking process was calculated as:

$$\text{contractility} = (L_{\text{before crosslinking}} - L_{\text{after crosslinking}})/L_{\text{before crosslinking}}.$$

A.2.4 Isolation of Human Meniscus Fibrochondrocytes

Meniscus specimens from three (3) male donors were collected from partial meniscectomy surgeries with the approval of the University of Alberta's Health Research Ethics Board - Biomedical Panel (Study ID: Pro00018778). Human meniscus fibrochondrocytes (hMFCs) were isolated enzymatically using collagenase digestion as previously described [398]. The primary hMFCs were plated at a density of 10^4 cells/cm^2 and expanded to passage 2 (P2) in monolayer culture in high glucose Dulbecco's Modified Eagle Medium (DMEM, Sigma Aldrich, Canada) supplemented with 10 v/v (%) fetal bovine serum (FBS), 1 ng/mL of TGF-β1 and 5 ng/ml of FGF-2 at 37 °C in normoxia (~20% O_2) conditions [398]. Donor information is shown in Table A.2 Meniscus donor information. The cumulative population doublings of the hMFCs at the end of P2 was 7.04 ± 0.21 (mean ± standard deviation).

Table A.2 Meniscus donor information

Donor	Sex	Age	Medical history	Anatomical site	Cumulative population doubling
1	Male	30	ACL reconstruction	Right knee medial	7.0
2	Male	27	Healthy	Left knee medial	7.3
3	Male	16	ACL tear	Right knee lateral	6.8

A.2.5 3D Bioprinting of TCNF/ALG and Collagen Bioinks

hMFCs at P2 were resuspended in a standard serum-free chondrogenic medium containing 10 ng/ml TGF-β3 [398]. The cell suspension was mixed with 7030, 8020 precursors (7030, 8020 bioinks), and type I collagen gel (COL bioink) to a cell density of 10^7 cells/mL.

To investigate the fibrocartilage formation of the bioprinted constructs after *in vitro* chondrogenic culture, hMFC-laden TCNF/ALG bioinks and COL bioink were bioprinted into cylindrical shapes (7 mm diameter, 3.5 mm height) with an infill rate of 70%. Then bioprinted constructs were crosslinked as before. At the same time, the hMFC-laden COL bioink were kept in a 37 ºC incubator for 30 minutes and then placed in a serum-free chondrogenic medium containing 10 ng/mL TGF-β3 (2 mL/ construct, twice per week) for 6 weeks under hypoxic conditions (3% O_2).

A.2.6 Viability in Bioprinted Constructs

hMFCs viability was assessed using Syto 13/Propidium iodide (PI) staining. Syto 13 (S7575, ThermoFisher, U.S.A.) is a green live-cell fluorescent nucleic acid stain, and PI (P3566, ThermoFisher) is a red dead-cell fluorescent nuclear and chromosome counterstain. The Syto 13 and PI concentrations in PBS were 6.25 μM and 15.0 μM, respectively.

Bioprinted constructs of TCNF/ALG (8020, 7030 bioinks) and COL bioinks after 1-day culture were incubated in Syto 13 and PI solution at room temperature for 30 minutes in the dark. The cell viabilities were viewed under a Nikon confocal laser scanning microscope (Leica TCS SP5). Fluorescence was quantified using Python.

A.2.7 Structural Integrity and Microstructural Evaluation of Bioprinted Constructs

Scanning electron microscopy (SEM., Zeiss Sigma 300 VP-FESEM) was used to observe the TCNF fibre diameter and the ECM formation of the bioprinted constructs after 6 weeks of *in vitro* culture. Each construct was fixed in sodium cacodylate trihydrate buffer containing 2% v/v glutaraldehyde and 2.5% v/v paraformaldehyde overnight. The samples were then cut in half and

washed twice with deionized water to wash away the fixation solution. The samples were further treated with osmium tetroxide and tannic acid before SEM observation. All the reagents were purchased from Electron Microscopy Sciences (Pennsylvania, USA).

A.2.8 Histological and Immunofluorescent Evaluation of Matrix Formation

Bioprinted constructs for three experiment groups (8020, 7030, COL) from the same donor were fixed in 10% (v/v) neutral buffered formalin, dehydrated through a series of alcohol washes, and then embedded in paraffin. The embedded samples were cut into 5 μm sections cross-sectionally.

For histological assessments, the sections were deparaffinized by the xylene substitute, then re-hydrated and stained with Safranin-O/Fast Green. Collagens I, II, and X as well as aggrecan were examined by immunofluorescence. In brief, sections were prepared as above. Collagens I and II were counterstained in one slide. Collagen X and aggrecan were stained separately in two slides. The primary antibodies for collagens I and II were rabbit anti-human type I collagen (CL50111AP-1, Cedarlane, Canada) and mouse anti-human type II collagen (II-II6B3, Developmental Studies Hybridoma Bank (DSHB), USA). The primary antibody for type X collagen (collagen X) was rabbit anti-human collagen X (rabbit polyclonal to collagen X, ab58632, Abcam, USA), and the primary antibody for aggrecan was a rabbit anti-human aggrecan (recombinant monoclonal to aggrecan, MA5-32695, ThermoFisher, USA).

After incubation with primary antibodies, the slides were incubated with secondary antibodies for 45 minutes. The secondary antibodies used for collagens I and II are goat anti-rabbit IgG Alexa Fluor 594 (ab150080, Abcam, USA) and goat anti-mouse IgG Alexa Fluor 488 (ab150117, Abcam, USA). The secondary antibodies used for collagen X and aggrecan were

goat anti-rabbit IgG Alexa Fluor 594 (ab150080, Abcam, USA). In addition, all the slides were also stained with 4',6-diamidino-2'- phenylindole (DAPI, Thermo Fisher Scientific) for 20 minutes at room temperature to examine the nuclei of hMFCs in each sample. A Nikon Eclipse Ti-S microscope coupled to a DS-U3/Fi2 Color CCD camera with 100x and 200x total magnification was used to capture the histological and immunofluorescent images.

A.2.9 Gene Expression Analysis

Quantitative real-time polymerase chain reaction (qRT-PCR) was used to analyze expression of genes that are chondrogenic and fibrochondrogenic specific (*ACAN, COL1A2, COL2A1, SOX9*) and chondrocyte hypertrophy-related (*COL10A1, MMP13, ALPL, RUNX2*). The analysis was conducted after 6 weeks (42 days) of *in vitro* chondrogenic culture. Total RNA was extracted using TRIzol (Life Technologies, USA). The complementary DNA (cDNA) was synthesized from 100 ng of total RNA using GoScript, Reverse Transcriptase kit (Promega, USA) and 1 µg of oligo (dT) primer. Primer sequences for qPCR were designed using Primer Express 3.0.1 (Thermo Fisher Scientific). Transcript levels for the interested genes were normalized to the housekeeping genes: *β-actin*, *B2M*, and *YWHAZ* using the delta CT method ($2^{-\Delta CT}$). Primer sequences are shown in Table A.3.

Table A.3 Primer sequences for quantitative real-time polymerase chain reaction

Gene	Forward Primer (5′)	Reverse Primer (3′)
B-actin	AAGCCACCCCAC-TTCTCTCTAA	AATGCTATCACCTCCCCTGTGT
B2M	TGCTGTCTCCATGTTT-GATGTATCT	TCTCTGCTCCCCACCTCTAAGT
YWHAZ	TCTGTCTTGTCACCAAC-CATTCTT	TCATGCGGCCTTTTTCCA
ACAN	AGGGCGAGTGGAATGATGTT	GGTGGCTGTGCCCTTTTTAC
COL1A2	GCTACCCAACTTGCCTTCATG	GCAGTGGTAGGTGATGTTCTGAGA
COL2A1	CTGCAAAA-TAAAATCTCGGTGTTCT	GGGCATTTGACTCACACCAGT

SOX9	CTTTGGTTT-GTGTTCGTGTTTTG	AGAGAAAGAAAAAGGGAAAGGTAAGTTT
COL10A1	GAAGTTATAATTTACAC-TGAGGGTTTCAAA	GAGGCACAGCTTAAAAGTTTTAAACA
RUNX2	GGAGTGGACGAGGCAAGAG-TTT	AGCTTCTGTCTGTGCCTTCTGG
VCAN	TGCTAAAGGCTGCGAATGG	AAAAAGGAATGCAGCAAAGAAGA
MMP13	AAAAAGGAATGCAGCAAA-GAAGA	CGGAGACTGGTAATGGCATCA
ALPL	GCTGTAAGGACATCGCC-TACCA	CCTGGCTTTCTCGTCACTCTCA

A.2.10 Biomechanical Characterization by Stress Relaxation Tests

The mechanical properties of bioprinted constructs were assessed using a stepwise stress relaxation test using a Biodynamic 5210 system (TA Instruments, USA). For each experimental group, constructs from n=3 donors were tested. The constructs were preconditioned by 15 cycles of sine wave dynamic compressive loading with an amplitude of 5% tissue height at a frequency of 1 Hz. The following stress relaxation test consisted of 4 incremental strain steps. In each step, the constructs were subjected to a 10% strain ramp at the rate of 50% strain/s and followed by 20 min relaxation under constant strain. All tested constructs reached equilibrium in the given relaxation period. Forces were recorded as a function of time, and stress was calculated by normalizing force to construct cross-section area. The peak modulus was calculated by dividing the maximum stress increment immediately after the compression increment by 10%, the strain increment.

A.2.11 Statistical Analysis

GraphPad Prism 8 was used to perform statistical analysis. The paired two-sample t-test was used to analyze the significance level between each sample group (8020 vs. COL, 7030 vs. COL,

7030 vs. 8020) in cell viability and in gene expression after taking the replicate means within donors. Two-way ANOVA was used to determine the statistical differences in stress relaxation tests for various bioinks at different strains with Tukey's test for multiple comparisons. The results were presented as mean ± standard deviation (SD).

A.3 Results

A.3.1 Rheology, and Printing Fidelity of TCNF/ALG Precursors

Figure A.2 presents the FTIR spectra of unmodified pure cellulose and TCNF. After TEMPO-oxidation, the characteristic absorption band of carboxyl group (C==O) stretching appeared around 1650 cm^{-1}, which is assigned to the formation of COO groups after the oxidation and release of nanofibers [484]. The enhancement of the -OH stretching group around 340 cm^{-1}, C-H at around 2900 cm^{-1}, and C-O-C at around 1050 cm^{-1} were also observed in TCNF, which indicated more -OH, C-O-C group are exposed.

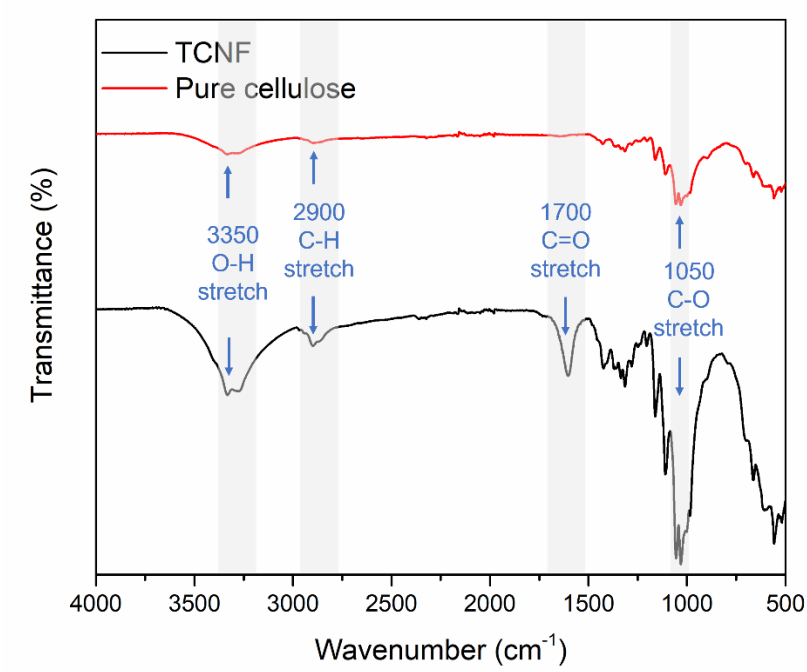

Figure A.2 Fourier transform infrared spectroscopy of the pure cotton cellulose and TCNF.

The rheology data of the TCNF/ALG precursors were measured to pre-estimate the printability as potential bioink materials. The viscosity vs shear rate (steady-state flow sweep) of all the TCNF/ALG precursors is shown in Figure A.3A. All TCNF/ALG precursors exhibited shear-thinning behaviour, in which the viscosity decreased as the shear rate increased. The Power Law model was also used to fit the viscosity vs shear rate curve (0.01 to 1000 s^{-1}) to describe the shear-shinning behaviour. The printing pressure of each TCNF/ALG precursors are shown in Table A.4. The viscosity and shear rate relationship can be described in the equation of the $\eta=K\dot{\gamma}^{n-1}$, where η is viscosity, $\dot{\gamma}$ is the shear rate, K and n are the empirical curves fitting parameters, known as the flow consistency index and flow behaviour index [171]. The fitted power-law parameters (K and n) are shown in Table A.4. For shear thinning fluid, n always less than 1. The lower the n, the better the shear-thinning behaviour responding to the increase of shear rate. TCNF, 8020, 9010 exhibited the highest zero-shear viscosity and the best shear thinning behaviour. 5050 exhibited the lowest zero-shear viscosity and the worst shear-thinning behaviour.

Table A.4 Fitted Power-Law parameters, thixotropy recovery rate, printing pressure, filament diameter and contractility after crosslinking

	ALG	2080	5050	6040	7030	8020	9010	TNCF
K	432.90	503.13	232.78	194.70	237.04	137.63	155.43	156.43
n	0.24	0.23	0.25	0.19	0.18	0.13	0.14	0.16
Recovery (%)	81.6±5.6	75.2±2.0	53.4±1.6	50.2±13.0	63.7±4.6	71.8±4.1	62.1±2.1	45.1±3.6
Pressure (kPa)	200	155	125	75	75	55	55	
Filament Diameter			0.88±0.02	1.04±0.08	0.79±0.02	0.72±0.00	0.76±0.02	
Contraction (%)	29.5%	28.8%	15.3%	10.2%	9.5%	4.3%	1.0%	

*The filaments of the mesh printed by pure ALG and 2080 bioink material fused together and their diameter could not be measured

The recovery and thixotropic properties were determined by applying a steady shear rate of 1 s^{-1} for 100 s suddenly increasing the shear rate to 1000 s^{-1} for 100 s, and then reducing it to 1 s^{-1} for 100 s. Figure A.3B depicts the thixotropic behaviour of the prepared hydrogels. The viscosity of the all the TCNF/ALG precursors rapidly dropped with an applied shear (printing stage) and recovered quickly after the shear force was removed (post-printing stage). However, all the samples were thixotropic and decreased in viscosity after recovery. The average viscosities of the TCNF/ALG precursors under the three shear rate stages are recorded in Table S1. The recovery rates (initial/final viscosity) are shown in Table A.4.

The frequency sweep tests were performed within the linear viscoelastic deformation region. Loss tangent (tan δ), the ratio of loss moduli (G'') and storage moduli (G'') for TCNF/ALG precursors as a function of frequency are shown in Figure A.3C. The loss tangent (tan δ) determines if a material is solid-like or liquid-like. All the TCNF/ALG precursors showed a solid-like

behaviour (G'>G'', tan δ<1). The pure TCNF, 8020, and 9010 showed the most solid-like behaviour followed by 6040, 7030, 2080, and pure ALG and 5050 showed the least solid-like behaviour.

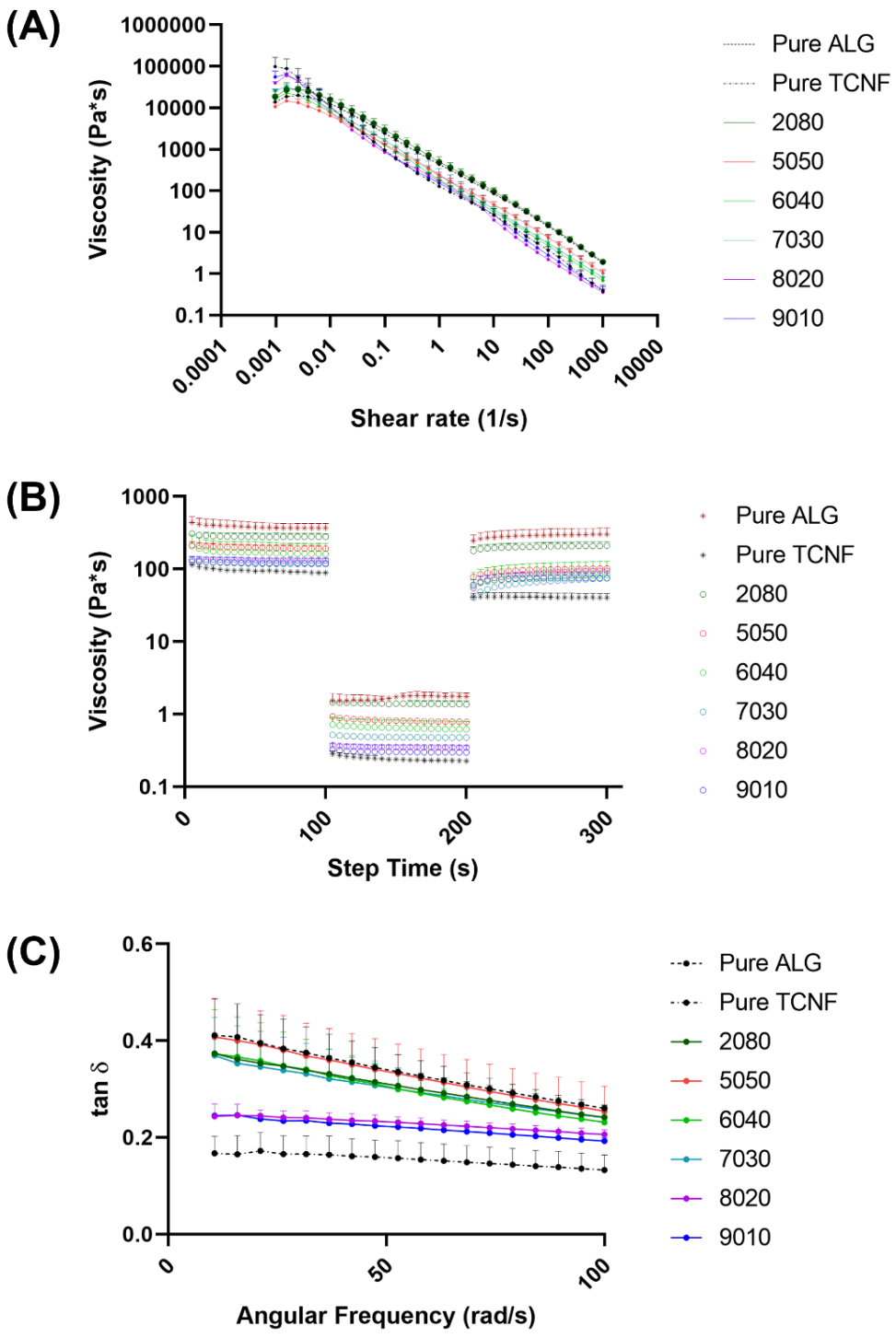

Figure A.3 The rheology behaviors of the TCNF/ALG precursors. (A) the steady state flow sweeps, strain rate from 0.001 to 1000 s-1 (B) three-step recovery and thixotropic behavior, low shear rate at 1 s-1 for 100 s for initial and final step, high shear rate at 1000 s-1 for 100s for middle step, (C) loss tangent of the TCNF/ALG precursors from 1 to 100 rad/s. The formulations are described in Table A.1.

The TCNF/ALG precursors were then bioprinted into mesh shapes and crosslinked using 100 mM of $CaCl_2$ solution. The bioprinted constructs before and after crosslinking are shown in Figure A.4A. The printing pressure, filament diameter and contractility after crosslinking are shown in Table A.4. Apparent size and shape contractions are observed in the TCNF/ALG precursors with low or no TCNF content (0100, 2080, 5050, 6040). On the other hand, the 7030, 8020, and 9010 showed the lowest contractility (≤10%) and best printing fidelity (finest filament diameter). Due to the relatively low alginate content, the 9010 was too soft to retain its shape during transfer or movement of the construct. Therefore, the 7030 and 8020 formulations were selected as bioinks to mix with hMFCs for further biochemical and biomechanical evaluations.

The LIVE/DEAD assay images after bioprinting using a 22 G needle are shown in Figure A.4B. No statistically significant difference was observed between 7030 and 8020 bioinks. The type I collagen bioink showed a significantly higher cell viability compared to the 8020 bioink.

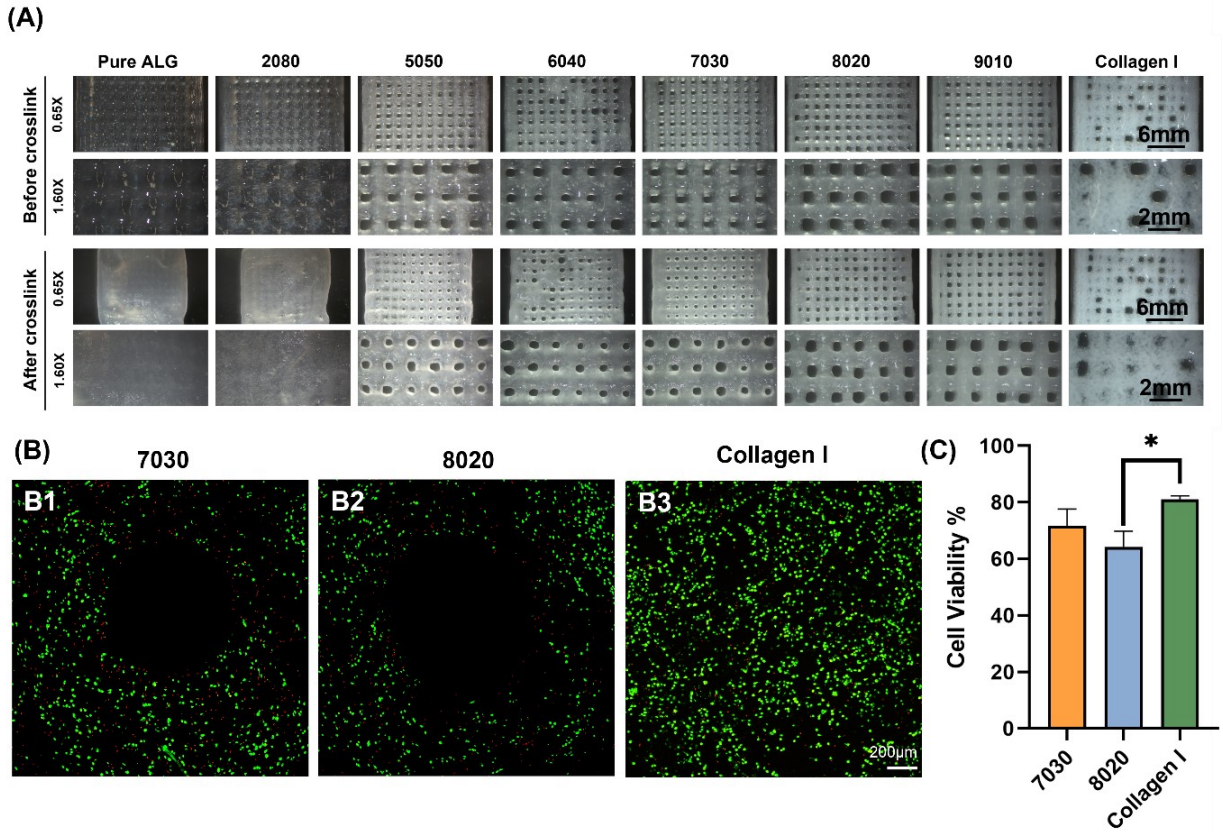

Figure A.4 (A) Printed mesh structures using different formulations of TCNF/ALG precursors (B) Live/dead images of the (B1) 7030, (B2) 8020, and (B3) COL bioinks. Live cells appear green and dead cells red. (C) Quantitative cell viability of the Live/Dead assay images

A.3.2 Histological and Biochemical Assessments

It is commonly understood that Safranin-O would only stain when sulfated GAG is present within the sample. Interestingly, we discovered that cellulose nanofibers (TCNF) could also be stained by Safranin-O despite lacking sulfated GAG, as shown in Figure S1 in supplemental materials. Previous studies which used CNFs as biomaterials for meniscus tissue engineering did not report this phenomenon [339]. Through comparing against cell-free CNF samples, it was still possible to distinguish the Safranin-O positive matrix throughout the histological sections of two TCNF/ALG bioink (Figure A.3A/B). In contrast, the bioprinted COL bioink did not show any positive safranin-O positive matrix deposition throughout the section (Figure A.5E, F).

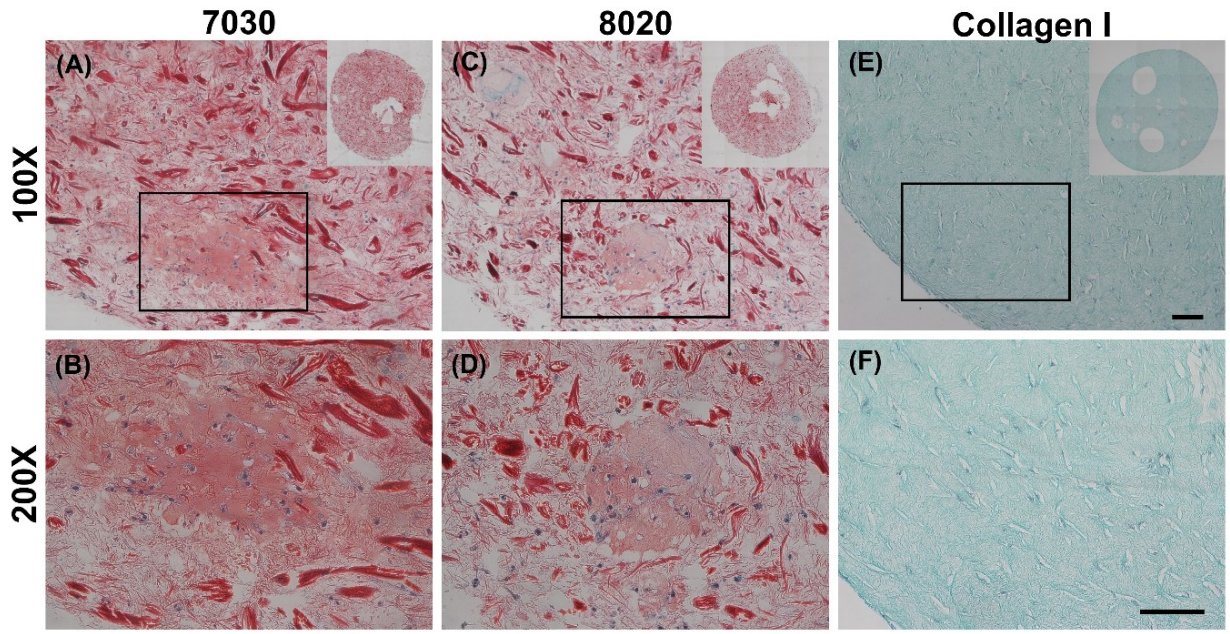

Figure A.5 Safranin-O staining (red, stained negatively charged proteoglycans and the TCNF) with Fast Green counterstain (green, stained proteins) and cells stained with hematoxylin of (A & B) 7030, (C & D) 8020, and (E & F) COL I bioinks. Scale bar is 100 μm.

Positive aggrecan immunofluorescent staining was shown in both TCNF/ALG bioinks (Figure A.6A&B) but not in the COL bioink (Figure A.6C), which was consistent with the Safranin-O staining results. The immunofluorescence staining also showed a universal presence of type I collagen in two TCNF bioinks (Figure A.6D&E) and the COL bioink (Figure A.6F). The COL bioink showed more densely packed type I collagen compared to the two TCNF/ALG bioinks. However, type II collagen was present in the two TCNF/ALG bioinks (Figure A.6D&E) and not in the COL bioink (Figure A.6F). The type II collagen matrix was most concentrated at the outer edges of the constructs. There was no detectable collagen X immunofluorescence in any constructs (6G, 6H and 6I). The SEM images of the 7030 and 8020 bioinks after 6 weeks of *in vitro* chondrogenic culture are depicted in Figure A.7. Newly synthesized ECM was observed on the surface of the bioprinted constructs for both 7030 and 8020 bioinks. The TCNF material was visible under the ECM.

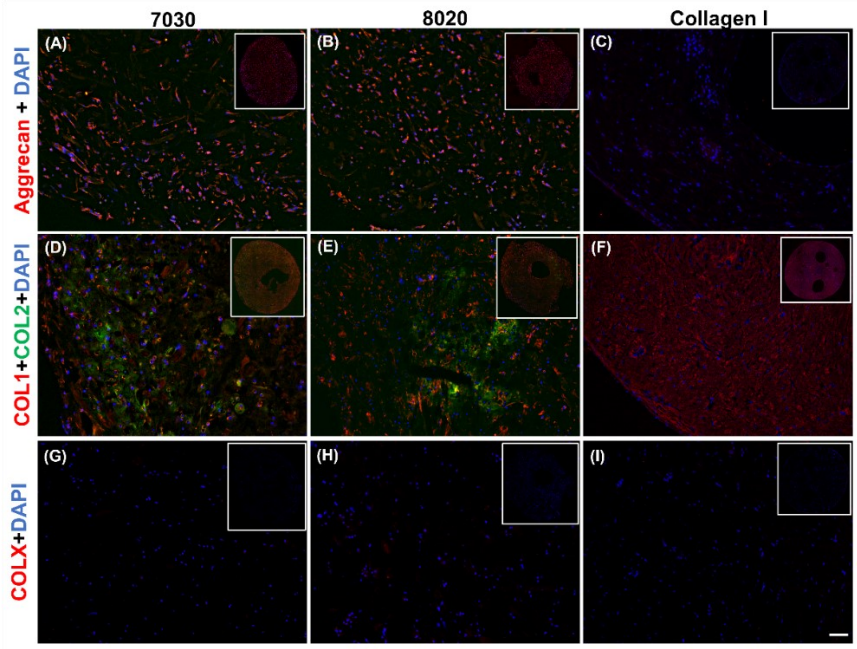

Figure A.6 Immunofluorescent staining of (A, B, & C) of aggrecan (red), (D, E & F) collagens I and II (red and green, respectively), and (G, H & I) collagen X. The staining of nuclei is blue. Scale bar is 100 µm

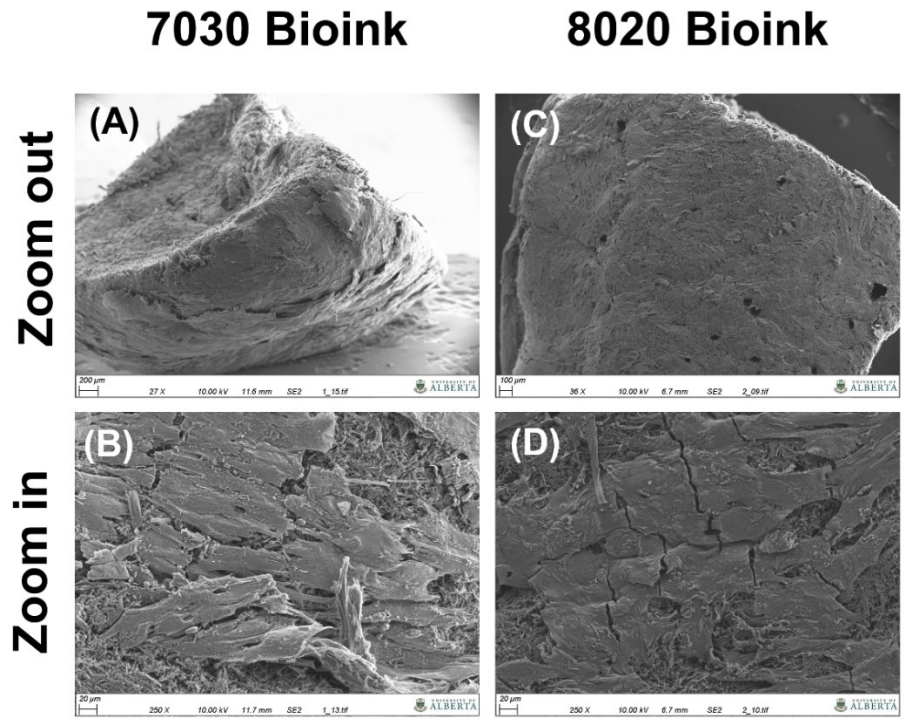

Figure A.7 SEM images of the bioprinted constructs after 6 weeks of *in vitro* culture, (A & B) the cross-section of the 7030 bioink (C & D) surface of the 7030 bioink, (E & F) cross-section of the 8020 bioink, (G & H) surface of the 8020 bioink

The mRNA expression of fibrocartilage-related (*ACAN*, *COL1A2*, *COL2A1*, *SOX9,* and *VCAN*) and bone-related (*COL10A1, MMP13, ALPL, RUNX2*) genes are shown in Figure A.8. For all these genes, no significant differences were observed between the 7030 and 8020 bioinks. The fibrous markers, *COL1A2* and *VCAN* in the COL bioink were higher than in 7030 bioinks with near statistical significance (i.e., p=0.086 and p=0.077, respectively). The cartilaginous marker *COL2A1* in the COL bioink was significantly lower compared to the 7030 bioink. No statistically significant difference was observed among the three bioinks in gene expression of *ACAN* and *SOX9*. No significant difference was noted in *ALPL*, and *RUNX2* among the three groups for these bone formation-related genes. On the other hand, there was an upregulation of *MMP13* in the COL bioink compared to 7030 and 8020 with near statistical significance (i.e., p=0.066 and p=0.076, respectively). The expression of *COL10A1* expression in the COL bioink for each donor increased but with no detectable significant difference.

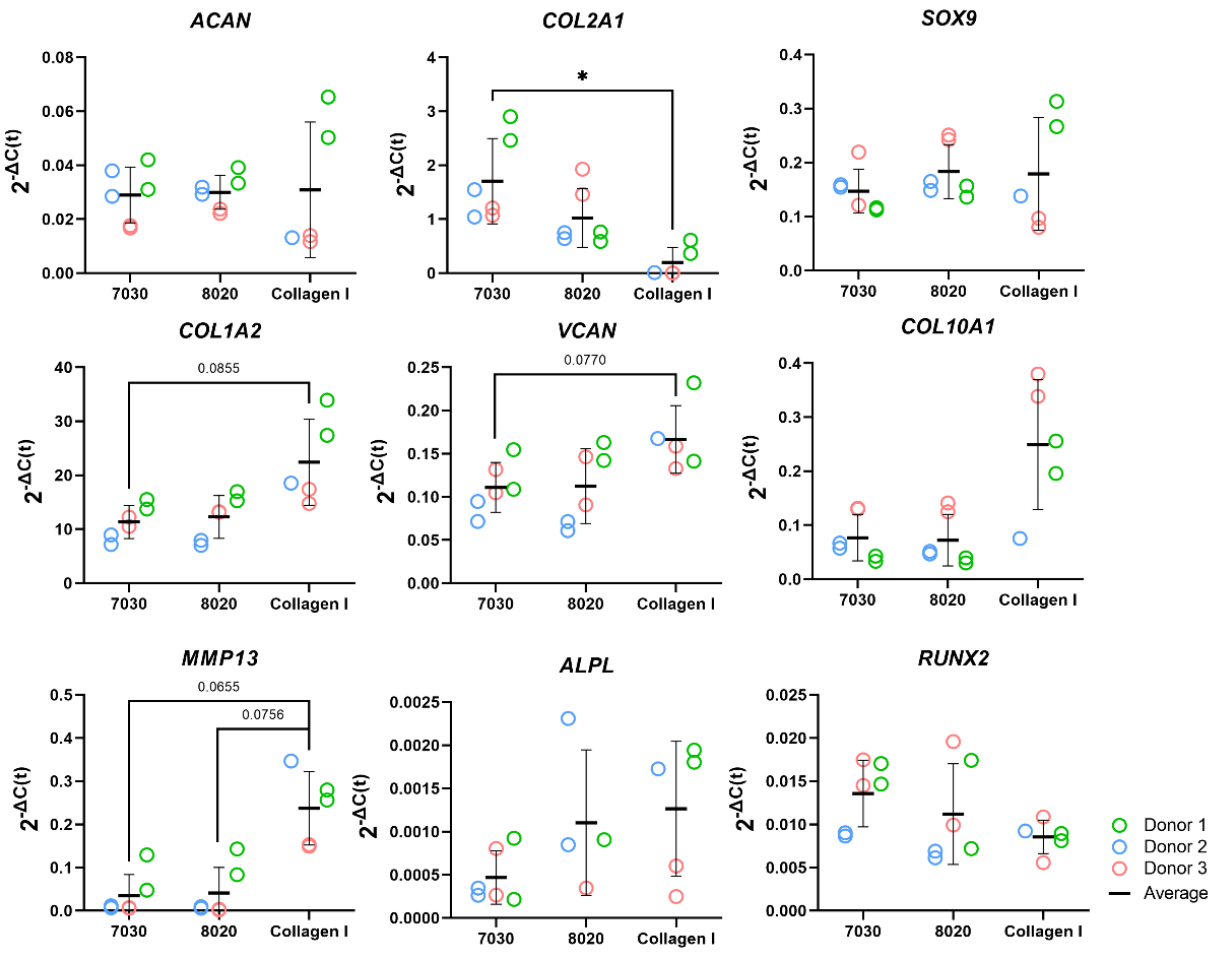

Figure A.8 Fibrocartilage related gene expression of bioprinted constructs after 6 weeks of *in vitro* chondrogenic culture (n=3). * represents $p<0.05$

After the strain-controlled unconfined compression test, the peak modulus (instantaneous modulus) was calculated using the force change between the peak and equilibrium forces at each relaxation period. The calculated values were normalized by the cross-sectional area of the 3D bioprinted tissues. The stepwise stress-relaxation as a function of time of one donor (0-10%, 10-20%, 20-30%, and 30-40% strain for each force jump) and the peak modulus as a function of the cumulative strain is shown in Figure A.9A and B. No significant interaction was observed between material type and strain in the two-way ANOVA. Therefore, only the main effects of each factor, i.e. strain and bioink material, were tested. Strain was the only significant main effect for

the compressive modulus, with the significant differences between each strain level, except for 30% vs, 40%.

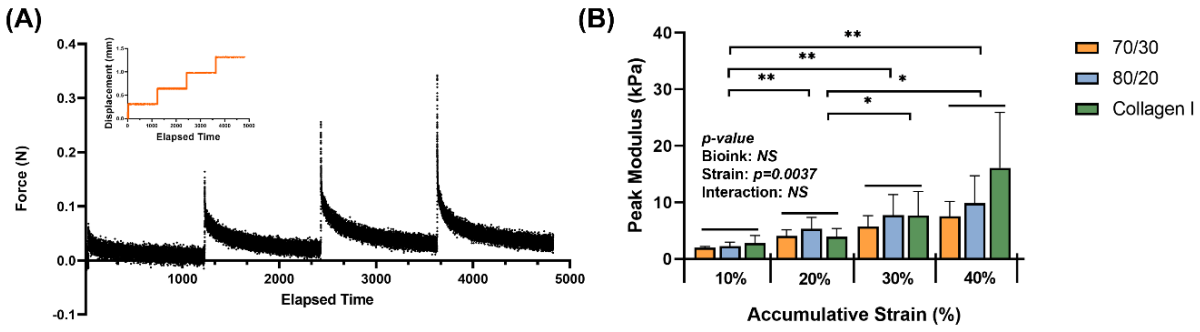

Figure A.9 Mechanical properties of the bioprinted constructs: (A) an example of data acquisition of the strain-controlled unconfined compression test (B) the peak modulus as a function of the cumulative strain (n=3). * represents $p<0.05$

A.4 Discussion

The newly appeared carboxyl group (C=O) indicated the successful oxidation of the cellulose using TEMPO. The exposure of O-H and C-O-C groups may be due to the mechanical processing of the cellulose. The smaller size of the cellulose fibres allowed for exposure of more surface groups.

In the steady-state flow sweep test (Figure A.3A), all TCNF/ALG precursors exhibited a shear-thinning behaviour, which may be attributed to the loss of chain entanglement as well as the alignment of polymeric chains/fibre under steady-state shear. As the shear rate increases, the entanglement of the hydrogel networks is weakened and the entrapped liquid that resists the flow is released, therefore induce decreased viscosity. Better shear-thinning behaviour is desired for the 3D bioprinting process, since under fixed printing speed and needle size lower bioink viscosities in the printing needle will result in lower shear stress experienced by cells, resulting in better cell viability. The formulation of the TCNF/ALG precursors has a strong effect on the shear-thinning

behaviour. For alginate rich TCNF/ALG precursors (TCNF content between 0 to 50%), increasing the TCNF content did not show an significant change in the shear thinning behavior of the fluid. In contrast, for TCNF-rich TCNF/ALG precursors (TCNF content between 50 to 100%), a higher TCNF content led to better shear-thinning behaviour. Under fixed printing speed, the required printing pressure decreased dramatically as the TCNF content increased due to the enhanced shear-thinning effect (Table A.4).

The thixotropic property is an important parameter to predict printing fidelity. Abouzeid et al found that the higher the recovery rate (initial/finial viscosity) of the bioinks, the better the printing fidelities. They found the printed scaffolds had the best printing fidelity with the most uniform widths and stable shapes at 66% recovery rate, which is the highest recovery rate among the investigated bioink formulations [485]. However, our results only partially agreed with their findings. The pure ALG (81.6%), 2080 (75.2%), 8020 (71.8%), 7030 (63.7%), and 9010 (62.1%) showed a relatively high recovery rate (recovery > 60%). Only 7030, 8020, and 9010 exhibited uniform width and clear edges throughout the printed shape. The filaments printed by pure alginate precursors, which has the highest recovery rate, collapsed and fused with neighbouring filaments. These results show that there are some other rheology parameters can affect printability as well. Gao et al stated that the loss tangent is an important parameter for predicting structural integrity and extrusion uniformity [486]. For pure alginate precursors, the tan δ is 0.41 in the low-frequency range (10 rad/s), which is in the relatively high loss tangent range stated by Gao et al [486]. The high loss tangent represents lower structural integrity (the collapse and fusion of the bioprinted structure), but better extrusion uniformity. The high tan δ explains the reason why pure alginate exhibits poor printing fidelity even it has a high thixotropic recovery rate. This statement is further validated in the bioprinting of type I collagen gel. In our previous study, the

type I collagen gel showed more liquid-like behaviour, requiring it to be printed in a support bath [215]. In this study, we directly printed the type I collagen gel without the supporting bath to compare the printability with TCNF/ALG precursors. We found that the printed type I collagen filaments tend to spread out after bioprinting, which resulted in poor printing fidelity.

It is also important for the bioink to retain its original shape during the crosslinking stage. We found that the alginate-rich TCNF/ALG precursors (0100, 2080, 5050, 6040) all exhibited high contractility after printing (≥10%). The contraction of the bioprinted constructs may contribute to the stability of the swelled alginate polymer chains in water after crosslinking. The alginate polymers are firstly dispersed and swelled in water. By adding the Ca^{2+} ions to alginate, the Ca^{2+} cations are coordinately bound to the COO^- group in the alginate polymer chain and arranged into an "egg-box" model[487, 488]. The 7030, 8020, and 9010 showed the best printing fidelity and lowest contractility after bioprinting. Due to the low alginate content of 9010, changing in shape is observed during transporting the bioprinted construct using 9010 (the distortion of the printed shape); therefore, only 7020 and 8020 were mixed with hMFCs (7030, 8020 bioinks) to generate tissue-engineered fibrocartilages.

A LIVE/DEAD assay was performed to investigate the biocompatibility of the bioprinted constructs. The COL bioink showed higher cell viability and higher cell numbers compared to the TCNF/ALG bioinks. It is speculated that the higher cell viability with the COL bioink is due to the relatively lower printing pressure, the presence of cell adhesive motifs in the protein-based hydrogel, and that the hMFCs' natural host material is type I collagen.

After 6 weeks of culture, hMFC-deposited ECM was observed in both 7030 and 8020 bioinks under SEM (Figure A.7). A dense layer of ECM covered the cellulose nanofibers. The histology

and immunofluorescence results further confirmed the ECM formation in the 7030 and 8020 bioinks. The staining results suggest that the hMFC-laden TCNF/ALG bioinks (7030, 8020) support development of a more inner meniscus fibrocartilage-like phenotype (presence of sGAG, type I and II collagens), while the (bovine) COL bioink supports a more outer meniscus phenotype of no Safranin-O positive ECM with the presence of newly-synthesized human type I collagen. Neither the cellulose nanofibers nor the alginate present a natural cell binding site. The lack of a cell-binding site forces the monolayer-expanded hMFCs into a round shape which is known to promote a chondrogenic phenotype [450]. In contrast, type I collagen presents natural cell-binding motifs through its interaction with the integrins that provide focal adhesion points to the hMFCs [489]. The focal adhesions can support cell spreading, which may facilitate the development of more outer meniscus-like phenotypes. The fibrocartilage matrix phenotypes at the mRNA level also agree with the histological and immunofluorescence findings (Figure A.8).

Our observations agree with Daly et al's finding that alginate and agarose bioinks (bioinks without cell-binding sites) support the development of hyaline-like cartilage tissue, while GelMA and PEGDA bioinks (bioinks with a native binding site) better support the development of fibrocartilage-like tissue [450]. As shown in Figure A.8, the lack of cell-binding sites in the TCNF/ALG bioinks correlated with reduced expression of *COL10A1* and *MMP13* (indicators of hypertrophic chondrocytes during endochondral ossification). The upregulation of these two genes is more likely to occur when integrin-binding (α2 integrin) between hMFCs and type I collagen is present. The α2 integrin is a subunit of the most known type I collagen receptor (α2β1). The interaction between this α2 integrin subunit and type I collagen facilitates osteoblastic differentiation, an important event in the expression of the osteogenic phenotype [490, 491].

Although proteoglycans mainly contribute to a tissue's compressive strength, the bioprinted TCNF/ALG bioink constructs did not show a higher compressive modulus compared to the COL bioink-based constructs. The average compressive modulus at the 30-40% strain step was higher than in the two TCNF/ALG bioinks, but no significant difference was observed. Hence, the engineered matrix composition does not fully correspond to the mechanical properties of the engineered tissue. One plausible explanation is that the crosslinking of the COL bioink constructs was augmented via endogenous lysyl oxidase expression, which can be induced by hypoxic culture [492]. The cations that crosslink alginate chains may also be released into the culture media and washed away during the media changes, which may diminish the mechanical properties of the TCNF/ALG constructs.

One limitation of the present study is the low number of human meniscus donors used, leaving uncertainty regarding donor-to-donor differences. Another limitation is the lack of an *in vivo* study of the bioprinted constructs. The *in vivo* stability of the deposited ECM within the constructs in regard to *in vivo* calcification, bone formation, vascularization, and the retention of the Safranin-O positive ECM after implantation merits future investigation.

A.5 Supplementary material

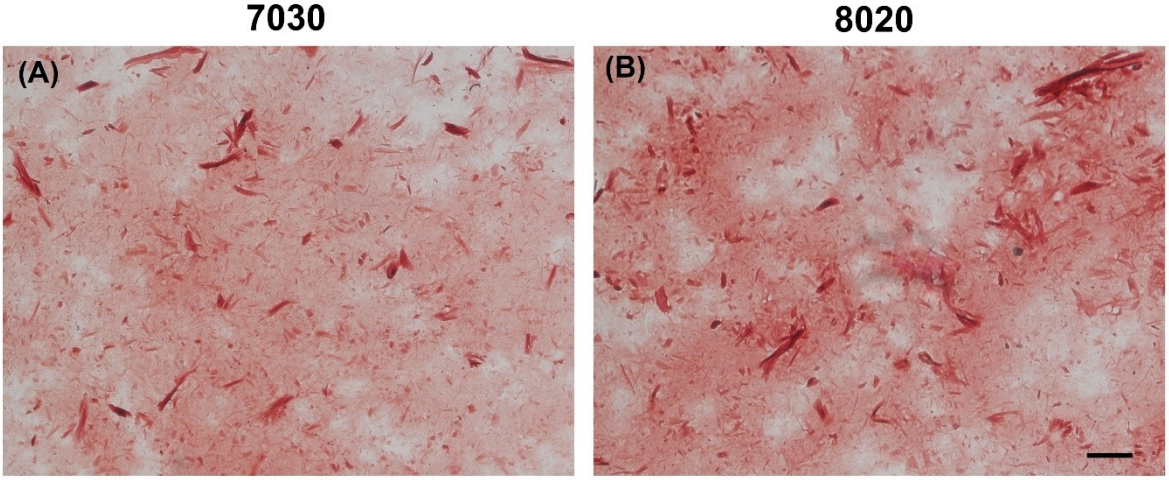

Figure A.S 1 Safranin-O staining of the empty TCNF/ALG scaffold (A) 7030 (B) 8020. Scale bar is 100 μm

Table A.S 1 Thixotropic viscosities of TCNF/ALG bioinks. The η is the measured viscosity for each shear step

	Pure ALG (0100)	2080	5050	6040	7030	8020	9010	Pure TCNF
Initial low strain phase η (Pa*s) Shear rate $\dot{\gamma}$ = 1 s^{-1}	367.0±47.3	277.6±25.5	191.3±15.7	161.8±52.0	117.2±2.5	131.6±6.3	120.0±17.0	88.9±5.3
High strain phase η (Pa*s) Shear rate $\dot{\gamma}$ = 1000 s^{-1}	1.8±0.2	1.4±0.1	0.8±0.0	0.6±0.1	0.5±0.0	0.30±0.0	0.3±0.1	0.2±0.0
Finial low strain phase η (Pa*s) Shear rate $\dot{\gamma}$ = 1 s^{-1}	301.5±54.0	209.3±23.4	102.0±6.0	82.9±36.4	74.5±2.8	94.5±5.6	74.9±12.4	40.2±4.6